

Electronic Properties of and Carrier Dynamics in self-organized Quantum Dots for Memories

vorgelegt von

Diplom-Physiker

Robert Tobias Heinrich Nowozin

aus Berlin

von der Fakultät II - Mathematik und Naturwissenschaften
der Technischen Universität Berlin
zur Erlangung des akademischen Grades

Doktor der Naturwissenschaften

- Dr. rer. nat. -

genehmigte Dissertation

Promotionsausschuss:

Vorsitzender: Prof. Dr. Michael Lehmann

Berichter/Gutachter: Prof. Dr. Dieter Bimberg

Berichter/Gutachter: Prof. Dr. Axel Lorke

Tag der wissenschaftlichen Aussprache: 14. Juni 2013

Berlin 2013

D83

Abstract

This work investigates the electronic properties of and carrier dynamics in self-assembled semiconductor quantum dots (QDs) by means of static capacitance-voltage (C-V) spectroscopy, Deep-Level Transient Spectroscopy (DLTS), and time-resolved current measurements. The background and motivation is to further increase the storage time in a memory device based on self-assembled QDs, and to study the read-out process in such a memory. Hence, the work consists of two parts.

In the first part, the electronic properties, such as the hole localization energy and the apparent capture cross section, are studied for various material systems. GaSb/GaAs QDs with and without $\text{Al}_x\text{Ga}_{1-x}\text{As}$ barriers are studied by DLTS. The localization energies found for the GaSb/GaAs QDs are between $460(\pm 20)$ meV and $760(\pm 20)$ meV. The maximum localization energy of $800(\pm 50)$ meV is reached with additional $\text{Al}_{0.3}\text{Ga}_{0.7}\text{As}$ barriers. The apparent capture cross sections are between $1 \cdot 10^{-12}$ cm² and $5 \cdot 10^{-11}$ cm². Based on the theory of thermal emission, a storage time at room temperature between 100 ns and 80 ms is extrapolated for these values. Compared to previous work, the localization energy in QDs was increased, but due to a smaller apparent capture cross section, the storage time is still smaller than previously achieved values. For the first time, GaSb/GaAs quantum rings (QRs) are studied by DLTS. As a result of their smaller size compared to QDs, a localization energy of just $380(\pm 10)$ meV is found, while the apparent capture cross section is comparable to the one of QDs. Also for the first time, a sample based on QDs in a GaP matrix is investigated. A mean activation energy of $450(\pm 20)$ meV with an apparent capture cross section of $2 \cdot 10^{-13}$ cm² is found for $\text{In}_{0.25}\text{Ga}_{0.75}\text{As}/\text{GaAs}/\text{GaP}$ QDs, resulting in a room temperature storage time of 3 μs .

In the second part, the coupling of a layer of InAs QDs to an adjacent two-dimensional hole gas (2DHG) is studied for a series of samples with different tunneling barriers. C-V measurements and time-resolved current measurements reveal the level-splittings of the many-particle hole levels in the InAs QDs. The values are found in good agreement with predictions from 8-band $\mathbf{k}\cdot\mathbf{p}$ theory. For the first time, these measurements are also performed at temperatures above 4 K. The emission and capture processes between the QDs and the 2DHG are studied and give insight into the type of the emission and capture processes, which change from pure tunneling to thermal-assisted tunneling when the temperature is increased.

Based on the results of this work, recommendations for novel heterostructures are given: GaSb/ $\text{Al}_x\text{Ga}_{1-x}\text{As}$ with an Al-content beyond 30%, $\text{GaSb}_x\text{P}_{1-x}/\text{Al}_y\text{Ga}_{1-y}\text{P}$ QDs, and nitride-based QDs. These materials further increase the localization energy and the storage time in a QD-based memory, possibly to more than ten years at 300 K. An enhanced device design optimizes the device for fast operation at room temperature.

Zusammenfassung

Die vorliegende Arbeit untersucht die elektronischen Eigenschaften und die Ladungsträgerdynamik in selbstorganisierten Halbleiter-Quantenpunkten (QDs) mittels Kapazitäts-Spannungs (C-V) Spektroskopie, Deep-Level Transient Spectroscopy (DLTS) und zeitaufgelösten Strommessungen. Der Hintergrund und die Motivation sind dabei die weitere Erhöhung der Speicherzeit in einem quantenpunkt-basierten Speicher, sowie die Untersuchung des Ausleseprozesses in einem solchen Speicher. Deshalb gliedert sich die Arbeit in zwei Teile.

Im ersten Teil werden die elektronischen Eigenschaften, also die Lokalisierungsenergie und der Einfangquerschnitt, für unterschiedliche Materialsysteme untersucht. GaSb/GaAs QDs mit und ohne $\text{Al}_x\text{Ga}_{1-x}\text{As}$ -Barrieren werden mittels DLTS untersucht. Die Lokalisierungsenergien für die GaSb/GaAs QDs liegen zwischen $460(\pm 20)$ meV und $760(\pm 20)$ meV. Die höchste Lokalisierungsenergie von $800(\pm 50)$ meV wird in einem System mit zusätzlichen $\text{Al}_{0.3}\text{Ga}_{0.7}\text{As}$ -Barrieren erreicht. Die Einfangquerschnitte liegen zwischen $1 \cdot 10^{-12}$ cm² und $5 \cdot 10^{-11}$ cm². Basierend auf der Theorie der thermischen Emission lassen sich mit diesen Werten die Speicherzeiten bei Raumtemperatur extrapolieren, welche zwischen 100 ns und 80 ms liegen. Im Vergleich zu früheren Arbeiten konnte die Lokalisierungsenergie in QDs also gesteigert werden, auf Grund des größeren Einfangquerschnitts liegt die Speicherzeit jedoch unterhalb des bisherigen Rekords für QDs. Zum ersten Mal wurden im Rahmen dieser Arbeit GaSb/GaAs Quantenringe (QRs) mittels DLTS untersucht. Durch die kleinere Größe im Vergleich zu den QDs, haben die QRs nur eine Lokalisierungsenergie von $380(\pm 10)$ meV, wobei der Einfangquerschnitt vergleichbar mit dem der QDs ist. Ebenso zum ersten Mal wurden QDs in einer GaP-Matrix untersucht. Hier wurde eine mittlere Aktivierungsenergie von $450(\pm 20)$ meV bei einem Einfangquerschnitt von $2 \cdot 10^{-13}$ cm² für $\text{In}_{0.25}\text{Ga}_{0.75}\text{As}/\text{GaAs}/\text{GaP}$ QDs bestimmt. Diese Werte führen zu einer Speicherzeit von 3 μs bei 300 K.

Im zweiten Teil der Arbeit wird die Kopplung einer Schicht von InAs QDs an ein benachbartes zweidimensionales Lochgas (2DHG) in einer Serie von Proben mit unterschiedlichen Tunnelbarrieren untersucht. C-V und zeitaufgelöste Strommessungen erlauben die Bestimmung der Energieabstände zwischen den einzelnen Vielteilchen-Lochzuständen in den InAs QDs. Die gemessenen Werte stimmen gut mit vorhergesagten Werten der 8-Band **k-p**-Theorie überein. Zum ersten Mal werden diese Messungen auch bei Temperaturen oberhalb von 4 K durchgeführt. Dabei werden die Emissions- und Einfangtransienten eingehender untersucht. Sie erlauben die Identifikation der zugrunde liegenden Prozesse, welche bei Erhöhung der Temperatur von reinen Tunnelprozessen zu thermisch-assistierten Tunnelprozessen übergehen.

Basierend auf den Ergebnissen dieser Arbeit werden Vorschläge für neue Materialkombinationen gemacht: GaSb/ $\text{Al}_x\text{Ga}_{1-x}\text{As}$ mit einem Al-Gehalt oberhalb von 30%, $\text{GaSb}_x\text{P}_{1-x}/\text{Al}_y\text{Ga}_{1-y}\text{P}$ QDs und Nitrid-basierte QDs. Diese Materialien werden die Lokalisierungsenergie und somit die Speicherzeit in einem QD-basierten Speicher weiter erhöhen, möglicherweise sogar bis zu zehn Jahren Speicherzeit bei 300 K. Vorschläge für ein verbessertes Design optimieren den Speicher für den schnellen Betrieb bei Raumtemperatur.

Publications

Parts of this work have been published:

- Dieter Bimberg, Andreas Marent, Tobias Nowozin and Andrei Schliwa
Antimony-based quantum dot memories
Proc. SPIE **7947**, 79470L (2011)
- T. Nowozin, A Marent, G. Hönig, A. Schliwa, D. Bimberg, A. Beckel, B. Marquardt, A. Lorke, and M. Geller
Time-resolved high-temperature detection with single charge resolution of holes tunneling into many-particle quantum dot states
Phys. Rev. B **84**, 075309 (2011)
- T. Nowozin, A. Marent, D. Bimberg, A. Beckel, B. Marquardt, A. Lorke, and M. Geller
Time-resolved detection of many-particle hole states in InAs/GaAs quantum dots using a two-dimensional hole gas up to 77 K
Phys. Status Solidi C **9**, No. 2, 243-246 (2012)
- T. Nowozin, A. Marent, L. Bonato, A. Schliwa, D. Bimberg, E.P. Smakman, J.K. Garleff, P.M. Koenraad, R.J. Young, and M. Hayne
Linking structural and electronic properties of high-purity self-assembled GaSb/GaAs quantum dots
Phys. Rev. B **86**, 035305 (2012)
- G. Stracke, A. Glacki, T. Nowozin, L. Bonato, S. Rodt, C. Prohl, H. Eisele, A. Schliwa, A. Strittmatter, U.W. Pohl, and D. Bimberg
Growth of $In_{0.25}Ga_{0.75}As$ quantum dots on GaP utilizing a GaAs interlayer
Appl. Phys. Lett. **101**, 223110 (2012)
- T. Nowozin, L. Bonato, A. Högner, A. Wiengarten, D. Bimberg, Wei-Hsun Lin, Shih-Yen Lin, C. J. Reyner, Baolai L. Liang, and D. L. Huffaker
800 meV localization energy in GaSb/GaAs/ $Al_{0.3}Ga_{0.7}As$ quantum dots
Appl. Phys. Lett. **102**, 052115 (2013)

Other publications:

- M. Geller, A. Marent, T. Nowozin, D. Bimberg, N. Akçay, and N. Öncan
A write time of 6 ns for quantum dot-based memory structures
Appl. Phys. Lett. **92**(9), 092108 (2008)
and Virtual Journal of Nanoscale Science & Technology **17**, 11 (2008)
- M. Geller, A. Marent, T. Nowozin, D. Feise, K. Pötschke, N. Akçay, N. Öncan,
and D. Bimberg
Towards an universal memory based on self-organized quantum dots
Physica E **40**(6), 1811-1814 (2008)
- M. Geller, A. Marent, T. Nowozin, and D. Bimberg
Self-organized quantum dots for future semiconductor memories
J. Phys. - Condens. Mat. **20**(45), 4 (2008)
- T. Nowozin, A. Marent, M. Geller, D. Bimberg, N. Akçay, and N. Öncan
*Temperature and electric field dependence of the carrier emission processes in a
quantum dot-based memory structure*
Appl. Phys. Lett. **94**(4), 042108 (2009)
and Virtual Journal of Nanoscale Science & Technology **19**, 6 (2009)
- A. Marent, T. Nowozin, J. Gelze, F. Luckert, and D. Bimberg
Hole-based memory operation in an InAs/GaAs quantum dot heterostructure
Appl. Phys. Lett. **95**(24), 3 (2009)
and Virtual Journal of Nanoscale Science & Technology **21**, 1 (2010)
- A. Marent, T. Nowozin, M. Geller, and D. Bimberg
The QD-Flash: a quantum dot-based memory device
Semicond. Sci. Technol. **26**, 014026 (2011)

Patent:

- A. Marent, M. Geller, T. Nowozin, D. Bimberg
Memory
US Patent Application 12/970,744 (16.12.2010)

Speicherzelle auf Basis von Nanostrukturen aus Verbindungshalbleitern
PCT Application PCT/EP2011/072181 (8.12.2011)

Book chapter:

- T. Nowozin, A. Marent, M. Geller, D. Bimberg
Quantum dot-based Flash memories

in “Nanoscale Semiconductor Memories”

edited by Santosh Kurinec and Kris Iniewski

CRC Press, Taylor & Francis Group, Boca Raton (to be published 2013)

Contents

1	Introduction	1
2	Fundamentals	5
2.1	Semiconductor heterostructures	5
2.2	Nanostructures	7
2.3	Two-dimensional carrier gases and field-effect transistors	8
2.3.1	Modulation-doping	8
2.3.2	Modulation-doped field-effect transistor	10
2.4	Quantum dots	10
2.4.1	Fabrication	11
2.4.2	Electronic structure	12
2.5	Charge-based memories	15
2.5.1	Semiconductor memories	16
2.5.1.1	Dynamic Random Access Memory (DRAM)	16
2.5.1.2	Flash	17
2.6	Quantum dot-based Flash memory (QD-Flash)	19
2.7	Summary	22
3	Charge carriers in quantum dots	23
3.1	Carrier capture and emission in quantum dots	23
3.1.1	Rate equation	23
3.1.2	Capture processes	26
3.1.3	Emission processes	28
3.1.3.1	Thermal emission	28
3.1.3.2	Temperature dependence of capture cross section	30
3.1.3.3	Thermal emission in electric fields	31
3.1.4	Tunnel emission	31
3.1.4.1	Direct tunneling	32
3.1.4.2	Thermally-assisted tunneling	32
3.1.5	Total emission rate	33

3.1.6	Storage time in quantum dots	33
3.2	Many-particle effects in quantum dots	35
3.3	Summary	36
4	Coupling of QDs to 2D gases	37
4.1	Coupling mechanisms	37
4.1.1	Remote impurity scattering	38
4.1.2	Capacitive coupling	40
4.1.3	Quantum capacitance	41
4.1.4	Temperature effects in the 2D detector	43
4.2	Summary	44
5	Measurement methods	45
5.1	Static Capacitance Spectroscopy	45
5.1.1	Pn junctions	45
5.1.1.1	Depletion region	46
5.1.1.2	Capacitance of a pn junction	47
5.1.1.3	Static Capacitance Spectroscopy	48
5.1.1.4	Quantum dots inside a pn junction	49
5.2	Time-resolved Capacitance Spectroscopy	50
5.2.1	Measurement principle	52
5.2.2	Rate window and Double-Boxcar Method	53
5.2.3	Charge-selective DLTS measurements	55
5.3	Capacitance and time-resolved conductance measurements of 2D gases .	56
5.4	Summary	60
6	Electronic properties of and storage times in QDs	63
6.1	GaSb/GaSb quantum dots	63
6.1.1	Sample QD-A: QDs	64
6.1.1.1	Sample structure	64
6.1.1.2	Static capacitance measurements	65
6.1.1.3	Conventional DLTS	66
6.1.1.4	Charge-selective DLTS	67
6.1.2	Sample QD-B: QDs with a single Al _{0.1} Ga _{0.9} As barrier	70
6.1.2.1	Sample structure	70
6.1.2.2	Static capacitance measurements	72
6.1.2.3	Conventional DLTS	73
6.1.2.4	Charge-selective DLTS	74
6.1.3	Sample QD-C: QDs	76
6.1.3.1	Sample structure	76

6.1.3.2	Static capacitance measurements and conventional DLTS	76
6.1.3.3	Charge-selective DLTS	77
6.1.4	Sample QD-D: QDs with double $\text{Al}_{0.3}\text{Ga}_{0.7}\text{As}$ barrier	79
6.1.4.1	Sample structure	80
6.1.4.2	C-V and conventional DLTS measurements	80
6.1.4.3	Charge-selective DLTS	81
6.2	GaSb/GaAs quantum rings	83
6.2.1	Sample structure	83
6.2.2	Static capacitance measurements	84
6.2.3	Conventional DLTS	84
6.2.4	Charge-selective DLTS	85
6.3	$\text{In}_{0.25}\text{Ga}_{0.75}\text{As}/\text{GaAs}/\text{GaP}$ quantum dots	86
6.3.1	Sample structure	87
6.3.2	Static capacitance measurements and conventional DLTS	88
6.4	Discussion	91
6.5	Conclusion	94
7	Carrier dynamics in quantum dots coupled to a 2DHG	97
7.1	Samples	97
7.2	Sample A (5 nm tunnel barrier)	99
7.2.1	Capacitance-Voltage measurements	100
7.2.2	Conductance measurements	103
7.2.3	Many-particle level splittings	104
7.2.4	Higher temperatures	107
7.3	Sample B (10 nm tunnel barrier)	108
7.3.1	Current measurements	108
7.3.2	Emission and capture time constants	109
7.3.3	Many-particle level splittings	111
7.3.4	Emission and capture of integer number of holes	112
7.4	Sample C (15 nm tunnel barrier)	114
7.4.1	Hysteresis measurements	115
7.5	Discussion	116
7.6	Conclusion	119
8	Summary and Outlook	121
A	Storage time as a function of the localization energy	125
B	Experimental details - Setup	127
C	Samples	131

D Sample Processing	133
E DLTS: Error of graphical analysis	139
F Extrapolation of storage times	147
Bibliography	151
Danksagung	165

Chapter 1

Introduction

The fabrication of the first practicable transistors by W. Shockley, J. Bardeen, and W. Brattain in the late 1940s [1–3] sparked the rapid rise of the application of semiconductors in everyday technology. Together with the invention of the integrated circuit by J. Kilby in the late 1950s [4] and the development of semiconductor heterostructures by H. Kroemer and Z. I. Alferov in the 1960s [5,6], the basis for modern information society was laid. The amount of data that can be stored, processed, and retrieved by mankind has grown exponentially ever since, and the total amount of data is expected to reach 8 Zettabytes¹ by 2015 [7] and 35 Zettabytes by 2020 [8], driven mainly by multimedia content on the internet and mobile applications. Besides increased efforts to extract useful information from all this data (*data mining*), these large amounts of data demand for an increased storage density. Consequently, the areal density with which information can be stored, has increased from 2000 bits/in² on the first hard disk in 1956 [9] to 635 Gbits/in² in 2010 [10], with the projection of 2500 Gbits/in² by 2014. The main competitor against hard drives is the NAND Flash, which offers key advantages, as it does not require any movable parts and is more energy-efficient, making it more suitable for mobile applications. However, being a much later invention, the NAND Flash has only seen an increase in areal density from 0.6 Gbits/in² in 1998 to 330 Gbits/in² in 2010, with a projection of 1300 Gbits/in² by 2014 [10].

For semiconductor memories, the recipe that made such a tremendous increase in the areal density of the storage capacity possible was the downscaling of the feature size of storage nodes, logic nodes, and contact circuitry, the effects of which were described by Gordon Moore in 1965 [11], coining the famous law, according to which the number of transistors which are found on a given area will double every 18 months. However, this approach is expected to reach its limits by 2020, when the feature sizes become so small that statistical fluctuations of the interface roughness might lead to uncontrollable tunneling leakage. Being aware of the problem, the International Technology Roadmap

¹Zettabyte= 10^{21} Bytes=1 Billion Terabytes

for Semiconductors (ITRS) demands for *new functionalities* in order to further sustain progress in the chip industry beyond the year 2020 [12].

Today, the semiconductor memory market is divided mainly between two memories, which both have their individual advantages and disadvantages. The Dynamic Random Access Memory (DRAM) is used as the main working memory in personal computers, servers, and mobile applications [13, 14]. It has a fast access time of ~ 10 ns, a good endurance of $> 10^{15}$ access cycles, but its great disadvantage is a very short storage time of just some ~ 10 ms, which requires the information to be periodically refreshed at a large energy expense. In contrast, the Flash memory has a long storage time of more than ten years, even without power supply [15, 16], which makes it a non-volatile memory, ideally suited for application in mobile data storage in USB-sticks, mp3 players, and smartphones. Lately, Flash memories have also hit the mass market in Solid State Disks (SSD), which might eventually replace conventional hard drives in computers [17, 18]. However, the main disadvantage of the Flash memory is the slow random single-bit write time in the order of some μ s and its bad endurance of typically not more than 10^6 write/erase cycles [15, 16].

The problem has long been recognized by the International Technology Roadmap for Semiconductors, which states in the 2009 edition [12]:

*The development of an electrically accessible **non-volatile** memory with **high speed** and high density would initiate a revolution in computer architecture.*

Consequently, the industry is seeking to combine the advantages of the DRAM and the Flash, and is currently pursuing various memory architectures which could fulfill this vision [19].

One possible candidate could be a memory device based on self-organized quantum dots (QDs) [20, 21]. The idea of the *QD-Flash* is to use the charge confining potential of self-organized III-V QDs as storage node, and a Modulation-Doped Field-Effect Transistor (MODFET) to perform the memory operations [22–26]. Preliminary work has already shown that seconds of storage time at room temperature can be achieved in QDs, with the prediction that non-volatility is possible for novel heterostructures [27]. Other work demonstrated, that the write time for writing information into the QD storage node is already in the range of the DRAM access time (< 20 ns) [28]. As a proof of principle, a fully operational memory device based on QDs has been demonstrated to operate at low temperatures (< 200 K) [23, 26]. Nevertheless, many problems have still to be solved in order to enhance the performance of the QD-Flash. The storage time needs to be increased to more than 10 years in order to reach non-volatility, the write and erase times need to be optimized for faster operation, and the read-out process needs to be optimized.

In this work, two particular problems are addressed which are both closely related to

the further development of the QD-Flash. In the first part, the potential of GaSb/GaAs QDs and GaP-based QDs to increase the storage time at room temperature beyond the present values is investigated by Deep-Level Transient Spectroscopy (DLTS). In the second part, the coupling of a layer of self-organized QDs to a two-dimensional hole gas (2DHG) is studied by capacitance-voltage (C-V) spectroscopy and current measurements. A detailed understanding of the coupling is necessary in order to optimize the read-out mechanism in the QD-Flash.

The work is organized into several chapters which at first elaborate the fundamentals and the theoretical background necessary to interpret the measured data and to understand the underlying physical processes. Then, the measurement methods are explained, followed by the measurement results which are presented in the experimental part. Finally, conclusions are drawn after a short summary of the results. An outlook describes possible future work. Additional information is given in the Appendix.

In particular, the chapters have the following content:

- *Chapter 2* presents the fundamental background of this work, starting with semiconductor heterostructures and nanostructures. The key concepts of the QD-Flash, the MODFET and quantum dots, are introduced. The chapter closes with a short overview of the architecture of the most common semiconductor memories DRAM and Flash.
- *Chapter 3* covers the carrier dynamics taking place in self-organized QDs. Capture and emission processes in QDs are explained and used to theoretically derive the storage time in QDs.
- *Chapter 4* explains the coupling mechanisms between a layer of self-organized QDs and a two-dimensional carrier gas. Remote impurity scattering, capacitive coupling, and the effects of thermal energy on the coupling are described.
- *Chapter 5* describes the measurement methods used in this work. The principles of static capacitance spectroscopy, Deep-Level Transient Spectroscopy (DLTS), and current measurements are presented.
- *Chapter 6* is the first experimental chapter. It investigates the electronic properties of various GaSb/GaAs QDs, $\text{In}_{0.25}\text{Ga}_{0.75}\text{As}/\text{GaAs}/\text{GaP}$ QDs, and GaSb/-GaAs quantum rings (QRs). The localization energies and apparent capture cross sections are determined by DLTS, while the structural properties are extracted from Atomic-Force Microscopy (AFM) and Cross-sectional Scanning Tunneling Microscopy (X-STM) measurements. From the electronic properties the storage times at room temperature (300 K) and at 358 K (85°C) are extrapolated.

- *Chapter 7* is the second experimental chapter. It studies the carrier dynamics in QDs coupled to a 2DHG. Three samples are investigated, each of which having a different barrier width between the QD layer and the 2DHG, resulting in different coupling constants. C-V and current measurements give detailed insights into the many-particle hole levels of the QDs and the nature of the emission and capture processes between the QDs and the 2DHG.
- *Chapter 8* summarizes the results obtained in this work and gives an outlook on possible work in the future.

Chapter 2

Fundamentals

The following chapter gives an overview of the fundamentals of this work. At first, semiconductor heterostructures are described, building the basis for MODFETs and quantum dots. An overview of the most common semiconductor memories used today, including their advantages and disadvantages, leads the way to the concept of a quantum dot-based memory device which is described at the end of this chapter.

2.1 Semiconductor heterostructures

With the maturing of the quality of semiconductor crystals grown by Molecular Beam Epitaxy (MBE) [29] and Metal-Organic Chemical Vapor Deposition (MOCVD) [30], it became possible to grow almost atomically-abrupt semiconductor layers on top of each other.

When two different semiconductors are brought into contact, a heterostructure is formed. The development of the heterostructure has led to numerous applications, such as the High-Electron Mobility Transistor (HEMT) [31,32], lasers [33], and amplifiers [34]. This is owed to the fact that the electronic properties of the entire device are determined by the heterostructure, allowing to design devices with specific electronic and optical properties. The most prominent one of such designed heterostructures is the double-heterostructure laser, invented by Zhores I. Alferov and Herbert Kroemer in 1963 [5,6], which was honored with the Nobel price in the year 2000.

The materials used in heterostructures are predominantly II-VI or III-V compound semiconductors. Besides commonly fabricating binary compounds, it is possible to create a variety of different ternary, quaternary, even quaternary compounds, which allow to specifically design the bandgap of the semiconductor. Figure 2.1 shows the bandgap versus the lattice constant of the most common III-V semiconductors with their ternary alloys [35]. The III-V compounds offer a wide variety of different materials which can be combined in a heterostructure in order to have a precisely controlled band design.

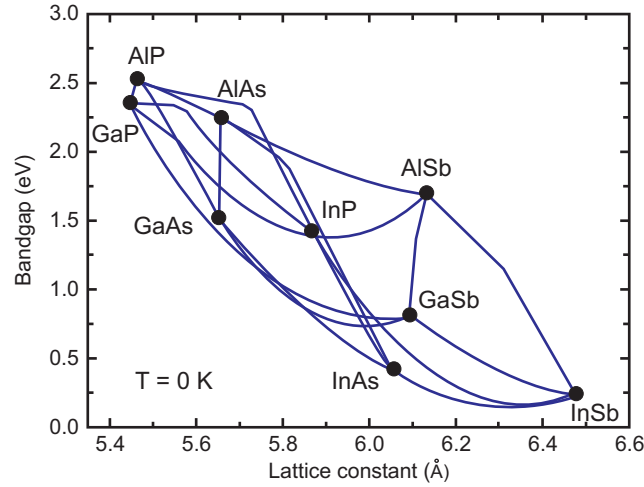


Figure 2.1: Energy band gap versus the lattice constant of III-V compound semiconductors. The black data points are the binary alloys and the blue lines the ternary alloys (after [35]).

From a device physics point of view, the key property of a heterostructure interface is the band alignment of the two semiconductors. Three different alignments are possible [36,37] which are shown in Fig. 2.2:

- *Type-I alignment.* The conduction band and the valence band of one semiconductor lie completely within the bandgap of the other semiconductor (Fig. 2.2[a]). If one semiconductor is surrounded by another semiconductor, charge carriers can be spatially restricted in their ability to move. Material systems of this kind are InAs/GaAs, GaAs/AlGaAs, and GaSb/AlSb.
- *Type-II staggered alignment.* The bandgap of one semiconductor does not lie completely within the bandgap of the other semiconductor, but there is still some overlap (Fig. 2.2[b]). In such a heterostructure, charge carriers of one type can be confined, while the other type is not confined or even experiences a barrier. A material system with this type of interface is GaSb/GaAs which plays an important role in this work.
- *Type-II broken-gap (also called Type-III) alignment.* The conduction and the valence band of one semiconductor lie completely above or below the conduction and valence band of the other semiconductor (Fig. 2.2[c]), the bandgaps of the two semiconductors do not overlap. An example for type-III alignment is the material combination InAs/GaSb.

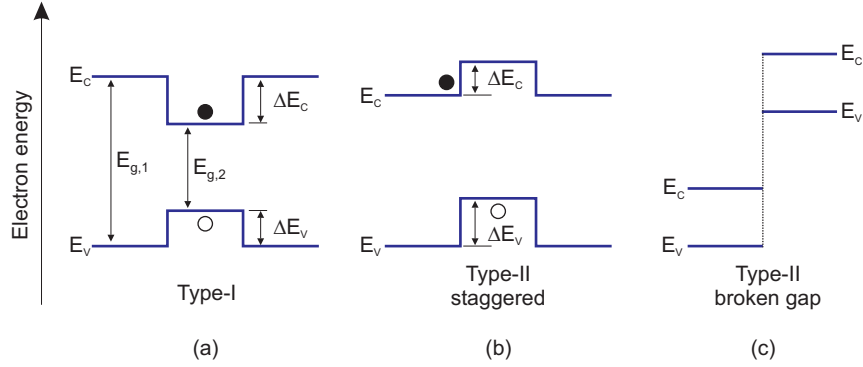


Figure 2.2: Different types of heterostructures: E_g is the bandgap of the semiconductor, ΔE_C and ΔE_V are the conduction band and the valence band offsets in the conduction band E_C and the valence band E_V , respectively. (a) Type-I: electrons and holes are confined within the same spatial region. (b) Type-II staggered: only one charge carrier type (here holes) is confined. (c) Type-II broken gap: no overlap of the band gaps.

2.2 Nanostructures

If the structural size of the functional element in a heterostructure enters the size range of the de Broglie matter wavelength, the electronic and optical properties are governed by size effects described by quantum mechanics. As a result of the reduced effective mass for electrons and holes in semiconductors, the de Broglie wavelength is in the nanometer range. Solving the Schrödinger equation for such nanometer-sized potentials results in quantization energies larger than kT , which ultimately leads to a completely discrete density of states. Figure 2.3 shows the densities of states for various structures, in which the directions in which charge carriers can freely move are further and further reduced. In a bulk semiconductor the movement of the charge carriers is not restricted and they can freely move in all three spatial dimensions. The density of states is proportional to \sqrt{E} . Two low-dimensional heterostructures are of importance in this work. In the first, the charge carriers can freely move within two dimensions and are restricted within only one dimension (see Fig. 2.3[b]). In such a *quantum well* (QW) the density of states for each energy level E_i is [38]

$$D_{2D}(E_i) = \frac{m^*}{\pi\hbar^2}, \quad (2.1)$$

with the effective mass m^* and the Planck constant \hbar . In the second structure, the movement of the carriers is restricted in all three spatial dimensions and the carriers are completely confined. In such a *quantum dot* (QD), complete quantization of the energy levels results in a completely discrete density of states [38], similar to those in

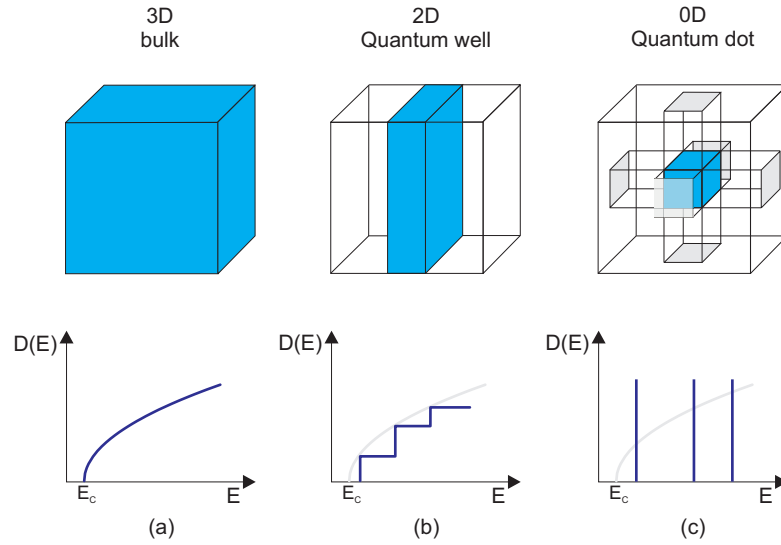


Figure 2.3: Density of states $D(E)$ in semiconductors. (a) Bulk semiconductor with a \sqrt{E} -shaped density of states. (b) Two-dimensional quantum well with a step-like density of states. (c) Zero-dimensional quantum dot with a completely discrete density of states.

an atom

$$D_{QD}(E) = \sum_i \delta(E - E_i), \quad (2.2)$$

with the energy levels at E_i .

2.3 Two-dimensional carrier gases and field-effect transistors

Based on the restriction of carrier movement in one spatial dimension, devices containing layers with very high carrier mobility can be built. These layers allow the fabrication of very fast transistors. The basic technique and device structure is described in the following sections.

2.3.1 Modulation-doping

The properties of semiconductors can be altered by doping. By incorporation of donors and acceptors, the conductance of a semiconductor can be enhanced by orders of magnitude. When the doping atoms release their surplus charges, ionized donors or acceptors are left behind and act as Coulomb scatterers (ionized impurity scattering) which can inhibit the motion of free charges [39], blur energy levels, and disrupt the interference of electron waves [38]. The solution of this problem is to separate the active region

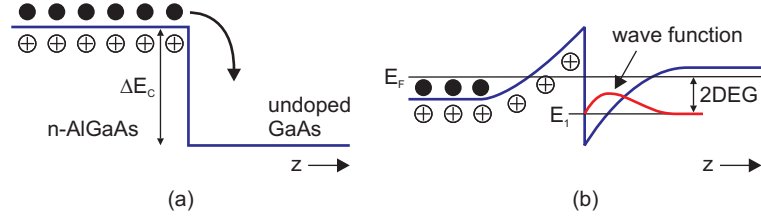


Figure 2.4: Conduction band around the interface of a heterojunction between n-doped AlGaAs and undoped GaAs. (a) The electrons released by the donors are diffusing to the GaAs and lose potential energy. (b) Field-induced band bending and formation of a two-dimensional electron gas in the triangular potential well.

of the device from the doping atoms, a method which is called remote or modulation doping [40]. Figure 2.4 schematically depicts the formation of a two-dimensional electron gas (2DEG) at the interface of a heterojunction between n-doped AlGaAs and undoped GaAs. Initially, the material is neutral (Fig. 2.4[a]) and the conduction band is flat in the AlGaAs and in the GaAs. When the electrons of the donors in the AlGaAs are released, they move around and some of them diffuse into the GaAs, where they lose potential energy and are trapped in the GaAs because they cannot overcome the barrier ΔE_C . The negatively charged electrons are now separated from the positively charged donors leading to an electric field which drives the electrons back towards the interface. The electrons are trapped in a field-induced triangular well with a typical width of ~ 10 nm. As the width of the well is below the de Broglie wavelength of the electrons, the quantization of the energy levels in z -direction becomes relevant. If only the lowest energy level is occupied, all electrons exhibit the same state in z -direction, but remain free to move in x - and y -direction. This way, a 2DEG is formed with the total energy of an electron sitting on the energy level E_n [38]

$$E_n(k_x, k_y) = E_n + \frac{\hbar^2 k_x^2}{2m^*} + \frac{\hbar^2 k_y^2}{2m^*}, \quad (2.3)$$

with the wave vectors k_x and k_y in x and y direction, and the effective mass m^* . Using the approach of modulation doping, later refined by inserting an undoped spacer layer between the donors and the heterojunction, very high electron mobilities of up to $>10^7$ cm²/Vs [41] can be achieved. Creating 2DEGs with such high mobilities at low temperature allowed the discovery of the Quantum Hall Effect [42, 43]. If p-doped AlGaAs is used instead of n-doped AlGaAs, a two-dimensional hole gas (2DHG) is formed in a similar way. Here, mobilities of up to 10^6 cm²/Vs [44] have been achieved. The invention of modulation doping has created high-speed device applications, such as the modulation-doped field-effect transistor (MODFET), also known as high-electron mobility transistor (HEMT) [37].

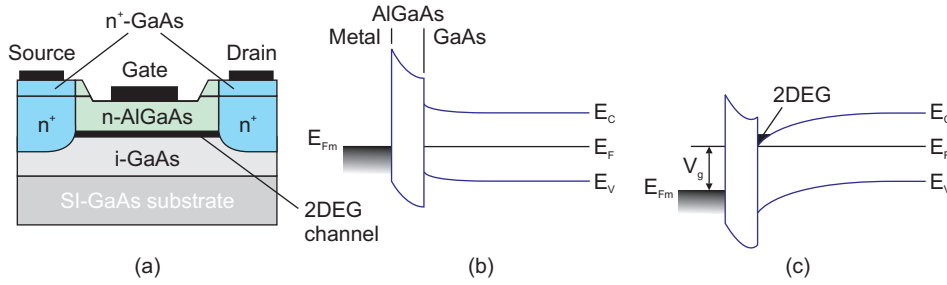


Figure 2.5: Modulation-doped field-effect transistor (MODFET) (after [37]). (a) Schematic device structure. (b) Energy band diagram of an enhancement mode MODFET at equilibrium. (c) Onset of threshold: if $V_g > V_T$ electrons accumulate at the heterointerface and a 2DEG is formed which acts as channel.

2.3.2 Modulation-doped field-effect transistor

The principle of modulation doping and the resulting high mobility is the key advantage of a modulation-doped field-effect transistor (MODFET) over conventional MOSFETs. Figure 2.5(a) depicts the schematic device structure of an enhancement mode AlGaAs/-GaAs MODFET. It consists of a layer of undoped GaAs and a top layer of n-doped AlGaAs. The electrons from the AlGaAs are transferred to the GaAs, and a 2DEG is formed. The 2DEG is contacted by two Ohmic source and drain contacts, which use highly doped regions fabricated either by ion implantation or introduction of dopants during the alloying step. A Schottky gate contact allows to alter the potential in the 2DEG. The working principle of this enhancement MODFET is shown in Figs. 2.5(b) and 2.5(c). In equilibrium ($V_g = 0$ V), the Fermi level $E_F = E_{Fm}$ is the same throughout the device, the channel conductance is very low and the transistor is off. If a gate voltage larger than the threshold voltage V_t is applied, the conduction and the valence band are tilted and the electrons in the GaAs accumulate at the heterointerface, forming a 2DEG inside the triangular well. The channel conductance is now very high and the transistor is on. This way, a controlled switching of the conductance of the channel is achieved.

2.4 Quantum dots

Self-organized quantum dots (QDs) [20,21] are low-dimensional heterostructures which confine the charge carriers within all three spatial dimensions. The behavior of such a zero-dimensional system is similar to real atoms and has coined the term *artificial atom* for QDs. The qualitatively distinct electronic and optical properties of QDs have led to numerous applications in devices such as field-effect transistors [45–47], memory cells [23, 26, 48–50], lasers [51–56], amplifiers [57], and single photon sources [58–60].

2.4.1 Fabrication

There are two fundamentally different approaches to fabricate QDs. In the *top-down* approach QDs are defined by patterning QWs using lithographical techniques (i.e. electron beam lithography) [20]. The quantum well material has a smaller bandgap than the surrounding material and confines the charge carriers within the growth direction. A mask is defined on the surface, framing the lateral size of the QD, which is then defined by using standard dry-etching techniques. The definition of these mesas leads to a spatial confinement of charge carriers within the QW layer, now becoming a QD. In the other approach, which was used for the fabrication of the QDs investigated in this work, the QDs are grown in a self-organized way [20]. In this *bottom-up* approach mainly two different techniques are used: molecular beam epitaxy (MBE) [29] and metal-organic chemical vapor deposition (MOCVD) [30]. During MBE growth, a molecular beam of the source materials is directed onto the substrate and an epitaxial layer is formed on the surface. Under ultra-high vacuum conditions (UHV), a crystalline compound semiconductor can be grown with a very high purity and quality. During MOCVD, precursor gases are transported to the surface of the substrate by a carrier gas. Within the reactor, a chemical reaction cracks the precursors into its constituents, creating a supersaturated gas phase which leads to condensation on top of the substrate surface, where the surface kinetics lead to the formation of an epitaxial layer.

If the epitaxially grown material and the substrate are different semiconductor materials, they usually exhibit a different lattice constant (see Fig. 2.1). Hence, the lattice constant of the deposited layer will adjust to the lattice constant of the layer underneath, leading to coherent strain. If growth proceeds, the successive layer will at some point reach its original lattice constant, as the strain is continuously reduced. If the difference of the lattice constants of the two materials is too large, the strain is relaxed and the deposited layer keeps its original lattice constant, leading to dislocations.

The coherent strain can be utilized to grow self-organized QDs. Essentially, there are three modes of heteroepitaxial growth. If the difference of the lattice constant of the two semiconductors is small, the strain is reduced within a few layers without creating dislocations. In this Frank-van der Merwe growth mode [61], the growth proceeds as a layer-by-layer growth, where the complete surface of the substrate is wetted by the epitaxial layer. If the difference in the lattice constants is larger, the strain can be reduced by a transition to three-dimensional island growth. In this Volmer-Weber [62] growth mode the total energy is minimized by the island formation [63]. In a mixture of the previous two growth modes, called Stranski-Krastanow mode [64], the surface of the substrate is first covered by a wetting layer (WL), followed by the formation of islands in the process of total energy minimization [63]. This growth mode is used to fabricate quantum dots with a few monolayers height and a few ten nanometers in

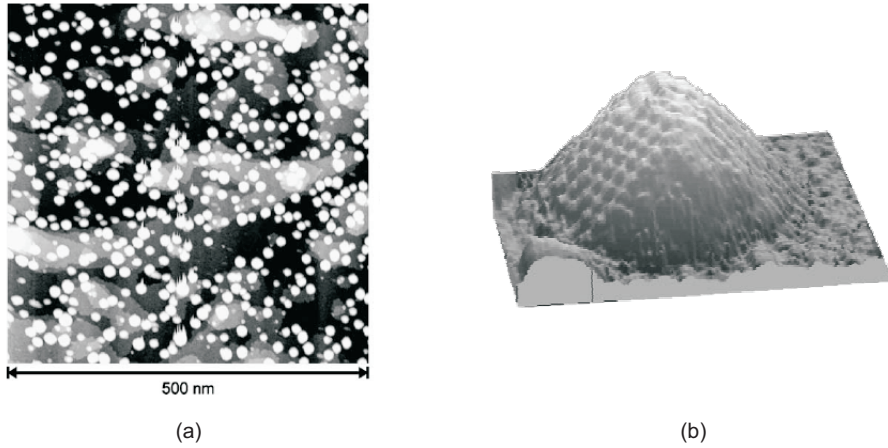


Figure 2.6: (a) Surface STM image of self-organized InAs QDs grown on GaAs(001) in the Stranski-Krastanow mode on an area of $500 \times 500 \text{ nm}^2$. The QDs (white), the wetting layer (grey), and the GaAs (black) can be clearly distinguished (Reprinted from [65], with permission from Elsevier). (b) High-resolution STM image of a single QD depicted as a three-dimensional model (Reprinted with permission from [66], Copyright 2001, American Institute of Physics).

diameter. Depending on the growth conditions, area densities of up to $1 \cdot 10^{11} \text{ cm}^{-2}$ can be reached. Figure 2.6 shows a Scanning Tunneling Microscope (STM) image of a surface covered with self-organized QDs and a three-dimensional depiction of a single QD.

All QDs in the samples investigated in this work were fabricated using the Stranski-Krastanow growth mode.

2.4.2 Electronic structure

As a result of the small structural size of self-organized QDs, they can confine charge carriers and restrict their motion in all three spatial dimensions. In the simplest theoretical model, QDs can be described as a quantum mechanical potential well with infinite barriers. It is well known from quantum mechanics, that the energy levels in such a potential well are quantized [67]. Nevertheless, this simple model neglects many other effects, which are important for the electronic structure. Strain, piezoelectric effects, and the chemical composition within the QDs and the surrounding matrix material have to be taken into account to determine the exact position of the energy levels within the QD.

The exact electronic structures of self-organized QDs can be calculated numerically using a three-dimensional model within the framework of 8-band- $\mathbf{k} \cdot \mathbf{p}$ theory [68–70]. Figure 2.7 shows the results of such a calculation for InAs QDs embedded into a GaAs matrix. It can clearly be seen that the energy levels for electrons and holes shift towards the respective band edge when the size of the QDs is reduced. This shift leads

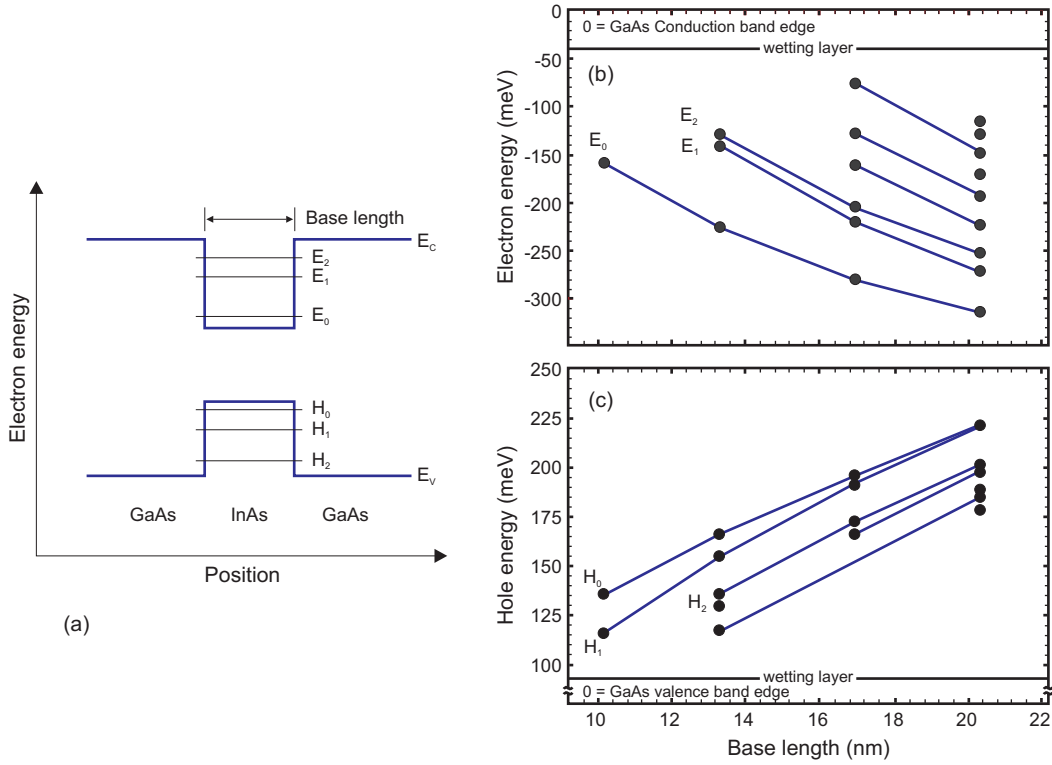


Figure 2.7: A quantum dot resembles a three-dimensional potential well. (a) InAs/GaAs QDs can confine electrons and holes due to the discontinuities in the conduction band E_c and the valence band E_v . (b) Electron and (c) hole energy levels in InAs/GaAs QDs calculated with 8-band $\mathbf{k}\cdot\mathbf{p}$ -theory using a continuum mechanical model for the strain (after [69]).

to a reduction of the number of bound states in the QDs with decreasing size. In this particular example QD, there is only one bound state for electrons and two bound states for holes at a base length of 10 nm, whereas the number increases to 9 electron states and 6 hole states at a base length of 20 nm.

Figure 2.8 shows the hole localization energy (energy difference between the hole ground state and the valence band edge of the surrounding material) for GaSb/GaAs QDs, which are investigated in this work. The calculations have been done by Andrei Schliwa at TU-Berlin. They also include strain and piezoelectric effects and model the QDs with a pyramidal or truncated-pyramidal shape. Similar to the InAs QDs, it can be seen that an increasing size of the QDs leads to an increasing localization energy for the holes in the GaSb QDs (Fig. 2.8[a]). If the shape is changed from truncated-pyramidal (with vertical aspect ratio of $VAR = 0.05$, defined by height divided by base length) to pyramidal-shaped ($VAR = 0.45$) QDs (Fig. 2.8[b]), the hole localization energy stays almost constant for the larger heights, while it increases slightly towards the smaller heights. This increase is due to a redistribution of strain from being predominantly hydrostatic for tall QDs to biaxial for flat QDs. If the QDs get flatter, the z -quantization

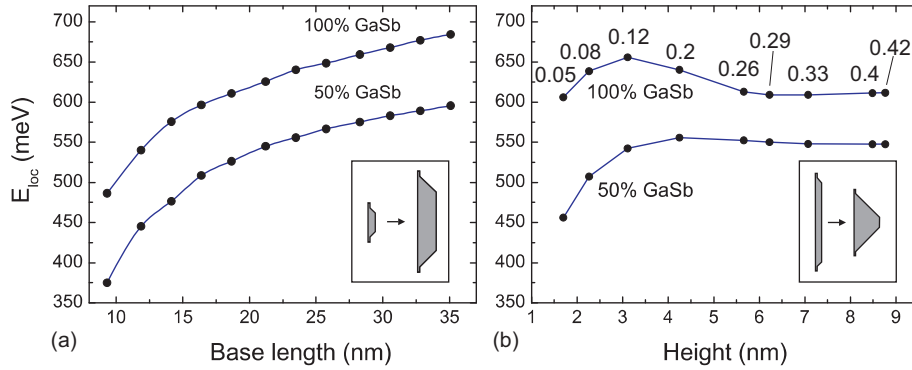


Figure 2.8: Hole localization energies E_{loc} in GaSb/GaAs QDs for two different chemical compositions as a function of (a) base length with constant vertical aspect ratio of $VAR = 0.2$ and (b) shape of the QDs (the numbers indicate the VAR for each data point). The calculations were performed by Andrei Schliwa at TU-Berlin.

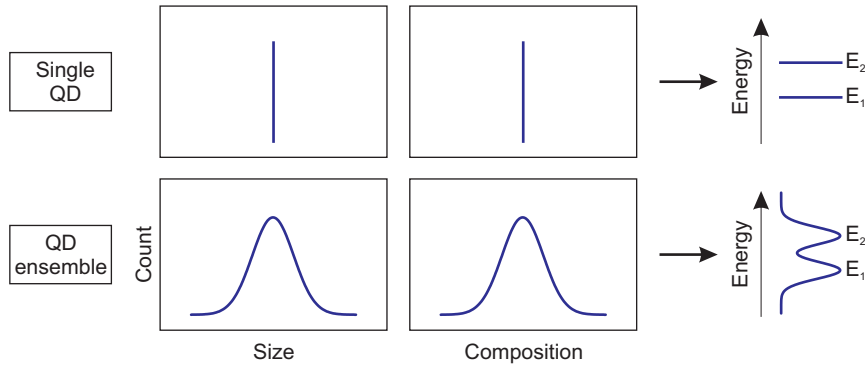


Figure 2.9: Inhomogeneous ensemble broadening: Due to the variations in size, shape and composition, the energy levels of the QD ensemble are broadened in comparison to the sharp energy levels of a single QD.

dominates and the localization energy decreases again. The z -quantization effect is more pronounced for the QDs with a smaller GaSb content. Here, the overall strain is smaller due to the smaller lattice mismatch to GaAs.

A given population of quantum dots grown by self-organization can be regarded as a statistical ensemble. As their growth process is governed by thermodynamics, their structural and chemical properties will scatter around a mean value, resulting in a Gaussian distribution of size, shape, and chemical composition. This *ensemble broadening* of the structural properties affects the electronic properties and leads to a similar distribution of the energy levels in the QDs, which is reflected as a Gaussian shaped broadening. The ensemble broadening is illustrated schematically in Fig. 2.9.

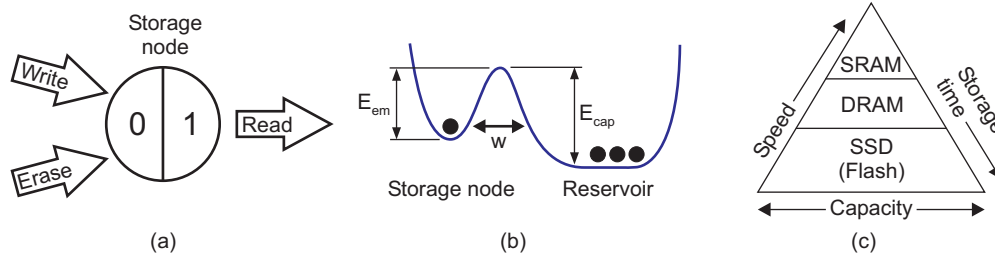


Figure 2.10: The constituents of an abstract memory cell. (a) Storage node which stores a single bit with the logic states 1 and 0. Write, erase, and read operations can be performed on the storage node. (b) Simple model of a potential minimum used as storage node. The storage node is separated from the electron reservoir by a barrier. Depending on the logic state that is stored, either the emission barrier E_{em} or the capture barrier E_{cap} is the limiting factor for the storage time. To write and erase information the electrons have to overcome or tunnel through the barrier. (c) Semiconductor memory hierarchy pyramid.

2.5 Charge-based memories

Modern data storage is based on encoding information within the binary system with the two logic states expressed as 0 and 1 [13, 14]. Digital data storage and data processing systems hence have to distinguish between two states, i.e. a transistor current is switched *on* or *off*. The amount of data stored per storage node is usually one single *bit* (binary digit). A schematic of an abstract binary storage node is depicted in Fig. 2.10(a). The basic operations that have to be performed on a storage node are: writing of information (expressed as writing of a logic 1 and erasing the logic 1 in order to reach the logic state 0) and the read-out of the information. A realization of such a storage node is shown in Fig. 2.10(b). The storage node is defined by a potential minimum, which is separated from an electron reservoir by a potential barrier. To store the logic 1 the potential minimum is occupied by one electron, whereas a logic 0 is represented by an unoccupied storage node. The storage of information always involves a non-equilibrium situation. The key properties which limit the performance (storage, write, and erase time) of such a storage node are determined by the energetic height and shape of the barrier which separates the storage node from the reservoir. If an electron is stored inside the storage node (logic 1), the electron will leave the potential minimum and overcome the barrier with a certain probability. The probability for the electron to tunnel through the barrier is determined by the height E_{em} , the shape, and width w of the emission barrier. With thermal energy present, the electron can also thermally overcome the barrier E_{em} , a process which is determined by the Boltzman statistics and hence proportional to $\exp(-E_{em}/(kT))$. Hence, the storage time for the 1 is limited by the barrier height E_{em} , the width w , the shape, and the temperature T . If the potential minimum is unoccupied (logic 0), electrons from the reservoir will leak into the storage node with a certain probability. The mechanisms are the same as

for the logic 1 . The storage time of the logic 0 is hence limited by the height, width, and shape of the capture barrier E_{cap} .

In order to reach a long storage time in the storage node, the barriers need to be designed in such a way that during storage only a very small probability exists for the carriers to transfer between the storage node and the reservoir. In contrast, when information is written or erased from the storage node, the transfer probability should be very high in order to reach fast access times. This dilemma between long storage times and fast access times is a commonly known *trade-off* in memories.

2.5.1 Semiconductor memories

In order to work around the limitations given by the trade-off between long storage times and fast access times, a hierarchy of different memories has been developed [16], with each individual memory type bridging the gap of a specific combination of speed, capacity, and storage time (see Fig. 2.10[c]). In the following, only semiconductor memories are considered. On the top of the hierarchy pyramid, at the very fast CPU level, the SRAM (Static Random Access Memory) is used as processor register. It has a total of six transistors for each cell which constitute a flip-flop type behavior. On the bottom of the hierarchy pyramid, the Flash memory in the form of solid-state disks (SSD) is used as data archive, having a slow write time, but a long storage time (>10 years, non-volatile). In between these two, the DRAM (Dynamic Random Access Memory) is used as a working memory in computers, where the data needed in the upcoming computation cycles of the CPU is stored and cached before it is transferred to the registers.

The semiconductor memory industry focuses mainly on two of these memories: the DRAM and the Flash. Hence, these two play the most important role in the semiconductor memory market. A brief overview of these two memory concepts is given in the following.

2.5.1.1 Dynamic Random Access Memory (DRAM)

The Dynamic Random Access Memory (DRAM) consists of a single access transistor and single storage capacitor per cell, the so-called 1T-1C design [13]. A schematic equivalent circuit of a single cell is shown in Fig. 2.11(a). The transistor is needed to access the individual storage node. The capacitor represents the storage node using the electrons on the capacitor plates to encode a single bit per cell. The 1T-1C cells are connected to the control circuits and sense amplifiers by an array of word lines and bit lines. The array matrix allows to address each cell individually. To initiate the reading or writing operation, the access transistor is switched on by activating the word line. This connects the capacitor with the bit line. In the reading operation the voltage is

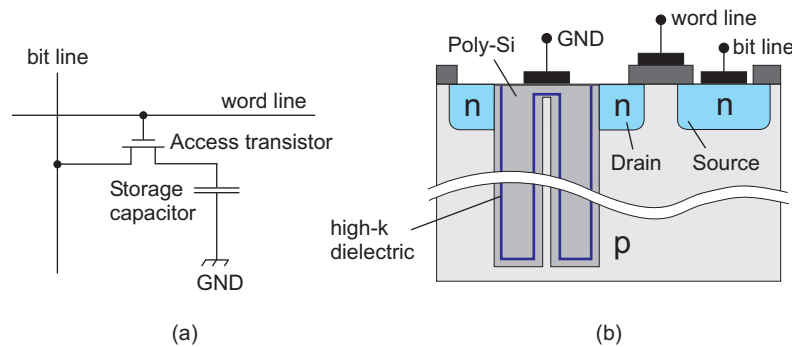


Figure 2.11: Schematic cell structure of the storage node in a DRAM. (a) Equivalent circuit of a 1T-1C cell design: the DRAM consists of an access transistor and a storage capacitor connected in an array of word lines and bit lines. (b) Cross section of an actual DRAM with a deep trench design (after [13]).

then sensed via the bit line, whereas in the writing operation electrons are transferred to the capacitor plates via the bit line. To securely detect the logic state stored in the capacitor, a minimum capacitance is required. To reach high bit area densities, today's DRAMs hence consist of deep trenches buried in a substrate material. The trenches are filled with a high-k dielectric (see Fig. 2.11[b]).

The main advantages of the DRAM are:

- Fast access time: typically ~ 10 ns,
- Good endurance: typically $> 10^{15}$ write/read cycles.

The disadvantages of the DRAM are:

- Short storage time: typically some 10 ms, requiring cyclical refresh of the information
- Destructive read-out: the read-out destroys the information and a refresh is needed
- Large number of charges per bit: each bit needs $\sim 10^4$ electrons, which have to be transferred when writing, reading, or refreshing the information. This leads to a large stand-by energy consumption.
- Limited scalability: due to the minimum capacitance required, the scalability is limited. However, a quick end to scaling is not yet in sight [71].

2.5.1.2 Flash

The most important non-volatile semiconductor memory is the Flash EEPROM (Electrically erasable read-only memory) memory [15, 16, 72], which in its modern design

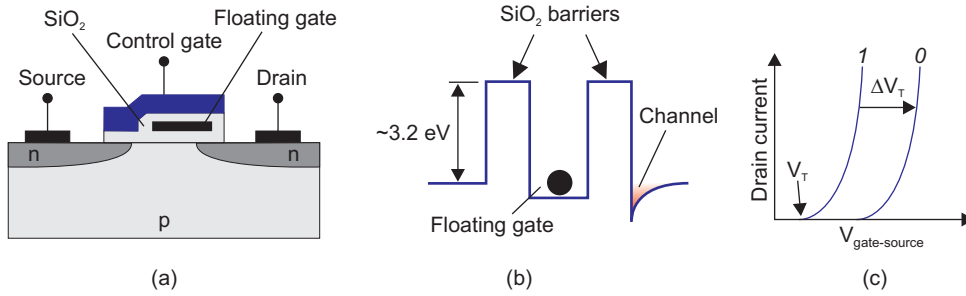


Figure 2.12: Flash EEPROM. (a) Schematic cross section of the Flash structure. A floating gate surrounded by an insulator is embedded in between the control gate and the channel. (b) Schematic conduction band in a Flash memory. Inside the floating gate a potential well is created due to the band discontinuity of ~ 3.2 eV between Si and the SiO_2 barriers. (c) Shift of the current-voltage characteristic due to charges inside the floating gate.

was invented in 1984 [73]. It can store information without any power supply. The design consists of a field-effect transistor with an additional gate between the control gate and the channel (see Fig. 2.12[a]). The additional gate is electrically isolated from its surroundings by a dielectric (e.g. by the native oxide of Silicon SiO_2), and is called *floating gate*. Electrons are trapped inside the potential well, which is formed by the floating gate and the surrounding barriers (Fig. 2.12[b]). The floating gate is capacitively coupled to the channel underneath. The electrons inside the floating gate affect the electron density in the channel by the field-effect. The change of the electron density in the channel can be directly measured in the drain current, which is illustrated in Fig. 2.12(c). If the floating gate is empty (which corresponds to the logic state 1), the transistor is turned on at the threshold voltage V_T . In contrast, if electrons are present in the floating gate (logic state 0), the 2DEG channel underneath is depleted and the threshold voltage is shifted by ΔV_T .

The main advantages of the Flash are:

- As a result of the high barriers, the Flash is non-volatile. It can store information for more than 10 years, even without power supply.
- The number of electrons required to store one bit is ~ 1000 , and hence smaller than in the DRAM.
- The read-out of the information is non-destructive.

The disadvantages of the Flash are:

- During writing and erasing of information, the electrons have to overcome or tunnel through the barriers with the fixed height of ~ 3.2 eV. Compared to the thermal energy of the charges in the order of $\sim kT$, the barriers are very high, which leads to very slow write and erase times of microseconds to milliseconds.

- The writing and erasing can be done either by hot electron injection or Fowler-Nordheim tunneling [16]. Due to the low injection efficiency and the high electric fields of 8-10 MV/cm [15] which are necessary in these processes, the oxide barriers are successively destroyed by the generation of defects within the barriers. This leads to a low endurance of just $\sim 10^6$ write/erase cycles.

Two different designs of the Flash exist [16]. Non-volatility and very high densities can be reached in the NAND Flash, and it is used at the basis of the memory hierarchy as data archive, mainly in mobile applications, such as smartphones, USB sticks, and mp3 players. In contrast to the NAND Flash, the NOR Flash has the advantage, that each cell can be randomly accessed individually. Additionally, it works with a very high reliability. It is used mainly in industrial and embedded equipment, where program code (i.e. Firmware or BIOS) and initial data has to be stored with high reliability.

2.6 Quantum dot-based Flash memory (QD-Flash)

The DRAM and the Flash memory as the most dominant memory types in the semiconductor memory market both have their advantages and disadvantages. In order to combine the advantages of both memories, the quantum dot-based Flash - the *QD-Flash* - was developed at TU-Berlin [22, 24]. There are three pillars on which the QD-Flash concept is built: the use of III-V compound semiconductors, the use of nanostructures (i.e. quantum dots) as storage units, and the use of a selectively-doped heterostructure to operate the memory.

The use of III-V compounds instead of the Si/SiO₂ material system with its fixed band offset allows a band structure design, in which the band discontinuities can be specifically tailored. A wide variety of III-V compounds exist (see Fig. 2.1) and can be combined with almost atomically abrupt interfaces which are free of defects. In addition, the III-V compounds can be doped to alter the band structure, which is not possible in SiO₂.

The use of nanostructures, and in particular of self-organized quantum dots, in the QD-Flash concept has many advantages. During the growth of quantum dots, the total energy is minimized (see Sect. 2.4.1) which leads to strain minimization and to dislocation-free interfaces. This results in very high localization energies in the QDs, even if the system is highly strained. It allows the combination of materials which have a large lattice mismatch. Furthermore, the large capture cross section of QDs (typically 10^{-14} to 10^{-12} cm²), which is orders of magnitude larger than for common traps in semiconductors [74], leads to extremely fast capture times for electrons and holes with time scales in the range of picoseconds [75, 76]. This could facilitate very fast write times in the QD-Flash. Write times in QDs have already been demonstrated to be in the range of the DRAM access time [28], yet limited by the parasitics of the device.

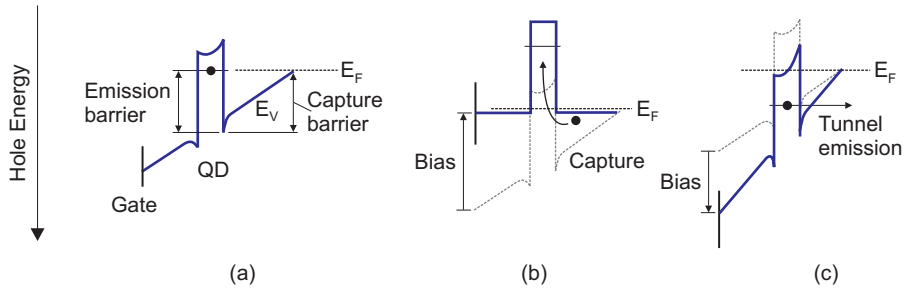


Figure 2.14: Schematic depiction of the memory operations in a hole-based QD-Flash. (a) Storage of information. A logic 0 (holes in the QD) requires an emission barrier, while the logic 1 (empty QDs) requires a capture barrier. (b) Writing of information by applying a forward bias. The capture barrier is completely eliminated and holes are captured into the QD. (c) Erasing of information by applying a reverse bias to the gate. This increases the electric field at the position of the QDs leading to a narrower tunnel barrier. The tunneling probability is increased and the holes tunnel out of the QD.

(see Fig. 2.10). This emission barrier is formed by the band discontinuity between the QDs and the matrix material. The potential well with the depth of the localization energy E_{loc} confines the holes inside the QDs and defines the emission probability and the storage time of the logic 1. To store a logic 0 (empty QDs), a capture barrier is needed to prevent holes from outside the QDs to enter the QDs. This capture barrier is formed by the band bending induced by the Schottky diode of the MODFET structure. Hence, the storage time of the 0 is also defined by the position of the QD layer within the device and the magnitude of the band bending. The storage of charges inside the QDs for various material systems has been investigated in [27, 81, 82]. The maximum storage time of 1.6 s at room temperature was achieved in InAs/GaAs QDs with an additional $\text{Al}_{0.9}\text{Ga}_{0.1}\text{As}$ barrier [27].

- *Writing.* In order to charge the QDs with holes (here defined as writing), a gate bias in forward direction of the Schottky diode is applied. Ideally, the device is designed in such a way, that the forward bias completely eliminates the capture barrier, and holes get captured into the QDs and thermally relax down to the lowest unoccupied state. As mentioned above, the capture time of charge carriers into QDs is extremely fast, on the order of some ps [75, 76]. It was demonstrated, that write times in QDs comparable to the DRAM access time can be achieved [28].
- *Erasing.* To discharge the QDs (here defined as erasing), a gate bias in reverse direction of the Schottky diode is applied. This increases the electric field around the QDs leading to a narrower emission barrier, which leads to an increased tunneling probability of the holes inside the QDs. Eventually, they will tunnel through the barrier, discharging the QDs. The erasing in QDs has been investi-

gated in [83].

- *Read-out.* To read-out the logic state stored in the QDs, a measurement of the conductance of the 2DHG underneath the QDs is performed. Holes inside the QDs decrease the mobility and the charge density in the 2DHG by scattering and the field effect (see Chapter 4). The effect can be directly measured in the source/drain current and can hence be used to detect the logic state in the QDs.

2.7 Summary

This chapter is summarized in the following:

- Semiconductor heterostructures and nanostructures allow the controlled confinement of charge carriers within all three spatial dimensions. Within these small dimensions, the electronic and optical properties can be specifically tailored by the size and the geometry of the nanostructures.
- Based on heterostructures, devices with very high mobility can be build. The MODFET is a prominent example for a two-dimensional confinement of charge carriers, which have been separated from their ionized dopant atoms.
- Quantum dots confine charge carriers within all three spatial dimensions. Hence, they are ideally suited to build a memory. Especially self-assembled QDs based on III-V compounds offer many advantages, such as their high-quality growth by self-organization, large confining potentials (large localization energy), and a wide variety of different materials that can be combined.
- The most important semiconductor memories are the DRAM and the Flash. Both have their advantages and disadvantages: the DRAM is fast but volatile, while the Flash is non-volatile, but slow. A way to combine the advantages of both memories is using self-assembled QDs embedded into a MODFET structure. In principle, fast write times and long storage times can be reached.

Chapter 3

Charge carriers in quantum dots

A self-organized quantum dot acts as a potential well and can confine electrons and holes. Depending on the conditions in the surroundings of the QD, the number of charges occupying the QD can change over time. The theory of carrier emission and capture is analogous to that of deep traps in semiconductors [84,85]. Past experiments investigating the carrier dynamics of QDs have shown that the theory derived for deep traps is also valid for QDs [25,81,86,87]. The following chapter will derive the theory of carrier dynamics and the underlying emission and capture processes in QDs.

3.1 Carrier capture and emission in quantum dots

3.1.1 Rate equation

The occupation of the electronic states in quantum dots with charge carriers can be changed by four elementary processes [85]. For electrons, these processes are (see Fig. 3.1[a]):

- Electron capture from the conduction band with the capture rate c_n
- Electron emission into the conduction band with the emission rate e_n
- Electron-hole pair generation (capture of electrons from the valence band)
- Electron-hole pair recombination (emission of electrons into the valence band)

Analogously, for holes the processes are:

- Hole capture from the valence band with the capture rate c_p
- Hole emission into the valence band with the emission rate e_p
- Electron-hole pair generation

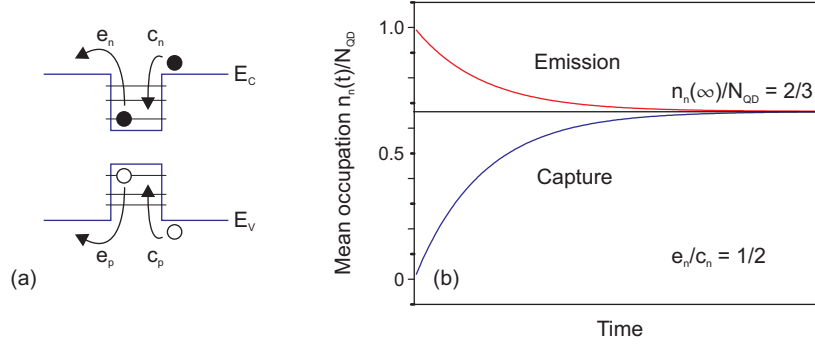


Figure 3.1: (a) Capture and emission processes and their rates in a simple rate equation model for electrons or holes. (b) Solution of the rate equation for electrons in a QD. The QD ensemble relaxes from the initial occupation state $n_n(0)$ to the equilibrium occupation $n_n(\infty)$ by mean emission or capture of electrons.

- Electron-hole pair recombination

As the measurements in this work are performed under dark conditions and the band gaps of the materials studied are large compared to kT , the generation of electron-hole pairs is neglected in the following. Furthermore, the minority carrier concentration in the samples studied in this work are orders of magnitude smaller than the majority carrier concentration, hence recombination processes are also neglected.

The carrier dynamics in the QDs are described by a rate equation approach. Neglecting ensemble broadening, an ensemble of N_{QD} QDs, of which all have the same energy level, is assumed. If $n_n(t)$ and $n_p(t)$ are the number of occupied electron or hole states in the QD, the number of unoccupied states in the QD ensemble is $N_{QD}^n - n_n(t)$ for electrons and $N_{QD}^p - n_p(t)$ for holes, respectively. The rates for electrons are then:

- e_n - Emission rate for electrons (rate per occupied electron state, independent of time).
- c_n - Capture rate for electrons (rate per unoccupied electron state, independent of time).
- $R_n^e(t)$ - Net emission rate, with which the electrons are emitted into the conduction band (time-dependent)

$$R_n^e(t) = e_n n_n(t). \quad (3.1)$$

- $R_n^c(t)$ - Net capture rate, with which electrons are captured from the conduction band into the QD (time-dependent)

$$R_n^c(t) = c_n [N_{QD}^n - n_n(t)]. \quad (3.2)$$

Similarly for holes:

- e_p - Emission rate for holes (rate per occupied hole state, independent of time).
- c_p - Capture rate for holes (rate per unoccupied hole state, independent of time).
- $R_p^e(t)$ - Net emission rate, with which the holes are emitted into the valence band (time-dependent)

$$R_p^e(t) = e_p n_p(t). \quad (3.3)$$

- $R_p^c(t)$ - Net capture rate, with which holes are captured from the valence band into the QD (time-dependent)

$$R_p^c(t) = c_p [N_{QD}^p - n_p(t)]. \quad (3.4)$$

The net rate of change of the mean occupation of the electron states is the difference between the net capture and emission rates¹:

$$\frac{dn_n(t)}{dt} = R_n^c(t) - R_n^e(t) = c_n [N_{QD}^n - n_n(t)] - e_n n_n(t). \quad (3.5)$$

This rate equation is a first-order inhomogeneous differential equation. With the initial condition $n_n = n_n(0)$ for $t = 0$, the general solution to Eq. 3.5 is

$$n_n(t) = n_n(\infty) - [n_n(\infty) - n_n(0)] \cdot \exp[-(e_n + c_n)t]. \quad (3.6)$$

The thermodynamic equilibrium state $\frac{dn_n(t)}{dt} = 0$ is reached for $t = \infty$:

$$n_n(\infty) = N_{QD}^n \left(1 + \frac{e_n}{c_n}\right)^{-1}. \quad (3.7)$$

Equation 3.6 can be rewritten as

$$n_n(t) = n_n(\infty) - [n_n(\infty) - n_n(0)] \cdot \exp\left(-\frac{t}{\tau}\right), \quad (3.8)$$

where the time constant τ is given by

$$\frac{1}{\tau} = e_n + c_n. \quad (3.9)$$

The solution of the rate equation leads to a mono-exponential relaxation into the equilibrium occupation $n_n(\infty)$, if the system is initially perturbed to an occupation $n_n(0)$.

¹The solution of the rate equation is derived for electrons. It is completely analogous for hole capture and emission.

The time constant τ of the relaxation process is the reciprocal sum of the emission rate e_n and the capture rate c_n . Depending on the initial condition, the mean process can either be the emission ($n_n(0) > n_n(\infty)$) or the capture ($n_n(0) < n_n(\infty)$) of electrons. The solution of the rate equation is shown schematically in Fig. 3.1(b) for two initial conditions (full QDs and empty QDs). The total rates for capture and emission are the sums of the individual processes, i.e. thermal capture/emission, tunnel capture/emission, and thermally-assisted capture/emission. The individual rates for these processes are described in the following.

3.1.2 Capture processes

The capture of charge carriers into quantum dots is a combined process of the capture of charge carriers from the band edge into the potential well of the QD, and the subsequent relaxation of the charge carriers to lower energy levels with a larger binding energy. If a capture barrier is present, the capture of carriers into QDs consists of three main capture paths, which are shown schematically in Fig. 3.2(a). In a pure tunneling capture, the charge carriers directly tunnel into an unoccupied state of the QD. If enough thermal energy is available, the charge carrier can also overcome the capture barrier by thermal excitation. In a combined process, the charge carrier is thermally excited to a higher energy level in the band continuum, and then tunnels through the barrier into the QD. If no capture barrier is present, the capture probability increases drastically and results in extremely fast capture times in QDs, which are in the order of some picoseconds [75, 76].

After the capture, the charge carrier may only be weakly bound to the QD. The subsequent relaxation to lower energy levels in the QD depends on the availability of mechanisms which can dissipate the excess energy of the charge carrier. At first, a *phonon-bottleneck* was assumed due to the zero-dimensionality of the QDs and a lack of phonons [88], but this assumption has proven to be wrong, as there are enough mechanisms that can dissipate the energy of the charge carriers [75, 89, 90]. According to [75], these mechanisms are:

- *Electron-electron or hole-hole scattering (Auger)*. The electron relaxes into the QD by giving the excess energy to another electron in the conduction band, which itself is energetically lifted to a higher energy (Fig. 3.2[b]). A successive relaxation down to the ground state of the QD is hence possible. The process is analogous for holes.
- *Multiple LO-phonon emission*. The electron relaxes to a lower state by giving its excess energy to several LO-phonons (Fig. 3.2[c]). The process is analogous for holes.

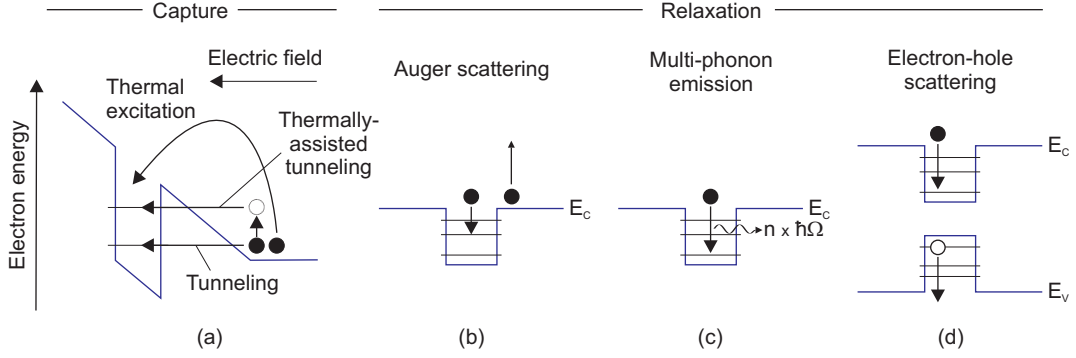


Figure 3.2: Capture and subsequent relaxation in QDs. (a) Capture mechanisms over/through a capture barrier: thermal excitation, tunneling, and thermally-assisted tunneling. (b) Auger scattering: the excess energy is transferred to another electron in the conduction band. (c) Multi-phonon-emission: the energy is transferred to several LO-phonons. (d) Electron-hole scattering: the energy of the electron excites a hole which is already confined in the QD.

- *Electron-hole scattering.* The electron relaxes to lower energies by giving the excess energy to a hole which is confined inside the same QD (Fig. 3.2[d]). The hole is excited to higher energy levels or is emitted out of the QD into the valence band. This process only works for type-I systems in which both charge carriers are confined.

In general, the electron capture and relaxation in a QD can be described by a capture rate c_n . The capture rate c_n is defined analogously to the concept used in nuclear physics. The QD is characterized by a capture cross section σ^n . Multiplied by the carrier flux, which is defined by the electron density around the QD n_{QD} and the root-mean-square thermal velocity of the electrons $\langle v_n \rangle$, the capture rate is

$$c_n = \sigma^n \langle v_n \rangle n_{QD}, \quad (3.10)$$

with

$$\langle v_n \rangle = \sqrt{\frac{3kT}{m_n^*}}, \quad (3.11)$$

where m_n^* is the effective mass for electrons. Accordingly, the hole capture rate is

$$c_p = \sigma^p \langle v_p \rangle p_{QD} \quad (3.12)$$

with

$$\langle v_p \rangle = \sqrt{\frac{3kT}{m_p^*}}, \quad (3.13)$$

where m_n^* is the effective mass for holes.

3.1.3 Emission processes

The potential well of the QDs can confine charge carriers spatially. With a certain probability, these charge carriers get emitted again from the QDs by various processes, which are illustrated in Fig. 3.3. The overall emission is a combined process of all emission processes. Depending on the ambient conditions around the QDs (light, fields, temperature etc.), the contribution of each type of emission process to the total emission rate is increased or decreased. The emission processes are:

- *Optical excitation.* A photon with sufficient energy can excite a charge carrier into the band continuum (Fig.3.3[a]). As light is not present in the energy ranges where the materials of this work are optically active (dark conditions), optical excitation is neglected in the following.
- *Thermal excitation.* Charge carriers are thermally excited over the barrier if sufficient thermal energy is available (Fig.3.3[a]).
- *Tunnel emission.* With a certain probability, which depends on the barrier height and its shape, the charge carriers tunnel from the QD state into an unoccupied state in the band continuum of the surrounding semiconductor matrix (Fig.3.3[a]). Although the electric field has no direct influence on the tunneling rate, it alters the shape of the barrier, and hence the tunneling rate is influenced by it.
- *Thermally-assisted tunneling.* In a combination of thermal excitation and tunneling, the charge carrier first gets excited by thermal energy to an intermediate energy level (real or virtual) and subsequently tunnels through the barrier, which is now effectively smaller and narrower than at the initial energy level (Fig.3.3[b]).

The emission processes can also take place for any other shape of the emission barrier. In particular, they are similar for the rectangular-shaped barriers which are also studied as part of this work (Chapter 7).

3.1.3.1 Thermal emission

To derive the thermal emission rate, a different approach than for the capture rate, where a model from nuclear physics was applied, has to be used. The dynamics of the charge carrier population within the QD was described in Sect. 3.1.1 by a simple rate equation (detailed balance). From Eq. 3.5 the mean occupation of the electron states in equilibrium was derived:

$$n_n(\infty) = N_{QD}^n \left(1 + \frac{e_n}{c_n} \right)^{-1}. \quad (3.14)$$

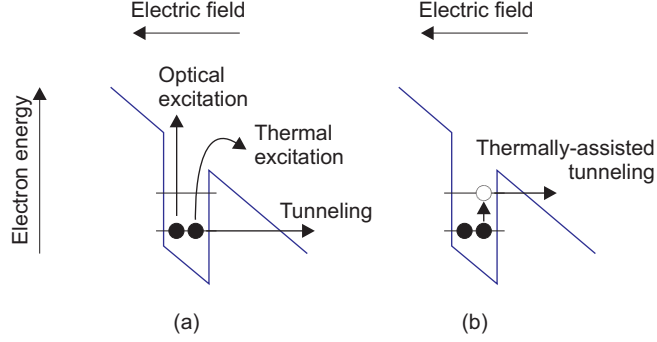


Figure 3.3: Emission processes of charge carriers in quantum dots. (a) Photons can optically excite charge carriers into the band continuum, the charge carriers can leave the QD by thermal excitation, or by tunneling through the barrier into the band continuum of the surrounding matrix. (b) The process combining thermal excitation to an intermediate energy level and subsequent tunneling through the triangular barrier is called thermally-assisted tunneling.

On the other hand, the mean occupation $n_n(\infty)$ of an electron state in the QD in thermal equilibrium is described by the Fermi-Dirac distribution [85]:

$$\frac{n_n(\infty)}{N_{QD}^n} = \frac{1}{1 + \frac{g_0}{g_1} \exp\left(\frac{E_0 - E_F}{kT}\right)}, \quad (3.15)$$

where E_0 is the energy level in the QD, and g_0 and g_1 the spin degeneracy of the unoccupied and occupied energy level, respectively. A common spin-degenerate energy level holds $\frac{g_0}{g_1} = \frac{1}{2}$ [86]. Inserting Eqs. 3.10 and 3.14 into Eq. 3.15 yields the electron emission rate

$$e_n = \sigma_n \langle v_n \rangle n_{QD} \frac{g_0}{g_1} \exp\left(\frac{E_0 - E_F}{kT}\right). \quad (3.16)$$

The free carrier density N_{QD} for a neutral non-degenerate ($n_{QD} < N_C$) n-type semiconductor in thermal equilibrium is given by the Boltzmann distribution with the Boltzmann constant k , the temperature T , and the energetic difference between the Fermi level E_F and the conduction band edge E_C . Using the effective density of states of the electrons at the conduction band edge N_C [37]² yields

$$n_{QD} = N_C \exp\left(-\frac{E_C - E_F}{kT}\right). \quad (3.17)$$

Inserting Eq. 3.17 into Eq. 3.16 leads to

$$e_n^{th} = \sigma_n \langle v_n \rangle \frac{g_0}{g_1} N_C \exp\left(-\frac{E_C - E_0}{kT}\right). \quad (3.18)$$

² $N_C = 2 \left(\frac{2\pi m_n^* kT}{h^2}\right)^{3/2}$

In the same way, the emission rate for holes with the hole energy level H_0 can be derived, using the difference of the Fermi level E_F to the valence band edge E_V , and the effective density of states for holes N_V at the valence band edge:

$$e_p^{th} = \sigma_p \langle v_p \rangle \frac{g_1}{g_0} N_V \exp\left(-\frac{H_0 - E_V}{kT}\right). \quad (3.19)$$

The energetic differences $E_C - E_0$ and $H_0 - E_V$ correspond to the emission barriers for electrons and holes, respectively. These barriers are also called *activation energy* E_a with $E_a = E_C - E_0$ and $E_a = H_0 - E_V$, respectively.

3.1.3.2 Temperature dependence of capture cross section

Since the processes involved in carrier capture, such as Auger scattering and/or phonon scattering, are temperature-dependent, the capture cross sections of the QDs for electrons and holes are also temperature-dependent [90]. Experimentally, the temperature dependence of the capture cross section seems to follow the law [91]:

$$\sigma_n(T) = \sigma_\infty^n \exp\left(-\frac{E_\sigma}{kT}\right), \quad (3.20)$$

with the temperature-independent *apparent capture cross section* σ_∞^n and a characteristic energy E_σ . Inserting Eq. 3.20 into Eq. 3.22 for the thermal emission rate yields:

$$e_n^{th}(T, \sigma_\infty^n, E_a) = \sigma_\infty^n \langle v_n \rangle \frac{g_0}{g_1} N_C \exp\left(-\frac{E_a + E_\sigma}{kT}\right). \quad (3.21)$$

with the *apparent activation energy* $E_a + E_\sigma$ for electrons. In QDs the temperature effect on the capture cross section expressed in terms of E_σ can be estimated by using the experimental data for the electron capture obtained by Müller *et al.* [75] and are found to be around $E_\sigma = 3$ meV for temperatures above 70 K [87]. Below 70 K, E_σ is even smaller than 3 meV. Hence, the change of the capture cross section with temperature can be neglected in QDs and the apparent capture cross section σ_∞^n is equal to the capture cross section σ_n . Also, the effect on the activation energy E_a is negligible and the apparent activation energy is taken for the actual activation energy E_a for charge carrier emission to the conduction or valence band continuum.

Inserting the root-mean-square thermal velocity, the effective density of states, and merging the constants into γ , the thermal emission rate for electrons is simplified to:

$$\boxed{e_n^{th}(T, \sigma_\infty^n, E_a) = \gamma_n T^2 \sigma_\infty^n \exp\left(-\frac{E_a}{kT}\right)}. \quad (3.22)$$

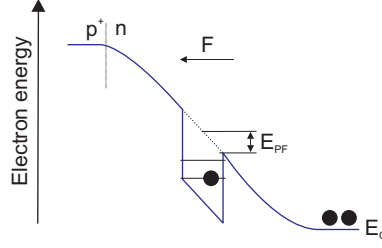


Figure 3.4: (a) Thermal emission of charge carriers in an electric field. The field-induced band bending lowers the emission barrier by E_{PF} (Poole-Frenkel effect [92]).

Analogously, the emission rate for holes is:

$$e_p^{th}(T, \sigma_\infty^p, E_a) = \gamma_p T^2 \sigma_\infty^p \exp\left(-\frac{E_a}{kT}\right). \quad (3.23)$$

3.1.3.3 Thermal emission in electric fields

The thermal emission rate derived in Section 3.1.3.1 is only valid in the absence of an electric field. If the QDs are inside an electric field, this has to be accounted for in the model. The electric field induced by the spatially fixed ionized donor and acceptor atoms creates a potential drop which leads to band bending around the QDs. The band bending lowers the emission barrier for charges inside the QDs by E_{PF} (see Fig. 3.4). This effect is the Poole-Frenkel effect [92]. Including the effect into the emission rate formula yields:

$$e_n^{th}(T, \sigma_\infty^n, E_a) = \gamma_n T^2 \sigma_\infty^n \exp\left(-\frac{E_a - E_{PF}}{kT}\right). \quad (3.24)$$

for electron emission, and

$$e_p^{th}(T, \sigma_\infty^p, E_a) = \gamma_p T^2 \sigma_\infty^p \exp\left(-\frac{E_a - E_{PF}}{kT}\right). \quad (3.25)$$

for hole emission. At the bias voltages used in the DLTS experiments, the Poole-Frenkel effect is $E_{PF} \approx 10$ meV, which is in the range of the error of the measurement (see Appendix E). Hence, the Poole-Frenkel effect is neglected in the DLTS analysis.

3.1.4 Tunnel emission

Besides leaving the QDs by thermal excitation, the charge carriers can also get emitted by tunneling through the barrier into an unoccupied state in the band continuum of the surrounding matrix material.

3.1.4.1 Direct tunneling

In a direct tunneling emission process the electron or hole tunnels directly through the barrier. The tunneling probability strongly depends on the height, the width, and the shape of the barrier. These properties are generally expressed in the *transparency* of the barrier. In a pn-junction, in the presence of an electric field F , the emission barrier with the height E_B has a triangular shape, and the transparency T becomes [93]:

$$T(E_B, F) = \exp \left[-\frac{4}{3} \sqrt{\frac{2m^*}{\hbar^2}} \cdot \frac{E_B^{3/2}}{eF} \right]. \quad (3.26)$$

Neglecting resonant tunneling effects, the transparency for arbitrary shapes of the barrier can be calculated using the WKB approach [38]. The transparency of a barrier with the energetic height of $V(z)$ between two points z_L and z_R is [94]

$$T(E_B, F) \approx \exp \left[-\frac{2}{\hbar} \left(\int_{z_L}^{z_R} \sqrt{2m^* \cdot (V(z) - E_B)} dz \right) \right]. \quad (3.27)$$

For a Dirac well with a triangular emission barrier the tunnel emission rate is [93]:

$$e^{tun}(E_B, F) = \frac{eF}{4\sqrt{2m^*E_B}} \exp \left[-\frac{4}{3} \sqrt{\frac{2m^*}{\hbar^2}} \cdot \frac{E_B^{3/2}}{eF} \right]. \quad (3.28)$$

In an adiabatic approximation with decoupled z (growth direction, parallel to the field), the resulting tunneling rate for a 1D confining potential of width L in a perpendicular field F , has a different pre-factor [95]:

$$e^{tun}(E_B, F, L) = \frac{\hbar\pi}{2m^*L^2} \exp \left[-\frac{4}{3} \sqrt{\frac{2m^*}{\hbar^2}} \cdot \frac{E_B^{3/2}}{eF} \right]. \quad (3.29)$$

The pre-factors have the unit s^{-1} and can be interpreted as the frequency with which the charge carriers hit the emission barrier E_B and attempt to tunnel through it (*attempt frequency*). As the pre-factor changes with the specific properties of the potential, it remains the largest unknown variable when calculating the tunneling rate.

3.1.4.2 Thermally-assisted tunneling

A combined process of thermal activation and tunneling is thermally-assisted tunneling. The emission takes place in two steps: first, the charge carrier is excited by thermal energy to an intermediate energy level which has a lower confinement energy. In the second step, the charge carrier tunnels from the intermediate level through the barrier, which is now effectively smaller and narrower than at the initial energy level. The

emission rate hence depends on the temperature, the barrier height and shape, and the electric field.

In a semi-classical approach, the emission rate is the product of the transparency of the barrier (Eq. 3.26 or 3.27) and the thermal activation rate for the charge carrier (see Eqs. 3.22 or 3.23) from the initial energy level E_A to the intermediate energy level E_i . The emission rate for a single intermediate energy level E_i and a triangular emission barrier of height E_A then becomes [93]:

$$e_n^{tat} = \gamma_n T^2 \sigma_n \cdot \exp\left(-\frac{E_A - E_i}{kT}\right) \cdot \exp\left[-\frac{4}{3}\sqrt{\frac{2m^*}{\hbar^2}} \cdot \frac{E_i^{3/2}}{eF}\right] \quad (3.30)$$

If all possible emission paths are included, the thermally-assisted emission rate has to be integrated over all possible intermediate energy levels E_i :

$$\boxed{e_n^{tat} = \gamma_n T^2 \sigma_n \cdot \int_0^{E_A} \exp\left(-\frac{E_A - E_i}{kT}\right) \cdot \exp\left[-\frac{4}{3}\sqrt{\frac{2m^*}{\hbar^2}} \cdot \frac{E_i^{3/2}}{eF}\right] dE_i.} \quad (3.31)$$

3.1.5 Total emission rate

The total emission rate is the sum of all emission processes that are present. Contrary to the proposition of Vincent *et al.* [93], which only takes into account the rates for thermal emission and thermally-assisted tunneling, a simulation of the emission rates for GaSb QDs in a pn junction [96], and comparing them with the experimentally determined rates [83], yielded that the pure tunneling rate has to be included in the total rate if the emission rate is calculated also for low temperatures. The total emission rate for electrons (and analogous for holes) hence becomes [25]:

$$\boxed{e_n^{tot} = e_n^{th}(T, E_a) + e_n^{tun}(F, E_B) + e_n^{tat}(T, F, E_A).} \quad (3.32)$$

For holes, it is:

$$\boxed{e_p^{tot} = e_p^{th}(T, E_a) + e_p^{tun}(F, E_B) + e_p^{tat}(T, F, E_A).} \quad (3.33)$$

3.1.6 Storage time in quantum dots

The storage of charges inside the QDs should take place in a voltage regime where the electric field is low. For the designs used in this work, tunneling processes can then be neglected and thermal emission is the process limiting the storage time [83]. The storage time τ can easily be derived from the emission rate e_a as it resembles the inverse

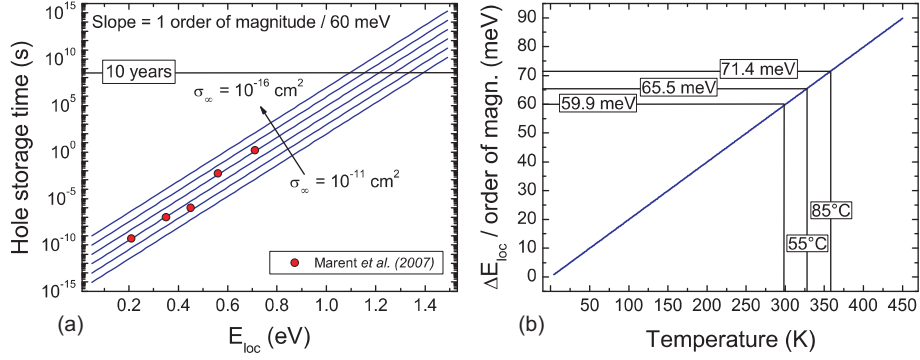


Figure 3.5: Theoretical hole storage times in QDs. (a) Hole storage time as a function of the localization energy E_{loc} for different apparent capture cross sections σ_{∞} at a temperature of 300 K. The data points are experimental values from [27]. (b) Inverse slope ($\Delta E_{loc}/dec$) as a function of the temperature. The temperatures relevant for semiconductor memories are indicated.

value ($\tau = 1/e_a$). As derived in Sect. 3.1.3.1, the thermal emission rate of holes from the QDs is:

$$e_a = \gamma T^2 \sigma_{\infty} \exp\left(-\frac{E_a}{kT}\right), \quad (3.34)$$

where E_a is the activation energy, T the temperature, k the Boltzmann constant, σ_{∞} the apparent capture cross section for $T = \infty$, and γ a temperature-independent constant. Besides the temperature, the emission rate depends on two parameters which completely characterize the electronic properties of a QD ensemble in terms of thermal emission. The apparent capture cross section σ_{∞} is a measure of how well the QDs couple to their surroundings, including interactions with LO-phonons or Auger scattering processes to exchange energy and momentum (see Sect. 3.1.3.1). According to Eq. 3.34, the emission rate is directly proportional to the apparent capture cross section σ_{∞} , hence the storage time is proportional to the inverse value of the apparent capture cross section. To isolate the relation between the activation energy E_a and the storage time, and to derive a rule of thumb for the effect of the localization energy E_{loc} on the storage time, the laws for logarithm conversion are used (see Appendix A for details). At constant temperature, the storage time increases by one order of magnitude for every $2.3 \cdot kT$ additional localization energy E_{loc} . At 300 K, this means that the storage time in the QDs increases by one order of magnitude for every 60 meV additional localization energy.

Figure 3.5(a) shows the hole storage time in a QD ensemble as a function of the localization energy for different apparent capture cross sections at a temperature of 300 K. The data points indicate values for QD ensembles that have been determined in previous work using capacitance spectroscopy [27]. The graph indicates that, experimentally, the apparent capture cross section varies by about three orders of magnitude.

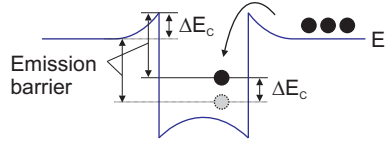


Figure 3.6: Carriers inside and outside the QD experience the Coulomb repulsion of another carrier inside the QD. The potential energy of the carrier inside the QD and the barrier are both increased by ΔE_C .

The inverse slope ($\Delta E_{loc}/dec$) for the increase by one order of magnitude in storage time is shown in Fig. 3.5(b). For 300 K the value is $\Delta E_{loc} = 59.9$ meV. For the two temperatures which are relevant to give figures of merit for semiconductor memories, the values increase to $\Delta E_{loc} = 65.5$ meV (55°C) and $\Delta E_{loc} = 71.4$ meV (85°C).

Based on the theory and the experimental data, an extrapolation can be made for the localization energy which is necessary to obtain ten years (non-volatility) of storage time in a memory. These values vary by about 300 meV depending on the apparent capture cross section of the QD ensemble. At 300 K, a localization energy of $E_{loc} \approx 1.1$ eV is necessary for $\sigma_\infty = 1 \cdot 10^{-16}$ cm², while this value increases to $E_{loc} \approx 1.4$ eV for $\sigma_\infty = 1 \cdot 10^{-11}$ cm². At 85°C , the values increase to 1.3 eV and 1.7 eV, respectively.

3.2 Many-particle effects in quantum dots

The quantum dots investigated in this work can confine more than one charge carrier. If more than one hole occupies a QD, a typical quantum mechanical many-particle problem arises. As a result of the properties of the self-assembled QDs (mainly their small size) the energy of the Coulomb repulsion between the holes is in the range of the quantization energy, and hence has to be taken into account. The effect of the Coulomb repulsion can be seen in the schematic in Fig. 3.6. If one electron is already confined in the QD, the degeneracy of the hole level is lifted and its potential energy is increased by ΔE_C . Another electron outside the QD is repulsed by the electron in the QD and has to overcome an additional barrier with the same height as ΔE_C . The overall emission barrier is not changed, hence the Coulomb repulsion cannot be seen in the DLTS experiments (Chapter 6), but it is visible in tunneling experiments (Chapter 7).

Besides the direct Coulomb repulsion, exchange interaction has also to be considered. The exchange interaction is a consequence of the indistinguishability of two electrons or holes (i.e. Fermions) and hence the Pauli principle, which demands an antisymmetric wavefunction [97].

In a many-particle system, energies for single electrons or holes cannot be given, only the total energy of the many-particle state is defined. In the case of QDs, the total

energy for a number of electrons or holes in the dots consists of the localization energy, the quantization energy, the direct Coulomb interaction, the exchange interaction, and the overlap energy. Hence, the level splittings derived in this work (see Chapter 7) are those between many-particle hole states.

A simple approximation for the individual contributions of the Coulomb repulsion and the exchange interaction in QDs can be found in [98] where the QDs are assumed to be two-dimensional with a parabolically-shaped potential. For more realistic geometrical shapes and potentials, the many-particle effects can also be included into 8-band $\mathbf{k}\cdot\mathbf{p}$ calculations [99].

3.3 Summary

The results of this chapter are summarized in the following:

- A charge in the matrix surrounding the QD can be captured by the QD. If a capture barrier is present, the capture can take place by thermal activation over the barrier, by tunneling through the barrier, or in a combined process by thermally-assisted tunneling. After capture, the charge will relax down to the levels with lower energies. During the process the energy is dissipated by phonon emission, Auger scattering, or electron-hole scattering.
- Charges that are confined inside a QD are re-emitted with a certain probability. The emission processes are similar to the capture processes: thermal activation over the emission barrier, tunneling through the barrier, and thermally-assisted tunneling. To derive the thermal emission rate the condition of detailed balance is applied in which re-capture processes also have to be taken into account. For DLTS experiments, only thermal emission is relevant.
- The storage time of charges in QDs can be derived from the thermal emission equation. It is determined by two parameters which are characteristic for a given QD ensemble: the capture cross section and the activation energy. While the storage time directly increases with the inverse of the capture cross section, it increases by one order of magnitude for every $2.3\cdot kT$ additional localization energy. At 300 K, the value is about 60 meV.
- If more than one charge is present in a QD, many-particle effects, such as Coulomb repulsion, exchange interaction, and correlation effects have to be taken into account.

Chapter 4

Coupling of quantum dots to two-dimensional carrier gases

The following chapter describes the coupling mechanisms between a QD ensemble and an adjacent two-dimensional carrier gas. Based on the coupling mechanisms, an equivalent circuit model allows to derive detailed information about the electronic structure of the QD ensemble.

4.1 Coupling mechanisms

If a quantum dot layer is inserted into a device in the vicinity of a 2D system, the charges in the QDs couple to the 2D system in two ways. First, the charges inside the QDs change the potential landscape at the position where the 2D gas resides. This increases the scattering of carriers in the 2D gas and changes their mobility. Second, the QDs are capacitively coupled to the 2D gas and charges inside the QDs will deplete the 2D gas by the field effect. In the Drude model, the conductance σ of the 2D gas is [38]:

$$\sigma = n_{2D}\mu q, \quad (4.1)$$

where n_{2D} is the area density of charges in the 2D gas, q the elementary charge, and μ the mobility of the charge carriers in the 2D gas with its usual expression [37]:

$$\mu = \frac{q\tau}{m^*}, \quad (4.2)$$

where m^* is the effective mass and τ the inverse of the sum of the individual scattering rates of all scattering processes present (following Matthiessen's rule):

$$\frac{1}{\tau} = \frac{1}{\tau_{ph}} + \frac{1}{\tau_{QDs}} + \dots, \quad (4.3)$$

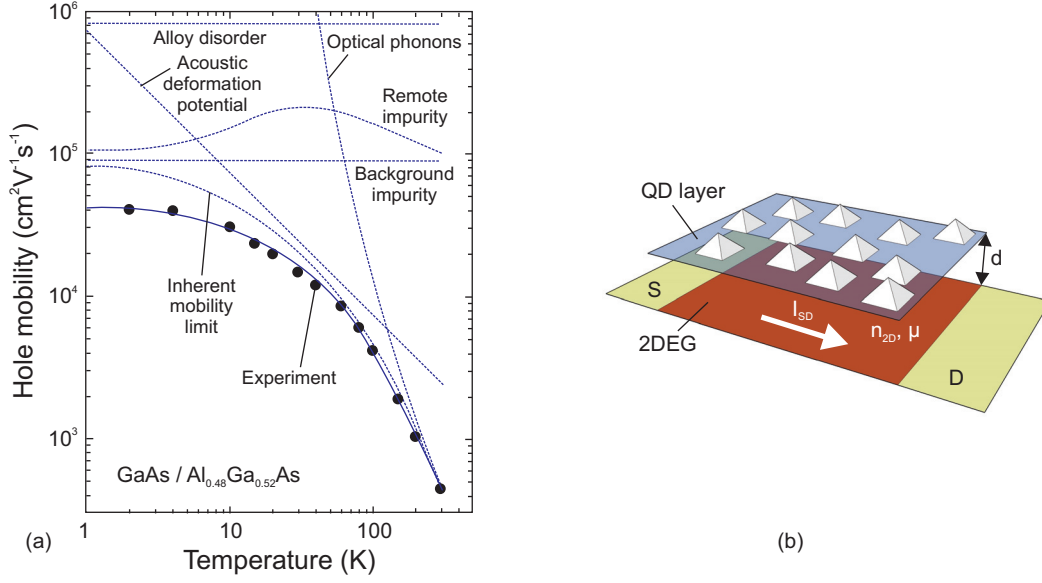


Figure 4.1: (a) Mobility contributions and total mobility in a 2DHG formed in an $\text{Al}_{0.48}\text{Ga}_{0.52}\text{As}/\text{GaAs}$ heterostructure (after [100]). (b) Schematic depiction of the scattering problem. The QD layer is separated by the distance d from the 2DEG or 2DHG. The source-drain current is determined by the mobility μ and the electron density n_{2D} in the 2DEG/2DHG.

in which the phonon scattering rate τ_{ph} and the QD-induced scattering rate τ_{QD} are given as examples here (see Fig. 4.1[a]).

The scattering rate τ_{QD} expresses the effect of charges in QDs on the mobility of the 2D system, while the area density n_{2D} of the 2D gas expresses the effect of the capacitive coupling.

4.1.1 Remote impurity scattering

A layer of charged QDs in the vicinity of a 2D gas changes the potential landscape at the position of the 2D gas by Coulomb interaction. This increases the scattering of electrons in the 2D gas, and hence the effect can be expressed as an additional scattering rate $1/\tau_{QD}$ induced by the charges in the QDs. In a collaboration with the Institute for Theoretical Physics of the TU-Berlin, Gerold Kießlich and Tobias Brandes modeled the scattering rate in a memory function approach [101, 102]. A schematic of the problem is shown in Fig. 4.1(b). For a QD layer with an area density of n_{QD} , charged with Z electrons, within a distance of d of the 2DEG/2DHG, the scattering rate with the wavevector k_F at the Fermi energy is [103]:

$$\frac{1}{\tau_{QD}} = \frac{Z^2 n_{QD}}{n_{2D}} \left(\frac{4E_F}{\hbar} \right) \int_0^1 \frac{1}{\sqrt{1-k^2}} \frac{k^2}{(2yk+1)^2} \exp[-4dk_F k] dk, \quad (4.4)$$

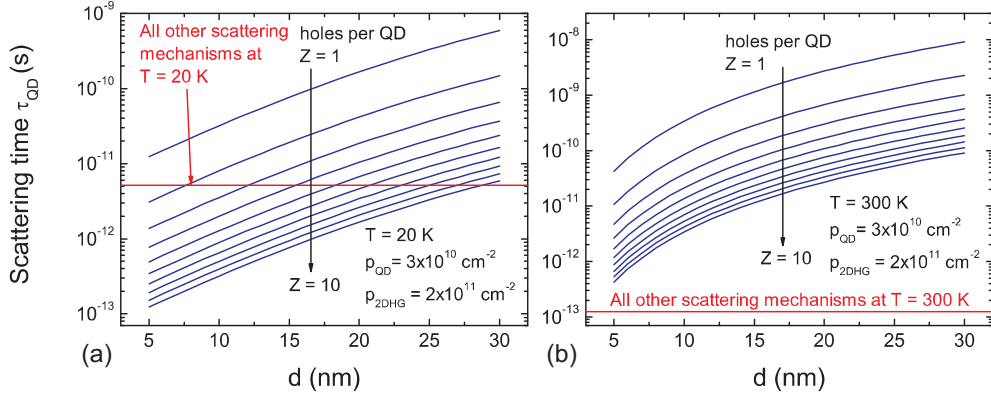


Figure 4.2: Calculated scattering time τ_{QD} induced by a number of Z holes inside the QDs at a distance d to the 2DHG at (a) 20 K and at (b) 300 K. At 20 K, the QD scattering time is in the range of the scattering time of all other scattering mechanisms. At 300 K, the scattering times of all other mechanisms are much shorter.

where $y \equiv k_F/q_{TF}$, with the Thomas-Fermi screening wave vector $q_{TF} = 2\pi e^2 \rho_F / (\epsilon_0 \epsilon_s)$. The Fermi level in the 2DEG/2DHG is:

$$E_F = \frac{\hbar^2 k_F^2}{2m^*} = kT \cdot \log \left[\exp \left(\frac{\pi \hbar^2 n_{2D}}{m^* kT} \right) \right] \quad (4.5)$$

A more convenient formula is derived by Davies for the scattering rate induced by remote impurities [38], which can be regarded as similar to charged QDs. This approach is used to calculate the quantum lifetime of a charge inside the 2DEG, and by inclusion of the direction dependence of the scattering processes which are adverse to transport of charges in the direction from the source to the drain contact of a device, the transport lifetime is calculated. The scattering time of charges in the 2DEG/2DHG is then:

$$\frac{1}{\tau_{QD}} = \frac{\pi \hbar_{QD}}{8m^* (k_F |d|)^3}, \quad (4.6)$$

where n_{QD} is the area density of the QDs, k_F the wavevector at the Fermi energy, which can be calculated by $k_F = \sqrt{n_{2D} 2\pi}$, and d the distance between the QD layer and the 2DEG.

If the 2DEG or 2DHG is used to detect the charge state in the QDs, the effect of the QD-induced scattering rate has to be larger than any other scattering effect. Hence the scattering rate of the QDs must be smaller than the scattering rates of the other scattering processes in the device. For the read-out by a current measurement between the source and the drain contact, the read-out efficiency can be defined as:

$$\frac{\Delta\sigma}{\sigma_0} = \frac{\sigma_0 - \sigma}{\sigma_0} = \frac{\tau_0}{\tau_0 + \tau_{QD}}, \quad (4.7)$$

where σ is the conductance and τ_0 the total lifetime of all other scattering processes. Figure 4.2 shows the scattering times calculated with Eq. 4.4 for 20 K and 300 K. At 20 K, a number of Z holes in the QDs at a distance of d from the 2DHG induces a scattering time τ_{QD} in the range of the scattering times of all other scattering mechanisms. Hence, the charges in the QDs have an effect on the conductance of the 2DHG. For 6 holes and a distance of 10 nm, the effect is $\Delta\sigma/\sigma_0 \approx 0.86$. Increasing the temperature results in an increasing phonon density, and the effect of the QDs on the 2DHG decreases to $\Delta\sigma/\sigma_0 \approx 1.3 \cdot 10^{-2}$ at 300 K.

4.1.2 Capacitive coupling

Besides their contribution to the total scattering rate, the charges inside the QDs are capacitively coupled to the channel, and by this coupling they have an effect on the charge carrier density of the 2D gas [38]. The effect is commonly known as field-effect and has found numerous applications, such as in the ubiquitous field-effect transistor [37]. Similar to the gate in a field-effect transistor, the QDs act as an additional gate, and depending on the number of charges in the QDs, the channel between the source and the drain contact is depleted of free charge carriers by Coulomb repulsion.

In a simple model, the storage time inside the QDs is assumed to be infinite, and any carrier dynamics are neglected. The QDs then act as a floating gate with constant charge, and following the equivalent circuit model in Fig. 4.3, the change of the channel charge can be derived assuming the conservation of charge within the device: [50, 104]:

$$dQ_{Ch} = -C_{QDs/Ch}dV_{QDs} - C_{Ch/G}dV_G, \quad (4.8)$$

where Q_{Ch} is the channel charge, $C_{QDs/Ch}$ the capacitance between the QDs and the channel, and $C_{Ch/G}$ the capacitance between the channel and the gate. dV_{QDs} is the change of the potential at the QD layer and dV_G the change of the gate potential. The change of the potential at the position of the QDs is:

$$dV_{QDs} = \frac{dQ_{QDs}}{C_\Sigma} + \frac{C_{QDs/G}}{C_\Sigma}dV_G, \quad (4.9)$$

with dQ_{QDs} the change of the charge inside the QDs, and the total capacitance $C_\Sigma = C_{QDs/Ch} + C_{Ch/G}$. Combining Eqs. 4.8 and 4.9 yields:

$$dQ_{Ch} = -\frac{C_{QDs/Ch}}{C_\Sigma}dQ_{QDs} - \left(C_{Ch/G} + \frac{C_{QDs/Ch}}{C_\Sigma}C_{QDs/G} \right) dV_G. \quad (4.10)$$

From Eq. 4.10 it can be seen that if the gate voltage is kept constant ($dV_G = 0$), a change in the charge in the QDs by dQ_{QDs} induces a change of the channel charge

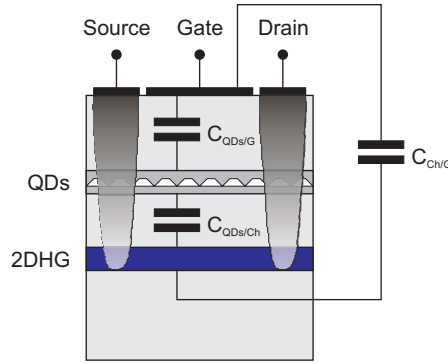


Figure 4.3: Equivalent circuit model used to extract the effects of the capacitive coupling. The device is assumed to consist of two geometric capacitances $C_{QDs/G}$ and $C_{QDs/Ch}$, and in the case of a covering gate, an additional capacitance $C_{Ch/G}$.

dQ_{Ch} by $-(C_{QDs/Ch}/C_{\Sigma})dQ_{QDs}$. The proportionality constant $-(C_{QDs/Ch}/C_{\Sigma})$ is an expression for the lever arm of the device, which determines how much the potential at the position of the QD layer is changed when the gate voltage is changed.

Another important figure of merit, which is commonly used to express the effect of a floating gate on the channel of a field-effect transistor, is the shift of the threshold voltage ΔV_T (see Fig. 2.12[c]). For that, a constant channel charge is assumed ($dQ_{Ch} = 0$). Then, the shift is:

$$\Delta V_T = \frac{\Delta Q_{QDs}}{C_{QDs/G} + \left(\frac{C_{\Sigma}}{C_{QDs/Ch}}\right) C_{Ch/G}}. \quad (4.11)$$

If the channel-gate capacitance can be neglected (i.e. no cover gate) and $Q_{QDs} = Z \cdot q$, this expression simplifies to:

$$\boxed{\Delta V_T = \frac{Z \cdot q}{C_{QDs/G}}}. \quad (4.12)$$

The capacitance between the QD layer and the gate can be approximated as the geometrical capacitance of a plate capacitor $C_{QDs/G} = (\epsilon_0 \epsilon_r A)/(d_{QDs/G})$, with A the area of the gate, and $d_{QDs/G}$ the distance between the plates.

4.1.3 Quantum capacitance

The 2D gas can also be used as detector to probe the density of states of the QD ensemble. Based on an iterative model, which can handle an arbitrary number of embedded quantum systems between a metallic top gate contact and a back contact, the total capacitance in dependence on the dot charge can be calculated [79]. In the special case of the devices studied in this work, the device can be separated into two geometri-

cal capacitances accounting for the MODFET structure, and a potential-dependent quantum capacitance accounting for the density of states of the QD ensemble and the GaAs QW into which the QDs are embedded (see Fig. 7.1[a] in Chapter 7). The geometric capacitances are:

$$C_{1,2} = \frac{\epsilon_r \epsilon_0 A}{d_{1,2}}, \quad (4.13)$$

with the relative dielectric constant ϵ_r , the vacuum electric constant ϵ_0 , the active gate area A , and the distance d_1 between the top gate contact and the QD layer, and d_2 the distance between the QD layer and the 2D gas. The quantum capacitance [105] for the QD ensemble is:

$$C_{QD} = q^2 D_{QD}(E_F) = \frac{q^2}{n} \sum_{i,k} \delta(E_F - E_i), \quad (4.14)$$

where q is the elementary charge, $D_{QD}(E_F)$ the density of states of the QD ensemble, n the number of dots, i the index running over the individual dots, k the index for each individual energy level in a QD, and E_F the Fermi level. Similarly, the quantum capacitance of the GaAs QW into which the QD layer is embedded is:

$$C_{QW} = q^2 D_{QW}(E_F) = \frac{q^2 m^*}{\pi \hbar^2}, \quad (4.15)$$

assuming that only the lowest subband is occupied by charges during the measurements. The capacitance of the quantum region containing the QD layer and the GaAs QW is then:

$$C_q = C_{QD} + C_{QW}. \quad (4.16)$$

For the total capacitance of the device, dependent on the potential energy E in the quantum region, then follows [79]:

$$\boxed{C_{tot}(E) = \frac{1}{\frac{1}{C_1} + \frac{1}{C_2 + C_q(E)}}}. \quad (4.17)$$

Equation 4.17 cannot be solved analytically without knowing the lever arm λ , which itself depends on the total capacitance C_{tot} . Defining the lever arm as:

$$\lambda = \frac{q}{\frac{dE}{dU}} = \frac{\frac{1}{C_{tot}}}{\frac{1}{C_2 + C_q}}, \quad (4.18)$$

the total capacitance can be written as:

$$C_{tot}(E) = \frac{dQ}{dU} = \frac{1}{\frac{dU}{dQ_1} + \frac{q^2}{\lambda} (D_{QD} + D_{QW})}. \quad (4.19)$$

C_{tot} can now be calculated numerically by starting with the lever arm λ for empty QDs (with $C_q = 0$). The bias voltage U is then increased by ΔU and the new Fermi level calculated for $U + \Delta U$ using the value of the current lever arm. With the new Fermi level E_F , the new density of states $D_{QD} + D_{QW}$ at E_F can be obtained. With these values, the total capacitance C_{tot} and the new lever arm are calculated. The peak positions, resembling the hole energy levels in the density of states of the QD ensemble (used as input parameters), are then adjusted by hand to fit the measured capacitance curve. The full width at half maximum of the peaks in the input curve is then related to the inhomogeneous broadening of the QD ensemble due to variations in size, shape and chemical composition of the individual QDs. Thus, the equivalent circuit model allows to determine the relative position and level splittings of the many-particle states of the QD ensemble.

4.1.4 Temperature effects in the 2D detector

Measurements of the tunneling currents resulting from the emission and capture processes between the QD ensemble and the 2DEG/2DHG can be used to derive the many-particle hole or electron states of the QD ensemble (see Chapter 5). However, in order to resolve individual many-particle states in the QD ensemble, the Fermi function has to be sufficiently steep, otherwise the peaks are blurred and cannot be resolved (see Fig. 4.4). At low temperatures (i.e. 4.2 K), temperature effects due to Maxwell-Boltzmann broadening of the Fermi function can be neglected, and the Fermi function is sharp enough. When increasing the temperature, the thermal broadening has to be included into the calculation of the total capacitance curve $C_{tot}(E)$. With the assumption that only a single subband is occupied by charge carriers in the 2D gas, the density of states of the 2D detector is constant. The temperature effects can then be approximated by multiplying the density of states $D_q(E)$ of the quantum region by the Fermi function $f(E, E_F, T)$ at the respective temperature T and Fermi level E_F (at the position of the QDs it is derived from the gate voltage by using the lever arm). The result is then integrated over the energies from below the first QD level up to where the Fermi level has decayed sufficiently (i.e. from 0 to ∞). This yields the total number of holes which can participate in the tunneling process:

$$p_{tot}(E_F, T) = \int_0^{\infty} f(E, E_F, T) D_q(E) dE. \quad (4.20)$$

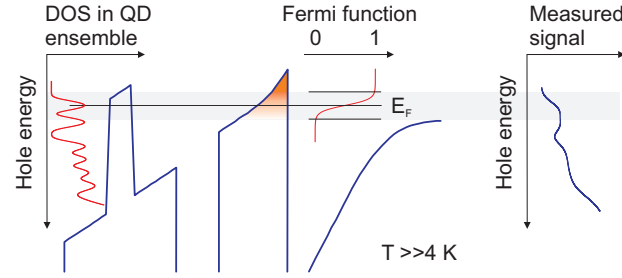


Figure 4.4: Effect of Maxwell-Boltzmann broadening of the Fermi function. Increasing the temperature smears out the density of states of the QD ensemble as seen by a 2D gas detector.

Then the derivative of $p_{tot}(E_F, T)$ is taken. This yields the thermally-broadened density of states of the quantum region (or in other words: it yields the DOS as it is seen by the 2D gas detector):

$$D_{q,T>4K}(E, T) = \left. \frac{dp_{tot}(E_F, T)}{dE_F} \right|_{E_F=E}. \quad (4.21)$$

With the thermally-broadened density of states $D_{q,T>4K}(E, T)$, the quantum capacitance D_q and the total capacitance C_{tot} can be calculated iteratively as described in Sect. 4.1.3.

4.2 Summary

The main results of this chapter are the following:

- Two mechanisms couple the QD ensemble to an adjacent 2D carrier gas: (remote impurity) scattering and capacitive coupling (field-effect).
 - Scattering induced by the charges in the QDs decreases the mobility in the 2D gas. However, the effect is only significant if other scattering mechanisms are not dominant. At 300 K, LO-phonon scattering dominates all other processes, and hence the scattering due to the charges in the QDs can be neglected.
 - In the capacitive coupling mechanism the charges in the QDs deplete the 2D gas. This effect is independent of the temperature and is widely used in field-effect transistors and Flash memories.
- An equivalent circuit model of a device with a layer of QDs allows to determine the level splittings of the many-particle energy levels of the QD ensemble.

Chapter 5

Measurement methods

The following chapter describes the measurement methods used in this work. In the first part, capacitance-voltage (C-V) spectroscopy and its application to the investigation of the electronic properties of QDs is described. The second part explains a time-resolved measurement method, from which the many-particle hole energy levels in a QD ensemble are derived, and the emission and capture processes between a QD ensemble and a 2DHG are studied.

5.1 Static Capacitance Spectroscopy

A standard tool to analyze the electronic properties of a semiconductor device and nanostructures is capacitance-voltage (C-V) spectroscopy [37, 85, 106]. A QD ensemble has a number of states, into which charge carriers can be captured and which they can get re-emitted from. As a consequence, QDs contribute to the total capacitance of a device. This can be used to investigate the electronic properties of quantum dots. For this purpose, the QDs are embedded into a pn junction.

5.1.1 Pn junctions

The conductance of a semiconductor can be increased by doping. Depending on the type of dopant (donors or acceptors), n-doped and p-doped semiconductors are distinguished. In an n-doped semiconductor the majority carriers are electrons, in a p-doped semiconductor holes are the majority carriers. The specific selection of the majority carrier type and the combination of alternately doped semiconductors build the foundation for devices such as diodes, transistors, and semiconductor memories, and has been the basis of all microelectronics. In this section, the basic properties of the simplest semiconductor device, a diode or pn junction, are described.

5.1.1.1 Depletion region

If an n-doped and a p-doped semiconductor are brought into contact, a *pn junction* is formed [37]. As a result of the opposite doping, an excess of free electrons in the n-doped region, and an excess of free holes in the p-doped region lead to a concentration gradient in the device. In the region around the interface the carriers diffuse across the junction into the oppositely doped region, leading to a diffusion current. The charge of the remaining ionized dopants is not compensated anymore by the free carriers, which leads to the creation of a space charge region with positive charges in the n-region and negative charges in the p-region. These fixed charges create an electric field which induces a drift current in the direction opposite to the diffusion current. In thermal equilibrium these currents compensate each other and the Fermi level is the same throughout the device. This leads to a band bending of the conduction and the valence band with the magnitude given by the built-in voltage V_{bi} (see Fig. 5.1). For the GaAs devices studied in this work, the built-in voltage at a temperature of 300 K is ~ 1.3 V.

The most important property of a pn junction is its rectifying behavior. Depending on the polarity of the applied external voltage, a current is flowing or not. The reason for this behavior is the voltage-dependent length of the depletion region and the resulting increase or decrease of the band bending. In forward bias, the length of the depletion region becomes smaller. When the external bias reaches the built-in voltage, the conduction band and the valence band are completely flat (flat-band condition) and the resistance becomes ohmic. In reverse direction, however, the width of the depletion region and the band bending increase and only a very small current is flowing. The width of the depletion region is [37]

$$w = \sqrt{\frac{2\epsilon_s}{q} \left(\frac{N_A + N_D}{N_A N_D} \right) V_{bi}}, \quad (5.1)$$

with the permittivity ϵ_s of the semiconductor material, the elementary charge q , the doping concentrations for donors N_D and acceptors N_A , and the built-in voltage V_{bi} . In this work, diodes are investigated which have an abrupt junction with a large difference in the doping concentrations. As a consequence, the depletion region extends almost entirely into the region with the lower doping. With the doping in the lower doped region N_B and an additional external bias V_{ext} , Eq. 5.1 becomes

$$w = \sqrt{\frac{2\epsilon_s(V_{bi} - V_{ext})}{qN_B}}. \quad (5.2)$$

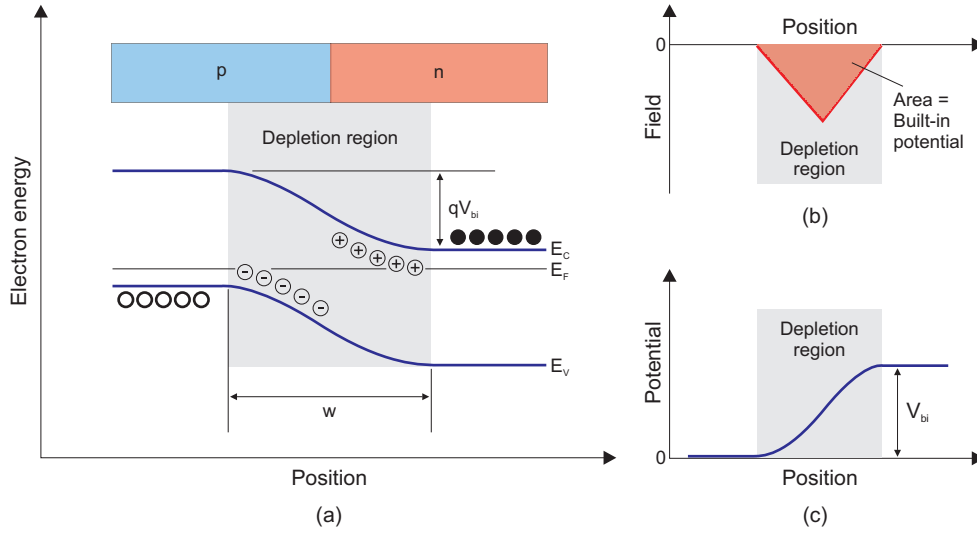


Figure 5.1: Conduction and valence band, electric field and potential of an abrupt pn junction (after [37]). (a) Concentration gradients of electrons and holes lead to a diffusion current across the junction. The remaining fixed ionized donor and acceptor atoms create an electric field which creates a drift current in the direction opposite to the diffusion current. In thermal equilibrium the Fermi level is the same throughout the device and a depletion region is created. The width of the depletion region is w , E_C the conduction band edge, E_V the valence band edge, E_F the Fermi level, and V_{bi} the built-in potential. (b) Electric field and (c) potential distribution inside the depletion region.

5.1.1.2 Capacitance of a pn junction

In a pn junction the fixed ionized donors and acceptor create a capacitance. As a consequence of the voltage dependence of the width of the depletion region, the differential capacitance $C = dQ/dV$ has to be examined. With the electric field $dE = dQ/\epsilon_s$ and the width of the depletion region w (Eq. 5.2), $dV = wdE$ can be approximated and hence the capacitance of a pn junction is

$$C = \frac{dQ}{dV} = \frac{dQ}{w \frac{dQ}{\epsilon_s}} = \frac{\epsilon_s}{w}. \quad (5.3)$$

This corresponds to the capacitance of a plate capacitor with unit area and a distance between the two plates which is equal to the width w of the depletion region. If the distance w is substituted by the expression in Eq. 5.2 for an abrupt pn junction with unequal doping concentrations in the two regions, Eq. 5.3 becomes

$$C = \frac{\epsilon_s}{w} = \sqrt{\frac{q\epsilon_s N_B}{2(V_{bi} - V_{ext})}}. \quad (5.4)$$

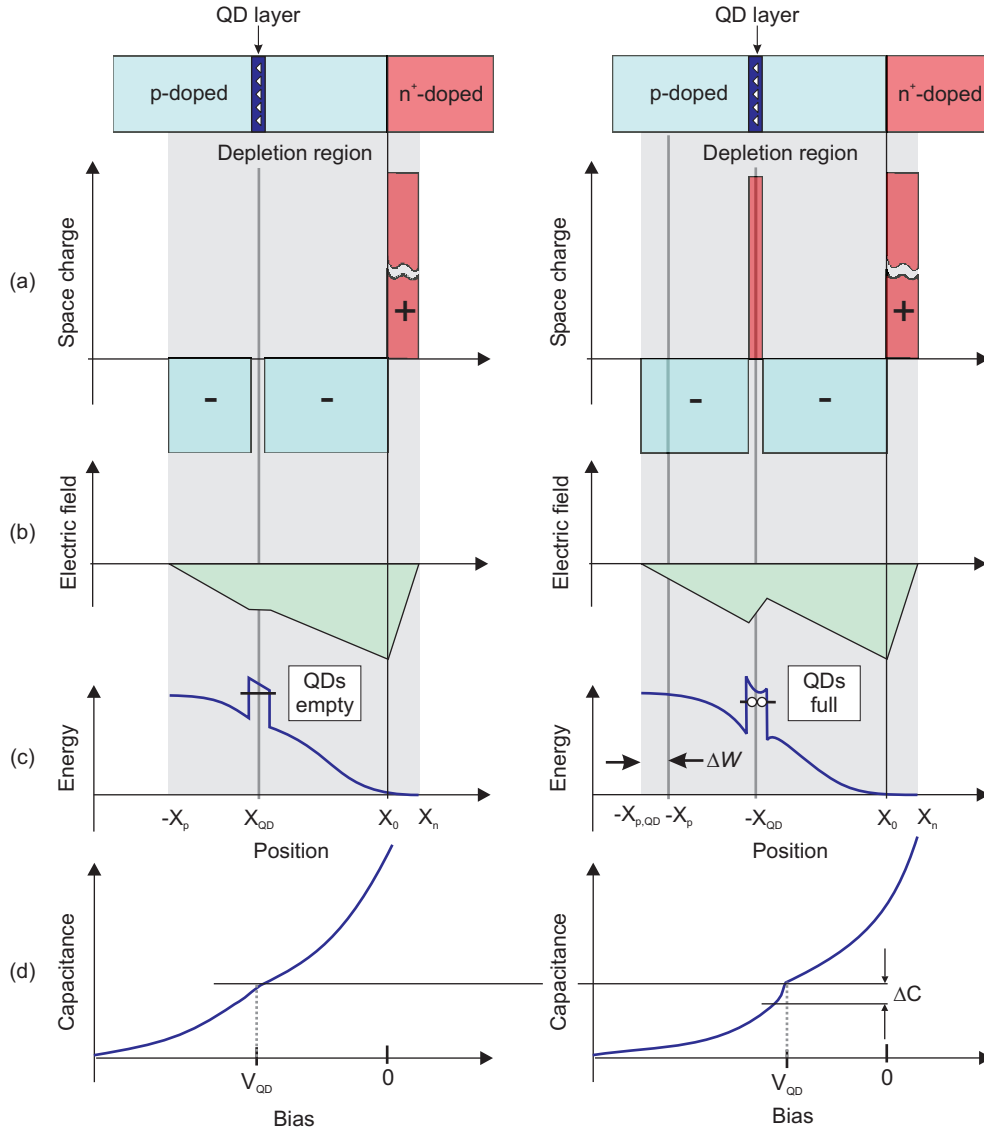


Figure 5.2: Quantum dots inside the p-doped region of a n^+p -junction. The left side depicts the situation for empty QDs, the right side for QDs filled with holes. (a) Fixed space charge distribution, (b) electric field, (c) valence band, and (d) capacitance. The depletion region is marked by the grey background, x_p and x_n mark the extension of the depletion region on the p-side and the n-side, respectively; x_{QD} is the position of the QDs, and x_0 the position of the pn junction. The difference in the width of the depletion region induced by the holes inside the QDs is Δw . V_{QD} marks the voltage at which the QDs enter the depletion region (adapted from [96]).

5.1.1.3 Static Capacitance Spectroscopy

Within the Schottky approximation, the charge carrier fluctuation due to the variation of the external bias only takes place at the edge of the depletion region of the pn junction (or Schottky diode). In an abrupt n^+p diode, where the doping concentration on the n-side is much higher than on the p-side, Eq. 5.2 can be used. When measuring

the capacitance as a function of the external bias voltage, the doping concentration can be extracted from Eq. 5.4 (here assuming that all donors/acceptors are ionized, which is a reasonable assumption at $T = 300$ K). This is easily done by plotting $1/C^2$ versus the bias voltage V_{ext} :

$$\frac{1}{C(V_{ext})^2} = \frac{2(V_{bi} - V_{ext})}{q\epsilon_0\epsilon_r A^2 N_B}. \quad (5.5)$$

If the doping concentration is constant throughout the p-doped region, $1/C^2$ versus V_{ext} will be a straight line, from which the doping concentration can be derived from the slope, while the x-axis intercept yields the built-in voltage V_{bi} . If the doping concentration changes within the device, a depth profile can be derived by partially differentiating Eq. 5.6, which yields:

$$N_B(V_{ext}) = -\frac{2}{q\epsilon_0\epsilon_r A^2} \left[\frac{1}{\frac{d}{dV_{ext}} \left(\frac{1}{C^2} \right)} \right]. \quad (5.6)$$

5.1.1.4 Quantum dots inside a pn junction

In the following, the case of QDs embedded into a pn diode is considered. If the QDs are within the p-doped region of a n^+p -diode, holes as majority carriers are confined in the dots¹. Hence, the holes inside the QDs have to be taken into account, when calculating the total capacitance of the diode. While the fixed ionized acceptors are negatively charged, the additional holes inside the QDs contribute with a positive charge, which leads to a local change of the electric field and the potential. As a consequence, the holes in the QDs locally compensate the charges of the ionized acceptors.

Figure 5.2 schematically depicts the space charge distribution, the electric field, the valence band, and the resulting capacitance curve for a pn junction with embedded QDs. The left side of Fig. 5.2 depicts the situation for empty QDs, while the right side shows the situation of QDs filled with holes. It can be seen in Fig. 5.2(c), that holes inside the QDs partly compensate the electric field induced by the fixed positive charges of the ionized acceptors, leading to a band bending around the QDs and an increase in the width of the depletion region by Δw , which results in a reduction of the capacitance by ΔC .

Including the positive charges of the holes in the QDs into Eq. 5.4 yields the total static capacitance

$$C_{QD} = \epsilon_s \sqrt{\frac{qN_B}{2(\epsilon_s(V_{bi} - V_{ext}) + qn_h N_{QD} x_{QD})}}, \quad (5.7)$$

¹If an electron (minority carrier) also gets captured into the QD, it instantly recombines with the hole, and hence only holes are stored inside the QDs.

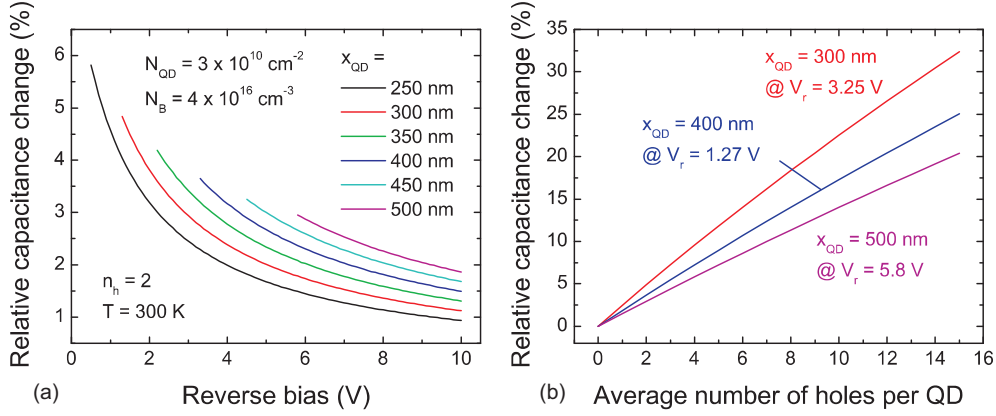


Figure 5.3: Relative influence of charged QDs inside a pn junction on the total capacitance of the diode. (a) Relative capacitance change versus the reverse bias for different distances x_{QD} of the QDs to the pn junction. The curves start at the reverse bias where the depletion region extends far enough to reach the QD layer. (b) Relative capacitance change versus the average number of holes per QD in the QD ensemble for different distances to the pn junction. The curves deviate only very slightly from a linear shape. The storage time of the holes inside the QDs is assumed to be infinite.

where n_h is the number of holes confined², N_{QD} is the density of the QDs, and x_{QD} the distance of the QD layer from the pn junction. The relative change in the capacitance of the diode caused by the charged QDs is then

$$\Delta C = \frac{C}{C_{QD}} = \sqrt{1 + \frac{qn_h N_{QD} x_{QD}}{\epsilon_s (V_{bi} - V_{ext})}}. \quad (5.8)$$

From Eq. 5.8 it can be seen that the relative change in capacitance does not only depend on the number of charges inside the QDs, but also on their position relative to the pn junction. Utilizing Eq. 5.8, Fig. 5.3(a) depicts the relative influence of charged QDs inside a pn junction for different distances x_{QD} between the QD layer and the junction. It can be seen, that the influence gets smaller, when the distance increases. Figure 5.3(b) shows the relative influence as a function of the number of holes inside the QDs. It can be seen, that increasing the number of holes has an almost linear effect on the total capacitance. This linearity allows to directly measure the emission (and capture) of holes from (into) the QDs by measuring the total capacitance of the diode.

5.2 Time-resolved Capacitance Spectroscopy

As described in the previous section, the width of the depletion region in a pn diode (or Schottky diode) depends on the applied external bias voltage and the doping concentration in the space charge region. It can be seen from Eq. 5.8, that the total capacitance

²It is assumed that the storage time of the holes in the QDs is infinite.

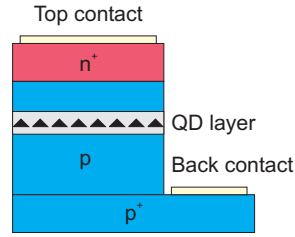


Figure 5.4: Schematic sample structure of a DLTS sample. A layer of QDs is embedded into a n^+p diode (to study the electron emission an p^+n diode has to be used). The charge state of the QDs can be manipulated by applying a bias voltage. The diode capacitance can be used to measure the emission processes.

is sensitive to any charges within the depletion region, i.e. deep levels, or in our case charges inside a layer of QDs. Hence, the carrier dynamics of such deep levels or QDs can be monitored using time-resolved capacitance spectroscopy. The method is referred to as *Deep-Level Transient Spectroscopy* (DLTS) and was initially developed to characterize deep levels and defects in semiconductors [85, 90, 107–109]. From the measured capacitance transients the activation energies and capture cross sections of the underlying emission process can be extracted [85]. As the width of the depletion region and the electric field at the position of the trap can be tuned by the external bias voltage, a depth profile of the trap concentration can be obtained and the influence of the electric field on the emission processes can be studied in detail [110, 111].

As QDs have a confining potential which can store charge carriers, they act as deep traps [86]. Hence, DLTS can be used to study the thermal emission processes in QDs. It allows to determine the activation energies and the capture cross sections of QD ensembles embedded into a pn diode. DLTS has been successfully used to study various QD systems [27, 81, 82, 112–118].

For the time-resolved measurement, Eq. 5.8 has to be modified. The storage time of the holes inside the QDs is not infinite anymore as assumed above. Hence, the time-dependent occupation of the QDs $n_h = n_h(t)$ has to be taken into account and yields the time-dependent capacitance of the pn diode with an embedded layer of QDs:

$$C_{QD}(t) = \epsilon_s \sqrt{\frac{qN_B}{2(\epsilon_s(V_{bi} - V_{ext}) + qn_h(t)N_{QD}x_{QD})}}, \quad (5.9)$$

and

$$\Delta C(t) = \frac{C}{C_{QD}(t)} = \sqrt{1 + \frac{qn_h(t)N_{QD}x_{QD}}{\epsilon_s(V_{bi} - V_{ext})}}. \quad (5.10)$$

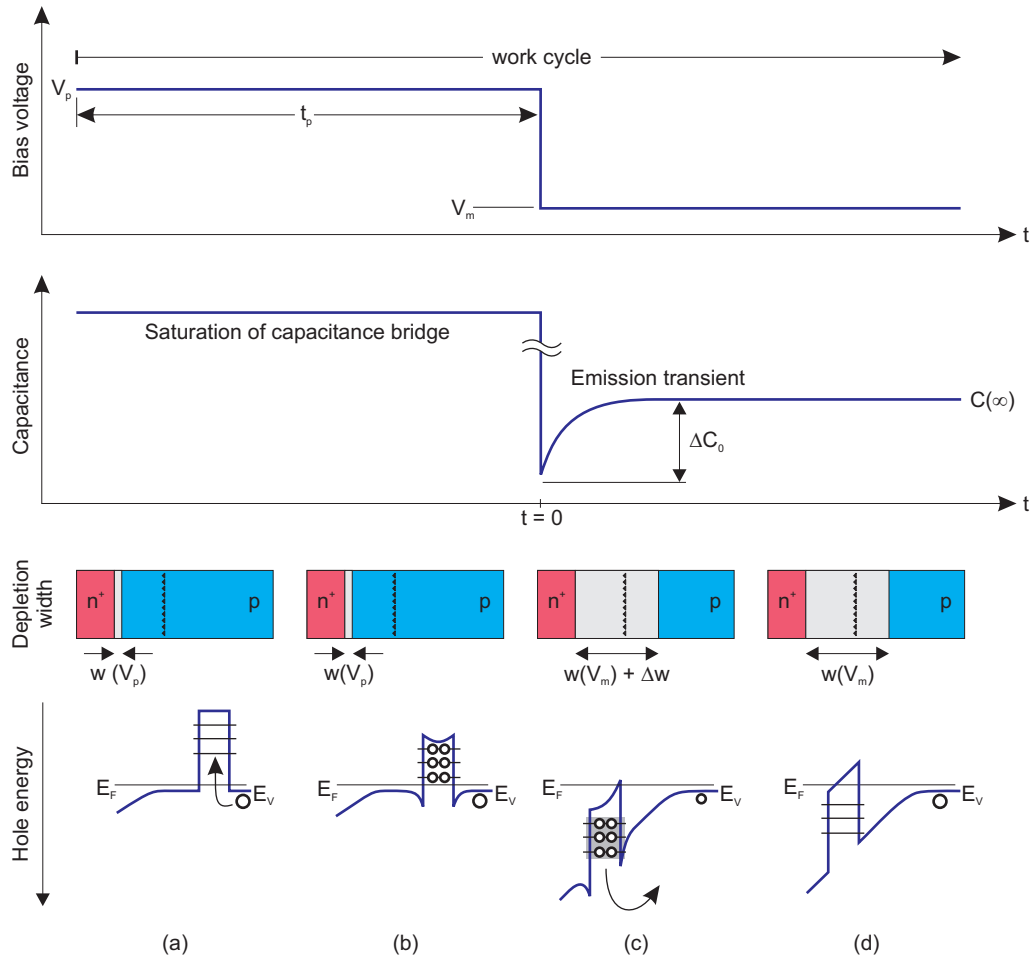


Figure 5.5: Work cycle of a DLTS measurement to study the hole emission from a layer of QDs embedded into a pn diode. (a) The bias voltage is set to V_p where the depletion region does not reach the QDs and the Fermi level E_F is well below the hole energy levels of the QDs. Holes are captured into the QDs. In this bias region, the capacitance bridge is usually going into saturation, which is indicated by the constant capacitance. (b) In the steady state condition, the QDs are full at V_p . (c) The measurement is started at $t = 0$ with setting the bias to V_m and recording the capacitance. The depletion region now extends well beyond the QD layer and the Fermi level E_F is well above the hole energy levels of the QDs. The holes in the QDs get thermally emitted, which leads to a capacitance transient with the amplitude ΔC_0 . (d) In the steady state, the QDs are empty at V_m and the capacitance reaches the value of $C(\infty)$.

5.2.1 Measurement principle

In the following, the measurement principle of DLTS is described for hole emission³. More details can be found in [85]. A single layer of self-organized QDs is embedded into the p-doped region of a n^+p diode, which is shown schematically in Fig. 5.4. The depletion region extends mainly into the p-doped region.

In the first step of the DLTS measurement cycle (Fig. 5.5[a]), the bias voltage is set to

³It is analogous for electrons.

V_p such that the depletion region does not reach the QD layer and the Fermi level is well above the hole energy levels of the QDs. Holes are now captured by the QDs from the band continuum of the surrounding matrix and relax down to the lowest energy levels by the mechanisms described in Section 3.1.2. Usually, the capacitance bridge used to measure the capacitance saturates and the capacitance stays constant during the filling pulse. In the steady state condition of this bias voltage, the QDs are full with holes (Fig. 5.5[b]). After filling the QDs with holes, the bias is set to the measurement bias V_m in reverse direction (Fig. 5.5[c]). Here, the recording of the capacitance is started ($t = 0$). At V_m , the hole energy levels of the QDs are below the Fermi level E_F and emit the holes by thermal emission. According to the relationship expressed in Eq. 5.10, the emission of the holes from the QDs can directly be observed as a capacitance transient with the amplitude of ΔC_0 . In the steady state condition at a bias voltage of V_m , the QDs are empty (Fig. 5.5[d]) and the capacitance reaches its steady state value of $C(\infty)$. After the measurement is over and all holes are emitted, the measurement cycle is repeated again. In general, the same emission transient is recorded several times (typically 20 to 30 times) and averaged afterwards to enhance the signal-to-noise ratio. The measurement of the hole emission is repeated at different temperatures.

5.2.2 Rate window and Double-Boxcar Method

After recording the capacitance transients, they are further analyzed. The main parameter which is derived from the analysis is the time constant of the emission process. From the time constant, the activation energy and the capture cross section can be derived according to the relationship expressed in Eqs. 3.22 and 3.23. An emission from a single energy level would be a mono-exponential with a certain time constant τ and an emission transient [85]:

$$C(t) = C(\infty) - \Delta C_0 \exp\left(-\frac{t}{\tau}\right), \quad (5.11)$$

with ΔC_0 the amplitude and $C(\infty)$ the steady state capacitance of the device (see Fig. 5.5). However, due to ensemble broadening, multiple emission paths, and many-particle effects, the emission processes from QDs are in general not mono-exponential, but show a multi-exponential behavior [119]. This renders a simple exponential fit of the measured emission transient impossible. Hence, the rate-window (*Boxcar*) concept has to be used, in which the contribution of the emission process to the signal at a certain time constant τ is analyzed. With the two times t_1 and t_2 , which define the

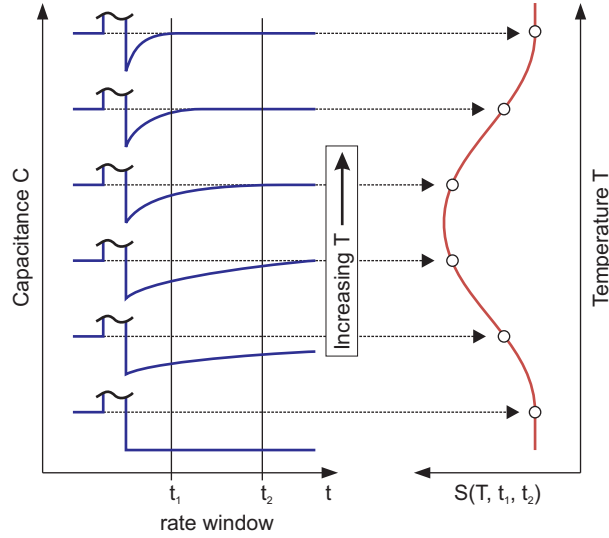


Figure 5.6: Analysis of the capacitance transient by using a rate window (defined by t_1 and t_2) to derive the DLTS Signal $S(T, t_1, t_2)$ at different temperatures T . For thermal emission, the emission rate increases with temperature. At low temperature, the emission is very slow and the change of capacitance ΔC_0 is very small within the rate window. When increasing the temperature, $S(T, t_1, t_2)$ goes through a maximum (DLTS peak) at a certain temperature as the emission becomes faster. At higher temperatures, the emission becomes too fast and the transients have decayed before the time reaches the rate window, and the DLTS signal decreases again.

edges of the rate-window, the DLTS signal at the temperature T is:

$$\begin{aligned} S(T, t_1, t_2) &= C(T, t_2) - C(T, t_1) \\ &= \Delta C_0 \left[\exp\left(-\frac{t_2}{\tau(T)}\right) - \exp\left(-\frac{t_1}{\tau(T)}\right) \right]. \end{aligned} \quad (5.12)$$

The peak signal can be derived by differentiating Eq. 5.12 with respect to τ . The maximum occurs if

$$\tau(T) = \tau_{ref} = \frac{t_2 - t_1}{\ln\left(\frac{t_2}{t_1}\right)}, \quad (5.13)$$

which defines the reference time constant τ_{ref} of the rate window. Plotting $S(T, t_1, t_2)$ versus the temperature T yields the DLTS spectrum with a maximum at the temperature where $\tau(T) = \tau_{ref}$ (see Fig. 5.6). It should be noted, that a maximum in the DLTS spectrum only occurs for thermally activated processes, while a tunneling process leads to a constant DLTS signal as the emission is independent of temperature [86].

For an ensemble of self-organized QDs, the inhomogeneously broadened DLTS spectrum resembles the mean emission process of all thermally activated emission processes involved. The derived time constant is hence the average time constant at the maximum of the Gaussian ensemble distribution of the QDs ensemble [119].

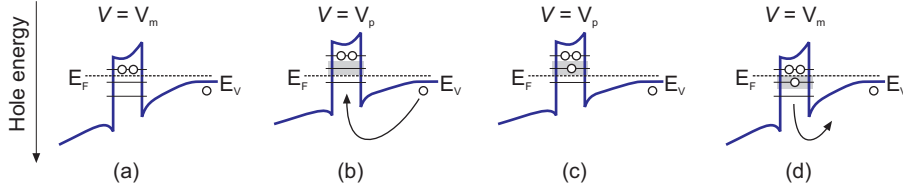


Figure 5.7: Work cycle of a charge-selective DLTS measurement. (a) At a reverse bias V_m , the QDs are partially charged up to the Fermi level E_F . (b) When a small bias pulse V_p is applied, a single hole energy level is above the Fermi level E_F , and a single hole is captured. (c) In the steady state, the energy level is filled with one hole. (d) The bias voltage is then switched back to V_m , the Fermi level E_F is now above the last occupied hole energy level and a single hole is emitted from the QDs.

To further analyze the DLTS spectrum, the time constant τ_{ref} is set equal to the inverse emission rate in Eq. 3.23 (here for hole emission):

$$\frac{1}{\tau_{ref}} = e_p = \gamma_p \sigma_p T^2 \exp\left(-\frac{E_a}{kT}\right). \quad (5.14)$$

Then Eq. 5.14 is linearized:

$$\ln(\tau_{ref} T^2 \gamma_p) = \frac{E_a}{k} \frac{1}{T} - \ln(\sigma_\infty). \quad (5.15)$$

Using different reference time constants τ_{ref} and plotting the results $\ln(\tau_{ref} T^2 \gamma_p)$ versus the inverse temperature T^{-1} yields an Arrhenius plot. By a linear fit the apparent capture cross section σ_∞ for infinite temperature can be derived from the intercept with the y-axis, and the activation energy E_a of the emission process from the slope of the Arrhenius plot.

An improvement of the signal-to-noise ratio (SNR) can be achieved if the capacitance transients are averaged over a time of t_{av} [120]. The SNR then scales with $\sqrt{t_{av}}$ [108]. The method is referred to as *Double-Boxcar Method* and the reference time constant is then given by:

$$\tau_{ref} = \frac{t_2 - t_1}{\ln\left(\frac{t_2 + \frac{1}{2}t_{av}}{t_1 + \frac{1}{2}t_{av}}\right)}. \quad (5.16)$$

5.2.3 Charge-selective DLTS measurements

During the DLTS measurements, the QDs are usually fully charged with carriers, and the emission of all these carriers is observed in the experiment. As a result of the emission from all hole energy levels of the QDs, the DLTS spectrum is broadened and a *mean* activation energy and apparent capture cross section is derived therefrom. To study the electronic structure of the QDs in more detail, a charge-selective method can be applied, where the emission (and possibly also the capture) of approximately

only one charge carrier per QD is observed. This method has been established for QDs by Geller *et al.* [87] and has been successfully used to study various material systems [27, 81, 82].

A schematic work cycle of the charge-selective DLTS for hole emission from and capture into QDs is shown in Fig. 5.7. In general, the bias voltage is kept at values where the QDs are in the depletion region. At a given bias voltage V_m , the QDs are partially charged with holes, up to the Fermi level E_F (Fig. 5.7[a]). When setting the bias voltage to V_p , a single hole energy level in the QDs moves above the Fermi level, and, on average, a single hole is captured into each QD (Fig. 5.7[b]). In steady state, the QDs are each charged with an additional hole up to the Fermi level E_F (Fig. 5.7[c]). The bias voltage is then set back to V_m , where the previously charged energy level in the QDs is now again below the Fermi level E_F , and a single hole per QD is emitted by thermal activation (Fig. 5.7[d]). When setting the charging pulse bias V_p and the measurement voltage V_m to a fixed distance $V_p = V_r + \Delta V$, where ΔV is the relative charging pulse height, the individual energy levels in the QDs can be probed, starting from the ground state up to the higher states. The DLTS peaks obtained in this way are much more narrow than the ones obtained by conventional DLTS. In this way, the ensemble-broadened energy levels of the QDs can be studied in more detail, and activation energies and apparent capture cross sections can be derived for each one of them.

Of particular interest are the parameters derived from the ground level emission, which yield the localization energy as key electronic parameter of the QD ensemble.

5.3 Capacitance and time-resolved conductance measurements of 2D gases

As described in Sect. 4.1.2, the QDs act as quantum capacitance and contribute to the total capacitance of the device. In this work, a layer of QDs is embedded into a MODFET structure. The majority of the holes resides in the 2DHG, which pins the Fermi level throughout the device. This pinning allows to precisely control the energetic position of the QD energy levels with respect to the Fermi level by varying the gate voltage, and to observe the emission and capture processes that occur due to the voltage change. Measuring the change in differential capacitance $C = dQ/dV$ gives detailed information about the electronic properties of the QD ensemble. The method has been successfully used for electron systems [98, 121–124] and hole systems [125–128].

If the gate voltage is adjusted such that the Fermi level is aligned with a hole energy level of the QD ensemble, the holes can tunnel to the QDs and back. If an ac voltage is added on top of the dc gate bias, the structure acts as plate capacitor (with the metal gate and the 2DHG resembling the plates) and an ac current with a phase shift

is induced. As the differential capacitance is proportional to the induced current, the measured capacitance increases for increasing current:

$$C(V_g) = \frac{I_{ac}}{f_{ac} V_{ac}} \Big|_{V_g}, \quad (5.17)$$

where I_{ac} is the induced current, f_{ac} the ac measurement frequency, and V_{ac} the measurement voltage added to the dc gate bias V_g .

If the density of states is constant (which is the case in this work, as $B = 0$), the total capacitance of the structure is given by (see Sect. 4.1.3):

$$C_{tot}(E) = \frac{1}{\frac{1}{C_1} + \frac{1}{C_2 + C_q(E)}}, \quad (5.18)$$

where C_1 is the geometrical capacitance between the gate contact and the QD layer, C_2 the geometrical capacitance between the QD layer and the 2DHG (including all other capacitances of the setup), and C_q is the capacitance of the quantum region (i.e. the contribution of the QD ensemble). Hence, the electronic density of states of the quantum dots can be directly measured in the steady state condition by measuring the total differential capacitance and analyzing the result in the way described in Sect. 4.1.3. It is worth noting, that if the temperature is low enough such that only coupling via tunneling is present between the QD ensemble and the 2DHG, the density of states of the QD layer can only be seen in the measurement, if the tunneling time constant τ_{tun} is smaller than the inverse of the measurement frequency:

$$\tau_{tun} \lesssim \frac{1}{f_{ac}}, \quad (5.19)$$

otherwise the charges cannot follow the applied ac voltage, do not contribute to the current, and remain invisible.

Besides measuring the capacitance between the channel and the gate, the transfer of holes from the QDs to the 2DHG and vice versa can also be measured directly. If holes are transferred from the 2DHG reservoir to the QD ensemble, these holes are missing in the 2DHG and its conductance is reduced. Hence, the 2DHG channel can also be used as a very sensitive detector for the charge state of the QDs [23, 129]. In contrast to the C-V measurements, it is also possible to make time-resolved measurements and record the real-time change of the occupation of individual energy levels of the QDs during hole emission from and hole capture into the QD ensemble. Whether an emission or capture process takes place or not depends on the initial occupation of the QDs. Either tunneling is allowed (a hole energy level of the QDs is unoccupied at the Fermi level) or blocked (hole energy levels of the QDs at the Fermi level are occupied). Using this mechanism for detecting the density of states of the QD ensemble, it is also possible to

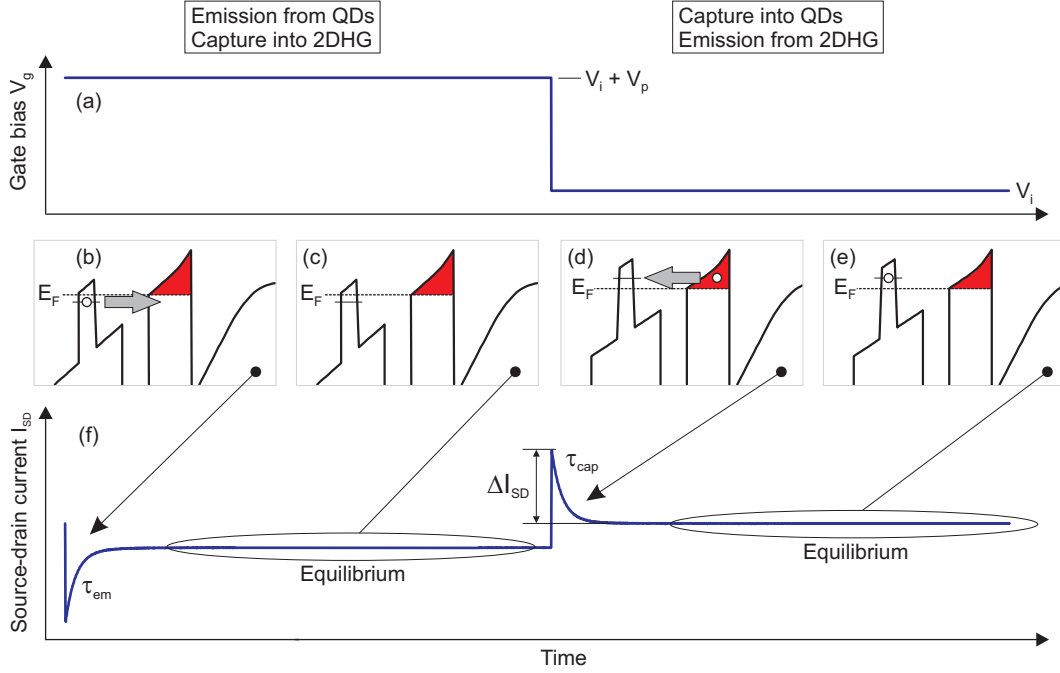


Figure 5.8: Schematic measurement principle for measuring the hole emission and capture in the time-resolved conductance of the 2DHG. (a) Gate bias for a single step in the measurement cycle. (b) Non-equilibrium: the Fermi level E_F is above the occupied hole energy level of the QDs, hence holes tunnel through the barrier into the 2DHG until (c) the equilibrium situation is reached. (d) The Fermi level E_F is below an unoccupied energy level of the QD ensemble, hence holes tunnel from the 2DHG through the barrier into the QDs until (e) the equilibrium situation is reached. (f) Change in the source-drain current I_{SD} as a result of the change of the charge density n_{2DHG} and the mobility μ_{2DHG} of the 2DHG. The amplitudes ΔI_{SD} of the emission and capture transients are a measure of the number of holes that are transferred during the voltage pulse V_p .

investigate non-equilibrium carrier dynamics [130].

The time-dependent hole density in the 2DHG can be derived by a time-resolved measurement of the source-drain current I_{SD} , which flows through the 2DHG when applying a constant voltage V_{SD} (see also Sect. 4.1):

$$I_{SD}(t) = C \cdot n_{2DHG}(t) \cdot \mu_{2DHG}(t) \cdot V_{SD}, \quad (5.20)$$

where C is a constant⁴, $n_{2DHG}(t)$ the hole density and $\mu_{2DHG}(t)$ the mobility of the holes in the 2DHG. Hence, the source-drain current can change by two mechanisms, which were already described in Chapter 4: change in the hole density and change in the mobility due to scattering. If a magnetic field is present, the individual contributions to the change in the source-drain current can be separated in a Hall measurement [131]. The measurement cycle for the time-resolved measurement is depicted schematically in Fig. 5.8. The gate voltage V_g is set to an initial value V_i . In equilibrium, the QDs are

⁴ $C = q \cdot A/l$, with A the area of the channel cross section, l the length of the channel, and q the elementary charge.

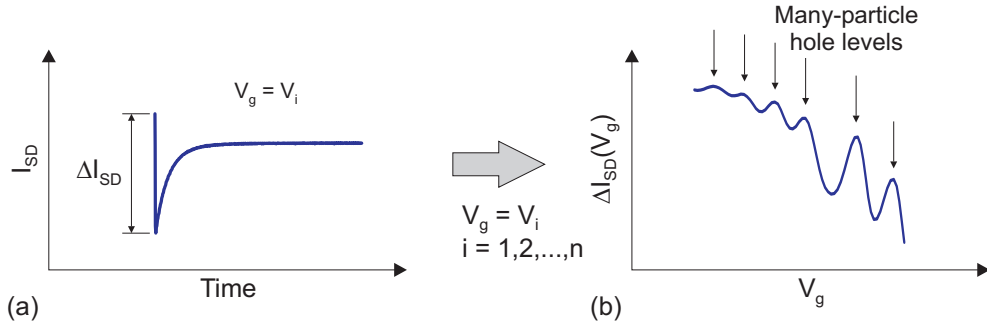


Figure 5.9: Analysis of emission and capture transients. (a) The amplitude ΔI_{SD} is a measure for the number of charges that is transferred between the QDs and the 2DHG during the pulse. The measurement probes the density of states of the QD ensemble around the Fermi level. (b) Amplitudes ΔI_{SD} as a function of the gate voltage V_g (and hence the Fermi level).

charged with holes up to the Fermi level E_F . When a small pulse (\sim mV) is applied $V_i + V_p$, the Fermi level E_F shifts above the last occupied hole energy levels of the QDs (see Fig. 5.8[b]). As the charging state of the QDs is a non-equilibrium situation now, the holes below the Fermi level get emitted from the QDs and are captured into the 2DHG via tunneling through the barrier. When the holes are transferred from the QD ensemble to the 2DHG the hole density in the 2DHG increases (Fig. 5.8[f]). As a consequence, the source-drain current increases according to Eq. 5.20. In contrast to single-particle tunneling in single-charge experiments where the change in charge density is discrete and abrupt due to its statistical nature [132–134], a QD ensemble shows an exponentially decaying transient with the time constant τ_{em} . This is due to the statistical nature of each individual tunneling process in time (each described by a Poisson distribution), which add up to an exponential decay in a QD ensemble. When equilibrium is reached, the QDs are filled with holes down to the Fermi level (Fig. 5.8[c]), and the source-drain current I_{SD} stays constant. In the next step, the gate voltage is set back to the initial voltage V_i . In a situation reversed to the previous one, unoccupied energy levels of the QDs are now above the Fermi level, and holes tunnel from the 2DHG into the QDs (Fig. 5.8[d]) until the equilibrium situation is reached and the QDs are charged again down to the Fermi level (Fig. 5.8[e]). As before, the tunneling capture of holes into the QDs results in an exponentially decaying transient in the source-drain current with the tunneling time constant τ_{cap} .

In the course of the measurement, the gate voltage V_i is swept in small steps (\sim mV), such that the Fermi level sweeps through the energy levels of the QD ensemble. This way, a small energetic region around the Fermi level is probed with each step. As the Fermi level sweeps through the density of states of the QD ensemble, the amplitudes ΔI_{SD} of the emission and capture transients resolve the density of states of the QD ensemble, since they are a measure of the number of holes that is transferred between the QDs and the 2DHG during the pulse. If the amplitudes are plotted versus the

respective gate voltage V_i , the resulting curve resembles the density of states of the QD ensemble⁵ (see Fig. 5.9) [78].

If the temperature is increased (> 4 K), thermally-assisted tunneling and thermal activation become relevant emission and capture processes. The nature of the underlying process can be identified by analyzing the time constants as a function of the temperature (see Chapter 3).

The method described above allows the detailed study of the carrier dynamics and density of states. A wide range of time constants can be measured, and the method can be used for strongly coupled (small time constants) and weakly coupled (large time constants) systems, and hence overcomes the limitations of the capacitance measurements. Another advantage of the method is, that in contrast to the capacitance measurements, the structures can be scaled down to a few, or possibly even a single QD without the loss of signal, if the gate width-to-depth ratio is kept constant.

5.4 Summary

The sections about the measurement methods described in this chapter are summarized in the following:

- Quantum dots act as quantum capacitance and contribute to the total capacitance of a device. As a consequence, the electronic properties and the carrier dynamics of the QDs can be studied by capacitance measurements.
- For DLTS measurements, the QDs are embedded into a pn diode. During the DLTS measurement, the thermal emission of holes from the QDs is observed in the time-resolved capacitance at different temperatures. By analyzing the transients with the Double-Boxcar method, the DLTS spectrum is obtained. Using different reference time constants, an Arrhenius plot is derived from the peak positions in the DLTS spectra, which is fitted with a linear curve. The slope and the intercept of the curve yield the activation energy and the apparent capture cross section of the QD ensemble. In the charge-selective DLTS, the electronic structure of the QDs is studied in more detail and the localization energy of the QD ensemble is derived.
- To investigate the coupling between a layer of QDs and a 2DHG, the QDs are embedded into a MODFET device. The many-particle density of states of the QD ensemble can be measured using capacitance spectroscopy and time-resolved measurements of the conductance of the 2DHG. The time-resolved measurements also yield the time constants of the underlying emission and capture processes

⁵The exact profile of the density of states is dependent on the lever arm, which itself depends on the charge state of the QDs and is hence not constant (see Section 4.1.2).

and allow to distinguish between different emission processes, when conducted at different temperatures.

Chapter 6

Electronic properties of and storage times in quantum dots

The following chapter presents in detail the results obtained by capacitance spectroscopy measurements for various GaSb/GaAs quantum dot and quantum ring samples, as well as for an $\text{In}_{0.25}\text{Ga}_{0.75}\text{As}/\text{GaAs}/\text{GaP}$ quantum dot sample. The outcome of the measurements are the electronic properties which characterize the quantum systems in their ability to trap and release holes. The key parameters are the localization energy and the apparent capture cross section for holes.

Parts of this chapter have already been published in [135–137].

6.1 GaSb/GaAs quantum dots

In the following section the results of GaSb/GaAs QD samples grown by MBE are investigated by static capacitance-voltage (C-V) spectroscopy and DLTS. The results are presented in ascending order of the total localization energy determined, hence the sample names are QD-X, with X in ascending order A, B, C, and D. If reference samples without QDs are available, they are labeled WL-X with the letter X corresponding the QD sample. The real names of the samples and the details of their origin are listed in Appendix C.

GaSb/GaAs QDs offer an interesting option to increase the localization energy for holes due to their type-II band alignment, which lets the difference in the band gap between GaSb and GaAs go almost completely into the valence band offset. Nevertheless, theory showed (see Section 2.4.2) that the hole localization energy can vary a lot, if the QDs have a different size or chemical composition.

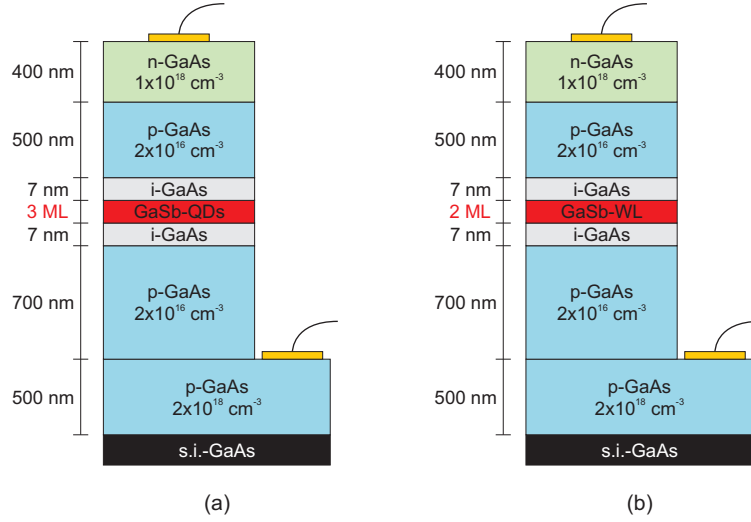


Figure 6.1: Sample structure of the GaSb/GaAs QD sample. (a) QD-A: a layer of GaSb QDs is embedded into a pn-diode structure. (b) WL-A: reference sample containing only a GaSb wetting layer.

6.1.1 Sample QD-A: QDs

The first sample consists of a single GaSb/GaAs QD layer inside a pn-diode structure. It was grown in the group of Shih-Yen Lin at Academia Sinica, Taiwan.

6.1.1.1 Sample structure

The schematic sample structure of QD-A is depicted in Fig. 6.1. On top of a semi-insulating GaAs substrate 500 nm highly p-doped (Be, nominally $2 \cdot 10^{18} \text{ cm}^{-3}$) GaAs is grown to form a back contact. It is followed by 700 nm lower p-doped (Be, nominally $2 \cdot 10^{16} \text{ cm}^{-3}$) GaAs. Subsequently, on top of a 7-nm-thick undoped GaAs layer, 3 ML of GaSb are deposited with a V/III ratio of 1.3 at a temperature of 490°C , followed by Sb soaking for 120 s at the same temperature until Stranski-Krastanow QDs (see Section 2.4.1) are formed, and another 7 nm of undoped GaAs. Details on the growth of the GaSb/GaAs QDs can be found in [138, 139]. On top of the QD layer, another 500 nm of p-doped GaAs (Be, nominally $2 \cdot 10^{16} \text{ cm}^{-3}$) are grown. Finally, 400 nm of highly n-doped GaAs (Si, nominally $2 \cdot 10^{18} \text{ cm}^{-3}$) form the top contact of the diode structure. A reference structure is grown in a similar way, however suppressing the QD formation by depositing only 2 ML of GaSb, such that only a WL is formed (Fig. 6.1[b]).

The structures are processed into $800\text{-}\mu\text{m}$ -wide round mesas with standard optical lithography techniques. The top and back contact are metallized using Ni/AuGe/Au and Ti/Pt/Au, respectively, and subsequent annealing for 3 min at 400°C (see Appendix D for details).

Figure 6.2 shows an Atomic Force Microscopy (AFM) picture of uncapped GaSb/GaAs

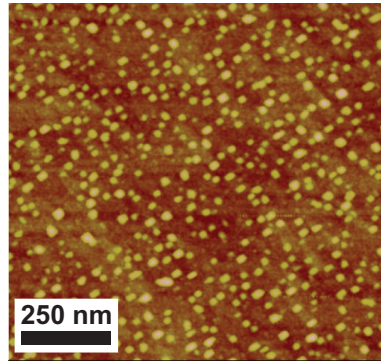


Figure 6.2: AFM measurement of a sample with uncapped GaSb/GaAs QDs grown by using the same growth parameters as used for QD-A. The QDs have an average height of $2(\pm 0.2)$ nm, an average diameter of $20(\pm 4)$ nm, and an area density of $5 \cdot 10^{10} \text{ cm}^{-2}$.

QDs. The growth parameters for the QDs at the surface are the same as for the QD layer in the pn-diode. The QDs have an average height of $2(\pm 0.2)$ nm, an average diameter of $20(\pm 4)$ nm, and an area density of $5 \cdot 10^{10} \text{ cm}^{-2}$.

6.1.1.2 Static capacitance measurements

As a basic characterization of the samples prior to the DLTS measurements, a static capacitance-voltage (C-V) measurement is performed. Figure 6.3(a) shows the C-V curve between a reverse bias of 0 and 15 V at a temperature of 300 K and a measurement frequency of 10 kHz. The C-V curve shows a plateau-like feature which is due to the hole emission and capture processes in the QD ensemble [28,83,140]. When the measurement is started, the QD layer lies outside the depletion region of the diode structure, hence the QDs are not visible in the capacitance measurement. Increasing the reverse bias increases the width of the depletion region and the capacitance decreases according to Eq. 5.4. At some point, the edge of the depletion region reaches the QD layer, and the ac measurement voltage causes the holes in the QDs to get emitted and re-captured if the time constants of the processes are smaller than the measurement frequency (processes with larger time constants cannot be seen in the measurement). The increase in the capacitance due to the QDs compensates the decrease of the diode capacitance and hence the total capacitance stays constant and exhibits a plateau. If the reverse bias is increased further, the QDs eventually have emitted all the holes and the curve returns to the normal diode-like shape. Taking the second derivative of the C-V curve indicates the beginning and end of the plateau and marks the reverse biases at which the QDs enter the depletion region, and at which they are completely discharged. Here, 0.4 V and 3.7 V are obtained, respectively. The values are needed for the DLTS experiments as they mark the region where hole emission and capture takes place.

If the bias voltage is swept in both directions and the sweep time is smaller than the

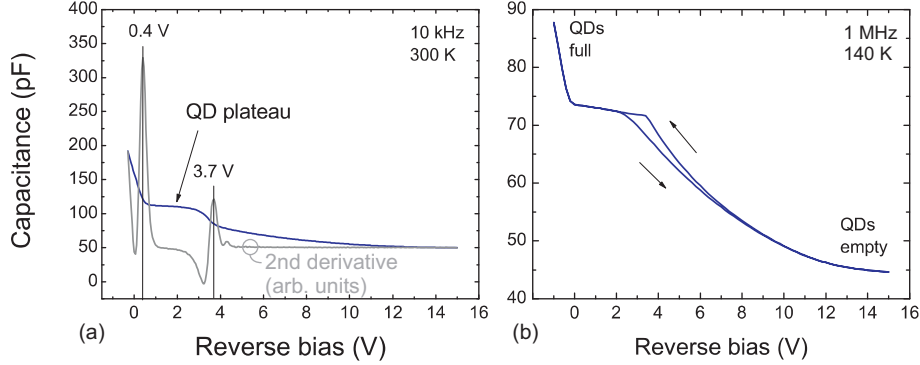


Figure 6.3: QD-A: (a) Static capacitance-voltage measurement. A plateau-like feature indicates the presence of additional carrier trapping related to density of states of the QD ensemble. (b) A C-V sweep shows a clear hysteresis opening due to the memory effect in the QD ensemble. If the QDs are full, the total capacitance is lower, if they are empty, the total capacitance is larger.

storage time of the holes in the QDs, a hysteresis curve is observed. Figure 6.3(b) shows the hysteresis curve for a measurement frequency of 1 MHz at a temperature of 140 K. For large reverse biases the QDs are empty, and if the voltage is swept back, a larger capacitance is measured than if coming from the fully charged QDs. This is in agreement with Eq. 5.7. As the temperature is much lower than in Fig. 6.3(a), the time constants of the emission processes are much larger. This moves the hysteresis opening to larger reverse biases as compared to the curve at 300 K. The effect of carrier dynamics in the otherwise static C-V curve is another reason that the pure diode C-V curve is not measured when coming from initially empty QDs, as the holes are re-captured before the bias reaches 0 V again.

6.1.1.3 Conventional DLTS

After the pre-characterization, the emission of all holes from the quantum dots is measured in a conventional DLTS measurement (see Sect. 5.2.1). The analysis of the time-resolved data yields the mean activation energy E_A and the mean apparent capture cross section σ_∞ .

The measurement bias is chosen in accordance with the C-V measurements. The charging pulse is set to $V_p = -0.5$ V (forward direction) while the hole emission is measured at a reverse bias of $V_m = 4$ V at which the QDs are completely discharged in equilibrium. The filling pulse width is set to 100 ms, while the emission transients are sampled for 2.5 s with a sample rate of 4 kHz. The temperature is increased from 20 K to 300 K in steps of 2.5 K. The transients are analyzed with the double-boxcar method (see Sect. 5.2.2) with t_1 set from 2 ms to 90 ms, $t_2 = 3t_1$ and $t_{av} = 0.5$. The resulting DLTS graphs for the QD and the WL sample are depicted in Fig. 6.4(a) for a reference time constant of $\tau_{ref} = 23$ ms. The QD sample exhibits a broad peak between 100 K

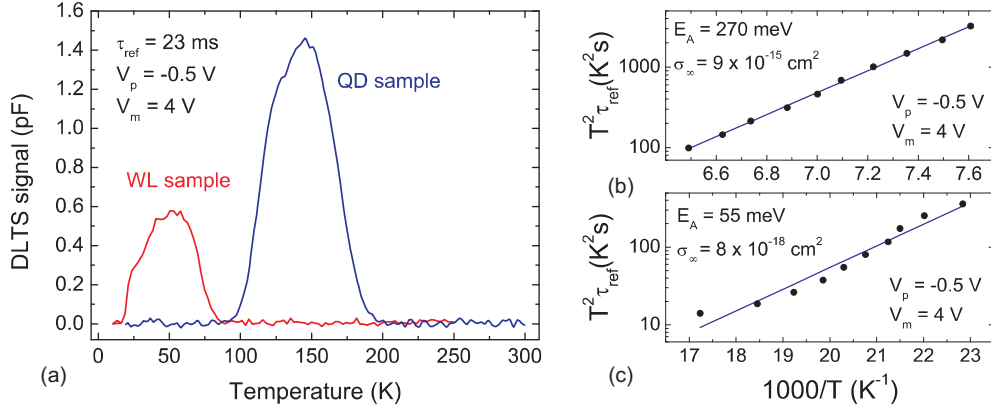


Figure 6.4: QD-A and WL-A: (a) DLTS measurements of the QD and the WL sample for a reference time constant of $\tau_{ref} = 23$ ms. (b) The Arrhenius plot for the QD sample yields a mean activation energy of $E_A = 270$ meV and an apparent capture cross section of $\sigma_\infty = 9 \cdot 10^{-15} \text{ cm}^2$. (c) The Arrhenius plot for the WL sample yields a mean activation energy of $E_A = 55$ meV and an apparent capture cross section of $\sigma_\infty = 8 \cdot 10^{-18} \text{ cm}^2$.

and 200 K, while the WL sample shows a peak between 20 K and 80 K. As the reference time constants are the same for both curves, the activation energy for the emission of holes from the WL can be expected to be much smaller than that for the emission from the QDs. In addition, the apparent capture cross section can be expected to be smaller for the WL sample.

Extracting the peak positions for different reference time constants allows the analysis of the data in Arrhenius plots (Figs. 6.4[b] and [c]). Linear fits of the data according to Eq. 3.23 and an effective hole mass of $m^* = 0.5$ yield a mean activation energy of $E_A = 270$ meV with an apparent capture cross section of $\sigma_\infty = 9 \cdot 10^{-15} \text{ cm}^2$ for the QD sample, and a mean activation energy of $E_A = 55$ meV with an apparent capture cross section of $\sigma_\infty = 8 \cdot 10^{-18} \text{ cm}^2$ for the WL sample. This is consistent with the picture that the WL exhibits a confining potential that is much smaller than that of the QDs.

6.1.1.4 Charge-selective DLTS

To investigate the electronic properties of the QD sample in more detail, charge-selective DLTS measurements (see Sect. 5.2.3) are performed. The charging pulse height is selected in such a way that on average just a very small number of holes (ideally one per QD) is transferred during the pulse. Here, a pulse height of 0.2 V is selected, at which transients for the emission are still observed. The measurement voltage V_m at which the emission is observed is set from 0.1 V to 4.1 V in steps of 0.2 V. The pulse bias is set to $V_p = V_m - 0.2$ V. The measurement is performed between temperatures of 95 K and 210 K in steps of 2 K. The transients are analyzed again with the double-boxcar method with t_1 set from 10 ms to 1000 ms, $t_2 = 3t_1$ and $t_{av} = 0.5$. This way, DLTS

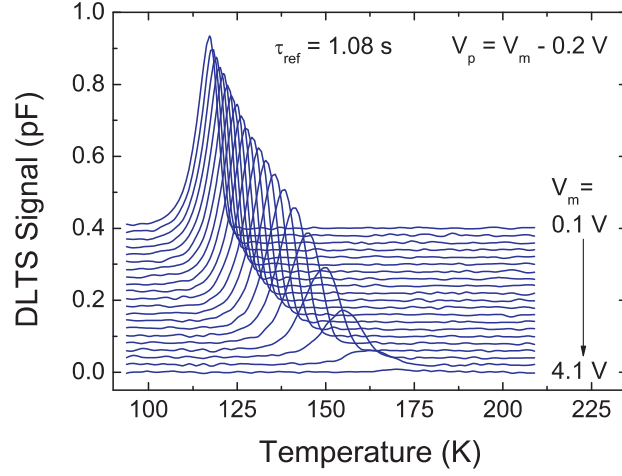


Figure 6.5: QD-A: Charge-selective DLTS graph for a time constant of $\tau_{ref} = 1.08$ s. The measurement voltage V_m is set from $V_m = 0.1$ V to 4.1 V in steps of 0.2 V while the pulse voltage is set to $V_p = V_m - 0.2$ V. With increasing reverse bias deeper lying hole energy levels of the QD ensemble are probed. For clarity, the graphs are offset by 0.02 pF each.

spectra for eight reference time constants are obtained.

Figure 6.5 depicts the DLTS graphs for all measurement voltages and a reference time constant $\tau_{ref} = 1.08$ s. The energy range along which the hole emission is probed during each pulse in the measurement is smaller than in the conventional DLTS measurement. Hence, the number of holes which is transferred during the emission process is also smaller, leading to a smaller peak width than in the conventional DLTS measurement [81, 116]. With increasing reverse bias, the peaks move to higher temperatures and the peak height becomes smaller. The reason for the peak shift is the increased activation energy which the holes occupying the deeper states of the QD ensemble have to overcome to leave the dots. The decrease of the peak height with increasing reverse bias V_m is related to the level spacing, which becomes smaller for the higher levels. In addition, the holes occupying the higher energy levels experience a smaller Coulomb repulsion than holes occupying the deeper energy levels, which is due to many-particle effects. Both effects lead to more holes per energy range for the higher levels in comparison with the deeper levels, and hence a larger contribution to the capacitance is measured.

From the peak positions at different reference time constants, an Arrhenius plot is obtained for each measurement bias V_m (see Fig. 6.6[b]). Linear fits of the data yield the activation energies E_A and the apparent capture cross sections σ_∞ . Figure 6.6(a) shows the activation energies as a function of the measurement bias V_m . The curve clearly shows that deeper lying hole energy levels are probed in the course of the measurement. It can be seen that for increasing reverse bias V_m , the activation energy increases, starting from a value of 302 meV at $V_m = 0.1$ V to 460 meV at $V_m = 3.9$ V.

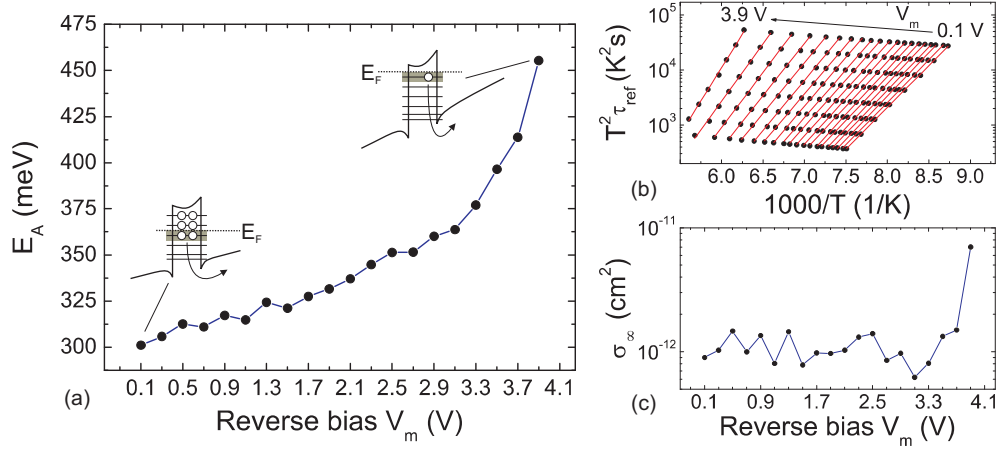


Figure 6.6: QD-A: Charge-selective DLTS measurements. (a) Activation energies E_A for each measurement bias V_m . The largest value belongs to the emission from the hole ground state and equals the localization energy E_{loc} . (b) Arrhenius plots for each measurement bias V_m of the charge-selective DLTS measurement. (c) Apparent capture cross sections σ_∞ for each measurement bias V_m .

The lower values belong to the upper hole energy levels. However, the individual hole energy levels lie too close to each other and cannot be distinguished due to ensemble and thermal broadening (i.e. the temperature is much higher than for the measurements performed in Sect. 7.2.1). If the value is compared to the sample studied in [81], which nominally has the same structure as the sample studied in this work, the lowest value is about 150 meV larger than for QD-A. Also, the reverse bias at which the lowest activation energy is measured is about 4 V larger. The reason for this deviation could be that the actual doping concentration is lower than the nominal one in sample QD-A [141]. This would shift the QD plateau in the C-V curve, and hence the bias range at which the QDs reach the depletion region of the diode, to lower voltages. As a consequence, the upper hole energy levels of the QDs (i.e. <302 meV) cannot be seen in the measurement.

The apparent capture cross sections σ_∞ are shown in Fig. 6.6(c). They stay almost constant at values around $10^{-12} cm^2$. However, the last value is more than one order of magnitude larger.

The errors in the determined values are mainly related to the graphical analysis of the data. The peak position has to be determined from the DLTS spectrum and asymmetries of the peaks and noise can complicate the analysis. To get an estimate of the magnitude of the error related to the graphical analysis, the analysis was repeated several times for the first DLTS spectrum at $V_m = 0.1$ V and the last DLTS spectrum at $V_m = 3.9$ V (see Appendix E for details). From Fig. 6.5 it can already be seen that the signal-to-noise ratio is increasing towards larger reverse bias due to the decreasing peak height. The uncertainty for the activation energies ranges between 5 meV at $V_m = 0.1$ V and 22 meV at $V_m = 3.9$ V. Hence, the overall error due to the graphical

analysis is assumed to be below 5 %. The apparent capture cross section has an error of about 0.7 orders of magnitude. Nevertheless, it should be noted that the values obtained for the activation energy and the apparent capture cross section are correlated due to the analysis method (see Appendix E for details). The error of the emission rate and the storage time are hence smaller with an uncertainty of about 0.3 orders of magnitude at a temperature of 300 K.

The largest activation energy, measured at $V_m = 3.9$ V, belongs to the hole ground state in the GaSb/GaAs QDs. This value is the key electronic property of the QD ensemble. The best estimate for the localization energy E_{loc} of the QD ensemble is hence $E_{loc} = 460(\pm 20)$ meV (rounded to significant digits) with an apparent capture cross section of $\sigma_\infty = 7 \cdot 10^{-12}$ cm² (with an uncertainty of 0.7 orders of magnitude). Using Eq. 3.23, the storage time at room temperature (300 K) can be extrapolated from E_{loc} and σ_∞ and yields a value of 100 ns (with an uncertainty of 0.3 orders of magnitude). This error margin means, that the storage time τ could also be half or double the value. At 85°C (358 K), the storage time drops to about 4 ns (with an uncertainty of 0.4 orders of magnitude).

6.1.2 Sample QD-B: QDs with a single Al_{0.1}Ga_{0.9}As barrier

In the following section, a QD sample grown by R. J. Young at Lancaster University, United Kingdom, is investigated. Three samples were grown in total: one, to investigate the structural properties by using cross-sectional scanning-tunnling microscopy (X-STM) measurements to obtain information on the structural properties. These measurements were performed by E. P. Smakman in the group of P. M. Koenraad at Eindhoven University of Technology, the Netherlands. The other two samples contained either a layer of GaSb/GaAs QDs (QD-B) or a GaSb WL (WL-B) embedded into a pn-diode structure in order to perform DLTS measurements, and obtain detailed information on the electronic properties. The growth parameters for the dots in both QD samples (X-STM and DLTS) are identical.

6.1.2.1 Sample structure

The schematic sample structures for the QD sample and the WL sample are depicted in Fig. 6.7. The design of the sample structures are almost identical to those of QD-A and WL-A (see Sect. 6.1.1.1). The parameters for the QDs are the result of a growth series, which systematically altered the growth conditions, such as the cold cap thickness and the maximum substrate temperature after dot formation. The details can be found in [142]. The only difference to sample QD-A is that an additional 20 nm-wide Al_{0.1}Ga_{0.9}As barrier is incorporated underneath the QD layer, which is necessary to prevent Be-diffusion into the GaSb layer. The barrier has to be taken into account,

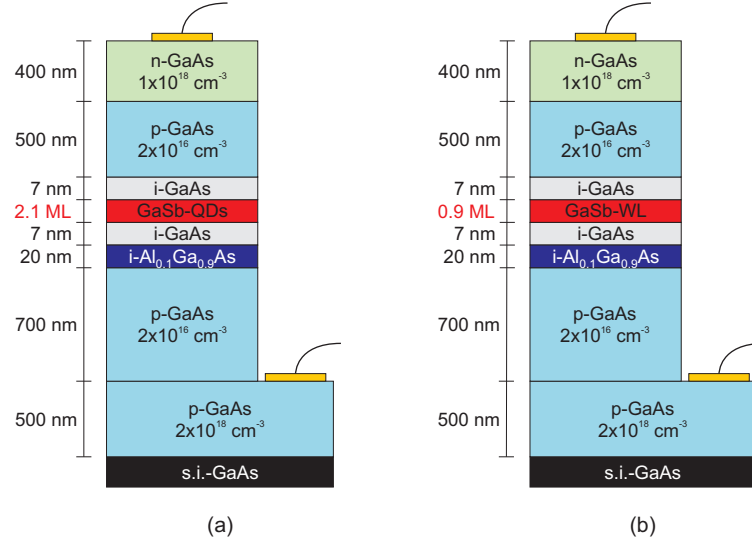


Figure 6.7: QD-B and WL-B: Sample structure of the QD sample and the WL sample. Underneath the GaSb/GaAs QD/WL layer a 20-nm-wide Al_{0.1}Ga_{0.9}As barrier is incorporated in order to prevent Be-diffusion into the GaSb layer.

when the DLTS measurements are analyzed. Also, apparently less GaSb material is deposited in the QD layer (2.1 ML) and the WL (0.9 ML).

The morphology of the QDs with these growth conditions were studied using X-STM measurements [142]. Figure 6.8 shows a selection of X-STM measurements and a statistical analysis of the data obtained from the cross sections of a total of 42 QDs. Because of surface relaxation, the locally highly-strained GaSb QDs appear higher, and therefore brighter in the X-STM measurements. This allows to determine the shape and the composition of the dots. Hence, a detailed study of the height and the base length is possible. For the present growth conditions, the apparent shape of the QDs is pyramidal with the majority of the QDs being truncated pyramids ($\text{VAR} \leq 0.5$, vertical aspect ratio VAR defined as height divided by base length). Qualitative assessment shows that the QDs are of high purity ($\sim 100\%$) and show almost no intermixing with the surrounding GaAs lattice. A density plot of the apparent height versus the apparent base length is shown in Fig. 6.8(b). As the lateral position at which the sample is cleaved ($\{110\}$ -plane) is random, the measured values overestimate the VAR and the distribution of the sizes [143]. Hence, the real vertical aspect ratio is expected to be lower than the apparent one. The measured base lengths and heights are shown as histograms in Fig. 6.8(c) and 6.8(d). The base lengths cluster around 11 nm with the majority of the QDs lying within a margin of ± 6 nm of this value. Above a base length of 18 nm, QDs are only sporadically found. The former group might be attributed to strained QDs and the latter to relaxed QDs. The QDs have a height of about 4-6 nm. The apparent VAR, calculated from the values in the density plot of Fig. 6.8(b), is

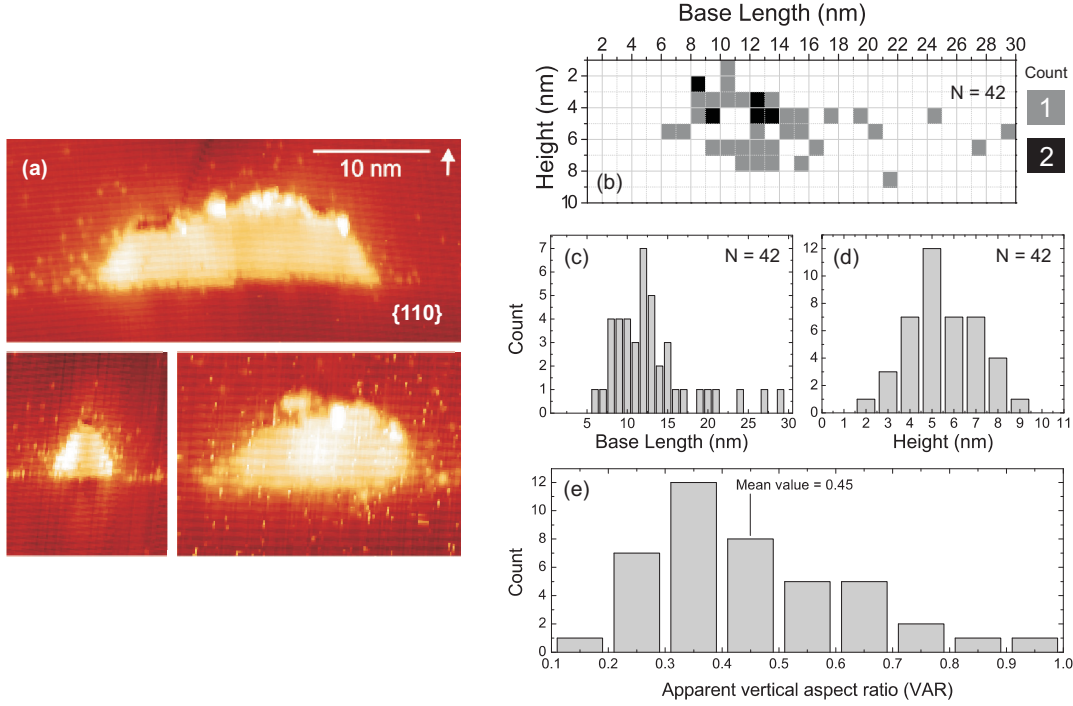


Figure 6.8: X-STM measurements of a total of $N = 42$ QDs with similar growth parameters as for the QDs in QD-B. The samples are cleaved at a $\{110\}$ -plane. (a) Cross-section of GaSb/GaAs QDs. The bright spots are Sb atoms. The QDs are of high purity ($\sim 100\%$ GaSb). (b) Base length and height distribution. (c) Base length histogram. (d) Height histogram. (e) Apparent vertical aspect ratio (VAR) determined from values of the distribution in (b).

shown in Fig. 6.8(e). The mean value of the histogram lies at an apparent VAR of 0.45, but as said above, the real VAR can be expected to be lower.

6.1.2.2 Static capacitance measurements

The static capacitance-voltage measurement of the QD sample and the WL are compared at a temperature of 300 K and a measurement frequency of 10 kHz in Fig. 6.9(a). The additional capacitance of the QDs forms a plateau between a reverse bias of 0 V and ~ 2 V (the second derivative does not show such clear peaks as in Fig. 6.3). The feature cannot be seen in the WL sample. The values roughly indicate the voltages at which the QD layer reaches the depletion region, and at which voltage they are completely discharged. Figure 6.9(b) shows the photoluminescence (P-L) spectrum of the QD sample at a temperature of 4 K and an excitation power of 10 mW at 532 nm CW on a spot of approximately 1 mm^2 . A broad peak appears around an energy of 1.22 eV with a FWHM of ~ 140 meV which can be attributed to the emission from the QD ensemble. As GaSb/GaAs forms a type-II heterostructure, the difference between the QD valence band and the conduction band of the GaAs can be estimated from the difference in the peak positions to be above ~ 270 meV (if band bending due to charging

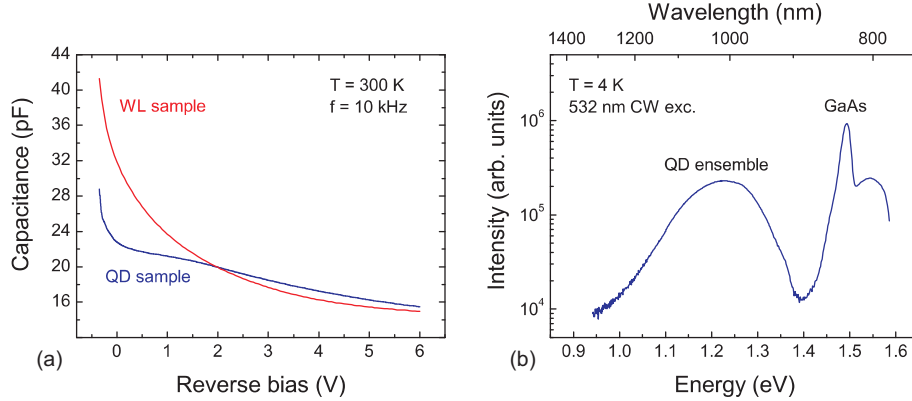


Figure 6.9: QD-B and WL-B: (a) Static capacitance-voltage measurements of the QD sample and the WL sample. A plateau can be seen in the QD sample between 0 V and ~ 2 V. (b) Photoluminescence (P-L) spectrum of the QD sample at 4 K and an excitation power of 10 mW on an area of about 1 mm^2 at 532 nm CW.

effects is assumed). The peak around 1.55 eV could be related to recombination at the $\text{Al}_{0.1}\text{Ga}_{0.9}\text{As}$ barrier.

6.1.2.3 Conventional DLTS

The activation energy and the apparent capture cross section of the QD ensemble is determined with conventional DLTS. The QDs are charged with holes by a 500 ms long pulse at a voltage of $V_p = 0$ V. The emission transients are recorded at a measurement voltage of $V_m = 3$ V. Under these conditions the QDs are completely filled with holes during the pulse and all holes are re-emitted from the dots when thermal equilibrium is reached at $V_m = 3$ V. Thus, the emission processes from all energy levels in the QD ensemble are observed and the mean activation energy is derived. The same measurement is performed for the WL sample. Figure 6.10(a) shows the conventional DLTS graphs for the QD sample and the WL sample for temperatures between 20 K and 340 K in steps of 1.5 K and a reference time constant of $\tau_{ref} = 80$ ms. A clear peak can be observed around a temperature of 270 K extending from 200 K to 325 K. The WL sample does not show any signal throughout the whole temperature range. An Arrhenius plot for different reference time constants yields a mean activation energy of $E_a = 520$ meV with an apparent capture cross section of $\sigma_\infty = 7 \cdot 10^{-16} \text{ cm}^2$. The activation energy represents the mean activation energy for all hole levels in the QD ensemble, where the activation energy of each hole level depends on the charge state of its QD. Hence, the resulting DLTS peak of the QD ensemble is broadened [81, 116]. The mean activation energy also includes the contribution of the $\text{Al}_{0.1}\text{Ga}_{0.9}\text{As}$ barrier. If a value of $\Delta E_{VB} = 54$ meV is assumed for the valence band offset (based on a 66:34 split of the band gap difference [35]) between GaAs and $\text{Al}_{0.1}\text{Ga}_{0.9}\text{As}$, and subtracted

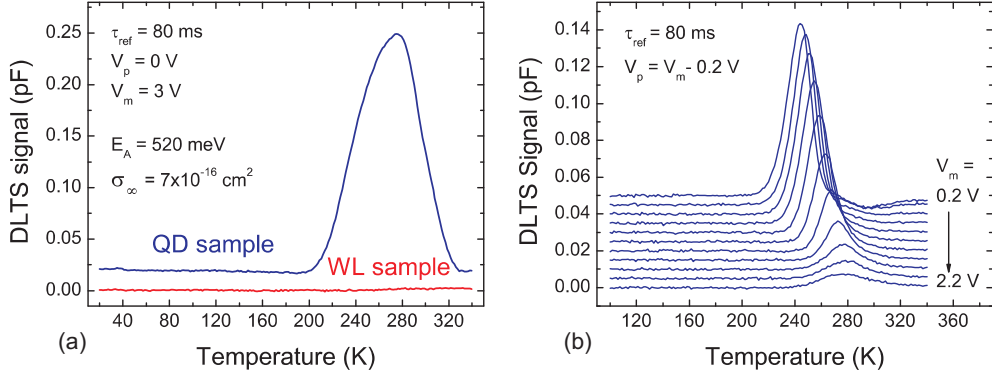


Figure 6.10: QD-B and WL-B: (a) Conventional DLTS graphs for the QD and the WL sample for a reference time constant of $\tau_{ref} = 80$ ms. The QD sample shows a broad DLTS peak due to the hole emission from the QD ensemble while the WL sample does not show any signal throughout the whole temperature range. (b) QD-B: Charge-selective DLTS graphs for different measurement bias V_m for a reference time constant of $\tau_{ref} = 80$ ms. When increasing the measurement voltage, deeper hole energy levels of the QD ensemble are probed. The curves are offset by 5 fF each for clarity.

from the data, a mean activation energy of ~ 466 meV is derived for the QD ensemble without the barrier.

6.1.2.4 Charge-selective DLTS

To study the electronic structure of the QD ensemble in more detail, charge-selective DLTS measurements are performed. The measurement bias is increased from $V_m = 0.2$ V to 2.2 V (reverse direction), while the pulse bias is changed according to $V_p = V_m - 0.2$ V. The temperature is increased from 100 K to 340 K in steps of 1.5 K. Figure 6.10(b) shows the DLTS graphs for a reference time constant of $\tau_{ref} = 80$ ms for the different measurement voltages V_m . Again, the peaks are smaller than the broad peak in the conventional DLTS graph due to the smaller energy range which is probed during the measurement. The peaks shift from about 245 K at $V_m = 0.2$ V to about 275 K at $V_m = 2.2$ V as deeper hole energy levels are probed during the subsequent charging and discharging of the QD ensemble. The pulse height also decreases as observed before (see Sect. 6.1.1.4).

From the shifts of the DLTS peaks for different reference time constants τ_{ref} the Arrhenius plots are obtained (Fig. 6.11[b]). By fitting the Arrhenius plots, the activation energies E_a and the apparent capture cross sections σ_∞ are derived for each individual measurement bias V_m . The values are shown in Figs. 6.11(a) and 6.11(c), respectively. The measured activation energies increase from 525 meV at $V_m = 0.2$ V to 670 meV at $V_m = 1.6$ V, while the apparent capture cross section increases from $\sigma_\infty = 2 \cdot 10^{-14}$ cm² at $V_m = 0.2$ V to $\sigma_\infty = 1 \cdot 10^{-12}$ cm² at $V_m = 1.6$ V. Normally, for the doping concentration nominally present in this sample, the lowest value of the activation energy measured can be expected to be much lower for measurement voltages in the range

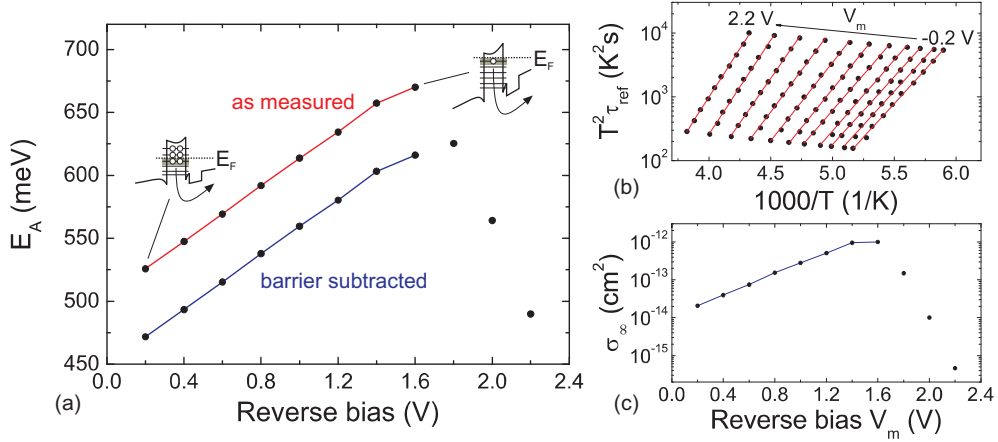


Figure 6.11: QD-B: (a) Activation energies E_A for the QD sample as measured and with the $Al_{0.1}Ga_{0.9}As$ barrier subtracted. (b) Arrhenius plot derived from the DLTS graphs for different reference time constants τ_{ref} . (c) Apparent capture cross sections σ_∞ for the QD sample.

used here. A possible reason for the deviation could be a doping concentration that is smaller than the nominal one, leading to a larger depletion region on the p-side which reaches the QDs already at a bias of 0 V. Then, it is not possible to measure the emission from the hole energy levels with activation energies smaller than 525 meV. Strong evidence that this is the case can be found for a similar sample in [141], where the doping concentration was altered and the position of the C-V-plateau of the QD ensemble shifts to a larger reverse bias, making the higher hole energy levels accessible.

The values for the activation energies and the apparent capture cross sections above a measurement bias of $V_m = 1.6$ V are decreasing again. They are hence not related to the QD emission but are attributed to emission processes from defect states related to the growth of QDs (i.e., GaSb clusters, relaxed QDs). The best estimate for the localization energy of QD-B is $E_{loc} = 670(\pm 10)$ meV with an apparent capture cross section of $\sigma_\infty = 1 \cdot 10^{-12}$ cm² (with an uncertainty of 0.2 orders of magnitude, see Appendix E for details). The storage time at room temperature and 358 K (85°C) can then be extrapolated according to Eq. 3.23 to $\tau(300 K) = 2$ ms (with an uncertainty of 0.02 orders of magnitude) and $\tau(358 K) = 20$ μ s (with an uncertainty of 0.05 orders of magnitude).

To obtain the localization energy of the QD ensemble alone, the contribution of the $Al_{0.1}Ga_{0.9}As$ barrier ($\Delta E_{VB} = 54$ meV [35]) is subtracted. The results are represented in the blue curve in Fig. 6.11(a). From this curve, a localization energy of $E_{loc} = 615(\pm 10)$ meV (rounded to significant digits) with the corresponding apparent capture cross section of $\sigma_\infty = 1 \cdot 10^{-12}$ cm² (with an uncertainty of 0.2 orders of magnitude) is derived for the present GaSb/GaAs QD ensemble. The extrapolated storage time at room temperature (300 K) now yields a value of $\tau(300 K) = 300$ μ s (with an

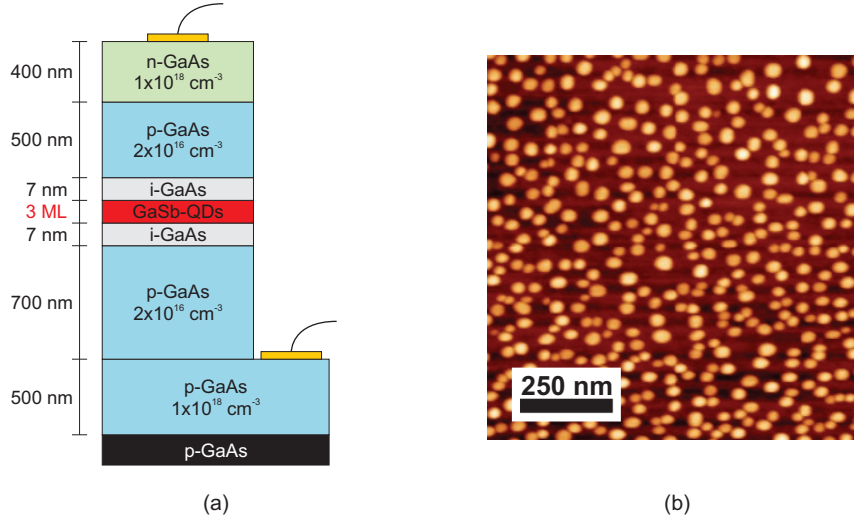


Figure 6.12: QD-C: (a) Schematic sample structure. A layer of GaSb/GaAs QDs is embedded into a pn-diode structure. (b) AFM measurement of uncapped GaSb/GaAs QDs with the same growth parameters for the QDs as used in QD-C. The QDs have a mean height of $4.5(\pm 0.2)$ nm and a mean lateral extension of $40(\pm 4)$ nm. The area density is $4 \cdot 10^{10}$ cm $^{-2}$.

uncertainty of 0.02 orders of magnitude). At 358 K (85°C), the storage time is now $\tau(358 K) = 5 \mu\text{s}$ (with an uncertainty of 0.05 orders of magnitude)

6.1.3 Sample QD-C: QDs

The sample investigated in the following section was grown by Charles J. Reyner in the group of Diana Huffaker at University of California Los Angeles (UCLA), USA. Similar to QD-A, it consists of a single layer of self-assembled GaSb/GaAs QDs embedded into a pn-diode structure. In contrast to the QDs that were studied before, they have a very large lateral extension and height, hence a large localization energy can be expected.

6.1.3.1 Sample structure

The schematic sample structure of QD-C is depicted in Fig. 6.12(a). The layer of self-assembled GaSb/GaAs QDs is embedded into the lower p-doped region of a pn-diode structure. Figure 6.12(b) shows an AFM measurement of uncapped GaSb/GaAs QDs which have been grown using the same growth parameters as for QD-C. The dome-shaped QDs have a mean lateral extension of about $40(\pm 4)$ nm with a mean height of $4.5(\pm 0.2)$ nm. The area density of the dots is $4 \cdot 10^{10}$ cm $^{-2}$.

6.1.3.2 Static capacitance measurements and conventional DLTS

To pre-characterize the sample, a simple C-V scan is performed at 300 K with a measurement frequency of 1 MHz. Figure 6.13(a) shows a sweep between -0.4 V and 7 V

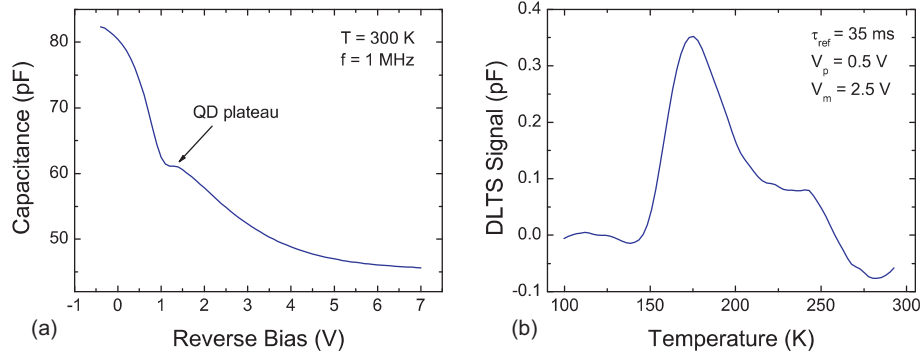


Figure 6.13: QD-C: (a) Capacitance-voltage scan of QD-C. A plateau can be seen due to the charging and discharging effects of the QD ensemble. (b) Conventional DLTS measurement of QD-C for a reference time constant of $\tau_{ref} = 35$ ms, a pulse bias of $V_p = 0.5$ V and a measurement bias of $V_m = 2.5$ V.

in reverse direction. A small, but clear plateau can be seen due to the charging and discharging of holes from the QD ensemble.

Based on the extension of the plateau in Fig. 6.13(a), a conventional DLTS measurement is conducted. Figure 6.13(b) shows the conventional DLTS measurement for a reference time constant of $\tau_{ref} = 35$ ms, a pulse voltage of $V_p = 0.5$ V with a pulse width of 100 ms, and a measurement voltage of $V_m = 2.5$ V. In thermal equilibrium the QDs should be completely discharged at that voltage. A broad peak can be seen around a temperature of 170 K which has a broad shoulder at the high temperature side. At larger temperatures, this shoulder drops to negative values, indicating some sort of minority carrier (electron) emission. The peak can be attributed to the QDs, and the shoulder possibly to the emission from deeper states in the QD ensemble, as they also appear in the charge-selective DLTS graph shown in Sect. 6.1.3.3. Where the negative part above 260 K comes from remains unclear as the charge-selective DLTS does not show any negative features in that temperature range. By analyzing the data for different reference time constants τ_{ref} an Arrhenius plot is created for the QD peak (not shown) and from a fit according to Eq. 3.23 a mean activation energy of $E_a = 410$ meV with an apparent capture cross section of $7 \cdot 10^{-13}$ cm² is derived.

6.1.3.3 Charge-selective DLTS

The sample is then investigated by charge-selective DLTS in order to derive the localization energy of the GaSb/GaAs QD ensemble. The measurement bias is set from $V_m = 0.2$ V to 2.4 V in steps of 0.2 V while the pulse voltage is set to $V_p = V_m - 0.2$ V with a pulse width of 100 ms. Figure 6.14 shows the charge-selective DLTS measurement for a reference time constant of $\tau_{ref} = 35$ ms. A narrow peak can be seen to shift from a temperature of about 155 K at a measurement bias of $V_m = 0.2$ V to 270 K

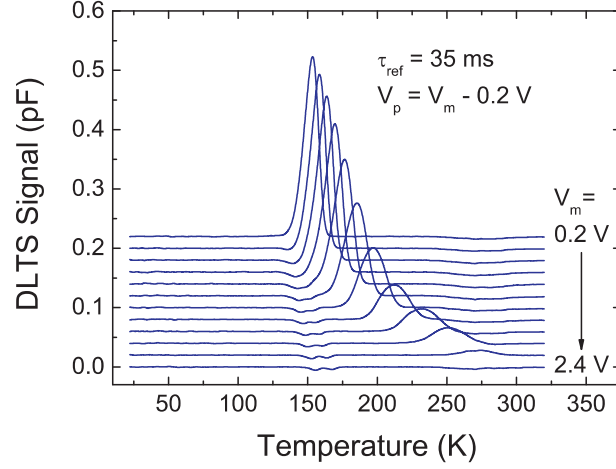


Figure 6.14: QD-C: Charge-selective DLTS measurement for different measurement voltages V_m and a reference time constant of $\tau_{ref} = 35$ ms. The pulse bias is set to $V_p = V_m - 0.2$ V.

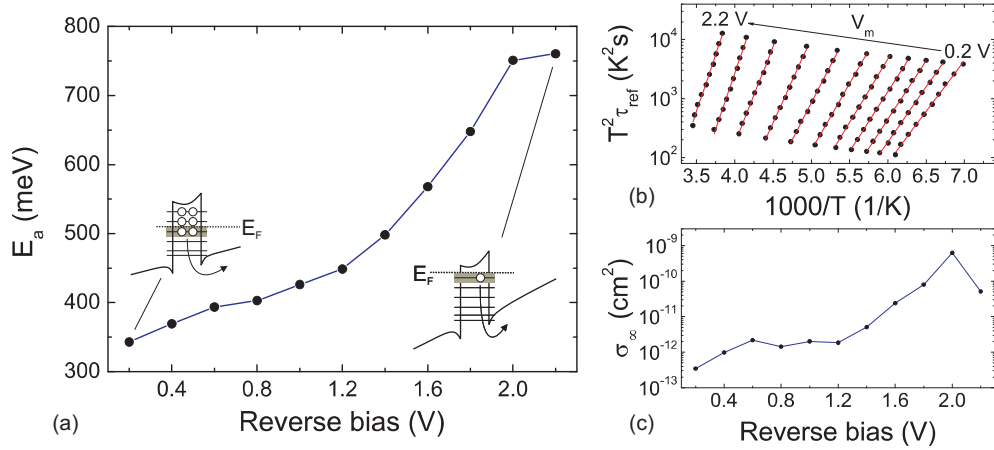


Figure 6.15: QD-C: (a) Activation energies E_a as a function of the measurement bias V_m . (b) Arrhenius plot derived from the charge-selective DLTS measurements for different reference time constants τ_{ref} and different measurement bias V_m . (c) Apparent capture cross sections σ_∞ for holes as a function of the measurement bias V_m .

at $V_m = 2.2$ V. In contrast to the conventional DLTS measurement, a negative feature above 250 K can not be seen, only two small dips at temperatures around 160 K are visible. As the feature is present at all measurement bias voltages it could be related to some sort of minority carrier trapping mechanism throughout the p-side of the pn-diode.

From the DLTS graphs with different reference time constants τ_{ref} , an Arrhenius plot is derived for each individual measurement voltage V_m , which is shown in Fig. 6.15(b). The activation energies derived from the Arrhenius plots are shown in Fig. 6.15(a). They increase from 343 meV at a reverse bias of $V_m = 0.2$ to 760 meV at a reverse bias

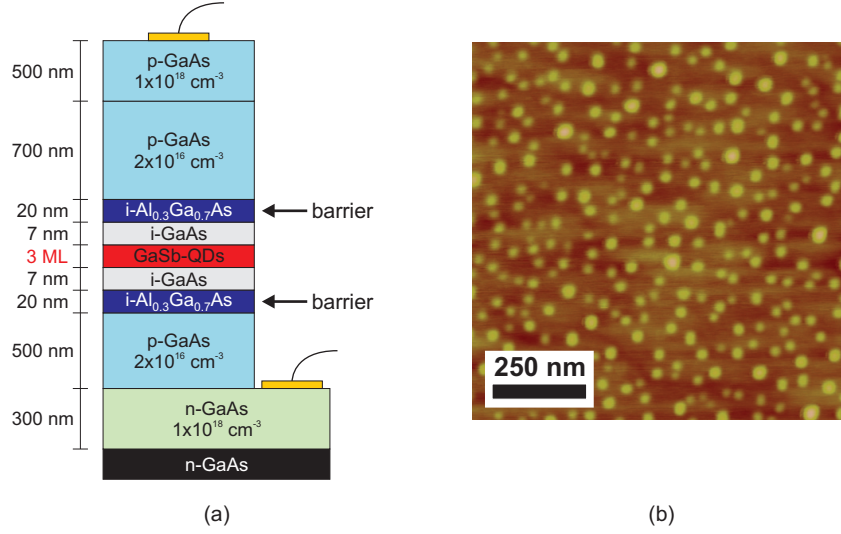


Figure 6.16: QD-D: (a) Sample structure. The QD layer is sandwiched between two $\text{Al}_{0.3}\text{Ga}_{0.7}\text{As}$ barriers in order to increase the emission barrier and the storage time. (b) AFM scan of an uncapped QD sample with growth parameters similar to those used during growth of the QD layer in QD-D. The QDs have a diameter of $24(\pm 4)$ nm, a height of $2.5(\pm 0.2)$ nm, and an area density of $3 \cdot 10^{10} \text{ cm}^{-2}$.

of $V_m = 2.2$ V, while the apparent capture cross section for the holes increases from $\sigma_\infty = 3 \cdot 10^{-13} \text{ cm}^2$ at $V_m = 0.2$ V to $\sigma_\infty = 6 \cdot 10^{-10} \text{ cm}^2$ at $V_m = 2$ V. For $V_m = 2.2$ V it decreases again by about one order of magnitude. Hence the localization energy is about $E_{loc} = 760(\pm 20)$ meV (rounded to significant digits) with an apparent capture cross section of $\sigma_\infty = 5 \cdot 10^{-11} \text{ cm}^2$ (with an uncertainty of 0.3 orders of magnitude). Using Eq. 3.23 the storage time at room temperature (300 K) can be extrapolated from E_{loc} and σ_∞ and yields a value of $\tau(300 \text{ K}) = 2$ ms (with an uncertainty of 0.02 orders of magnitude). At 358 K (85°C), the storage time is $\tau(358 \text{ K}) = 10 \mu\text{s}$ (with an uncertainty of 0.06 orders of magnitude).

6.1.4 Sample QD-D: QDs with double $\text{Al}_{0.3}\text{Ga}_{0.7}\text{As}$ barrier

The main parameter which can be altered in order to increase the storage time in QDs is the height of the emission barrier. Hence, the localization energy is the key parameter which has to be increased. This can be done by adding additional barriers. From Fig. 2.1 it can be seen that $\text{Al}_x\text{Ga}_{1-x}\text{As}$ has a larger band gap than GaAs and, in addition, is lattice-matched to GaAs. It is the ideal candidate to increase the localization energy and thus the storage time [26, 27].

In this subsection a sample with GaSb/GaAs QDs is investigated which has two additional $\text{Al}_{0.3}\text{Ga}_{0.7}\text{As}$ barriers above and below the QD layer. The samples were grown in the group of Shih-Yen Lin at the Research Center for Applied Sciences, Academia Sinica, Taiwan.

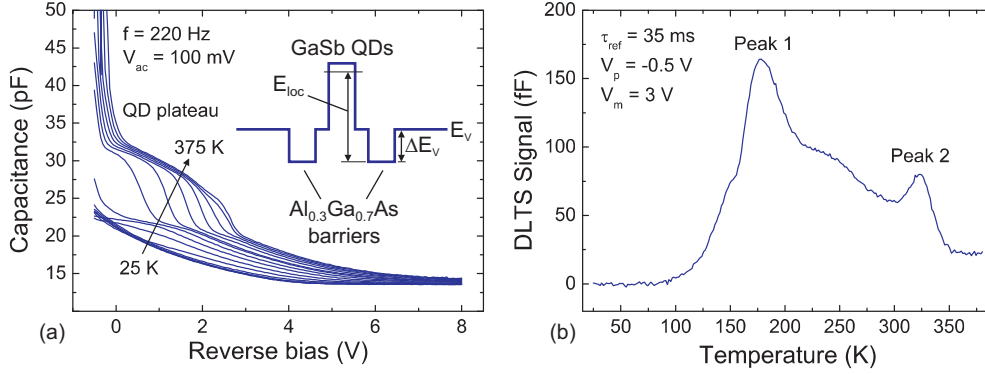


Figure 6.17: QD-D: (a) Capacitance-voltage (C - V) scan at different temperatures for a measurement frequency of 220 Hz. The charging and discharging of the QDs form a plateau compensating for the decrease of the diode capacitance. In this configuration, the QDs are completely discharged (i.e. all holes in the QD ensemble participate in the measurement) around 3 V, indicated by the converging C - V curves at higher temperatures. Inset: Schematic valence band structure. The $\text{Al}_{0.3}\text{Ga}_{0.7}\text{As}$ barriers add an additional barrier ΔE_V to the localization energy E_{loc} of the QDs. (b) Conventional DLTS measurement with $V_p = -0.5$ V and $V_m = 3$ V for a reference time constant $\tau_{ref} = 35$ ms. Two distinct peaks are visible at the edges of a broad feature.

6.1.4.1 Sample structure

The basic sample structure of QD-D differs slightly from the one of QD-A. It is depicted schematically in Fig. 6.16(a). The diode structure is grown upside down on top of an n-type GaAs substrate, starting with the n-doped region, then followed by the p-doped regions. The QD layer between the two 7-nm-thick undoped GaAs layers is sandwiched between two additional $\text{Al}_{0.3}\text{Ga}_{0.7}\text{As}$ barriers. The processing of the sample is the same as for QD-A, the mesa diameter is 400 μm for QD-D.

Figure 6.16(b) shows a $1 \times 1 \mu\text{m}^2$ picture of an AFM measurement from an uncapped sample which was grown in the same batch as QD-D, with the same growth parameters of the QD layer in QD-D. The QDs have a diameter of $24(\pm 4)$ nm, a height of $2.5(\pm 0.2)$ nm, and an area density of $3 \cdot 10^{10} \text{ cm}^{-2}$.

6.1.4.2 C - V and conventional DLTS measurements

To pre-characterize sample QD-D, static capacitance-voltage measurements are performed. As the total activation energy of the QDs and the additional barrier can be expected to be higher than for the QDs alone (see inset in Fig. 6.17[a]), the temperature range is increased to 375 K and a temperature scan is performed, sweeping the reverse bias from -0.5 V to 8 V with a measurement frequency of 220 Hz. Figure 6.17(a) shows the C - V curves with temperature steps of 25 K. At first, the emission time constants for hole emission from the QDs over the barrier are much larger than the inverse measurement frequency. Hence, the holes in the QDs do not participate in the measurement and the C - V curve is just the one of the pn-diode. From a temperature starting

at 175 K, the upper energy levels have emission and capture time constants in the range of the inverse measurement frequency, and a plateau starts to form. Increasing the temperature further lets more and more energy levels participate in the emission process as the time constants decrease further. At a temperature of 350 K, a saturation of the plateau extension is visible. From that temperature on, all hole energy levels participate and hence the curves converge, the plateau does not extend further to larger reverse biases.

From the extension of the plateau it can be derived, that at a reverse bias of about 3 V the Fermi level lies above the QDs and the QDs are empty in equilibrium. Hence the DLTS measurements are performed between a reverse bias of -0.2 V and 3 V.

Figure 6.17(b) shows the conventional DLTS measurement for a reference time constant of $\tau_{ref} = 35$ ms at a measurement voltage $V_m = 3$ V and a 2 s long charging pulse to $V_p = -0.5$ V (forward direction). A broad feature is visible between 100 K and 350 K, in which two distinct peaks are visible at the edges. A third peak can be seen in between the two peaks, but it is less distinct. Peak 1 has an activation energy of $E_a = 340$ meV with an apparent capture cross section of $\sigma_\infty = 4 \cdot 10^{-15}$ cm², while peak 2 has an activation energy of $E_a = 840$ meV with an apparent capture cross section of $\sigma_\infty = 4 \cdot 10^{-12}$ cm². The exact origin of the peaks is unclear. Possibly, they are related to many-particle effects within the QDs. The many-particle effects would change during the emission as a result of the decreasing number of holes inside the QDs. The features are not visible in the charge-selective measurements (see next section), where much fewer holes are transferred during the pulse.

6.1.4.3 Charge-selective DLTS

Charge-selective DLTS measurements are performed with the measurement bias V_m ranging from -0.2 V to 3 V (reverse direction), according to the extension of the plateau in Fig. 6.17(a). The pulse bias for each measurement bias is set to $V_p = V_m - 0.2$ V with a pulse width of 2 s. The temperature is increased from 25 K to 380 K in steps of 1.5 K. The capacitance transients are analyzed with the double-boxcar method with t_1 chosen between 2 ms and 90 ms, $t_2 = 3t_1$, and $t_{av} = 0.5$, this way generating 10 DLTS graphs with different reference time constants τ_{ref} .

Figure 6.18 depicts the charge-selective DLTS measurement for a reference time constant τ_{ref} of 35 ms. The peaks start at 180 K at $V_m = -0.2$ V and shift towards higher temperatures up to 315 K at $V_m = 3$ V. Again, the peak height decreases as the emission process is shifted towards the deeper hole energy levels of the QD ensemble. The features seen in the conventional DLTS measurement (see Fig. 6.17[b]) are no longer visible, because the many-particle effects do not change as much in the course of the emission as in the conventional DLTS measurement. The peak positions for different reference time constants are extracted for each measurement bias, and

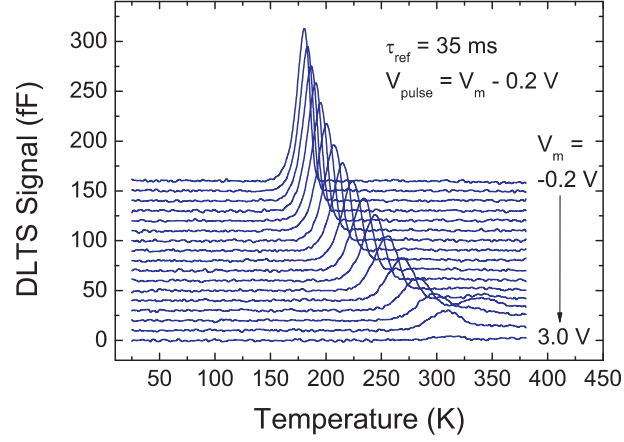


Figure 6.18: QD-D: Charge-selective DLTS graph for a reference time constant of $\tau_{ref} = 35$ ms. The measurement voltages V_m are chosen according to the extension of the plateau in Fig. 6.17. The pulse bias is kept at $V_p = V_m - 0.2$ V. For clarity, the curves are offset by 10 fF each.

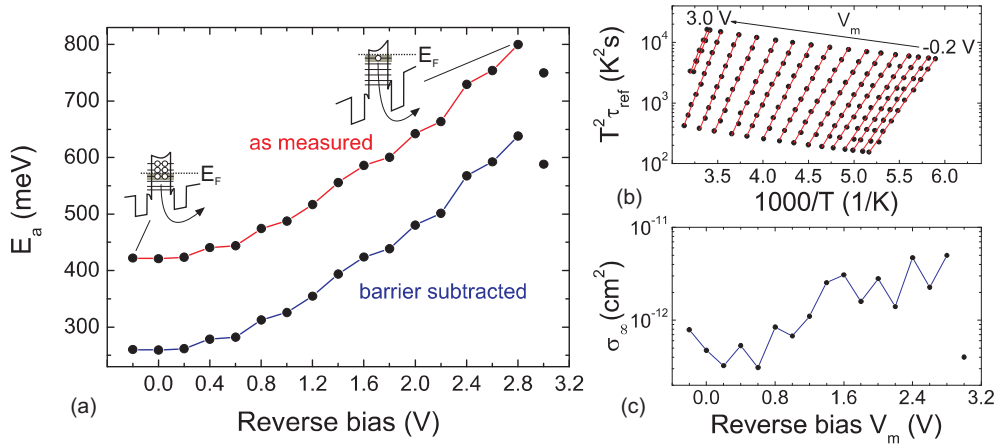


Figure 6.19: QD-D: Charge-selective DLTS. (a) Activation energies E_a as a function of the measurement bias V_m . The red curve shows the activation energies as measured, in the blue curve the height of the $\text{Al}_{0.3}\text{Ga}_{0.7}\text{As}$ barriers is subtracted. (b) Arrhenius plots for the different measurement voltages. (c) Apparent capture cross sections for holes as a function of measurement bias.

Arrhenius plots are created from the data, which are depicted in Fig. 6.19(b). For the two largest reverse biases not all DLTS graphs can be analyzed as the signal-to-noise ratio is becoming too small. From the linear fits of the data, the activation energies E_A and the apparent capture cross sections σ_{∞} are derived. Figure 6.19(a) shows the activation energies as a function of the measurement bias. As previously observed, the activation energies increase with increasing reverse bias. At $V_m = -0.2$ V a value of 422 meV is found, increasing to a value of 800 meV at $V_m = 2.8$ V. As already observed for QD-A, the apparent capture cross sections stay roughly within one order of magnitude around a value of 10^{-12} cm² (Fig. 6.19[c]). As the value beyond $V_m = 2.8$ V

decreases again and the signal-to-noise ratio decreases rapidly, the value at $V_m = 2.8$ V is taken as the activation energy of the ground state. Hence, the best estimate of the localization energy of the QD ensemble in QD-D is $E_{loc} = 800(\pm 50)$ meV (rounded to significant digits) with an apparent capture cross section of $\sigma_\infty = 5 \cdot 10^{-12}$ cm² (with an uncertainty of 0.8 orders of magnitude, see Appendix E for details). Using Eq. 3.23, the storage time at room temperature (300 K) can be extrapolated from E_{loc} and σ_∞ and yields a value of 80 ms (with an uncertainty of 0.01 orders of magnitude). The storage time at 358 K (85°C) is $\tau(358 \text{ K}) = 350$ μ s (with an uncertainty of 0.1 orders of magnitude).

As the GaSb/GaAs QDs are sandwiched between two Al_{0.3}Ga_{0.7}As barriers, the contribution to the localization energy by the barriers has to be subtracted in order to get a value for the localization energy of the QDs alone. If a value of $\Delta E_{VB} = 162$ meV for the valence band offset (based on a 66:34 split of the band gap difference [35]) between GaAs and Al_{0.3}Ga_{0.7}As is assumed and subtracted from the data, a localization energy of $E_{loc} = 640(\pm 50)$ meV (rounded to significant digits) with an apparent capture cross section of $\sigma_\infty = 5 \cdot 10^{-12}$ cm² is derived for the QD ensemble. The extrapolated storage times are then $\tau(300 \text{ K}) = 150$ μ s (with an uncertainty of 0.01 orders of magnitude) and $\tau(358 \text{ K}) = 2$ μ s (with an uncertainty of 0.1 orders of magnitude).

6.2 GaSb/GaAs quantum rings

Besides growing self-assembled QDs, it is also possible to grow self-assembled GaSb quantum rings (QRs) on GaAs. These can also form during growth of QDs, and by altering the growth conditions the type of nanostructure, i.e. dot or ring, can be selected [139, 142, 144]. In the following, a sample with a layer of GaSb/GaAs QRs embedded into a pn-diode structure is investigated. The samples were grown in the group of Shih-Yen Lin at the Research Center for Applied Sciences, Academia Sinica, Taiwan.

6.2.1 Sample structure

Figure 6.20(a) shows the schematic sample structure of QR-A. It is similar to the DLTS samples studied in the previous sections, again with an upside-down structure. A layer of GaSb/GaAs QRs is embedded into a pn-diode within the p-doped layer. An AFM measurement of an uncapped sample of GaSb/GaAs QRs with the same growth parameters as used in the DLTS sample is shown in Fig. 6.20(b). The QRs have a mean peak-to-peak diameter of about $25(\pm 4)$ nm with a mean ring width of $9(\pm 4)$ nm, and a mean height of about $0.8(\pm 0.2)$ nm. The area density of the QR ensemble is $3 \cdot 10^{10}$ cm⁻².

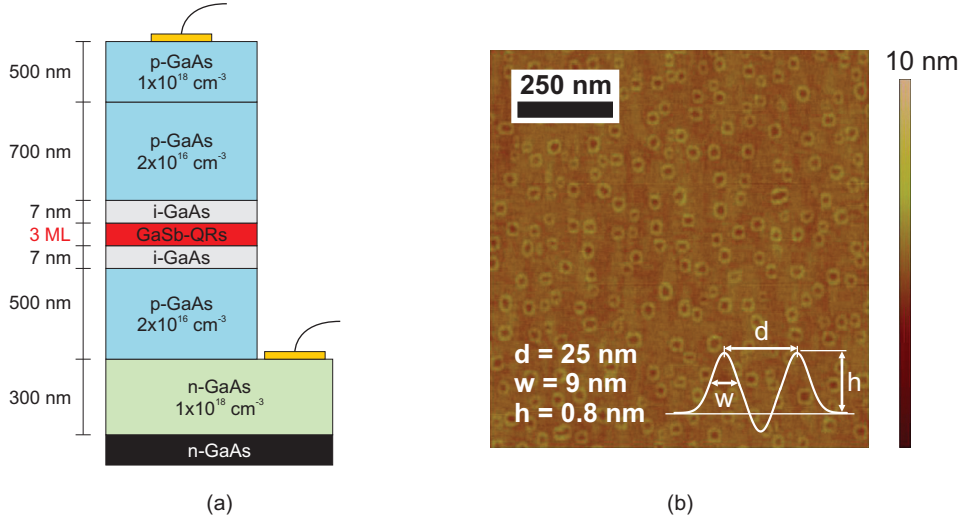


Figure 6.20: QR-A: (a) Schematic structure of the GaSb QR sample. The layer sequence is basically the same as for the QD samples. (b) AFM measurement of an uncapped QR sample with the same growth parameters as for the DLTS sample. The inset shows the schematic profile of the QRs, which have a mean ring width of $9(\pm 4)$ nm, a mean peak-to-peak diameter of $25(\pm 4)$ nm, a mean height of $0.8(\pm 0.2)$ nm, and an area density of $3 \cdot 10^{10} \text{ cm}^{-2}$.

6.2.2 Static capacitance measurements

The sample is pre-characterized using a C-V scan at different temperatures. The C-V sweeps (Fig. 6.21[a]) start from a temperature of 25 K up to a temperature of 350 K with a step width of 25 K and a measurement frequency of 1 MHz. A clear plateau-like feature can be seen between a reverse bias of -0.2 V and 2 V, which is related to the hole emission and capture processes of the GaSb/GaAs QRs. Above a temperature of 275 K, the extension of the plateau starts to saturate, which indicates that in equilibrium the QRs are completely discharged above a reverse bias of 2 V. Again, as observed for the other samples which were studied in the previous sections, the position of the plateau on the voltage axis indicates that the doping concentration in the p-doped region might be smaller than the nominal one [141].

6.2.3 Conventional DLTS

Based on the C-V measurements, a conventional DLTS measurement is performed for temperatures between 25 K and 350 K. Figure 6.21(b) shows the DLTS graph for a reference time constant of $\tau_{ref} = 35$ ms at a measurement bias of $V_m = 2$ V and a pulse bias of $V_p = -0.5$ V. A peak can be seen between 75 K and 175 K with the maximum around 110 K. The peak has a slight asymmetry of which the origin cannot be identified. Possibly, it is related to the total density of states of the QR ensemble, in which the shallow hole states are more numerous than the deeper hole states. For

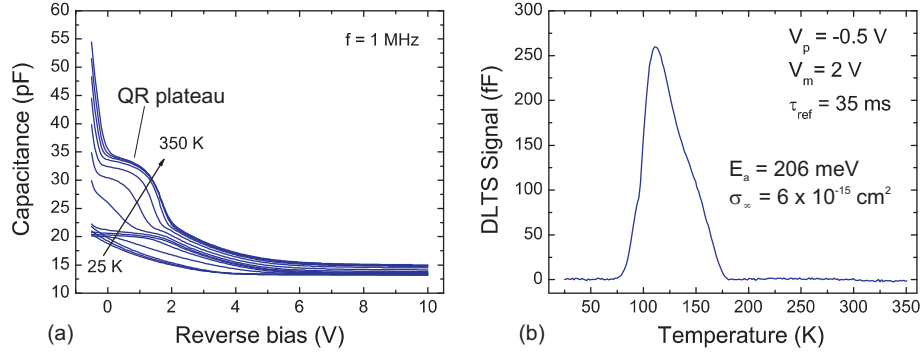


Figure 6.21: QR-A: (a) C-V scan at different temperatures from 25 K to 350 K in steps of 25 K and a measurement frequency of 1 MHz. A clear plateau-like feature can be seen due to hole emission and capture into the GaSb QRs. At 275 K the extension of the plateau begins to saturate, which means that the QRs are completely discharged above a reverse bias of 2 V. (b) Conventional DLTS graph at a measurement bias of 2 V and a reference time constant of $\tau_{ref} = 35$ ms.

different reference time constants τ_{ref} an Arrhenius plot is derived (not shown) and by a fit according to Eq. 3.23, the mean activation energy of $E_a = 206$ meV and the apparent capture cross section of $\sigma_\infty = 6 \cdot 10^{-15}$ cm² are derived for the QR ensemble.

6.2.4 Charge-selective DLTS

A charge-selective DLTS measurement is performed for measurement voltages between $V_m = -0.2$ V and $V_m = 2.4$ V, while the pulse voltage is set to $V_p = V_m - 0.2$, and the pulse width to 1 s. The DLTS graph for the different measurement voltages is depicted in Fig. 6.22 for a reference time constant of $\tau_{ref} = 35$ ms. The peak positions shift from 108 K at a reverse bias of $V_m = -0.2$ V to 163 K at a reverse bias of $V_m = 2$ V, indicating a larger activation energy and hence a shift to the emission from deeper hole energy levels of the QR ensemble. The peak feature disappears in the last two curves which is consistent with the end of the plateau in the C-V curve (Fig. 6.21[a]). From the peak positions an Arrhenius plot is derived for each measurement bias V_m (Fig. 6.23[b]). A fit according to Eq. 3.23 yields the activation energies E_a and the apparent capture cross sections σ_∞ for each individual measurement voltage. The signal in the last two parameter sets at $V_m = 2.2$ V and $V_m = 2.4$ V becomes too noisy to be analyzed. The values for E_a and σ_∞ are shown in Figs. 6.23(a) and 6.23(c), respectively. The activation energies increase from 218 meV at $V_m = -0.2$ V to 380 meV at $V_m = 2$ V while the apparent capture cross sections increase from $\sigma_\infty = 7 \cdot 10^{-14}$ cm² at $V_m = -0.2$ V to $\sigma_\infty = 7 \cdot 10^{-13}$ cm² at $V_m = 2.0$ V. The localization energy is hence $E_{loc} = 380(\pm 10)$ meV (rounded to significant digits) with an apparent capture cross section of $\sigma_\infty = 7 \cdot 10^{-13}$ cm² (with an uncertainty of 0.2 orders of magnitude). Hence, the localization energy of the QRs is smaller than the one typically found for

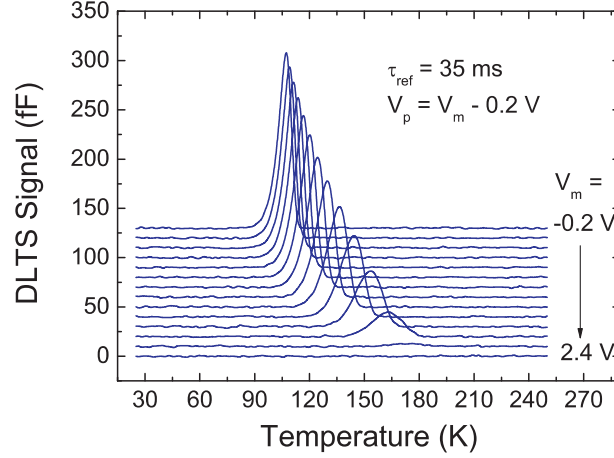


Figure 6.22: QR-A: Charge-selective DLTS graph for measurement voltages between a reverse bias of $V_m = -0.2$ V and $V_m = 2.4$ V. The pulse bias is set to $V_p = V_m - 0.2$ V. The curves are offset by 10 fF each for clarity.

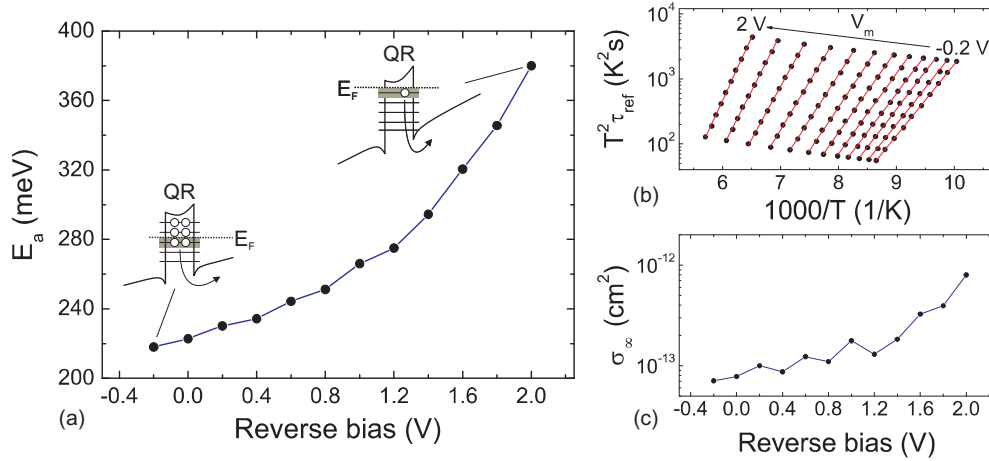


Figure 6.23: QR-A: (a) Activation energies E_a versus the measurement bias V_m . (b) Arrhenius plot derived from the charge-selective DLTS for different reference time constants τ_{ref} . (c) Apparent capture cross sections σ_∞ versus the measurement bias V_m .

GaSb QDs (i.e. 455 meV for QD-A to 760 meV for QD-C). The storage time at room temperature is then $\tau(300 \text{ K}) = 50$ ns (with an uncertainty of 0.08 orders of magnitude) and $\tau(358 \text{ K}) = 3$ ns (with an uncertainty of 0.1 orders of magnitude) at 358 K (85°C).

6.3 $\text{In}_{0.25}\text{Ga}_{0.75}\text{As}/\text{GaAs}/\text{GaP}$ quantum dots

Quantum dots based on GaAs have been studied in great detail throughout the last two decades [20, 21]. Nevertheless, for reaching large localization energies and long storage

times, other material systems might be equally or better suited. An interesting material option are QDs based on GaP as matrix material. As a consequence of the larger band gap in GaP, the hole localization energies of InAs and GaSb QDs can be expected to be larger in GaP than in GaAs [25, 68, 145]. Another advantage over GaAs is that the lattice constants of GaP and Si are similar, which would in principle allow a full integration of GaP-based devices into conventional Si- and CMOS-technology [146]. The samples studied in the following section were grown by Alexander Glacki and Gernot Stracke at TU-Berlin.

6.3.1 Sample structure

Three samples were grown in order to investigate $\text{In}_{0.25}\text{Ga}_{0.75}\text{As}$ QDs on a GaAs interlayer inside a GaP pn-diode structure. The schematic sample structures are depicted in Fig. 6.24. In principle, the structures are similar to those for the DLTS measurements of GaAs-based samples, only the doping concentrations are slightly larger (highly p-doped contact layer with $1 \cdot 10^{18} \text{ cm}^{-3}$ and Zn as acceptor, lower p-doped layer with $5 \cdot 10^{16} \text{ cm}^{-3}$, and the highly n-doped top contact layer with $6 \cdot 10^{18} \text{ cm}^{-3}$ and Si as donor).

In the first sample (QD-GaP, see Fig. 6.24[a]), $\text{In}_{0.25}\text{Ga}_{0.75}\text{As}$ QDs are grown by depositing 2.3 ML of InGaAs on a 3 ML GaAs interlayer which was previously grown on the GaP. The dots are then capped by 6 nm undoped GaP. The exact growth parameters can be found in [136]. The second sample (GAAS-GaP) does not contain a layer of QDs, but only the GaAs interlayer (Fig. 6.24[b]). The third sample (PN-GaP) only consists of a pn-diode structure (Fig. 6.24[c]). The second and the third sample are used as reference samples. All samples are processed into 400 μm -wide round mesa structures by using standard optical lithography and dry etching methods (see Appendix D for details). For the metallization process Ni/AuGe/Au and Ni/Zn/Au was used for the n-side and p-side, respectively.

Figure 6.25(a) shows a $2 \times 2 \mu\text{m}^2$ AFM measurement of $\text{In}_{0.25}\text{Ga}_{0.75}\text{As}$ QDs on 3 ML GaAs on GaP. The QDs have been capped with 6 nm undoped GaP. The growth parameters for the QDs are the same as for QD-GaP. The QDs have a height between 4 nm and 8 nm and a lateral extension of 70 nm to 100 nm with an area density of $1 \cdot 10^{10} \text{ cm}^{-2}$. The capping of the QDs leads to an overestimation of the size of the QDs by AFM. The structural parameters do change if uncapped QDs are analyzed. For uncapped QDs that were grown by depositing 2 ML of $\text{In}_{0.25}\text{Ga}_{0.75}\text{As}$ the height is 1.5 nm to 4.0 nm with diameters of 22 nm to 39 nm and an area density of $1.3 \cdot 10^{11} \text{ cm}^{-2}$.

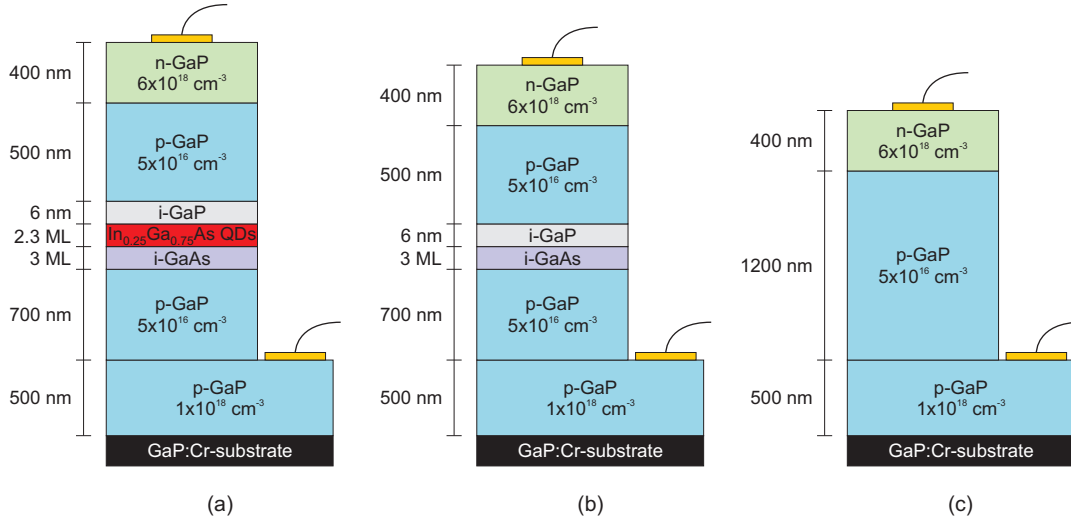


Figure 6.24: GaP-based DLTS samples. (a) QD-GaP: $In_{0.25}Ga_{0.75}As$ QDs on an undoped GaAs interlayer inside a GaP pn-diode structure. (b) GAAS-GaP: GaAs layer inside a GaP pn-diode structure. (c) PN-GaP: GaP pn-diode structure.

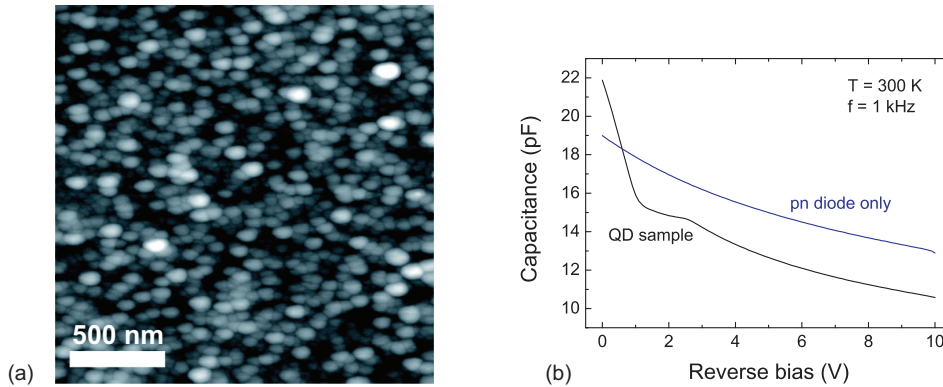


Figure 6.25: (a) AFM measurement of a sample containing $In_{0.25}Ga_{0.75}As$ QDs on a GaAs interlayer on top of GaP. The QDs are capped with 6 nm undoped GaP. The QDs have a height between 4 nm and 8 nm and a lateral extension between 70 nm and 100 nm. (b) C-V measurements of the QD and pn-diode sample. The curve of the QD sample exhibits a plateau-like feature due to the charging and discharging of the QDs. The C-V measurement of the pn-diode structure shows the normal diode-like shape.

6.3.2 Static capacitance measurements and conventional DLTS

For all three samples C-V measurements are performed at room temperature and a measurement frequency of 1 kHz. The curves are depicted in Fig. 6.25(b). The sample which contains the QDs exhibits a plateau between a reverse bias of 1 V and 2.7 V due to the charging and discharging of the QDs. The sample PN-GaP does not show such a plateau-like feature.

Based on the extension of the plateau in the C-V measurement, a conventional DLTS

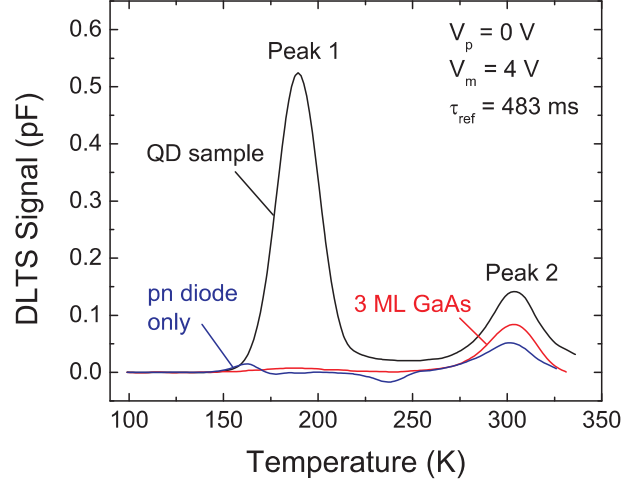


Figure 6.26: Conventional DLTS measurement of the three GaP-based samples for a reference time constant of $\tau_{ref} = 483$ ms. The sample with the $\text{In}_{0.25}\text{Ga}_{0.75}\text{As}$ QD layer (QD-GaP) shows a large peak (Peak 1) around a temperature of 190 K while the other samples without QDs (GAAS-GaP and PN-GaP) show only very small features in this temperature region (around 160 K and 188 K). All samples show a peak (Peak 2) around a temperature of 300 K.

measurement is conducted between a temperature of 100 K and 330 K with a measurement bias of $V_m = 4$ V (reverse direction) and a pulse bias of $V_p = 0$ V with a pulse width of 100 ms. The results for all three samples can be seen in Fig. 6.26 for a reference time constant of $\tau_{ref} = 483$ ms. The curve for the QD sample (QD-GaP) shows a large peak (Peak 1) around a temperature of 190 K which can be attributed to the thermal emission of holes from the $\text{In}_{0.25}\text{Ga}_{0.75}\text{As}$ QDs as the other samples do not display such a large feature. However, very small peaks can also be found in the other two samples: the sample with the 3 ML GaAs (GAAS-GaP) also shows a broad, but very small, peak around 190 K, while the pn-diode structure without the layers (PN-GaP) shows a small peak at 160 K and a negative peak around 235 K. A negative peak usually indicates carrier capture or the emission of minority carriers (i.e. electrons). As the diode is biased in reverse direction, capture processes are unlikely, hence the negative peak belongs to some sort of electron emission of unknown origin. All three samples show a peak around a temperature of 305 K. An interesting feature in QD-GaP is a constant DLTS signal between Peak 1 and Peak 2, which could indicate a temperature-independent contribution by tunneling emission.

From the peak positions at different reference time constants τ_{ref} , an Arrhenius plot is derived for each of the three samples. It is depicted in Fig. 6.27. The $\text{In}_{0.25}\text{Ga}_{0.75}\text{As}$ QD ensemble (Fig. 6.27[a]) has a mean activation energy of $E_a = 450$ meV and an apparent capture cross section of $\sigma_\infty = 2 \cdot 10^{-13}$ cm². Peak 1 for the 3 ML GaAs sample comes from an emission process with an activation energy of $E_a = 380$ meV with an apparent capture cross section of $\sigma_\infty = 1 \cdot 10^{-15}$ cm². In the pn-diode structure, the first peak

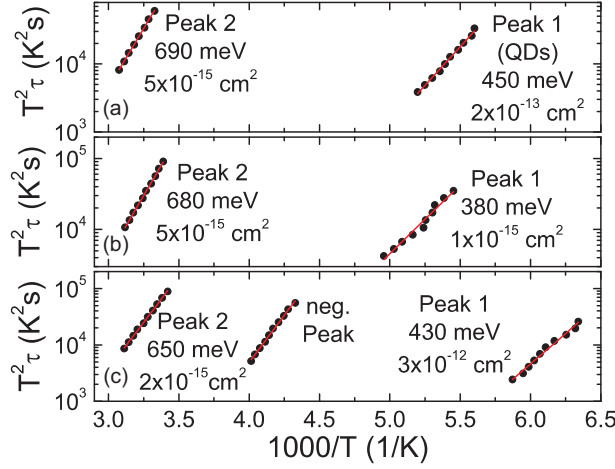


Figure 6.27: Arrhenius plots derived from the DLTS measurements by using different reference time constants τ_{ref} . (a) QD-GaP: QD sample. (b) GAAS-GaP: GaAs layer in GaP pn-diode. (c) PN-GaP: GaP pn-diode.

yields $E_a = 430$ meV with an apparent capture cross section of $\sigma_\infty = 3 \cdot 10^{-12}$ cm². The negative peak at 235 K yields 660 meV with an apparent capture cross section of $\sigma_\infty = 6 \cdot 10^{-12}$ cm². The activation energies for Peak 2 at 305 K are between 650 meV and 690 meV with an apparent capture cross section between $\sigma_\infty = 2 \cdot 10^{-15}$ cm² and $\sigma_\infty = 5 \cdot 10^{-15}$ cm². Although various hole traps in GaP are listed in literature tables [147], the exact origin of Peak 2 could not be identified and remains unclear. However, as the feature appears in all three samples, it is clearly not related to the QD growth.

The use of the charge-selective DLTS method is not possible. The dopants used for the n-side and p-side have large ionization energies (85 meV for Si and 70 meV for Zn [74]), which leads to a freeze-out of the free carriers with decreasing temperature. The effect becomes critical for the charge-selective DLTS because a much smaller number of holes has to be detected during capture and emission as compared to the conventional DLTS measurements where the QDs are completely charged and discharged.

Hence, the best estimate (see Appendix E) for the mean activation energy of the $\text{In}_{0.25}\text{Ga}_{0.75}\text{As}$ QD ensemble is $E_a = 450(\pm 20)$ meV (rounded to significant digits) with an apparent capture cross section $\sigma_\infty = 2 \cdot 10^{-13}$ cm² (with an uncertainty of 0.6 orders of magnitude). The storage time at room temperature is then $\tau(300 \text{ K}) = 3 \mu\text{s}$ (with an uncertainty of 0.2 orders of magnitude) and $\tau(358 \text{ K}) = 100 \text{ ns}$ (with an uncertainty of 0.3 orders of magnitude) at 85°C.

Sample	w (nm), h (nm)	E_{loc} (meV)	σ_{∞} (cm ²)	τ (300 K)	τ (358 K)
QD-A	20(\pm 4), 2(\pm 0.2)	460(\pm 20)	$7 \cdot 10^{-12}$ (0.7)	100 ns (0.3)	4 ns (0.4)
QD-B+B	9-14, 4-6	670(\pm 10)	$1 \cdot 10^{-12}$ (0.2)	2 ms (0.02)	30 μ s (0.05)
QD-B-B	9-14, 4-6	615(\pm 10)	$1 \cdot 10^{-12}$ (0.2)	300 μ s (0.02)	5 μ s (0.05)
QD-C	40(\pm 4), 4.5(\pm 0.2)	760(\pm 20)	$5 \cdot 10^{-11}$ (0.3)	2 ms (0.02)	10 μ s (0.06)
QD-D+B	24(\pm 4), 2.5(\pm 0.2)	800(\pm 50)	$5 \cdot 10^{-12}$ (0.8)	80 ms (0.01)	350 μ s (0.1)
QD-D-B	24(\pm 4), 2.5(\pm 0.2)	640(\pm 50)	$5 \cdot 10^{-12}$ (0.8)	150 μ s (0.01)	2 μ s (0.1)
QR-A	$d = 25(\pm 4)$ nm $w = 9(\pm 4)$ nm $h = 0.8(\pm 0.2)$ nm	380(\pm 10)	$8 \cdot 10^{-13}$ (0.2)	40 ns (0.08)	3 ns (0.1)
QD-GaP	22-39, 1.5-4	450(\pm 20)	$2 \cdot 10^{-13}$ (0.6)	3 μ s (0.2)	100 ns (0.3)
WL-A		55	$8 \cdot 10^{-18}$		
WL-B		-	-		

Table 6.1: Summary of the DLTS results for the samples studied in this work. The values for the localization energy E_{loc} and the apparent capture cross section σ_{∞} are best estimates (see Appendix E). The suffixes +B/-B indicate if the AlGaAs barrier is included or subtracted from the localization energy E_{loc} . The uncertainties of the apparent capture cross section σ_{∞} and the storage time τ are given in brackets as orders of magnitude. The storage times τ (300 K) and τ (358 K) are extrapolated using Eq. 3.23. The results have been rounded to significant digits [148].

6.4 Discussion

The six samples studied in this chapter show a variety of different localization energies and apparent capture cross sections. The results are listed in Table 6.1. The samples which contain a barrier are listed twice, once with the data including the barrier, and once excluding the barrier, which allows to compare the QD contribution to the total localization energy.

The localization energy varies between 380(\pm 10) meV and 800(\pm 50) meV, while the apparent capture cross sections are between 10^{-13} cm² and 10^{-10} cm². Except for one sample, all apparent capture cross sections lie within one order of magnitude around 10^{-12} cm² (see Fig. 6.28). The apparent capture cross section is a phenomenological pre-factor of the exponential function in the thermal emission rate equation (see Eq. 3.23). It includes the effects of the extension of the wavefunctions, the coupling to the phonon bath, and possible Auger scattering. The modeling of all three effects and the precise control of the apparent capture cross section of QDs during epitaxial growth remains yet to be achieved.

In order to compare the localization energies of the samples with each other, the six samples are split into groups: one group for the GaSb/GaAs QD samples and the other for the QR sample and the GaP-based sample. The first group contains four samples. To compare just the QDs alone, the contribution of the Al_xGa_{1-x}As barriers is subtracted. QD-A has the smallest localization energy of 460(\pm 20) meV, followed by QD-B-B with

615(± 10) meV, QD-D-B with 640(± 50) meV, and QD-C with 760(± 20) meV. Hence, the range between the smallest and the largest localization energy is 300 meV. This difference must come from the different structural properties of the GaSb/GaAs QDs, such as geometry, size (base length and height), and chemical composition [69, 70, 149]. For three samples, AFM measurements are available for uncapped QD samples (Figs. 6.2, 6.12, and 6.16), each of which was grown with the same parameters for the QDs as in the corresponding DLTS samples. Hence the QDs can be expected to be very similar to those present in the DLTS samples. One sample has been studied with X-STM and offers a cross section of the QDs (Fig. 6.8). The structural information derived from the AFM measurements hint that the different localization energies are caused by the different sizes of the QDs. When comparing the sizes of samples QD-A, QD-D-B, and QD-C, the disc equivalent diameter increases from 20(± 4) nm to 24(± 4) nm and 40(± 4) nm, with the heights increasing from 2(± 0.2) nm to 2.5(± 0.2) nm and 4.5(± 0.2) nm, respectively. The localization energy increases in the same order. From the X-STM measurements, the base length of the GaSb/GaAs QDs in QD-B can be constrained to 9-14 nm, which would yield a disc equivalent diameter of about the same size. The height is around 4-6 nm. Although not directly comparable with the other samples, the localization energies of QD-B-B and QD-D-B are comparable, hence QD-B also roughly fits into the series of samples if the large height is taken into account. In addition, the X-STM measurements for QD-B have shown that the chemical composition of the QDs is pure ($\sim 100\%$) GaSb. This suggests, that the other samples also have a very high GaSb content, as with smaller GaSb content these high localization energies would not be feasible for the present sizes [149].

When comparing the experimental results with the 8-band $\mathbf{k}\cdot\mathbf{p}$ calculations shown in Fig. 2.8, it can be concluded that the values are in good agreement with the predictions, except for QD-C which has a much larger localization energy than predicted. This deviance might be due to the large size of the dots as compared to the other samples. In addition, another conclusion can be drawn. The classical literature value of 830 meV [150] used for the valence band offset between GaSb and GaAs is too high. The value was already questioned by North *et al.* [151], and using this value in a previous prediction led to a localization energy of 853 meV [27] for QDs similar to the ones studied in this work. In contrast, the valence band offset of 580 meV, proposed by Wei *et al.* [152], results in the values shown in Fig. 2.8, which are in good agreement with the experimental values determined in this work.

Compared to the QDs, the QR sample QR-A has a much smaller localization energy. It is about 80 meV smaller than the value for QD-A. This is a result of the smaller size. In QRs the diameter can be neglected, while the width and the height of the ring play the crucial role, limiting the localization energy. As a result of the formation process of the rings, which are usually formed after dot growth by removing material from the

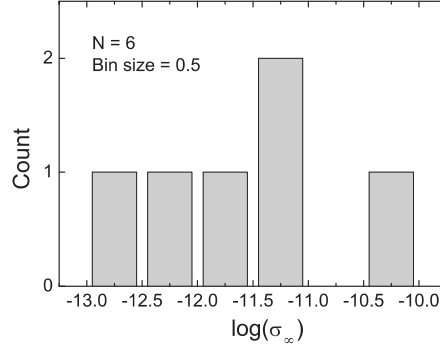


Figure 6.28: Histogram of the apparent capture cross sections of the QDs in the samples investigated in this work. The histogram bin size is 0.5.

center of the dot [139, 153], the ring width and height are smaller than the diameter and height of the original QD. Hence, a smaller localization energy can be expected. However, the apparent capture cross section is comparable to those of the QDs.

For the $\text{In}_{0.25}\text{Ga}_{0.75}\text{As}/\text{GaAs}/\text{GaP}$ QDs, the results are not directly comparable to the results of the other samples. Due to the large ionization energy of the dopants, charge-selective measurements could not be conducted and only the mean activation energy of the QD ensemble could be measured. Hence, the actual localization energy of the QD ensemble can be expected to be larger than the mean activation energy of 450 (± 20) meV. From the other samples it can be seen that the ratio between the mean activation energy \overline{E}_a of the QD ensemble and the localization energy is about $\overline{E}_a/E_{loc} \approx 1.4-1.9$, which would yield a localization energy of $E_{loc} \approx 630-850$ meV for the $\text{In}_{0.25}\text{Ga}_{0.75}\text{As}/\text{GaAs}/\text{GaP}$ QDs. Theoretical calculations of the localization energy in InAs/GaP QDs have resulted in values of ~ 700 meV [25], so that the value for the estimated localization energy can be expected to be on the lower end around 630 meV. The apparent capture cross section is comparable to those of the other samples. However, the corresponding apparent capture cross section for the localization energy can be expected to be larger than the one determined for the mean activation energy, it usually increases by about two to three orders of magnitude for the value corresponding to the localization energy as compared to the value corresponding to the mean activation energy of the QD ensemble.

Based on Eq. 3.23, the values for the localization energy E_{loc} , and the apparent capture cross section σ_∞ , the storage time in a quantum dot based memory can be extrapolated at room temperature (300 K) and at 358 K (85°C). For this extrapolation the values including the barriers are used. The results are listed in Table 6.1 and are plotted as hole storage time versus the localization energy for the two temperatures in Fig. 6.29.

The storage times of all samples studied in this work are smaller than the maximum one listed in [27]. Although the localization energies achieved in the QDs of samples

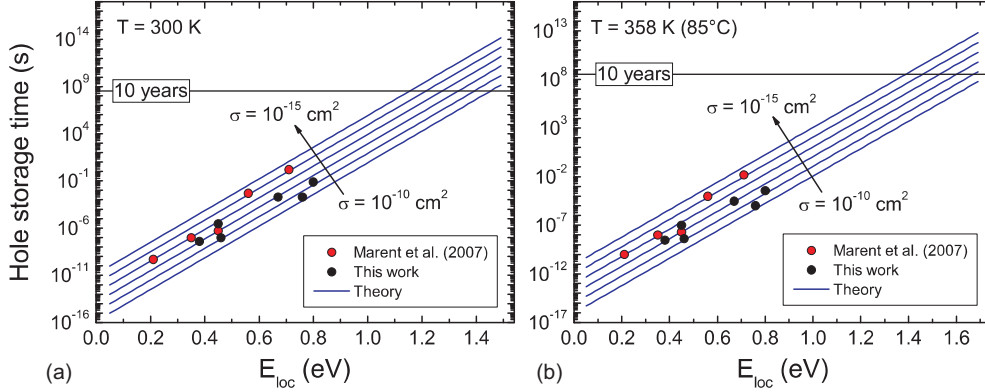


Figure 6.29: Extrapolated hole storage time in QDs at (a) 300 K and at (b) 358 K (85°C) versus the hole localization energy E_{loc} of the QD ensemble. The lines are the values obtained from the theory (see Sect. 3.1.6) for different apparent capture cross sections. The data points are values determined in this work and from [27].

QD-C and QD-D+B are about 50 meV and 90 meV, respectively, larger than for InAs QDs with an additional $\text{Al}_{0.9}\text{Ga}_{0.1}\text{As}$ barrier, the storage time does not increase and is actually about 800 times smaller for QD-C and 20 times smaller for QD-D+B. This is due to the much larger apparent capture cross sections of the QDs investigated in this work ($\sim 10^{-12} \text{ cm}^2$ as compared to $\sim 10^{-15} \text{ cm}^2$ in [27]).

At 358 K (85°C), the storage times decrease drastically. The effect of the increased thermal energy on the storage time is not constant and increases for increasing localization energy E_{loc} . Compared to the values at 300 K, the storage time decreases about 13 times for QR-A, and about 230 times for QD-D+B.

6.5 Conclusion

The following conclusions can be drawn from the results of this chapter:

- The GaSb/GaAs QDs studied in this work have localization energies between $460(\pm 20)$ meV and $760(\pm 20)$ meV. The trend of increasing localization energies is most likely related to the increasing sizes of the dots.
- The apparent capture cross sections determined for the GaSb/GaAs QDs are between $1 \cdot 10^{-12} \text{ cm}^2$ and $5 \cdot 10^{-11} \text{ cm}^2$, which is larger than the apparent capture cross sections observed in previous work [27].
- The maximum localization energy for holes was achieved in GaSb/GaAs QDs with additional $\text{Al}_{0.3}\text{Ga}_{0.7}\text{As}$ barriers. This resulted in a total localization energy of $800(\pm 50)$ meV. This is the highest value ever measured for QDs. With a

capture cross section of $5 \cdot 10^{-12} \text{ cm}^2$ this leads to a room temperature storage time of 80 ms (0.01), and 350 μs (0.1) at 358 K (85°C). These are the maximum storage times of all samples investigated in this work. However, due to the larger apparent capture cross sections, the storage time is smaller than the maximum value achieved in previous work (1.6 s, [27]).

- The GaSb/GaAs QRs show a localization energy of 380(\pm 10) meV with an apparent capture cross section of $8 \cdot 10^{-13} \text{ cm}^2$ (0.2). Compared to the QD samples, the localization energy is smaller, a result of the smaller width and height of the QRs. The capture cross section is comparable to those of the QDs.
- Only one of the two WL samples showed a localization of holes with an activation energy of 55 meV and an apparent capture cross section of $8 \cdot 10^{-18} \text{ cm}^2$.
- In theoretical calculations the GaSb/GaAs valence band offset of 580 meV, proposed by Wei *et al.* [152], should be used.

Chapter 7

Carrier dynamics in quantum dots coupled to a 2DHG

The following chapter presents the results of the investigation of the coupling between a layer of self-assembled QDs and an adjacent two-dimensional hole gas (2DHG). In total, three samples are investigated, of which each has a different tunneling barrier between the QDs and the 2DHG, resulting in a different coupling strength. The samples are analyzed using capacitance-voltage (C-V) spectroscopy and time-resolved measurements of the source-drain current which flows through the 2DHG.

Parts of this chapter have already been published in [154, 155].

7.1 Samples

To investigate the carrier dynamics and the coupling of QDs to a 2DHG, a set of samples is grown, in which a layer of self-organized InAs QDs is inserted into a MODFET structure. The QD layer is placed in the vicinity of the 2DHG channel. In order to change the coupling strength between the QD layer and the 2DHG, three samples were designed, each with a tunneling barrier of different width.

A schematic depiction of the sample layer structure can be seen in Fig. 7.1(a). The samples are grown by molecular beam epitaxy (MBE). A single InAs/GaAs QD layer with a nominal QD density of $3 \cdot 10^{10} \text{ cm}^{-2}$ is embedded into a GaAs QW, inside a nominally undoped $\text{Al}_{0.9}\text{Ga}_{0.1}\text{As}$ matrix. Underneath the QD layer a 2DHG is formed in 8 nm GaAs, with holes provided by an adjacent 30-nm-wide p-doped layer ($p = 2 \cdot 10^{18} \text{ cm}^{-3}$). Sample A has a 5-nm-thick $\text{Al}_{0.9}\text{Ga}_{0.1}\text{As}$ barrier between the QD layer and the 2DHG, while the barrier in Sample B and Sample C is 10 nm and 15 nm thick, respectively. As the $\text{Al}_{0.9}\text{Ga}_{0.1}\text{As}$ barrier is sandwiched between GaAs layers, the total tunneling length from the QD ground state to the 2DHG amounts to 18 nm, 23 nm,

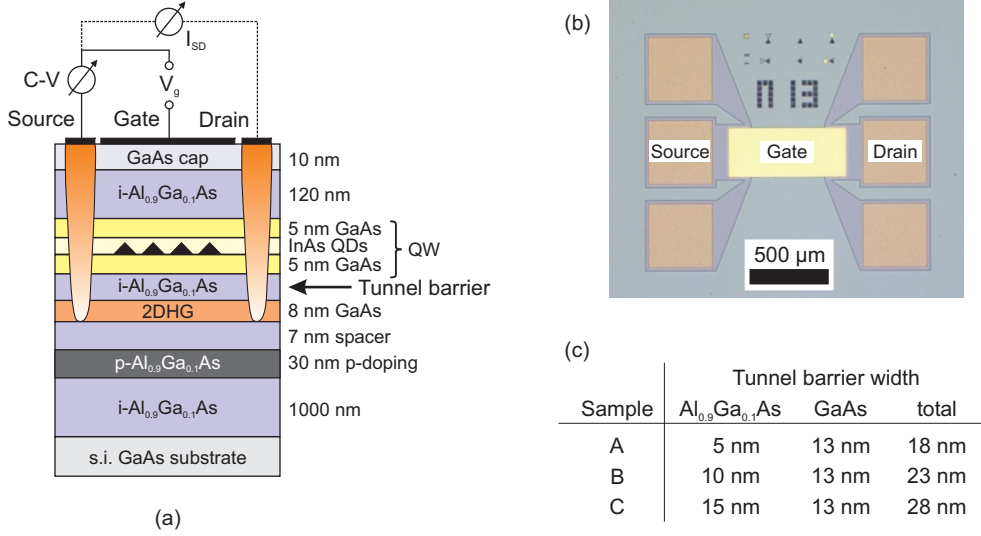


Figure 7.1: (a) Sample structures and measurement setup: a layer of InAs-QDs is embedded into a GaAs QW inside an $\text{Al}_{0.9}\text{Ga}_{0.1}\text{As}$ MODFET. Three samples are investigated, each containing a tunneling barrier of different width between the QD layer and the 2DHG. The capacitance-voltage measurements are performed between the source and the gate contact. In the conductance measurements, the source-drain current I_{SD} is measured while changing the gate bias V_g . (b) Top-view photograph of the hall bar mesa structure. The gate width is 740 by $310 \mu\text{m}^2$. (c) The tunnel barriers comprise of the 5-nm-thick layer of GaAs directly underneath the QDs, the $\text{Al}_{0.9}\text{Ga}_{0.1}\text{As}$ barriers of different widths between 5 and 15 nm, and 8 nm GaAs of the QW in which the 2DHG is formed.

and 28 nm, respectively (see table in Fig. 7.1[c]).

The samples are processed by standard chemical wet-etching into Hallbar mesa structures with an effective gate area of $740 \mu\text{m}$ by $310 \mu\text{m}$ (see Fig. 7.1[b]). Ohmic source and drain contacts are formed by thermal evaporation of a Ni/Zn/Au and subsequent annealing to contact the 2DHG layer. The Schottky gate contact is made by evaporation of Ni and Au after the annealing step (see Appendix D for details).

Transfer length measurements (TLM) at room temperature yield a sheet resistance of $12.8 \text{ k}\Omega$ and a specific contact resistance of $1 \cdot 10^{-5} \Omega\text{m}^2$ for Sample B. Hall measurements show a mobility for Sample B of $191 \text{ cm}^2/\text{Vs}$ and a sheet density of $2.3 \cdot 10^{12} \text{ cm}^{-2}$ at 300 K and $2010 \text{ cm}^2/\text{Vs}$ and a sheet density of $1.6 \cdot 10^{12} \text{ cm}^{-2}$ at 77 K, respectively. The simulation of the valence band of Sample A is depicted in Fig. 7.2 for a temperature of 25 K at a gate voltage of $V_g=0 \text{ V}$ ¹. The total localization energy of the holes in the QDs has been taken from Deep Level Transient Spectroscopy (DLTS) measurements on similar QDs as 710 meV (210 meV for the QDs and 500 meV for the band offset between GaAs and $\text{Al}_{0.9}\text{Ga}_{0.1}\text{As}$ [27]). At low temperatures ($<250 \text{ K}$), most of the holes from the doping layer reside inside the 8-nm-wide QW, in which the 2DHG is formed. This sheet charge pins the Fermi level E_F throughout the whole structure.

¹It should be noted that the device has been simulated without the QDs. The QD potential well was later added by hand.

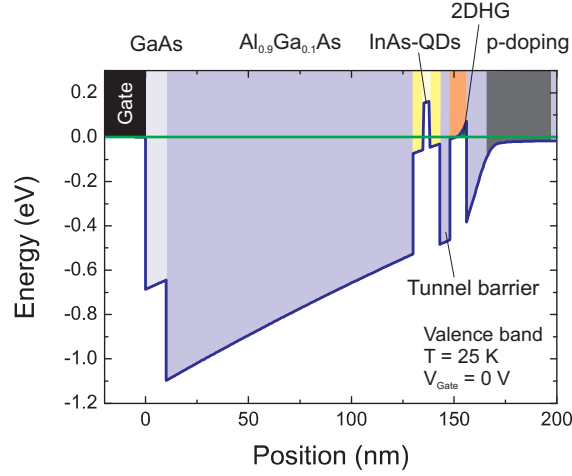


Figure 7.2: Sample A: (a) Calculated valence bandstructure for a temperature of 25 K (calculated with *nextnano*³ [156]). The Fermi level is indicated as green line. As most of the holes reside in the 2DHG, it pins the Fermi level. Hence, the position of the hole energy levels of the QD ensemble can be altered relative to the Fermi level by changing the gate voltage. This way, the charge state of the QDs can be prepared. The colors correspond to the layers of the structure shown in Fig. 7.1(a).

Hence, the position of the energy levels of the QD ensemble can be adjusted relative to the Fermi level by changing the gate bias V_g . This allows the controlled charging and discharging of the QDs with a specific number of charges per dot. The charge transfer from the 2DHG to the QDs and vice versa occurs by means of tunneling emission, and at higher temperatures also due to thermal and thermally-assisted emission. As a result of the different widths of the tunneling barriers, Samples A, B, and C exhibit different coupling constants. Sample A has the thinnest barrier and the coupling is the strongest (smallest tunneling time constant), where Sample C has the widest tunnel barrier and has the weakest coupling constant (largest tunneling time constant). Sample B is somewhere in between Sample A and C. Therefore, not all measurement methods work on every sample: C-V and time-resolved conductance measurements are possible only on Sample A, while the time constants are already so large in Sample B and C, that on these samples only the time-resolved conductance measurements can be performed.

7.2 Sample A (5 nm tunnel barrier)

This section investigates Sample A which has a 5-nm-wide $\text{Al}_{0.9}\text{Ga}_{0.1}\text{As}$ tunneling barrier. First, the capacitance-voltage measurements are presented, followed by the time-resolved current measurements.

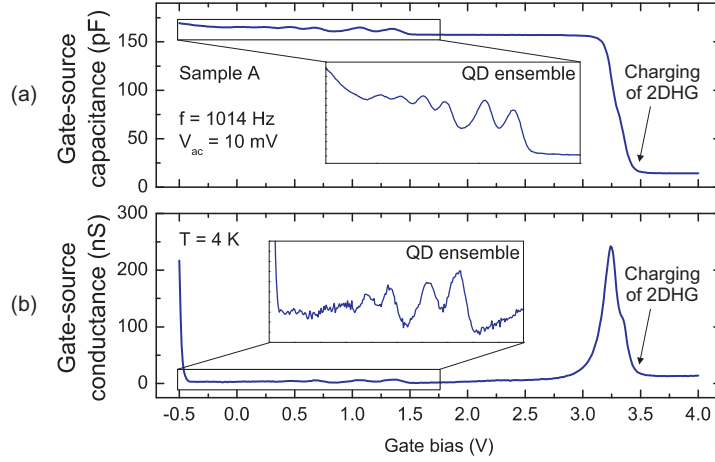


Figure 7.3: Sample A: (a) Capacitance-voltage sweep. At $V_g = 4$ V the 2DHG and the QD ensemble are empty and the depletion region reaches far into the device below the 2DHG. When the gate voltage is decreased to 3.5 V the 2DHG is charged until 3 V. Lowering the gate voltage further leads to a charging of the QDs between 1.5 V and -0.1 V (see inset). (b) Conductance-voltage sweep. The charging peak of the 2DHG can be clearly seen around 3.25 V. The charging curve of the QD ensemble looks similar to the curve of the C-V sweep.

7.2.1 Capacitance-Voltage measurements

In Sample A the QD ensemble is strongly coupled to the 2DHG. The narrow barrier ($\text{Al}_{0.9}\text{Ga}_{0.1}\text{As}$) exhibits a small tunneling time constant which is small enough that C-V measurements can be conducted. A sweep of the gate-to-source capacitance for different gate voltages with a measurement frequency of 1014 Hz at a temperature of 4 K is shown in Fig. 7.3(a), and the gate-to-source conductance is shown in Fig. 7.3(b). Starting at a gate voltage $V_g = 4$ V, the upper part of the device until well below the 2DHG is depleted of holes. When the gate voltage is decreased, the 2DHG gets charged with holes around a gate voltage of 3.5 V. This charging can be seen as an increase in the capacitance and a peak in the differential conductance. The capacitance increases to a plateau of about 157 pF, where the 2DHG is fully charged. The Fermi level is now pinned by the 2DHG throughout the device, and the 2DHG can be treated as a spatially fixed back contact. Further decreasing the gate voltage shifts the unoccupied hole energy levels of the QD ensemble above the Fermi level, and the QDs get charged with holes from the 2DHG, which tunnel through the barrier. The individual energy levels of the QDs, broadened by the ensemble, can be distinguished, and six levels are clearly visible in the C-V curve, while in the dG-V curve only four levels can be clearly seen (see inset of Fig. 7.3[b]).

The details of the charging of the QD ensemble can be seen in Fig. 7.4. With the device set at different temperatures, the gate voltage is swept within the region in which the QD ensemble is charged (2 to -0.1 V). In total, six peaks are clearly visible

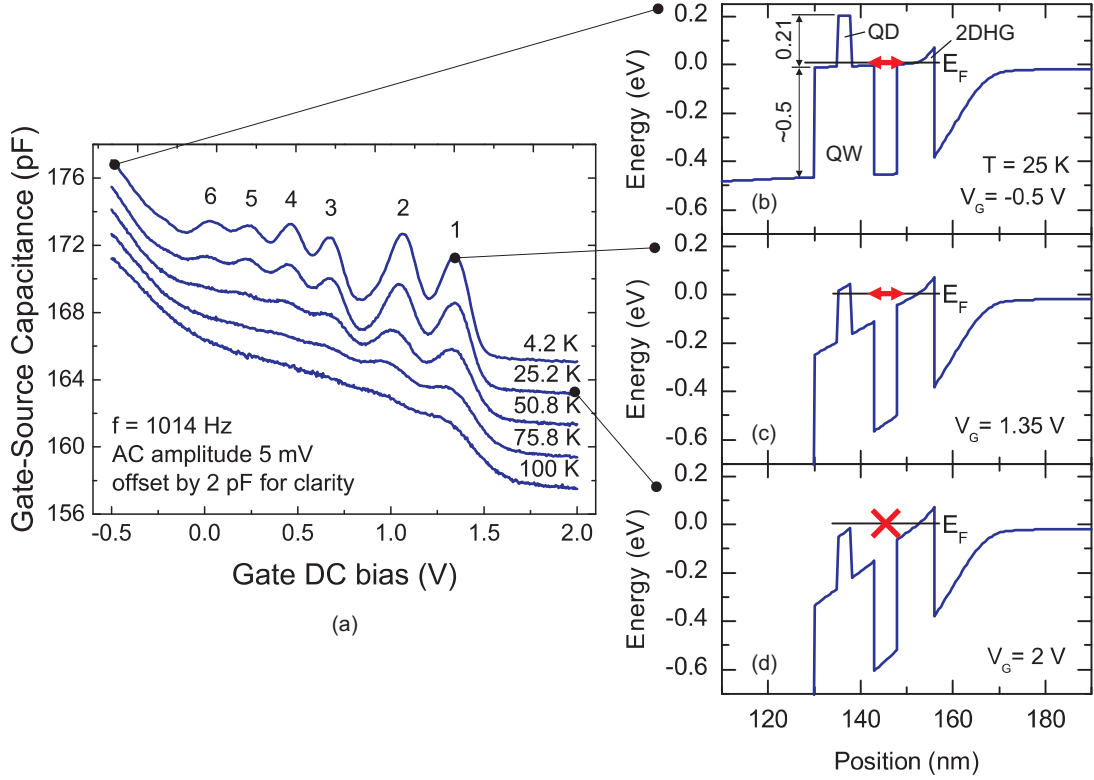


Figure 7.4: Sample A: (a) Capacitance-voltage sweeps at different temperatures. Peaks are clearly visible whenever the Fermi level aligns with a local maximum in the density of states of the QD ensemble. (b) Valence bandstructure at a gate voltage of -0.5 V, (c) 1.34 V, and (d) 2 V.

in Fig. 7.4(a) up to a temperature of 50 K. However, even at a temperature of 100 K peaks 1 and 2 can be observed.

The charging of the QDs takes place in the following sequence. At a gate bias of 2 V the hole energy levels of the QDs are below the Fermi level E_F , and holes in the 2DHG cannot tunnel into the QDs due to the lack of hole states (see Fig. 7.4[d]). At 1.35 V (peak 1), the ground state of the QD ensemble is aligned with the Fermi level of the device, and holes can tunnel into the unoccupied hole energy levels of the QD ensemble. In equilibrium, each QD is filled with one hole (see Fig. 7.4[c]). The ground state of a QD in the ensemble is two-fold degenerate. A second hole added to the ground state of a QD has to overcome the Coulomb repulsion by the first hole, leading to a shift of the (unoccupied) energy level to higher energies (see Sect. 3.2). Hence, the second hole per QD will transfer to the QDs not at the same gate bias as the first hole, but at a gate bias of 1.1 V (peak 2). Each additional hole adds to this Coulomb repulsion and shifts the energy levels to higher energies with respect to the unoccupied energy levels [98]. Further decreasing the gate bias leads to a filling of higher energy levels in the QD ensemble (peak 3 to peak 6). Hence, the peaks belong to the many-particle hole states of the QDs filled with two to six holes (level one is a single-particle level).

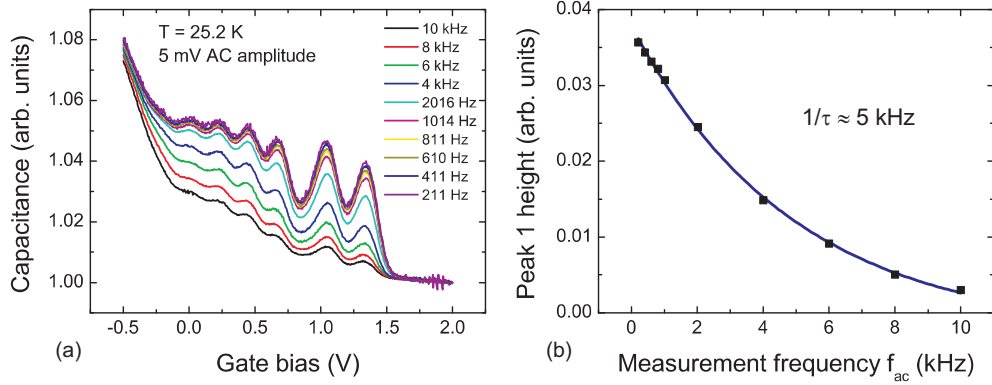


Figure 7.5: (a) C - V measurements at 25 K for different measurement frequencies. The height of the QD peaks in the curves saturates for frequencies above 1 kHz, while it decreases for higher frequencies. (b) Height of peak 1 relative to an artificial ground line as a function of the measurement frequency.

If the gate voltage is further decreased, such that the Fermi level is completely below the hole energy levels of the QDs, the energy levels of the GaAs QW, into which the layer of QDs is embedded, are populated (see Fig. 7.4[b]). This can be seen as a step increase in the capacitance and in the conductance below a gate voltage of -0.1 V.

In order to study the time constants involved in the tunneling processes of the C - V measurements, the ac frequency is changed to values below 1014 Hz. In Fig. 7.5(a) it can be seen that the height of the peaks in the C - V curves start to saturate for frequencies below 1 kHz. This indicates, that all levels in the QDs participate in the tunneling processes and are periodically charged and discharged by the ac voltage. In contrast, when the ac frequency is set to higher values than 1014 Hz, the heights of the QD peaks decrease and the peaks vanish towards frequencies above 10 kHz. This decrease can be related to the time constants of the tunneling processes involved in the charging and discharging of the QD ensemble. Nevertheless, as the peak heights of the other peaks change similarly with the frequency, it is more likely that the value arises from the parasitics of the device structure. The estimated cutoff frequency of the device RC low pass, derived from the gate area and the sheet resistance, is around 20 kHz and can be seen as a hint that the processes governing the time constants are not the tunneling emission and capture, but the parasitics of the device. Although the value determined from the exponential decay fit in Fig. 7.5(b) is about a quarter of that value, it is still very likely that the parasitics limit the device performance, such that the real time constants are faster than the cutoff frequency. Another argument in favor of this interpretation is the fact, that the time-constants determined in the time-resolved conductance measurements (see Sect. 7.2.2) stay roughly constant throughout a large temperature range which can only be explained by a cutoff frequency limiting the measurements.

A Gaussian fit yields an area under the first peak of $\Delta C dU = 1.2 \cdot 10^{-12}$ C. Multiplying

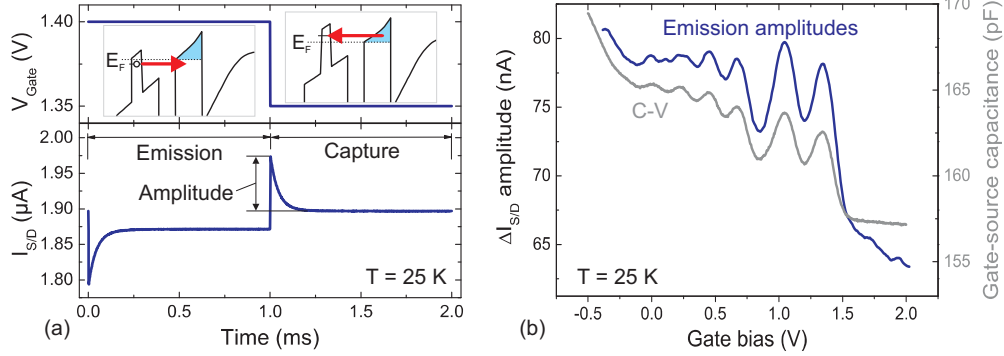


Figure 7.6: Sample A: (a) Time-resolved measurement of the source-drain current I_{SD} while applying a voltage pulse to the gate. The transients show the emission and capture of holes in the QD ensemble. The amplitudes ΔI_{SD} of the transients are a measure for the number of holes that are transferred between the QDs and the 2DHG during the pulse. (b) Transient amplitudes of the source-drain current ΔI_{SD} as a function of the gate voltage V_g . The curve is smoothed by the Savitzky-Golay algorithm [157] with a fit window of 100 mV. The amplitudes resemble the C-V curve, and the same peak structure is visible.

it with an estimated geometric lever arm of $\lambda \approx 156 \text{ nm}/18 \text{ nm} = 8.7$, and dividing it by the elementary charge and the active gate area, yields a hole density in the QD layer of $2.8 \cdot 10^{10} \text{ cm}^{-2}$ which is in very good agreement with the nominal QD density of $3 \cdot 10^{10} \text{ cm}^{-2}$ of the structures.

7.2.2 Conductance measurements

While the C-V measurements give access to the static energy levels of the many-particle hole states, the carrier dynamics can be investigated by time-resolved measurements of the current which flows through the 2DHG.

To study the tunneling processes in detail, the gate bias is swept in steps of 10 mV. At each step, a pulse of 50 mV height is applied to change the energetic position of the hole energy levels of the QD ensemble relative to the Fermi level of the structure. The sweep is started at 2 V, where the QDs are empty. By lowering the gate bias, the QD ensemble is successively charged with holes, which are transferred from the 2DHG to the QDs by tunneling through the barrier. The transfer of holes from the 2DHG to the QDs reduces the hole density of the 2DHG and hence the conductance is lowered, which can be directly measured in the source-drain current.

A time-resolved source-drain current measurement of Sample A is depicted in Fig. 7.6(a) for a gate bias of $V_g = 1.35 \text{ V}$ at a temperature of 25 K. The source-drain measurement voltage V_{SD} is 5 mV. When the pulse of 50 mV is applied at $t = 0$, the highest occupied hole levels of the QD ensemble are below the Fermi level E_F (see inset of Fig. 7.6[a]), and are emitted to the 2DHG to reach equilibrium again. As the emitted holes accumulate in the 2DHG, the hole density rises, which can be seen as an increase

in the source-drain current I_{SD} . When the gate voltage is set back to 1.35 V, the same hole energy levels of the QDs (now unoccupied) are above the Fermi level, and consequently, the holes are emitted from the 2DHG and captured back into the QDs. The result is a decreasing source-drain current until equilibrium is reached again. This kind of measurement is now repeated for gate voltages between 2 V and -0.5 V in steps of 10 mV.

The amplitudes of the transients obtained for each measurement step are a measure of how many holes are transferred during the pulse. If the amplitudes ΔI_{SD} are plotted as a function of the respective gate voltage V_g , they resemble the same peak structure as in the C-V curve (Fig. 7.6[b]). Again, a distinct peak structure is visible at those gate voltages where the Fermi level aligns with a peak in the density of states of the QD ensemble. The four first peaks can clearly be distinguished, whereas the last two peaks are distorted to some degree, but can also be seen. The difference in the last two peaks stems from noise and the analysis method as the signal decreases for the higher peaks. The C-V measurement is a two terminal measurement, while the current measurement is a three terminal measurement, being an additional source of noise. Also, due to the longer measurement time for each step of the current measurements, the overall number of averages taken per measurement step is lower than for the C-V measurements.

Although time-resolved measurements can be performed on Sample A, the time constants that are derived from the emission and capture transients stay constant with temperature and hence do not resemble the ones related to the tunneling processes, but are the result of the parasitics of the RC low pass of the device structure, a problem which was already mentioned in Sect. 7.2.1.

7.2.3 Many-particle level splittings

The positions of the peaks in the C-V curves are a complex result of the energetic position of the (unoccupied) hole energy levels of the QDs in the ensemble and the Coulomb and exchange interaction between holes inside a single QD (see Sect. 3.2). From the C-V curves, the many-particle level splittings with respect to the gate voltage can be obtained. However, due to the lever arm (the ratio of gate voltage change to potential change at the position of the QDs) which is dependent on the charge state of the QDs, the many-particle level splittings cannot be directly obtained. An equivalent circuit model in combination with an iterative analysis method, which are both described in Sect. 4.1.3, have to be applied. To exclude temperature effects, the C-V curve taken at 4 K is used in the analysis. Here, the broadening of the Fermi function (see Sect. 4.1.4) can be neglected and the Fermi level is sufficiently sharp.

The device model is separated into two constant geometric capacitances which account for the MODFET structure. The potential-dependent quantum capacitance accounts for the QD ensemble and the GaAs QW in which the QD layer is embedded. The

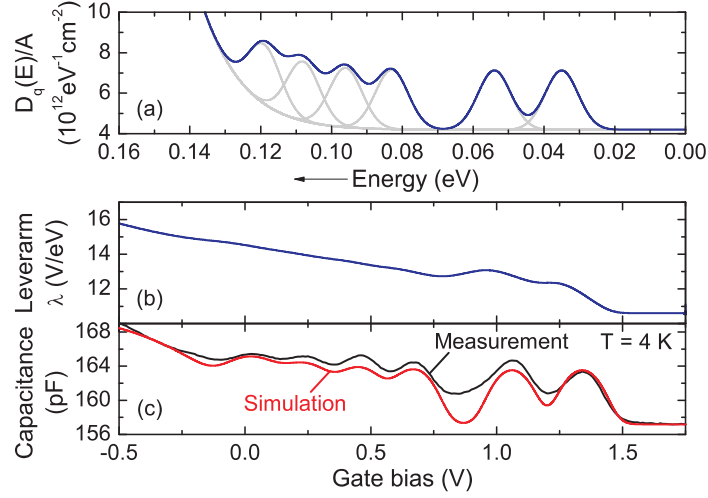


Figure 7.7: Sample A: (a) Density of states of the quantum region (QD ensemble and GaAs QW) per area $D_q(E)/A$ which was used in the simulation and was the result of an iterative adaptation of the peak positions. The grey curves are the six Gaussians at the energetic position of the many-particle hole states. (b) Occupation-dependent lever arm λ as the ratio between the gate voltage change to potential change at the position of the QDs. (c) Measured (black curve) and simulated (red curve) capacitance. The peak positions were manually adapted in the DOS to fit the measured curve.

geometrical capacitance between the gate and the QD layer yields $C_1 = 159$ pF, and the geometrical capacitance between the QD layer and the 2DHG $C_2 = 1.5$ nF. The density of states of the QD ensemble is assumed to consist of six Gaussians accounting for the many-particle hole states. The density of states of the GaAs QW is described by the slope of a Gaussian. The total density of states in the quantum region (QD ensemble and GaAs QW) per area is shown in Fig. 7.7(a).

The density of states is then used as input for the quantum capacitance (see Eq. 4.16) within the capacitance network (see Eq. 4.19). Then the iterative algorithm described in Sect. 4.1.3 is used to extract the peak positions in the density of states of the QD ensemble. The results are shown in Fig. 7.7(c). The peaks are manually shifted and the algorithm re-run until they fit the peak positions of the measurement. The exact shape of the measured C-V curve cannot be resembled, as the slope of the Gaussian of the density of states of the GaAs QW is the main unknown in the simulation. From the manually fitted C-V curve, the peak positions and the inhomogeneous broadening of the QD ensemble due to deviations in shape, size, and chemical composition are extracted. After the iterations, the full width at half maximum of the hole density of states of the QD ensemble is set to 9 meV.

The lever arm, as a result of the ratio of the gate voltage change to the potential change at the position of the QD layer, is depicted in Fig. 7.7(b). It changes its value due to the charges which are added to the QDs when changing the gate bias. Before the Fermi level passes the first hole energy level of the QDs, the lever arm is about 11 and stays

Holes (peak no.)	Level splitting (meV)	
	Sample A	8 band $\mathbf{k}\cdot\mathbf{p}$ theory
Δ		
1-2	19 (± 1)	20.6
2-3	29 (± 1)	29.8
3-4	13 (± 1)	15.2
4-5	12 (± 2)	15.3
5-6	11 (± 2)	17.7

Table 7.1: Energy level splittings of the many-particle hole states of Sample A obtained using an equivalent circuit model with a quantum capacitance for the quantum region (QD ensemble and GaAs QW) at 4.2 K and values from 8 band- $\mathbf{k}\cdot\mathbf{p}$ theory. The errors are given in brackets and are mostly related to the uncertainty of the exact slope of the Gaussian for the density of states of the GaAs QW.

constant, while after the last peak has passed, the lever arm has increased to a value of about 16. The values for the many-particle level splittings obtained for Sample A are listed in Tab. 7.1. The main uncertainty of the values comes from the density of states assumed for the GaAs QW, in which the QD layer is embedded. As the effect of the density of states D_{QW} is stronger on the higher peaks (especially peaks 5 and 6), the uncertainty increases for the higher peaks.

As the unoccupied first hole level in the QDs is two-fold degenerate (spin-up and spin-down), the many-particle level splitting between the first two holes of $19(\pm 1)$ meV is solely the contribution of the Coulomb repulsion between the first and the second hole. The level splitting between the second and the third hole of $29(\pm 1)$ meV comprises of the level splitting between the first and the second hole level in the unoccupied QDs, the Coulomb repulsion between the first two holes and the third hole entering the QD, and the exchange interaction between all three holes inside the QD. With more holes inside the QDs, the individual contributions to the many-particle level splittings become more complicated.

The many-particle hole level splittings can also be derived from theory². First, the many-particle hole state energies are calculated for an InAs/GaAs QD model structure using the Hartree-Fock approximation on top of the 8-band $\mathbf{k}\cdot\mathbf{p}$ theory [70, 158]. The QDs in the model structure have a truncated pyramid shape with a base length of 20 nm, a height of 3 nm, and an average In composition of 90 %. From the many-particle hole state energies, each level splitting can be derived by subtracting all contributions of the previous many-particle hole energies:

$$\Delta_{1-2} = E_2 - E_1 - (E_1 - E_0), \quad (7.1)$$

$$\Delta_{2-3} = E_3 - E_2 - (E_2 - E_1), \quad (7.2)$$

²The calculations were performed by Gerald Hönig at TU-Berlin.

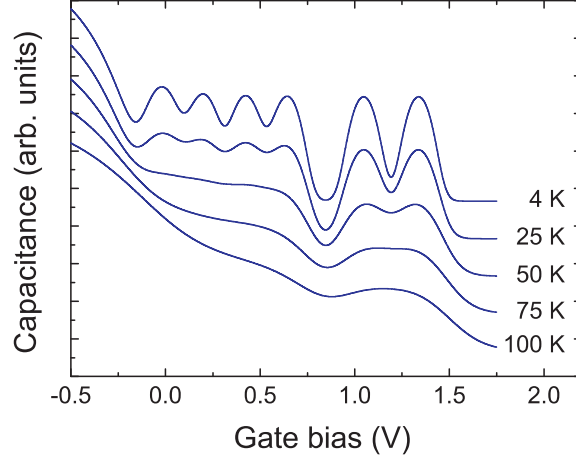


Figure 7.8: Sample A: Simulated influence of thermal broadening of the Fermi function on the capacitance curves. The smearing-out of the peaks compares qualitatively well with the measured curves (see Fig. 7.4).

$$\Delta_{3-4} = E_4 - E_3 - (E_3 - E_2) \text{ etc.}, \quad (7.3)$$

where E_n is the total energy of the many-particle system with n participating holes in the dots. The energetic distance $\Delta_{(n-1)-n}$ is the additional energy which a hole needs in order to be added to the complex as compared to the previously added hole. The derived values include Coulomb charging effects and exchange interaction. Correlation effects are not considered. The many-particle level splittings derived in this way are listed in Tab. 7.1. A comparison of the theoretical values with the experimental ones yields a good agreement for the first four level splittings, while the fifth level splitting is about 7 meV larger than the experimental value. This deviation could be related to the uncertainty of the density of states of the GaAs QW, which becomes more critical for the higher peaks, as mentioned already above, thus best agreement is found for the first two peaks.

7.2.4 Higher temperatures

When increasing the temperature above 4.2 K, the thermal Maxwell-Boltzmann broadening of the Fermi function has to be taken into account in the simulation (see Sect. 4.1.4). The broadening is accounted for by using a thermally-broadened density of states as derived in Eq. 4.21 in the simulation. All other parameters are similar to the ones used in Sect. 7.2.3. The results for the C-V curves are shown in Fig. 7.8 for temperatures between 4 K and 100 K. With increasing temperature a smearing-out of the peak structure can be observed. The simulated curves compare qualitatively well with the measured curves. Again, the main error comes from the exact shape of the density of states of the GaAs QW, into which the QD layer is embedded.

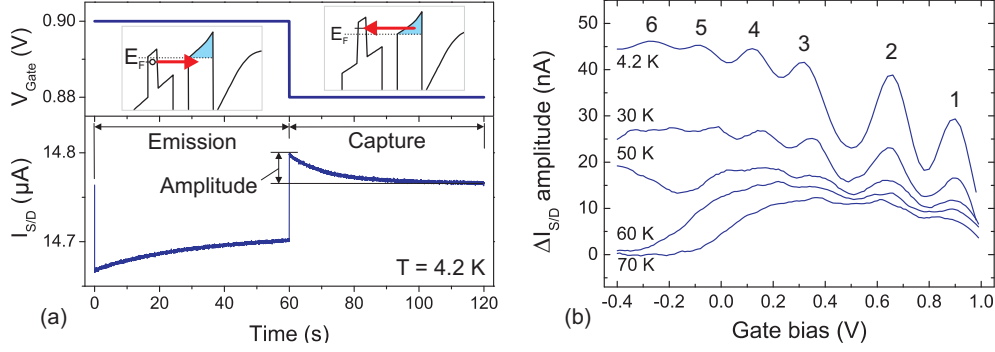


Figure 7.9: Sample B: (a) Source-drain current transients for the emission of holes from the QDs to the 2DHG, and capture of holes from the 2DHG into the QDs. The gate voltage is corresponding to peak 1 in (b), corresponding to the ground state in the QD ensemble. (b) Capture transient amplitudes ΔI_{SD} versus the gate bias V_g at different temperatures. The curves have been smoothed by the Savitzky-Golay algorithm [157] with a fit window of 100 mV. A distinct peak structure is visible which is related to the many-particle density of states of the QD ensemble.

7.3 Sample B (10 nm tunnel barrier)

The time constants of the emission and capture transients of Sample A are governed by the parasitics related to the RC low pass behavior of the device structure. Hence, the time constants have no relation to the physical emission and capture processes occurring between the QDs and the 2DHG. The situation is completely different for Sample B, where the tunnel barrier is thicker. As a consequence, Sample B shows a weaker coupling between the QDs and the 2DHG, resulting in longer tunneling time constants for the emission and capture processes. The tunneling time constants are now in the range of several seconds, and C-V measurements are thus no longer feasible. However, the time constants are not limited by the RC parasitics and can be investigated by current measurements of the 2DHG.

7.3.1 Current measurements

In a series of charging and discharging pulse sequences, the QDs are charged and discharged while the resulting change in the 2DHG conductance is directly recorded by a measurement of the source-drain current. The pulse offset bias is swept in small steps of 10 mV, while the pulse amplitude is set to 20 mV. Due to the longer time constants and the resulting limitation to fewer averaging, the source-drain measurement voltage V_{SD} is now set to 30 mV in order to increase the signal. The emission and capture transients for a gate bias of 0.88 V at a temperature of 4.2 K are shown in Fig. 7.9(a). In Fig. 7.9(b) the amplitudes of the capture transients versus the corresponding gate bias at which they were recorded are depicted. Distinct peaks of the many-particle hole states are visible, similar to those of Sample A shown in Fig. 7.6(b). The gate

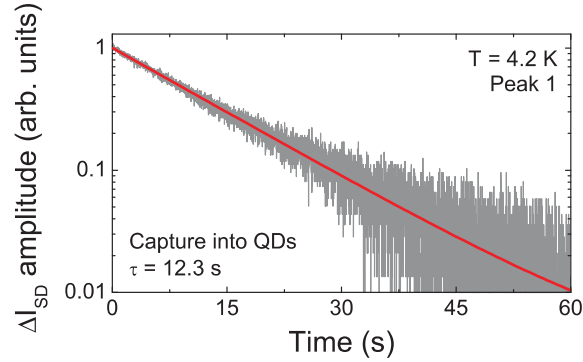


Figure 7.10: Sample B: Current transient for the tunneling capture of holes from the 2DHG into the QDs, corresponding to the first peak (at $V_g = 0.88$ V) in the density of states of the QD ensemble. The time constant can be directly extracted by a linear fit on a semi-logarithmic scale.

voltage range at which the peak structure occurs is reduced compared to Sample A due to the thicker tunneling barrier and the resulting change in the lever arm of the device. When the temperature is increased above 4.2 K, the peaks become less distinct, and vanish completely for temperatures above 70 K. Nevertheless, although the peak structure is not resolved anymore in the amplitudes at these temperatures, emission and capture transients can still be seen in the time-resolved measurements as tunneling still takes place between the QDs and the 2DHG. The reason for the smearing-out of the peak structure is related to the Maxwell-Boltzmann broadening of the Fermi function in the device, which makes the Fermi level less sharp and hence broadens the energetic resolution of the measurement. When comparing the measurement with the C-V measurements of Sample A, the graph is more noisy as the time constants are longer and the number of averages has to be reduced in order to reach reasonable measurement times.

The drop in the amplitude below a gate voltage of 0 V for curves above 50 K (Fig. 7.9[b]) comes from a drastic decrease in the time constants of the capture processes at these temperatures and gate biases. The tunneling capture into the upper levels of the QD ensemble becomes too fast and the transients shift out of the measurement time window, hence the amplitudes get smaller and decrease towards zero.

7.3.2 Emission and capture time constants

The time constants of the emission and capture processes in Sample B are well above the time constant related to the RC parasitics. Hence, the emission and capture transients directly resemble the tunneling emission and capture processes, and the time constants that are derived from the transients are the ones of the tunneling processes. The transients are mono-exponential and can easily be fitted with a linear fit on a semi-logarithmic scale as is shown for the capture transient belonging to peak 1 at a

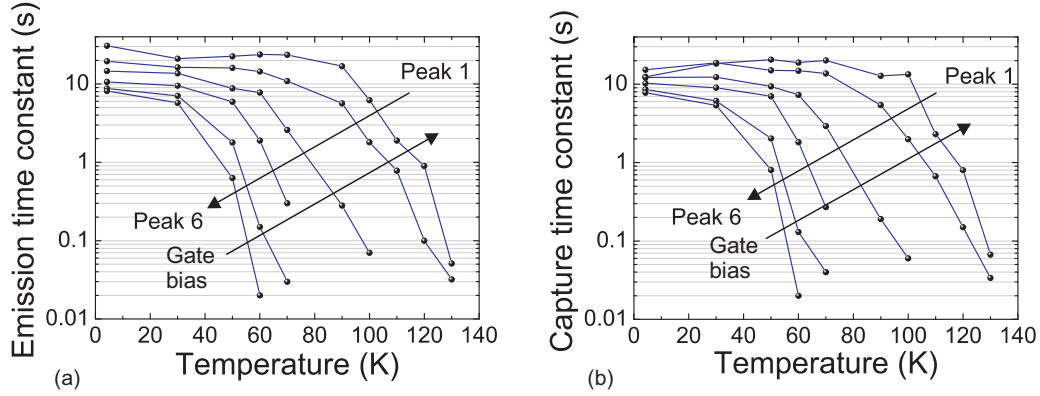


Figure 7.11: Sample B: (a) Emission and (b) capture time constants at the gate biases referring to the peak positions in the many-particle density of states of the QD ensemble versus the temperature. The emission and capture processes become faster due to enhanced thermally-assisted tunneling. It can clearly be seen that the upper levels (peaks with higher index) benefit much earlier from the additional thermal energy. This is due to the overall higher emission and capture probability (smaller barrier) for the upper levels. The lines are guides to the eye.

temperature of 4.2 K (see Fig. 7.10).

The emission and capture time constants for a set of different temperatures between 4.2 K and 130 K are shown in Fig. 7.11. From the temperature dependence of the time constants, the dominant emission and capture processes can be identified. As described in Chapter 3, the emission (capture) will always take place via the emission (capture) process with the highest rate. Thus, by adding thermal energy through increasing the temperature, it can be expected that the dominating process moves from a pure tunneling process to a thermally-assisted tunneling process [83, 93].

At 4.2 K up to 25 K, the emission and capture processes are independent of the temperature, and aside from some slight shifts due to noise, the time constants stay constant. However, due to the different height in the tunneling barrier which the holes from different energy levels have to tunnel through, the time constants decrease with an increasing number of holes (decreasing gate bias) in the QD ensemble. Hence, at low temperature, a pure tunneling process, which only depends on the barrier height and width, is observed. When increasing the temperature further to 50 K, the tunneling processes related to the first two peaks do not change their time constants, but the time constants related to the upper hole levels (peaks 3 to 6) start to decrease. As a result of the smaller tunnel barriers, the decrease of the time constants is more pronounced for the upper hole levels. The thermal energy is now large enough to increase the thermally-assisted tunneling rate for the upper levels, such that it becomes larger than the pure tunneling rate, and hence dominates the overall process. A further increase in temperature increases the negative slope $d\tau/dT$ with which the time constants change, as the contribution of the thermal energy to the emission and capture processes becomes more

Holes (peak no.) Δ	Level splitting (meV)	
	Sample B	8 band $\mathbf{k}\cdot\mathbf{p}$ theory
1-2	21 (± 1)	20.6
2-3	31 (± 1)	29.8
3-4	14 (± 1)	15.2
4-5	13 (± 2)	15.3
5-6	12 (± 2)	17.7

Table 7.2: Sample B: Energy level splittings of the many-particle hole states obtained using the equivalent circuit model with a quantum capacitance for the quantum region (QD ensemble and GaAs QW) at 4.2 K and values from 8 band- $\mathbf{k}\cdot\mathbf{p}$ theory. The errors are given in brackets and are mainly related to the uncertainty of the exact slope of the Gaussian for the density of states of the GaAs QW.

and more dominant. Finally, at temperatures around 70 K, the time constants for the processes related to the first two many-particle energy levels also begin to decrease. Hence, the processes for all energy levels, from the upper levels down to the ground state of the QDs, are based on thermally-assisted tunneling. In total, the graph shows a decrease of the time constants by three orders of magnitude for a temperature increase from 4.2 K to 130 K. Of course, all time constants will decrease further, but in this experiment the measurement time scales were limited to some 10 ms.

The reason for the constant time constants of the emission and capture processes from/into the ground state of the QD ensemble (peak 1) up to a temperature of about 70 K is that temperature effects become less important for larger tunneling barriers (due to the exponential dependence on the height of the barrier and the resulting very low thermal emission rate). In contrast, the higher many-particle energy levels (peaks 3 to 6) have smaller tunneling barriers, and hence thermally-assisted tunneling becomes more important for the emission and capture processes. Thus the time constants begin to decrease already at lower temperatures. The temperature effect can also be seen in Fig. 7.9(b), where the higher peaks (3 to 6) shift to higher gate voltages for increasing temperature, which means, the thermally-assisted tunneling shifts the tunneling path to slightly higher energies and the same density of states of the QDs is measured at a higher gate bias.

7.3.3 Many-particle level splittings

Similar to Sample A, the many-particle level splittings can be derived for Sample B. According to the similarity of the resulting curves derived for Sample A from the C-V and the current measurements in Fig. 7.6(b), the positions of the peaks in the density of states is assumed to be equal for both measurement methods. Hence, a capacitance simulation of the peak positions can be used to derive the peak positions in the density of states of QD ensemble for Sample B. The results of the iterative simulation are shown

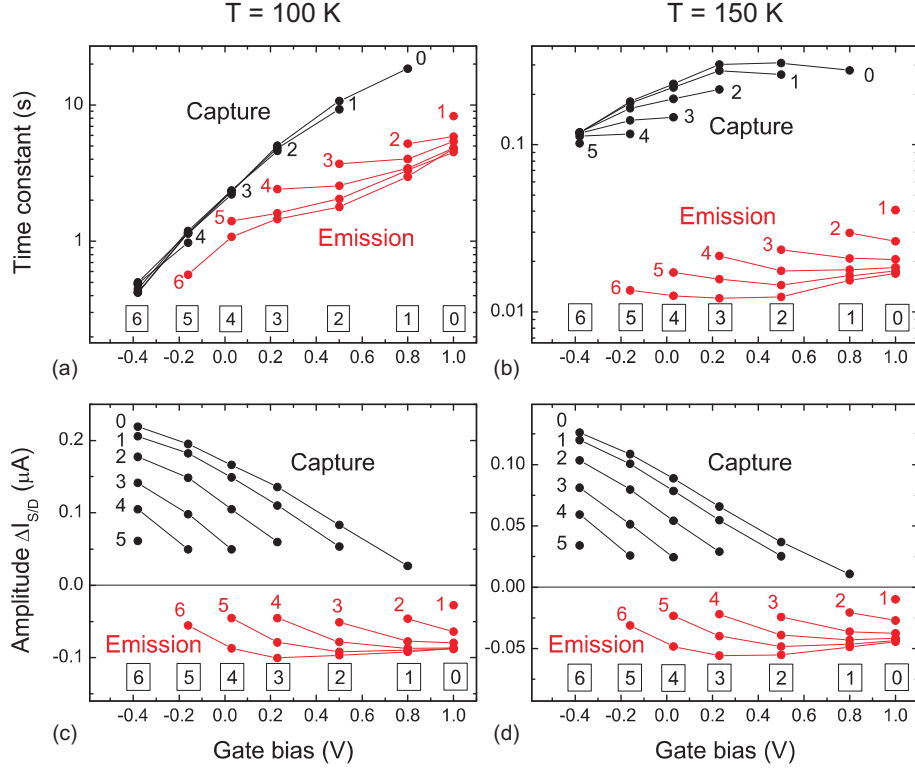


Figure 7.12: Sample B: Capture and emission processes for integer number of holes. The numbers indicate the initial number of holes in the QDs, while the boxed numbers indicate the final number of holes in the QDs. (a) Time constants of the capture and emission processes at 100 K. (b) Time constants of the capture and emission processes at 150 K. (c) Current amplitudes for the capture and emission processes at 100 K. (d) Current amplitudes for the capture and emission processes at 150 K.

in Table 7.2, again in comparison with the theoretical values derived from 8-band $\mathbf{k}\cdot\mathbf{p}$ theory.

The values derived for Sample B are about 1 meV larger than for Sample A. This might come from an uncertainty that derives from the analysis method, and the uncertainty that comes from the density of states of the GaAs QW, into which the QD layer is embedded. Nevertheless, within the error margins, the values are in good agreement with the theoretical values, except again (see Sample A) for the highest level splitting (peaks 5 and 6).

7.3.4 Emission and capture of integer number of holes

The time constants analyzed in Sect. 7.3.2 belonged to emission and capture processes related to the peak positions of the amplitude spectra (see for example Fig. 7.9[b]). As the peak positions in the amplitude spectra are known, the valleys in the curve resemble the gate voltages at which the QD ensemble is (on average) filled with an integer number of holes per QD. This allows to study the hole dynamics between different charge states

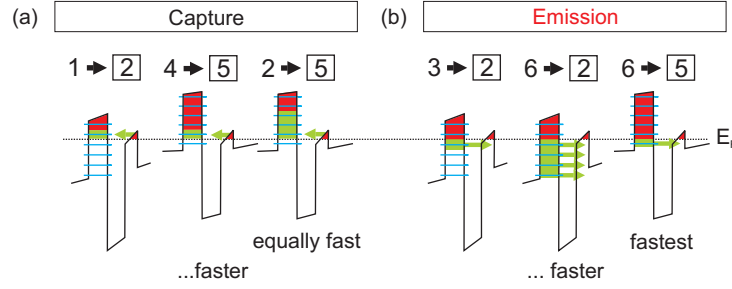


Figure 7.13: Sample B: Schematic explanation of the time constants as a consequence of the tunnel barrier height. (a) Capture processes at 100 K: only the final state is of importance as it determines the barrier height. (b) Emission processes: Initial and final state determine the time constant. The final state determines the tunneling barrier height and shape, while the initial state determines the occupation and hence the effective barrier height which each hole has to tunnel through.

of the QDs.

Therefore, the QDs are prepared setting the gate voltage to the value of the initial state, and after the steady-state hole occupation is reached, the gate voltage is set to the gate voltage of the final state, while simultaneously recording the capture or emission transient in the source-drain current. Then, the time constants and amplitudes are derived.

Figure 7.12 shows the time constants and the amplitudes related to the emission and capture processes between the (integer) charge states of the QD ensemble for two temperatures. At 100 K (Fig. 7.12[a]), the capture time constants depend only on the initial state and almost not on the final state. This can be understood if the height of the tunneling barrier at a given gate voltage is taken into account. If the final state is 5 holes inside the QDs, then the tunneling barrier height and shape is the same for the initial states of 4 holes and 2 holes (see Fig. 7.13[a]). Hence, the capture rate should also be comparable. If the gate voltage is decreased to set the final state to a smaller number of holes, the effective tunnel barrier height is also decreased. As a consequence, the tunneling time constant decreases from 11 s (1 hole in the final state) down to 0.5 s (6 holes in the final state).

When the temperature is increased to 150 K, the time constants for equal final states do change in dependence on the initial state (Fig. 7.12[b]). This is due to the additional thermal energy, which increases the rate for thermally-assisted capture, and hence increases the contribution to the overall capture rate. All capture time constants have decreased to some 0.1 s.

The emission time constants at 100 K show a different picture (Fig. 7.12[a]). Here, the initial state and the final state are of importance. The initial state is responsible for the energy level up to which the QDs are charged. The emission barrier for each additional hole becomes effectively smaller than for the previous hole (the degeneracy of the unoccupied states is lifted due to many-particle effects, and every hole has a

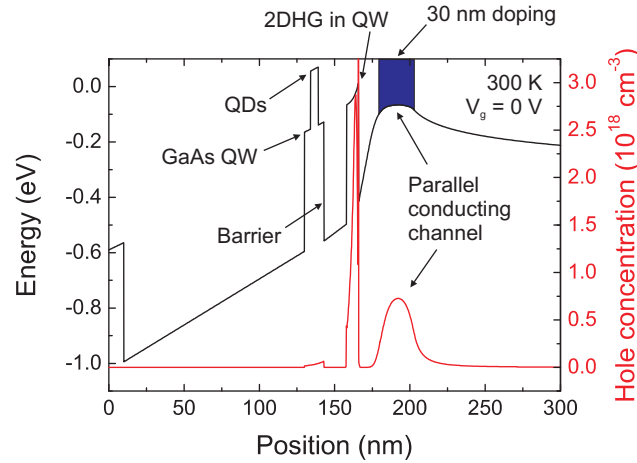


Figure 7.14: Sample C: Simulated valence bandstructure showing the formation of a parallel conducting channel at the position of the p -doped layer at a temperature of 300 K (becoming critical above ~ 260 K). This leads to charging and discharging effects between the 2DHG and the parallel channel, obscuring the detection of the QD dynamics. The simulation was done with Snider’s Poisson-Schrödinger Solver [159].

different emission barrier). Hence, the mean time constants decrease for an increasing number of holes in the QDs. The final state, again, has an influence on the tunneling barrier height and shape (see Fig. 7.13[b]). At 150 K, the influence of the barrier shape (and hence the contribution of the pure tunneling rate to the total rate) becomes less important as the thermal energy is increased and thermally-assisted tunneling becomes the dominating contribution to the total emission rate (Fig. 7.12[b]).

The source-drain current amplitudes are easier to interpret (Figs. 7.12[c] and 7.12[d]). If slight deviation (due to slightly different depletion of the 2DHG at different gate voltages) is neglected, the amplitudes depend only on the difference in the number of holes between the initial and the final state. This makes sense, as the number of holes that is transferred during the measurement is also proportional to the number of holes that is added or subtracted to/from the 2DHG. It should be noted that the amplitudes of the capture processes are larger than those of the emission of the same number of holes. A plausible explanation for this difference was not found. In general, the amplitudes decrease if the temperature is increased to 150 K. This comes from an increase in the scattering rate due to increased phonon population, and the decreasing hole localization within the 2DHG.

7.4 Sample C (15 nm tunnel barrier)

In this section Sample C is investigated. It has a total tunnel barrier width of 28 nm (15 nm $\text{Al}_{0.9}\text{Ga}_{0.1}\text{As}$ sandwiched between 5 nm and 8 nm GaAs on either side). The time constants of the thermally-assisted tunneling processes can hence be expected

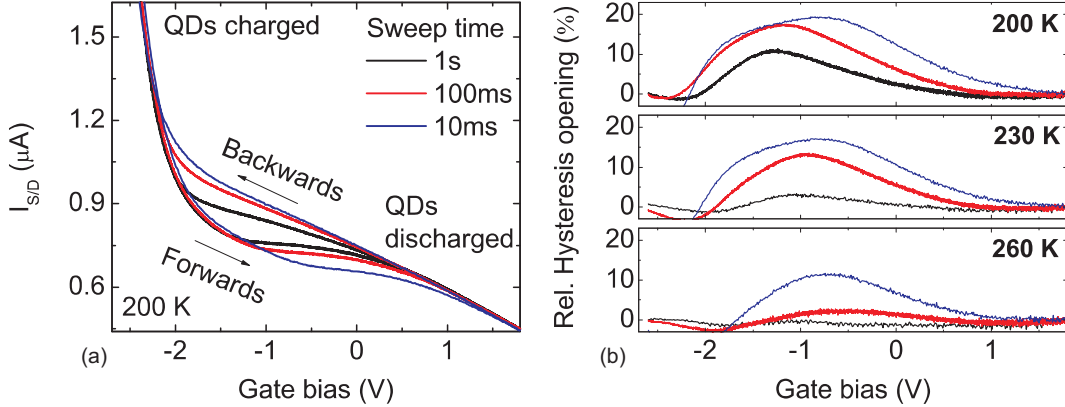


Figure 7.15: Sample C: (a) Hysteresis curves for three different sweep times at a temperature of 200 K. The curves are averaged from 10 identical measurements. (b) Relative hysteresis opening at three different temperatures. The values are derived with respect to the upper backwards path in the hysteresis curve.

to increase. However, the design of the sample structure is not suitable for room temperature operation. The reason is the formation of a parallel conducting channel [38] in the p-doped region of the structure (see Fig. 7.14). As the in-diffusion regions of Zn, which are needed to form the Ohmic source and drain contacts, do not have sharp edges and their penetrating depth in the device is not controllable to the extent of some nanometers, they also reach the p-doped layer. As a consequence, the total current through the 2DHG and the parallel channel at the position of the p-doped layer is measured when measuring the source-drain current. At low temperatures, the hole concentration is sufficiently low in the p-doped layer such that conductance through the parallel channel can be neglected. However, at higher temperatures (>250 K) the carrier density becomes critical. This leads to charging and discharging effects between the 2DHG and the parallel conducting channel whenever the gate voltage is changed. These processes obscure the transfer between the QDs and the 2DHG. Hence, time-resolved measurements cannot be conducted. Nevertheless, some information can be gained from hysteresis measurements.

7.4.1 Hysteresis measurements

A hysteresis can generally be seen, when the measurement cycle of sweeping the gate bias is shorter (or in the same range) than the emission and capture time constants of the thermally-assisted tunneling processes. The hysteresis of Sample C is measured by measuring the source/drain current ($V_{SD} = 20$ mV) while simultaneously sweeping the gate bias between -2.5 V and 1.75 V. The hysteresis curves for such a sweep are shown for three different sweep times in Fig. 7.15(a). The curves have been averaged from 10 identical measurements. Below -2.25 V, the QDs are fully charged and the hysteresis

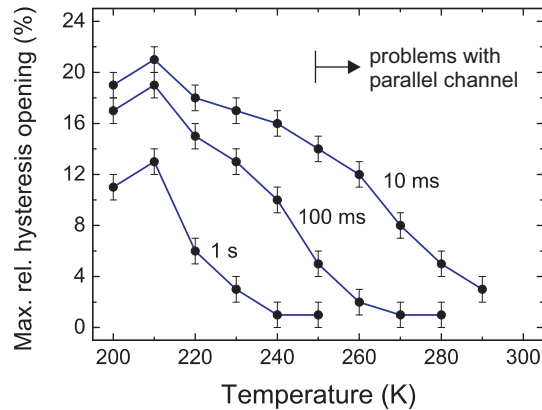


Figure 7.16: Sample C: Maximum relative hysteresis opening as function of the temperature. The sweep times are indicated next to the curves.

opening is closed. Above 1.5 V, the QDs are completely discharged. Depending on the direction of the voltage change, the upper path or the lower path in the curve is measured. When the sweep time is decreased from 1 s down to 10 ms, the hysteresis opening increases as the QDs have not been charged (backwards path) or discharged (forward path) by the same amount as before, and hence more holes are visible in the measurement. In general, it can also be observed, that the hysteresis opening is in a region which is at lower gate voltages as in Sample A and B, which is consistent with the increased lever arm due to the wider tunnel barrier in Sample C. The time constants for the emission and capture of all holes can hence be estimated to lie in the order of some ten milliseconds to seconds.

When increasing the temperature, the thermally-assisted tunneling processes become faster and the hysteresis decreases also (see Fig. 7.15[b]). The maximum relative³ hysteresis opening as a function of the temperature is shown in Fig. 7.16 for three different sweep times. The problems with the parallel conducting channel make the data above 250 K questionable and should only be seen as qualitative estimates. The maximum relative hysteresis opening for the shortest sweep time of 10 ms decreases from about 20 % at 200 K to 3 % at 290 K, which means the time constants around 300 K can be expected to be in the order of milliseconds.

7.5 Discussion

The results described in this chapter show that the 2DHG is an excellent detector for the charges in a QD layer. At low temperatures, the many-particle hole states of the QD ensemble can be detected with single charge resolution. The first two states can be discriminated even up to nitrogen temperature (77 K).

³The relative value is derived with respect to the backwards path in the hysteresis curve.

When analyzing the results with respect to the suitability of a 2DHG as detector, two possibilities have to be distinguished. The first, is the ability to detect the presence of holes inside the QD layer. As a result of the spatial confinement of the holes within the thin layer of the GaAs QW, in which the 2DHG is formed, the sensitivity is improved in contrast to an ordinary 3D back contact, where the extent and hence the edge of the contact varies with the applied gate voltage as a result of a change in the width of the depletion region. The detection of the presence of holes is in principle temperature-independent, hence a detection of the hole occupation in the QD layer is possible also at room temperature. The coupling due to the field effect is also used in the read-out process in ordinary Flash memories [15, 37].

The second possibility is the detection and discrimination of different many-particle hole levels in the QD ensemble. Here, low temperature is a prerequisite in order to obtain a steep Fermi function, which is sharp enough to discriminate the many-particle levels. At higher temperatures, the Fermi function becomes less steep and smears out, leading to a broadening of the measured many-particle levels. The peak structures observed in Sample A and Sample B vanish completely at temperatures above 100 K. A possible way to detect many-particle states even at higher temperatures could be to shrink the structure with respect to its dimensionality. If a 1D source-drain channel is used, the 1D density of states consists of a spike-like function for each energy level. If the channel is designed properly, the individual energy levels in the channel are sufficiently spaced apart, such that only one level is occupied (even at room temperature). This condition can be reached more easily in an electron system than in a hole system, due to the lower effective mass of electrons, which results in a larger level spacing in the 1D channel. If the channel is made sufficiently short, the number of QDs residing on top of the channel will also decrease drastically, which results in a discrete number of energy levels. Thinking further, the ultimate detector would be a 0D point-like detector (i.e. a very short 1D channel), through which charge carriers tunnel laterally from the source to the drain contact. Charges in a QD residing on top of the point-like channel would change the position of the energy levels of the channel, and hence inhibit the charge transport through the channel (Coulomb blockade). This principle is used for detection in single electron transistors (SET) [160–162].

The time-resolved measurements of the emission and capture processes of the three samples yielded a broad range of time constants at all temperatures, which is due to the different width of the tunnel barriers. Of particular interest are the time constants at room temperature, which are estimated to be in the millisecond range for Sample C, and can be expected to be orders of magnitude smaller for Samples A and B. If the time constant for Sample C is compared with the emission time constant (or storage time) of a similar material system (InAs QDs on GaAs with an additional $\text{Al}_{0.9}\text{Ga}_{0.1}\text{As}$ barrier), a large difference can be noticed. DLTS measurements yielded an emission

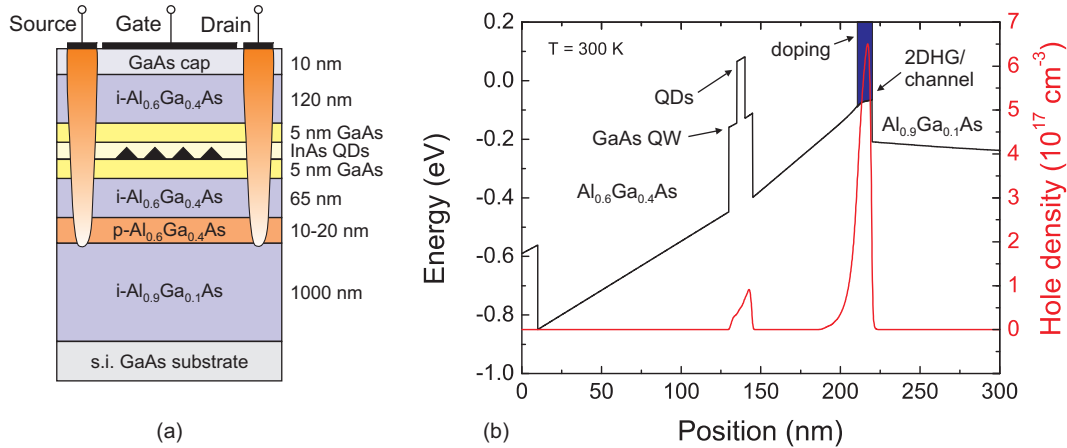


Figure 7.17: Alternative type of heterostructure avoiding the 2DHG QW. This way the capture process can take place directly from the band edge of the material surrounding the QDs. The simulation was done with Snider’s Poisson-Schrödinger Solver [159].

time constant (storage time) of 1.6 s at room temperature [27], which is 3 orders of magnitude larger than the value estimated for Sample C. The reason for this large deviance might be related to the tunnel barrier which was 20-nm-wide $\text{Al}_{0.9}\text{Ga}_{0.1}\text{As}$ in the DLTS sample, while it was only 15-nm-wide $\text{Al}_{0.9}\text{Ga}_{0.1}\text{As}$ in Sample C. Although, pure thermal emission should be independent of the width of the barrier, thermally-assisted tunneling strongly depends on it. If the tunnel barrier is narrower, the tunnel rate increases, and the intermediate energy level at which the thermally-activated holes tunnel through the barrier is lowered. This drastically increases the emission rate (and in case of Sample C also the capture rate). If the same storage times are to be reproduced in future experiments, the $\text{Al}_{0.9}\text{Ga}_{0.1}\text{As}$ barriers should be of a width of at least 20 nm in order to be able to directly compare the results to the DLTS measurements.

Geller *et al.* have studied the write time in InAs/GaAs QDs [28], and found the value to be in the nanosecond range. When comparing this value to the fastest capture time constants of Sample B and C (in Sample A the time constants are limited by the parasitics of the structure and cannot be used for comparison), the write time in [28] was at least three orders of magnitude smaller. The reason for this is the underlying physical process. In the sample studied in [28], the holes are captured directly from the valence band edge of the surrounding matrix material (i.e. GaAs). In the samples studied in this work, the holes are captured by tunneling or thermally-assisted tunneling starting from the 2DHG, which means in both cases they have to overcome a barrier in order to be captured into the QDs. This barrier inhibits the capture process and increases the time constants. In order to get faster capture times, the structure has to be altered in such a way, that hole capture directly from the band edge becomes possible. A structure

which could fulfill that requirement is shown schematically in Fig. 7.17. It is also based on a heterostructure, although it is avoiding the formation of a 2DHG within a QW. Instead, the channel is formed at the interface of a single heterostructure (in contrast to the double heterostructure of a QW). To create a conducting channel, the region close (between 10 to 20 nm) to the heterointerface is doped, while the rest of the device is nominally undoped. In such a structure, capture times in the range of picoseconds should be possible, as demonstrated before for band-edge-to-QD capture [75, 76]. Prerequisite for the design of such a structure is a sufficiently large band offset between the two materials. Additionally, the localization energy of the QDs has to be large enough to reach a sufficient storage time at room temperature. These requirements limit the possible choice of material systems.

The structure proposed in Fig. 7.17 would also solve the problem with the parallel conducting channel. An alternative solution would be to make the p-doped layer in Samples A, B, and C sufficiently small, such that the parallel channel can be neglected. Typically, this is done by incorporating just one single layer of dopant atoms, called δ -doping [163, 164].

7.6 Conclusion

The following conclusions can be drawn from the results of this chapter:

- A 2DHG is a sensitive detector to measure the many-particle hole level splittings of InAs QDs up to 77 K, and to determine the emission and capture time constants in time-resolved measurements over a wide range of temperatures.
- The sample structure used for Sample A, B, and C has a 30-nm-wide p-doped layer. In order to operate the 2DHG channel at room temperature which is required for a memory device, the doped layer should be changed to a δ -doping in order to avoid the formation of a parallel conducting channel.
- Another option to avoid the parallel conducting channel is to use a doped channel adjacent to a single heterostructure, instead of a double heterostructure quantum well. For the operation at 300 K, the band offset at the heterojunction needs to be sufficiently large to keep the charges in the channel at 300 K.
- The time constants determined for the emission and capture processes (as figure of merit for the erase and write times in a memory) are much larger than theoretically possible for a QD system. The reason is the tunnel emission and capture through the barrier. To reach time constants of some picoseconds for the capture process, the device needs to be designed in such a way, that direct capture from the band edge of the surrounding matrix material into the QDs becomes possible.

The erasing process could be enhanced by using a superlattice structure which allows resonant tunneling emission [24, 25].

- To reproduce the same storage times which were measured for QDs before (1.6 s at 300 K [27]), the tunnel barrier thickness should be increased to at least 20 nm.

Chapter 8

Summary and Outlook

The present thesis investigated two fields which are relevant for the improvement of a memory device based on self-organized quantum dots. First, the electronic properties of QDs were studied by DLTS. From the measurements on different material systems, the key parameters, such as the hole localization energy and the apparent capture cross section were extracted. They were used to extrapolate the hole storage time at room temperature and industry standard temperature. Second, the coupling between a layer of self-assembled QDs and a 2DHG was investigated for samples with different coupling constants.

To analyze the potential of GaSb/GaAs QDs for increasing the localization energy and hence the storage time in QDs, several samples from different groups were studied by DLTS (see Fig. 8.1). The maximum localization energy is reached in GaSb/GaAs QDs which are sandwiched between two $\text{Al}_{0.3}\text{Ga}_{0.7}\text{As}$ barriers. The maximum localization energy is $800(\pm 50)$ meV with an apparent capture cross section of $5 \cdot 10^{-12}$ cm^2 . Based on these values, a room temperature (300 K) storage time of 80 ms is calculated. At 358 K (85°C), this value decreases to 350 μs . Although the measured localization energy is larger than for QDs in previous work [27], the storage time has not increased. The reason for that is the apparent capture cross section which is about 2-3 orders of magnitude larger than for the QDs in [27].

Besides QDs, also GaSb/GaAs QRs were investigated for the first time with DLTS in this work. The localization energy is smaller than the one of the QDs, whereas the apparent capture cross section is comparable to those of the QDs. Also for the first time, QDs based on GaP were studied, where a mean activation energy of $450(\pm 20)$ meV with an apparent capture cross section of $2 \cdot 10^{-13}$ cm^2 was found.

Based on the results of this part of the work, the following recommendations on possible work in the future are given:

- *Increasing the Al content in the barrier.* To increase the total localization energy further, the Al content in the $\text{Al}_x\text{Ga}_{1-x}\text{As}$ barriers should be further increased

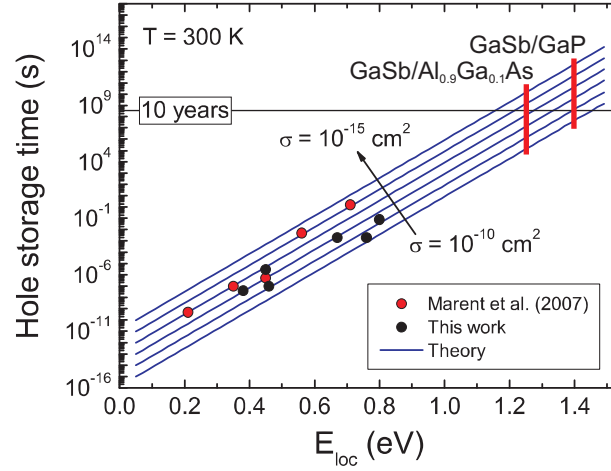


Figure 8.1: Room temperature hole storage times as function of the localization energy E_{loc} for the samples studied in this work and from previous work [27]. Predicted localization energies are given for GaSb/Al_{0.9}Ga_{0.1}As and GaSb/GaP QDs.

to values in the range of $x = 0.9$ (see Appendix F for details).

- *GaSb QDs in GaP.* A potential candidate for reaching non-volatility at 300 K is a heterostructure based on GaSb in GaP. Theoretically, a localization energy of ~ 1.4 eV is predicted for this material system. Introducing Al in the matrix would even further increase the total localization energy to values of up to ~ 1.9 eV (see Appendix F for details).
- *Nitride-based materials.* Although technologically less advanced, nitride-based materials (i.e. GaN/AlN) could also offer very large localization energies for electrons (~ 2 eV) [165,166].

For the second part of the thesis, C-V and time-resolved current measurements were performed on p-MODFETs with embedded layers of self-assembled InAs QDs. The measurements revealed the many-particle hole levels of the QD ensemble which were detected up to a temperature of ~ 77 K. Using time-resolved measurements, the time constants for the individual hole capture and emission processes were extracted and the underlying emission processes were identified. An equivalent circuit model allowed to extract the many-particle hole level splittings, which are in good agreement with values calculated by 8-band $\mathbf{k}\cdot\mathbf{p}$ theory.

Based on the results of this part of the work, the following recommendations on possible work in the future are given:

- *Downscaling.* The devices investigated in this work have a large gate area ($\sim \text{mm}^2$). This can lead to problems with the RC parasitics which makes the observation

of very fast processes impossible. The solution is to downscale the gate length to optimize the parasitics.

- *Optimized device design for room temperature operation.* At higher temperatures (>250 K), a parallel channel builds up at the position of the doping layer. With a smaller doping layer (ideally just a δ -doping) or the doping layer placed inside the channel, this could be avoided.
- *Non-equilibrium measurements.* The tunnel measurements in this work have always been close to the equilibrium situation of the device. Non-equilibrium measurements could be performed in order to study also the non-equilibrium many-particle spin states. This has been done electrically with similar devices for electron systems [130], but so far never for hole systems.

Appendix A

Storage time as a function of the localization energy

From the thermal emission rate for holes (see Sect. 3.1.3.1)

$$e_a = \gamma T^2 \sigma_\infty \exp\left(-\frac{E_{loc}}{kT}\right), \quad (\text{A.1})$$

the hole storage time ($1/e_a$) can be derived as a function of the localization energy E_{loc} using a semi-logarithmic scale, assuming a constant apparent capture cross section σ_∞ and a constant temperature T . The emission rate then solely depends on the exponential factor

$$\exp\left(-\frac{E_{loc}}{kT}\right). \quad (\text{A.2})$$

To obtain a linear fit on a semi-logarithmic scale of the form

$$y = 10^{A \cdot E_{loc} + B}, \quad (\text{A.3})$$

the following equation has to be solved

$$10^B \cdot \exp\left(-\frac{E_{loc}}{kT}\right) = 10^B \cdot 10^{A \cdot E_{loc}}, \quad (\text{A.4})$$

which yields

$$A = \frac{\log_{10}\left[\exp\left(-\frac{E_{loc}}{kT}\right)\right]}{E_{loc}}. \quad (\text{A.5})$$

With the law for logarithm conversion

$$\log_a(x) = \frac{\ln(x)}{\ln(a)}, \quad (\text{A.6})$$

one gets for the nominator of Eq. A.5

$$\log_{10} \left[\exp \left(-\frac{E_{loc}}{kT} \right) \right] = \frac{\ln \left[\exp \left(-\frac{E_{loc}}{kT} \right) \right]}{\ln(10)}, \quad (\text{A.7})$$

and

$$A = \frac{\ln \left[\exp \left(-\frac{E_{loc}}{kT} \right) \right]}{\ln(10) \cdot E_{loc}} = \frac{1}{\ln(10) \cdot kT} \approx \frac{1}{2.3 \cdot kT}. \quad (\text{A.8})$$

In words, Eq. A.8 expresses that if the localization energy E_{loc} is increased by $2.3 \cdot kT$, the storage time increases by a factor of 10, if the apparent capture cross section and the temperature are kept constant. At room temperature (300 K), a value of ~ 60 meV is derived. Values for other temperatures are shown in Fig. 3.5(b).

Appendix B

Experimental details - Setup

In the following sections the experimental setups for the DLTS measurements (Chapter 6), and the capacitance-voltage and current-voltage measurements (Chapter 7) are shown.

DLTS

The schematic setup used for the DLTS measurements in Chapter 6 is shown in Fig. B.1. The sample is placed in a cryostat, where either a continuous flow or a closed-cycle

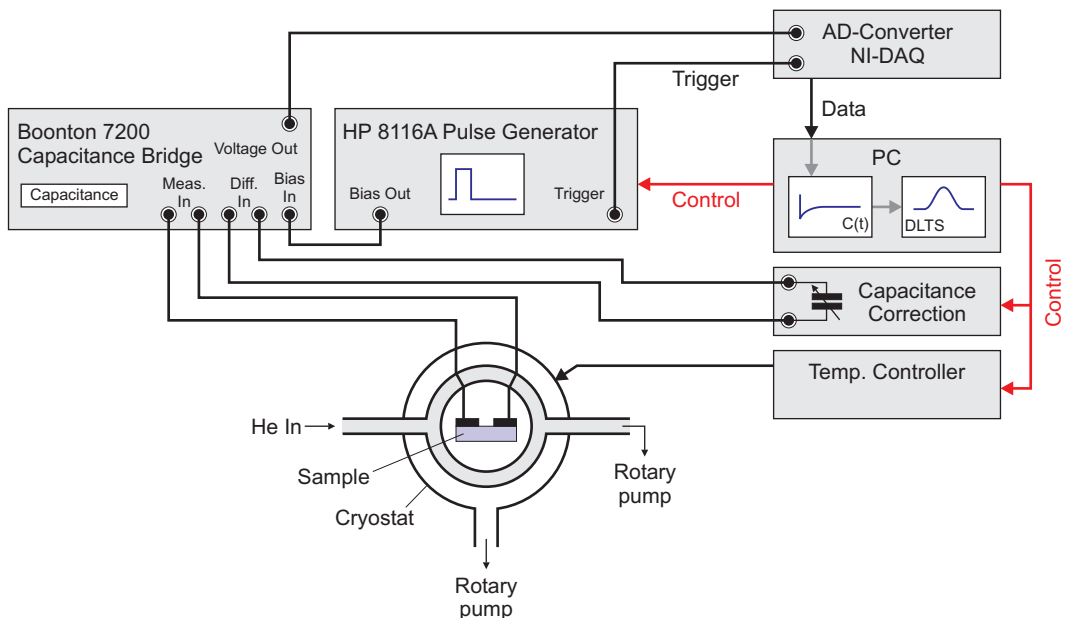


Figure B.1: Schematic setup for the conventional and charge-selective DLTS measurements. The emission process is recorded as a capacitance transient which is measured for different bias voltages at different temperatures. From the capacitance transients at different temperatures the DLTS graph is derived for a specific reference time constant.

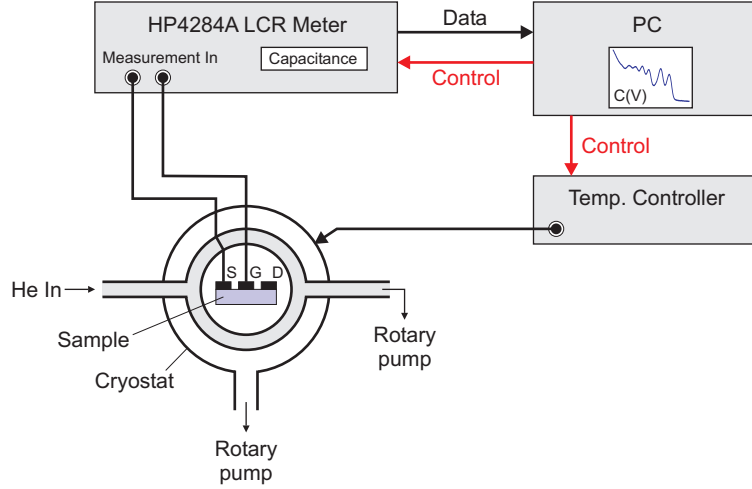


Figure B.2: Schematic setup for the capacitance-voltage (C-V) measurements. The capacitance is measured between the source and the gate contact while sweeping the gate voltage at different temperatures.

system is used. The capacitance is measured with a Boonton 7200 capacitance bridge. The measured capacitance is converted to an equivalent voltage which is measured by a NI-DAQ A/D-converter card. The external bias is provided by an HP8116A pulse generator. The charging pulse is fed through the capacitance bridge. In order to increase the resolution of the capacitance bridge during the measurement by using a smaller dynamic range, the capacitance is adjusted by a custom-built capacitance correction (a motor-controlled variable capacitor which adds or subtracts a constant offset to the diode capacitance), which is connected to the *Diff* port of the bridge. The pulse and the start of the measurement is triggered by a trigger pulse from the NI-DAQ. The hole setup is controlled by a personal computer (PC). The data coming from the A/D-converter is analyzed in the PC by a LabView program, where the recorded transient is filtered with the boxcar method in order to obtain the DLTS graphs.

Coupling between QDs and a 2DHG

The setup for the measurement of the capacitance of Sample A in Chapter 7 is shown in Fig. B.2. For the measurement at 4.2 K, the sample is dipped into a can with liquid Helium. For temperatures >4 K, the sample is put inside a continuous-flow cryostat, in which gaseous He is expanded in order to cool the sample. The measurement of the gate-source capacitance is performed with an HP4284A LCR meter, which also provides the bias voltage. The LRC meter and the temperature are controlled by a personal computer which also reads out the data.

The time-resolved current measurements are performed in the same cryostat, the

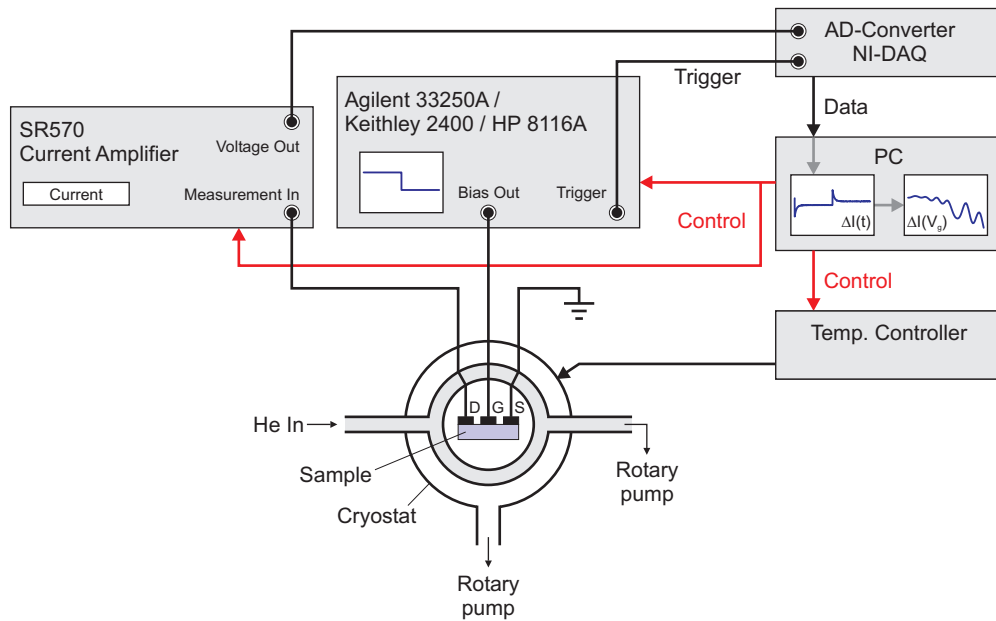


Figure B.3: Schematic setup for the time-resolved measurements of the current between the source and the drain contact at different temperatures. The gate voltage is changed periodically by applying a bias pulse. From the recorded emission and capture transients the individual many-particle charging peaks are derived.

schematic setup is shown in Fig. B.3. The source-drain current is measured by a Stanford Research SR570 current amplifier with the source contact connected to the cryostat chassis (grounded) and the measurement input connected to the drain contact. The gate voltage is set by an Agilent 33250A pulse generator for the fast pulses (Sample A) and a triggered Keithley 2400 source meter for the slow pulses (Sample B). For temperatures above 125 K, an HP8116A pulse generator is used. The current measured by the SR570 is converted to a voltage and then digitized by a National Instruments DAQ A/D-converter card. The charging and discharging pulses are triggered by a pulse from the NI-DAQ card. The recorded data is then analyzed on a personal computer (PC), which also controls the complete setup.

Appendix C

Samples

GaSb/GaAs QDs

- *Sample QD-A*
 - Real name: TW454
 - WL-A real name: TW455
 - Grown in the group of Shih-Yen Lin at the Research Center for Applied Sciences, Academia Sinica, Taiwan.
- *Sample QD-B*
 - Real name: A0441
 - WL-B real name: A0440
 - X-STM sample: A0415
 - Grown by R. J. Young and Manus Hayne at Lancaster University, United Kingdom.
 - X-STM measurements performed by E. P. Smakman in the group of P. M. Koentraad at Eindhoven University of Technology, the Netherlands.
- *Sample QD-C*
 - Real name: A-MEMA
 - Grown by Charles J. Reyner in the group of Diana L. Huffaker at University of California Los Angeles (UCLA), USA.
- *Sample QD-D*
 - Real name: TW737
 - Grown in the group of Shih-Yen Lin at the Research Center for Applied Sciences, Academia Sinica, Taiwan.

GaSb/GaAs QRs

- *Sample QR-A*
 - Real name: TW708
 - Grown in the group of Shih-Yen Lin at the Research Center for Applied Sciences, Academia Sinica, Taiwan.

In_{0.25}Ga_{0.75}As/GaAs/GaP QDs

- *Sample QD-GaP*
 - Real name: TU9739
 - GAAS-GaP real name: TU9738
 - PN-GaP real name: TU9737
 - Grown by Alexander Glacki and Gernot Stracke in the group of Dieter Bimberg at Technische Universität Berlin, Germany.

InAs QDs inside a MODFET structure

- *Sample A*
 - Real name: DO1880B
 - Grown by Innolume GmbH, Dortmund, Germany.
- *Sample B*
 - Real name: DO1881C
 - Grown by Innolume GmbH, Dortmund, Germany.
- *Sample C*
 - Real name: DO1882B
 - Grown by Innolume GmbH, Dortmund, Germany.

Appendix D

Sample Processing

The following two sections will briefly summarize the sample processing used to prepare the DLTS samples and the MODFET samples. All samples were processed at the Center of NanoPhotonics at Technische Universität Berlin.

DLTS samples

The DLTS samples based on GaAs are all processed according to the following recipes. After preparing the top Ohmic contact, the mesa structure is defined and etched wet-chemically. The Ohmic back contact is then defined on the highly-doped layer underneath the mesa structure.

1. Lithography and metallization of the Ohmic top contact
 - Sample Cleaning
 - Rinse sample 2× in Aceton on a hotplate at 76°C.
 - Rinse sample 2× in Isopropanol on a hotplate at 76°C.
 - Dry with N₂.
 - Lithography of top contact
 - Put sample on hotplate at 120°C for 5 min.
 - Spin on photoresist MaN-440 (at 2500 rpm for 35 s).
 - Put sample on hotplate at 90°C for 5 min.
 - Let sample cool down for 5 min.
 - Exposure with mask at 6 mW/cm² for 10 s.
 - Develop with MaD-532S for ca. 90 s.
 - Stop development with H₂O dip (2×) and DI water cascade.
 - Use plasma oxidation (150 W, 50 Pa, 76 ml/min O₂, 3 min) to remove remaining photoresist.

- Evaporation of top contact
 - 20:80 HCl/H₂O dip for 30 s.
 - DI water cascade.
 - Dry with N₂.
 - Metal evaporation:
 - * n-type (GaAs and GaP): 8 nm Ni, 100 nm Au-Ge(88:12), 300 nm Au
 - * p-type (GaAs): 30 nm Ti, 50 nm Pt, 300 nm Au
 - * p-type (GaP): 8 nm Ni, 100 nm Zn, 300 nm Au
 - Annealing at 400°C for 3 min in N₂ atmosphere.
- Lift-off
 - Lift-off remaining photoresist with remover.
 - Rinse sample 2× in Aceton on a hotplate at 76°C.
 - Rinse sample 2× in Isopropanol on a hotplate at 76°C.
 - Dry with N₂.

2. Wet etching of mesa (GaAs samples)

- Sample Cleaning
 - Same as above.
- Lithography of mesa structure
 - Put sample on hotplate at 120°C for 5 min.
 - Spin on photoresist MaP-1215 (at 3000 rpm for 35 s).
 - Put sample on hotplate at 100°C for 2 min.
 - Let sample cool down for 5 min.
 - Exposure with mask at 6 mW/cm² for 13 s.
 - Develop with MaD-331 for ca. 60 s.
 - Stop development with H₂O dip (2×) and DI water cascade.
 - Use plasma oxidation (150 W, 50 Pa, 76 ml/min O₂, 3 min) to remove remaining photoresist.
- Wet-chemical etching
 - Etch sample with 100 ml H₂O, 1 ml H₂SO₄, 8 ml H₂O₂ (100:1:8), the etch rate is approx. 7 nm/s.
 - Stop etching with 2× H₂O.
 - Dry with N₂.

- Check etch depth with profiler.
- Lift-off
 - Same as above.

3. Lithography and metallization of Ohmic back contact

- Same as for the top contact.

For the GaP samples the mesa etching is done with reactive ion etching (RIE).

- Lithography of mesa structure
 - Put sample on hotplate at 120°C for 5 min.
 - Spin on photoresist AZ-MIR701 (at 3000 rpm for 35 s).
 - Put sample on hotplate at 100°C for 2 min.
 - Let sample cool down for 5 min.
 - Exposure with mask at 6 mW/cm² for 35 s.
 - Develop with AZ351B for ca. 25 s.
 - Stop development with H₂O dip (2×) and DI water cascade.
 - Use plasma oxidation (150 W, 50 Pa, 76 ml/min O₂, 3 min) to remove remaining photoresist.
- Dry-etching of mesa
 - Use a dummy process first to check the etch rate and adjust the etch time (line 31) in recipe accordingly.
 - The following recipe¹ was used to etch the mesa in a Sentech Instruments GmbH ICP-RIE SI 500 reactor.

```

1 [Info]
2 Filetype=SENTECH Instruments SI Systems recipe file
3 Anlage=SI 500/D-2M TUB
4 Reaktor=2
5 [Lines]
6 0=DIM ZEIT AS INTEGER = 300
7 1=Druck Wafer Rücks.kühlung 1000,0 Pa
8 2=Wartezeit 10
9 3=Temperatur Elektrode 20,0 °C
10 4=Wartezeit 10
11 5=Gas ein MFC 3 5,0 sccm ' Ar
12 6=Gas ein MFC 1 20,0 sccm ' BC13
13 7=Reaktordruck 1,000 Pa
14 8=Quellen-Matching manuell 55,9
15 9=HF-Matching manuell 74,0

```

¹Developed by M. Stubenrauch at TU-Berlin.

```

16 10=Wartezeit 10
17 11=Quelle ein 300,0 W
18 12=Wartezeit 10
19 13=HF-Generator ein Bias -200,0 V
20 14=Quellen-Matching automatisch
21 15=HF-Matching automatisch
22 16=Wartezeit ZEIT
23 17=HF-Generator aus
24 18=Quelle aus
25 19=Gas aus MFC 3 ' Ar
26 20=Gas aus MFC 1 ' BC13
27 21=Reaktordruck 0,000 Pa
28 22=Wartezeit 20
29 23=Wafer aussch. ohne Belüftung
30 [Internal Lines]
31 0=Dim ZEIT As Integer = 300
32 1=OutAA AA_HED 1000.0 Pa
33 2=WZeit 10
34 3=OutAA AA_TEL 20.0 °C
35 4=WZeit 10
36 5=GasEin MFC 3 5.0 sccm ' Ar
37 6=GasEin MFC 1 20.0 sccm ' BC13
38 7=RxDruck 1.000 Pa
39 8=QMBMan 55.9
40 9=HFMBMan 74.0
41 10=WZeit 10
42 11=Qein 300.0 W
43 12=WZeit 10
44 13=HFein Bia -200.0 V
45 14=QMBAuto
46 15=HFMBAuto
47 16=WZeit ZEIT
48 17=HFaus
49 18=Qaus
50 19=GasAus MFC 3 ' Ar
51 20=GasAus MFC 1 ' BC13
52 21=RxDruck 0.000 Pa
53 22=WZeit 20
54 23=WafAusOB}

```

- Lift-off

- Same as above.

MODFET samples

1. Lithography and metallization of Ohmic contacts

- The lithography is the same as for the Ohmic contacts of the DLTS samples.
- Metallization:
 - p-type (to contact the 2DHG): 8 nm Ni, 200 nm Zn, 300 nm Au

- Annealing at 400°C for 3 min in N₂ atmosphere.
2. Lithography and evaporation of gate contact
 - The lithography is the same as for the Ohmic contacts of the DLTS samples.
 - Metallization:
 - Schottky contact: 8 nm Ni, 300 nm Au
 3. Wet etching of mesa
 - Lithography and etching is the same as for the mesa etching of the DLTS samples.
 - Note: If the Al-content is large in the Al_xGa_{1-x}As, the etch rate is faster.

Appendix E

DLTS: Error of graphical analysis

QD-A

The DLTS graph is analyzed manually by extracting the peak position for different reference time constants τ_{ref} . This graphical analysis is a source of error. To get an estimate of how large this error due to the graphical analysis by hand is, the same DLTS graph was analyzed $N = 16$ times for each reference time constant. For each of the 16 sets of sample values the activation energy E_a and the apparent capture cross section σ_∞ is derived.

The error analysis is shown representatively for the DLTS data of sample QD-A. The DLTS signal has its maximum value for a measurement bias of $V_m = 0.1$ V and its smallest value for $V_m = 3.9$ V (see Fig. 6.5). To get an estimate of the range of the error, the same data of these two sets are analyzed $N = 16$ times.

The histograms for the activation energies obtained for the same DLTS graph are shown in Fig. E.1 for the two parameter sets. The histogram for the logarithmized apparent capture cross section is shown in Fig. E.2.

Due to the analysis method¹, the derived activation energy and the apparent capture cross section are interconnected. This can be seen in Fig. E.3 (where the interconnection is expressed as a correlation coefficient r close to 1). This means, if a larger activation energy is derived from the analysis, it comes with a larger apparent capture cross section. Hence, the error values for the emission rate (and hence the storage time) derived from the activation energy and the apparent capture cross section according to Eq. 3.23 are much smaller than for the individual parameters, as the individual errors compensate each other due to the interconnection. This can be seen in Fig. E.4 for the logarithmized product of the exponential function $\exp(-E_a/(kT))$ and the apparent

¹The activation energy is derived from the slope of the Arrhenius plot. When the slope changes due to different data points, the intersection from which the apparent capture cross section is derived also changes.

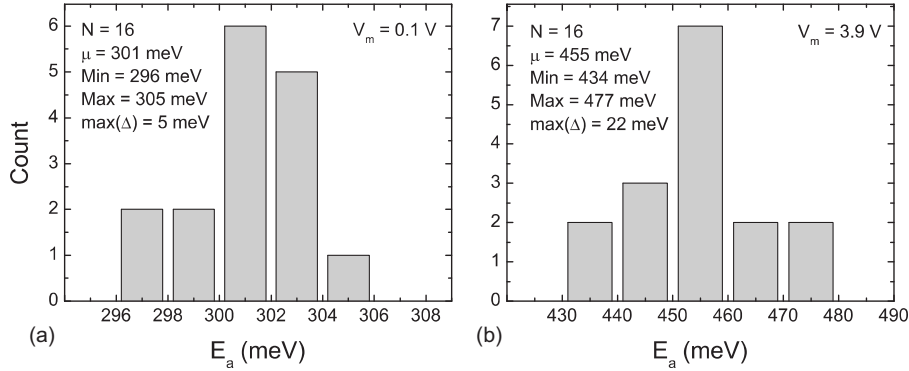


Figure E.1: Histograms of activation energies E_a obtained from graphical analysis of the DLTS graph for (a) $V_m = 0.1$ V and (b) $V_m = 3.9$ V.

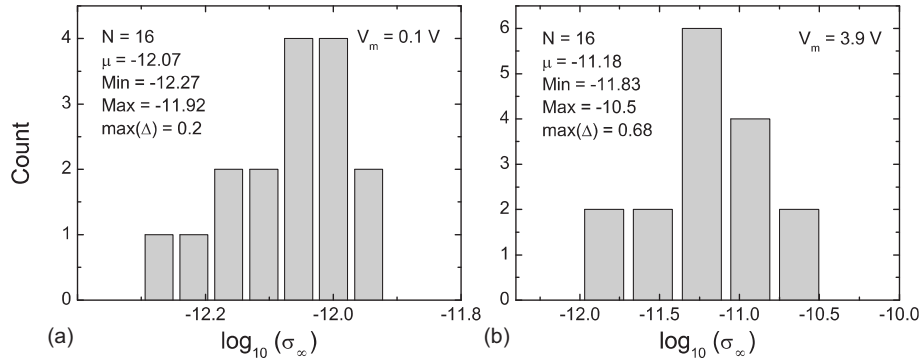


Figure E.2: Histograms of the logarithmized apparent capture cross sections σ_∞ obtained from graphical analysis of the DLTS graph for (a) $V_m = 0.1$ V and (b) $V_m = 3.9$ V.

capture cross section σ_∞ . The range of the determined values is much smaller.

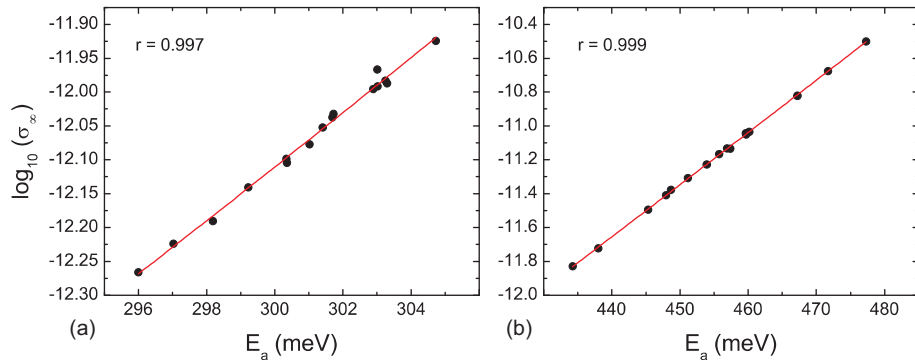


Figure E.3: Logarithmized apparent capture cross section σ_∞ versus the corresponding activation energy E_a determined $N = 16$ times for the same DLTS measurement (a) at $V_m = 0.1$ V and (b) at $V_m = 3.9$ V. The two parameters are interconnected (expressed in the correlation coefficient r which is given in the graphs).

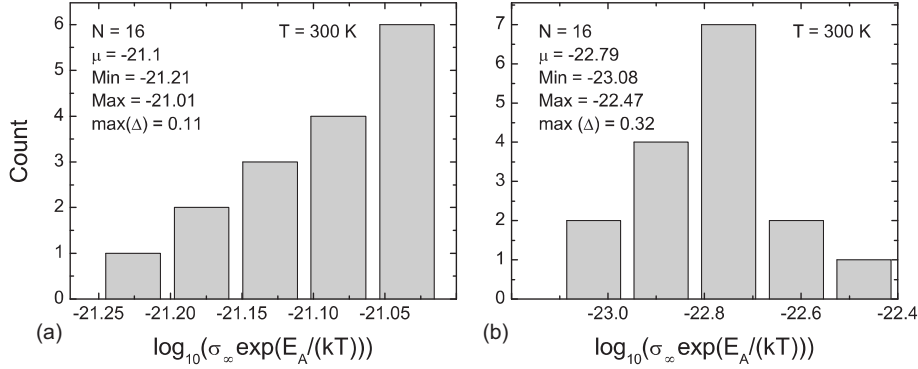


Figure E.4: Logarithmized product of the exponential term and the apparent capture cross section used to get an estimate for the error margin of the emission rate and the storage time.

In order to get quantitative numbers of the error, the mean value and the maximum and minimum values of the activation energy, the apparent capture cross sections, and the logarithmized product $\exp(-E_a/(kT)) \cdot \sigma_\infty$ are extracted for $V_m = 0.1$ V and $V_m = 3.9$ V. The mean value resembles the best estimate, while the deviation resembles the uncertainty [148]. The values are listed in Table E.1 and Table E.2, respectively.

As expected from the signal of the DLTS graphs, the error is larger for $V_m = 3.9$ V

Parameter	Mean value	Min	Max	$max(\Delta)$
E_a	301 meV	296 meV	305 meV	5 meV
$\log_{10}(\sigma_\infty)$	-12.07	-12.27	-11.92	0.2
$\log_{10}(\sigma_\infty \exp(-E_a/(k \cdot 300 K)))$	-21.1	-21.21	-21.01	0.11

Table E.1: QD-A: The DLTS graphs are analyzed $N = 16$ times. Mean, minimum and maximum values, and the maximum deviation from the mean value for a measurement bias of $V_m = 0.1$ V. The $max(\Delta)$ is assumed as error margin.

Parameter	Mean value	Min	Max	$max(\Delta)$
E_a	455 meV	434 meV	477 meV	22 meV
$\log_{10}(\sigma_\infty)$	-11.18	-11.83	-10.5	0.68
$\log_{10}(\sigma_\infty \exp(-E_a/(k \cdot 300 K)))$	-22.79	-23.08	-22.47	0.32
$\log_{10}(\sigma_\infty \exp(-E_a/(k \cdot 358 K)))$	-17.56	-17.91	-17.19	0.37

Table E.2: QD-A: The DLTS graphs are analyzed $N = 16$ times. Mean, minimum and maximum values, and the maximum deviation from the mean value for a measurement bias of $V_m = 3.9$ V. The $max(\Delta)$ is assumed as error margin.

as compared to the values at $V_m = 0.1$ V. As the localization energy of the QDs is derived from the last measured DLTS graph, the localization energy for QD-A is $455(\pm 22)$ meV. Hence, the relative error is about 5 %. The corresponding apparent

capture cross section is $\sigma_\infty = 7 \cdot 10^{-12} \text{ cm}^2$. The apparent capture cross section can be derived within an error margin of 0.7 orders of magnitude. According to Eq. 3.23, the storage time is then $\tau = 86 \text{ ns}$ with an error margin of 0.3 orders of magnitude. This error margin means, that the storage time τ could also be half or double the value. The final values and uncertainties rounded to significant digits [148] for QD-A are then

- $E_{loc} = 460(\pm 20) \text{ meV}$.
- $\sigma_\infty = 7 \cdot 10^{-12} \text{ cm}^2$ (with an uncertainty of 0.7 orders of magnitude)
- $\tau(300 \text{ K}) = 100 \text{ ns}$ (with an uncertainty of 0.3 orders of magnitude)
- $\tau(358 \text{ K}) = 4 \text{ ns}$ (with an uncertainty of 0.4 orders of magnitude)

QD-B

With the same method, the errors of the other samples are analyzed. The results of the error analysis of the charge-selective DLTS measurement of QD-B at a measurement bias of $V_m = 1.6 \text{ V}$ are listed in Table E.3.

Parameter	Mean value	Min	Max	$max(\Delta)$
E_a	674 meV	664 meV	687 meV	13 meV
$\log_{10}(\sigma_\infty)$	-11.84	-12.01	-11.61	0.23
$\log_{10}(\sigma_\infty \exp(-E_a/(k \cdot 300 \text{ K})))$	-23.1	-23.12	-23.09	0.02
$\log_{10}(\sigma_\infty \exp(-E_a/(k \cdot 358 \text{ K})))$	-21.29	-21.33	-21.24	0.05

Table E.3: QD-B: The DLTS graphs are analyzed $N = 16$ times. Mean, minimum and maximum values, and the maximum deviation from the mean value for a measurement bias of $V_m = 1.6 \text{ V}$. The $max(\Delta)$ is assumed as error margin.

The final values and uncertainties rounded to significant digits [148] for QD-B are then

- $E_{loc} = 670(\pm 10) \text{ meV}$
- $\sigma_\infty = 1 \cdot 10^{-12} \text{ cm}^2$ (with an uncertainty of 0.2 orders of magnitude)
- $\tau(300 \text{ K}) = 300 \mu\text{s}$ (with an uncertainty of 0.02 orders of magnitude)
- $\tau(358 \text{ K}) = 30 \mu\text{s}$ (with an uncertainty of 0.05 orders of magnitude)

If the $\text{Al}_{0.1}\text{Ga}_{0.9}\text{As}$ barrier is subtracted ($\Delta E_{VB} = 54 \text{ meV}$) the following values are obtained

- $E_{loc} = 615(\pm 10)$ meV
- $\sigma_{\infty} = 1 \cdot 10^{-12}$ cm² (with an uncertainty of 0.2 orders of magnitude)
- $\tau(300\text{ K}) = 300$ μ s (with an uncertainty of 0.02 orders of magnitude)
- $\tau(358\text{ K}) = 5$ μ s (with an uncertainty of 0.05 orders of magnitude)

QD-C

The results of the error analysis for the last parameter set of QD-C at a measurement bias of $V_m = 2.2$ V are listed in Table E.4. The final values and uncertainties rounded

Parameter	Mean value	Min	Max	$max(\Delta)$
E_a	755 meV	743 meV	770 meV	15 meV
$\log_{10}(\sigma_{\infty})$	-10.37	-10.57	-10.1	0.27
$\log_{10}(\sigma_{\infty} \exp(-E_a/(k \cdot 300\text{ K})))$	-22.98	-23	-22.96	0.02
$\log_{10}(\sigma_{\infty} \exp(-E_a/(k \cdot 358\text{ K})))$	-20.95	-21	-20.89	0.06

Table E.4: QD-C: The DLTS graphs are analyzed $N = 16$ times. Mean, minimum and maximum values, and the maximum deviation from the mean value for a measurement bias of $V_m = 2.2$ V. The $max(\Delta)$ is assumed as error margin.

to significant digits [148] for QD-C are then

- $E_{loc} = 760(\pm 20)$ meV
- $\sigma_{\infty} = 5 \cdot 10^{-11}$ cm² (with an uncertainty of 0.3 orders of magnitude)
- $\tau(300\text{ K}) = 2$ ms (uncertainty 0.02 orders of magnitude)
- $\tau(358\text{ K}) = 10$ μ s (uncertainty 0.06 orders of magnitude)

QD-D

The results of the error analysis for the last two parameter sets of the charge-selective DLTS measurements for QD-D are shown in Table E.5 and Table E.6. As the activation energy for $V_m = 2.8$ V is larger and the uncertainty is smaller, this value is taken as the localization energy. As the uncertainty margin of the measurement at $V_m = 3$ V overlaps with the value of the localization energy, there is no discrepancy. The final values and uncertainties rounded to significant digits [148] for QD-D are then

Parameter	Mean value	Min	Max	$max(\Delta)$
E_a	803 meV	757 meV	837 meV	46 meV
$\log_{10}(\sigma_\infty)$	-11.33	-12.1	-10.75	0.77
$\log_{10}(\sigma_\infty \exp(-E_a/(k \cdot 300 K)))$	-24.75	-24.75	-24.74	0.01
$\log_{10}(\sigma_\infty \exp(-E_a/(k \cdot 358 K)))$	-22.58	-22.71	-22.48	0.13

Table E.5: QD-D: The DLTS graphs are analyzed $N = 16$ times. Mean, minimum and maximum values, and the maximum deviation from the mean value for a measurement bias of $V_m = 2.8$ V. The $max(\Delta)$ is assumed as error margin.

Parameter	Mean value	Min	Max	$max(\Delta)$
E_a	745 meV	683 meV	831 meV	86 meV
$\log_{10}(\sigma_\infty)$	-12.4	-13.43	-10.97	1.43
$\log_{10}(\sigma_\infty \exp(-E_a/(k \cdot 300 K)))$	-24.85	-24.87	24.82	0.03

Table E.6: QD-D: The DLTS graphs are analyzed $N = 16$ times. Mean, minimum and maximum values, and the maximum deviation from the mean value for a measurement bias of $V_m = 3$ V. The $max(\Delta)$ is assumed as error margin.

<ul style="list-style-type: none"> • $E_{loc} = 800(\pm 50)$ meV. • $\sigma_\infty = 5 \cdot 10^{-12}$ cm² (with an uncertainty of 0.8 orders of magnitude) • $\tau(300 K) = 80$ ms (with an uncertainty of 0.01 orders of magnitude) • $\tau(358 K) = 350$ μs (with an uncertainty of 0.1 orders of magnitude)

If the $Al_{0.3}Ga_{0.7}As$ barrier is subtracted, the following values are derived

<ul style="list-style-type: none"> • $E_{loc} = 640(\pm 50)$ meV. • $\sigma_\infty = 5 \cdot 10^{-12}$ cm² (with an uncertainty of 0.8 orders of magnitude) • $\tau(300 K) = 150$ μs (with an uncertainty of 0.01 orders of magnitude) • $\tau(358 K) = 2$ μs (with an uncertainty of 0.1 orders of magnitude)

QR-A

The results of the error analysis for the last parameter set of QR-A (QRs) at a measurement bias of $V_m = 2$ V are listed in Table E.7. The final values and uncertainties rounded to significant digits [148] for QR-A are then

Parameter	Mean value	Min	Max	$max(\Delta)$
E_a	377 meV	372 meV	383 meV	6 meV
$\log_{10}(\sigma_\infty)$	-12.17	-12.33	-11.99	0.18
$\log_{10}(\sigma_\infty \exp(-E_a/(k \cdot 300 K)))$	-18.47	-18.54	-18.39	0.08
$\log_{10}(\sigma_\infty \exp(-E_a/(k \cdot 358 K)))$	-17.45	-17.54	-17.35	0.1

Table E.7: QR-A: The DLTS graphs are analyzed $N = 16$ times. Mean, minimum and maximum values, and the maximum deviation from the mean value for a measurement bias of $V_m = 2$ V. The $max(\Delta)$ is assumed as error margin.

- $E_{loc} = 380(\pm 10)$ meV
- $\sigma_\infty = 8 \cdot 10^{-13}$ cm² (with an uncertainty of 0.2 orders of magnitude)
- $\tau(300 K) = 40$ ns (with an uncertainty of 0.08 orders of magnitude)
- $\tau(358 K) = 3$ ns (with an uncertainty of 0.1 orders of magnitude)

QD-GaP

The results of the error analysis for the conventional DLTS measurement of QD-GaP (GaP) at a measurement bias of $V_m = 4$ V are listed in Table E.8. The final values and

Parameter	Mean value	Min	Max	$max(\Delta)$
E_a	449 meV	434 meV	473 meV	24 meV
$\log_{10}(\sigma_\infty)$	-12.73	-13.14	-12.11	0.61
$\log_{10}(\sigma_\infty \exp(-E_a/(k \cdot 300 K)))$	-20.23	-20.43	-20	0.23
$\log_{10}(\sigma_\infty \exp(-E_a/(k \cdot 358 K)))$	-19.02	-19.25	-18.72	0.3

Table E.8: QD-GaP: The DLTS graphs are analyzed $N = 16$ times. Mean, minimum and maximum values, and the maximum deviation from the mean value for a measurement bias of $V_m = 4$ V. The $max(\Delta)$ is assumed as error margin.

uncertainties rounded to significant digits [148] for QD-GaP are then

- $E_{loc} = 450(\pm 20)$ meV
- $\sigma_\infty = 2 \cdot 10^{-13}$ cm² (with an uncertainty of 0.6 orders of magnitude)
- $\tau(300 K) = 3$ μ s (with an uncertainty of 0.2 orders of magnitude)
- $\tau(358 K) = 100$ ns (with an uncertainty of 0.3 orders of magnitude)

Appendix F

Extrapolation of storage times

This Appendix describes the extrapolation of the hole localization energies and storage times for two heterostructures: GaSb/ $\text{Al}_x\text{Ga}_{1-x}\text{As}$ and GaSb $_x\text{P}_{1-x}$ / $\text{Al}_y\text{Ga}_{1-y}\text{P}$. Both of them are potentially interesting for reaching large hole localization energies and long storage times in QDs at room temperature and at industry standard temperature (358 K).

Figure F.1 shows the hole localization energies for GaSb/ $\text{Al}_x\text{Ga}_{1-x}\text{As}$ QDs extrapolated from the values obtained in this work for GaSb/GaAs QDs and an additional $\text{Al}_x\text{Ga}_{1-x}\text{As}$ barrier according to the GaAs/ $\text{Al}_x\text{Ga}_{1-x}\text{As}$ valence band offset found in [35]:

$$E_{loc}^{total} = E_{loc}^{QDs} + \Delta E_{VB}^{GaAs/AlAs} \cdot x = E_{loc}^{QDs} + 0.54 \text{ eV} \cdot x. \quad (\text{F.1})$$

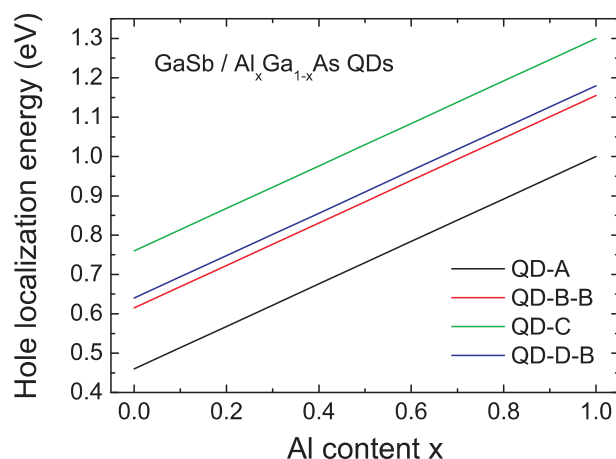


Figure F.1: Hole localization energies for GaSb/ $\text{Al}_x\text{Ga}_{1-x}\text{As}$ QDs extrapolated from the values obtained in this work for GaSb/GaAs QDs and an additional $\text{Al}_x\text{Ga}_{1-x}\text{As}$ barrier according to the GaAs/ $\text{Al}_x\text{Ga}_{1-x}\text{As}$ valence band offset found in [35].

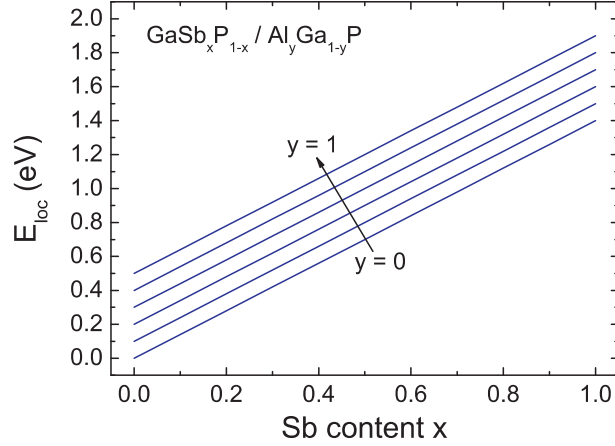


Figure F.2: Extrapolated hole localization energies of $\text{GaSb}_x\text{P}_{1-x}/\text{Al}_y\text{Ga}_{1-y}\text{P}$ QDs. The lines represent different Al contents in steps of 0.2. For 100 % Al the localization energy increases by 500 meV. The extrapolation is based on the GaSb/GaP value taken from [25].

The maximum values that can be achieved are between 1 eV and 1.3 eV, depending on the localization energy of the GaSb/GaAs QDs that is taken as basis of the extrapolation. The theoretical localization energies for the ternary combinations of $\text{GaSb}_x\text{P}_{1-x}/\text{Al}_y\text{Ga}_{1-y}\text{P}$ are extrapolated based on the value of 1.4 eV for the localization energy of GaSb/GaP QDs [25], a linear interpolation between GaSb and GaP , and a linear interpolation of the valence band offset of between GaP and AlP (0.5 eV):

$$E_{loc}^{total} = E_{loc}^{QDs} \cdot x + \Delta E_{VB}^{GaP/AlP} \cdot y = 1.4 \text{ eV} \cdot x + 0.5 \text{ eV} \cdot y. \quad (\text{F.2})$$

The extrapolated hole localization energies for different combinations of x and y are shown in Fig. F.2. Based on the predicted localization energies, the storage times can be calculated and are shown for the apparent capture cross sections of $\sigma_{\infty} = 10^{-11} \text{ cm}^2$ and $\sigma_{\infty} = 10^{-14} \text{ cm}^2$ at 300 K in Fig. F.3, and at 358 K (85°C) in Fig. F.4. For various combinations of x and y non-volatility can be reached. However, at the industry-standard temperature of 358 K (85°C) and a large apparent capture cross section, 10 years of storage time are achieved only for very large Sb and Al contents (Fig. F.4[a]).

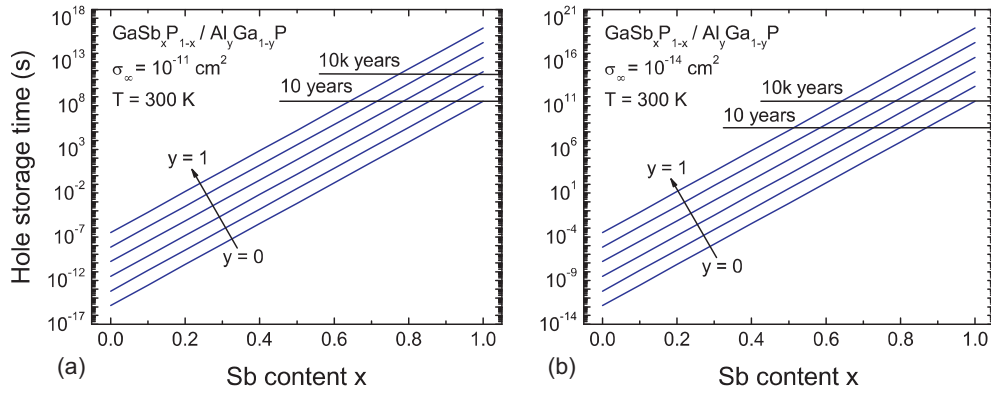


Figure F.3: Extrapolated hole storage times in $\text{GaSb}_x\text{P}_{1-x}/\text{Al}_y\text{Ga}_{1-y}\text{P}$ QDs based on the values from Fig. F.2 at 300 K. (a) Using an apparent capture cross section of $\sigma_\infty = 10^{-11}\text{ cm}^2$. (b) Using an apparent capture cross section of $\sigma_\infty = 10^{-14}\text{ cm}^2$.

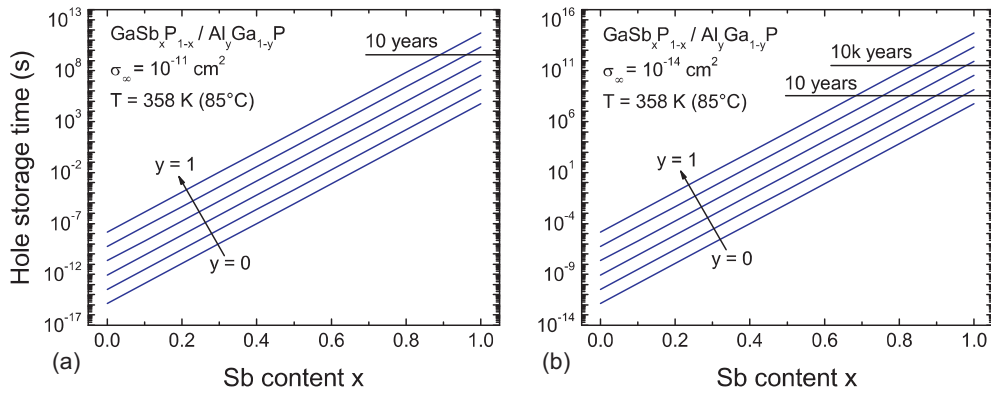


Figure F.4: Extrapolated hole storage times in $\text{GaSb}_x\text{P}_{1-x}/\text{Al}_y\text{Ga}_{1-y}\text{P}$ QDs based on the values from Fig. F.2 at 358 K (85°C). (a) Using an apparent capture cross section of $\sigma_\infty = 10^{-11}\text{ cm}^2$. (b) Using an apparent capture cross section of $\sigma_\infty = 10^{-14}\text{ cm}^2$.

Bibliography

- [1] J. Bardeen and W. H. Brattain, The transistor, a semiconductor triode, *Phys. Rev.* **74**, 230 (1948).
- [2] J. Bardeen and W. H. Brattain, *Three-electrode circuit element utilizing semiconductive materials*, *US Patent No. 2,524,035* (1950).
- [3] W. Shockley, *Circuit element utilizing semiconductive material*, *US Patent No. 2,569,347* (1951).
- [4] J. S. Kilby, *Miniaturized electronic circuits*, *US Patent No. 2,524,035* (1964).
- [5] Z. I. Alferov and R. F. Kazarinov, Semiconductor laser with electric pumping, Inventor's certificate No. 181737 (in Russian), 1963.
- [6] H. Kroemer, A proposed class of hetero-junction injection lasers, *Proceedings of the IEEE* **51**(12), 1782 (1963).
- [7] J. Gantz and D. Reinsel, *Extracting Value from Chaos*, IDC iView (2011).
- [8] J. Gantz and D. Reinsel, *The Digital Universe Decade - Are You Ready?*, IDC iView (2010).
- [9] T. Noyes and W. E. Dickinson, Engineering Design of a Magnetic-Disk Random-Access Memory, AIEE-IRE '56 (Western) Papers presented at the February 7-9, 1956, joint ACM-AIEE-IRE western computer conference , 42-44 (1956).
- [10] R. E. Fontana, S. R. Hetzler, and G. Decad, *Tape Based Magnetic Recording: Technology Landscape Comparisons with Hard Disk Drive and Flash Roadmaps*, IBM White Paper (2011).
- [11] G. E. Moore, Cramming more components onto integrated circuits, *Electronics* **38**(8) (1965).
- [12] *International Technology Roadmap for Semiconductors (ITRS) - 2009 Edition*, (2009).

-
- [13] R. Waser, *Nanoelectronics and Information Technology*, Wiley-VCH, Berlin, 2003.
- [14] R. Waser, *Nanotechnology Volume 3: Information Technology I*, Nanotechnology, Wiley-VCH, Weinheim, 2008.
- [15] R. Bez, E. Camerlenghi, A. Modeli, and A. Visconti, Introduction to Flash Memory, Proceedings of the IEEE **91**(4) (2003).
- [16] J. E. Brewer and M. Gill, *Nonvolatile Memory Technologies with Emphasis on Flash*, John Wiley Sons, Inc. Hoboken, New Jersey, 2008.
- [17] B. Beard, SSD Moving into the Mainstream as PCs Go 100 percent Solid State, Computer Technology Review, Samsung Semiconductor Inc. (2009).
- [18] B. Panzer-Steindel, Technology, Market and Cost Trends 2012, CERN IT Paper (2012).
- [19] L. Geppert, The new indelible memories - It's a three-way race in the multibillion-dollar memory sweepstakes, IEEE Spectrum **40**(3), 48–54 (2003).
- [20] D. Bimberg, M. Grundmann, and N. N. Ledentsov, *Quantum Dot Heterostructures*, John Wiley & Sons, Chichester, 1998.
- [21] D. Bimberg, editor, *Semiconductor Nanostructures*, Springer, Berlin Heidelberg, 2008.
- [22] M. Geller, A. Marent, and D. Bimberg, *Speicherzelle und Verfahren zum Speichern von Daten (Memory cell and method for storing data)*, International patent EP/2097904, 2006.
- [23] A. Marent, T. Nowozin, J. Gelze, F. Luckert, and D. Bimberg, Hole-based memory operation in an InAs/GaAs quantum dot heterostructure, Appl. Phys. Lett. **95**, 242114 (2009).
- [24] A. Marent, M. Geller, T. Nowozin, and D. Bimberg, *Speicherzelle auf Basis von Nanostrukturen aus Verbindungshalbleitern*, International patent application PCT/12/970,744, 2010.
- [25] A. Marent, *Entwicklung einer neuartigen Quantenpunkt-Speicherzelle*, Dissertation, Technische Universität Berlin, 2010.
- [26] A. Marent, T. Nowozin, M. Geller, and D. Bimberg, The QD-Flash: a quantum dot-based memory device, Semicond. Sci. Technol. **26**, 014026 (2011).

- [27] A. Marent, M. Geller, A. Schliwa, D. Feise, K. Pötschke, D. Bimberg, N. Akçay, and N. Öncan, 10^[sup 6] years extrapolated hole storage time in GaSb/AlAs quantum dots, *Appl. Phys. Lett.* **91**(24), 242109 (2007).
- [28] M. Geller, A. Marent, T. Nowozin, D. Bimberg, N. Akçay, and N. Öncan, A write time of 6 ns for quantum dot-based memory structures, *Appl. Phys. Lett.* **92**(9), 092108 (2008).
- [29] J. R. Arthur, Molecular beam epitaxy, *Surface Science* **500**, 189–217 (2002).
- [30] G. B. Stringfellow, *Organometallic Vapor-Phase Epitaxy: Theory and Practice*, Academic Press, San Diego, 2nd edition, 1999.
- [31] T. Mimura, S. Hiyamizu, T. Fujii, and K. Nanbu, A New Field-Effect Transistor with Selectively Doped GaAs/n-Al_xGa_{1-x}As Heterojunctions, *Jpn. J. Appl. Phys.* **19**, L225–L227 (1980).
- [32] D. Delagebeaudeuf, P. Delescluse, P. Etienne, M. Laviron, J. Chaplart, and N. T. Linh, Two-dimensional electron gas MESFET structure, *Electron. Lett.* **16**(17), 667–668 (1980).
- [33] I. Hayashi, M. B. Panish, P. W. Foy, and S. Sumski, Junction lasers which operate continuously at room temperature, *Appl. Phys. Lett.* **17**, 109 (1970).
- [34] D. Schicketanz and G. Zeidler, GaAs-Double-Heterostructure Lasers as Optical Amplifiers, *IEEE Journal of Quantum Electronics* **11**(2) (1975).
- [35] I. Vurgaftman, J. R. Meyer, and L. R. Ram-Mohan, Band parameters for III–V compound semiconductors and their alloys, *J. Appl. Phys.* **89**(11), 5815–5875 (2001).
- [36] H. Kroemer, Barrier control and measurements: Abrupt semiconductor heterojunctions, *J. Vac. Sci. Technol. B* **2**(3), 433–439 (1984).
- [37] S. M. Sze and K. K. Ng, *Physics of Semiconductor Devices*, John Wiley & Sons, 3rd edition, 2006.
- [38] J. H. Davies, *The Physics of low-dimensional Semiconductors*, Cambridge University Press, 1998.
- [39] E. Conwell and V. F. Weisskopf, Theory of Impurity Scattering in Semiconductors, *Phys. Rev.* **77**(3), 388–390 (1950).
- [40] R. Dingle, H. L. Störmer, A. C. Gossard, and W. Wiegmann, Electron mobilities in modulation-doped semiconductor heterojunction superlattices, *Appl. Phys. Lett.* **33**(7), 665 (1978).

-
- [41] C. T. Foxon, Three decades of molecular beam epitaxy, *Journal of Crystal Growth* **251**, 1–8 (2003).
- [42] K. v. Klitzing, G. Dorda, and M. Pepper, New Method for High-Accuracy Determination of the Fine-Structure Constant Based on Quantized Hall Resistance, *Phys. Rev. Lett.* **45**(6), 494–497 (1980).
- [43] K. v. Klitzing, The quantized Hall effect, *Rev. Modern Physics* **58**(3), 519–531 (1986).
- [44] M. J. Manfra, L. N. Pfeiffer, K. W. West, R. d. Picciotto, and K. W. Baldwin, High mobility two-dimensional hole system in GaAs/AlGaAs quantum wells grown on (100) GaAs substrates, *Appl. Phys. Lett.* **86**, 162106 (2005).
- [45] S. Tiwari, F. Rana, K. Chan, L. Shi, and H. Hanafi, Single charge and confinement effects in nano-crystal memories, *Appl. Phys. Lett.* **69**(9), 1232 (1996).
- [46] K. Koike, K. Saitoh, S. Li, S. Sasa, M. Inoue, and M. Yano, Room-temperature operation of a memory-effect AlGaAs/GaAs heterojunction field-effect transistor with self-assembled InAs nanodots, *Appl. Phys. Lett.* **76**(11), 1464 (2000).
- [47] H. Kim, T. Noda, T. Kawazu, and H. Sakaki, Control of Current Hysteresis Effects in a GaAs/n-AlGaAs Quantum Trap Field Effect Transistor with Embedded InAs Quantum Dots, *Jpn. J. Appl. Phys.* **39**, 7100 (2000).
- [48] G. Yusa and H. Sakaki, Trapping of photogenerated carriers by InAs quantum dots and persistent photoconductivity in novel GaAs/n-AlAs field-effect transistor structures, *Appl. Phys. Lett.* **70**(3), 345 (1997).
- [49] C. Balocco, A. M. Song, and M. Missous, Room-temperature operations of memory devices based on self-assembled InAs quantum dot structures, *Appl. Phys. Lett.* **85**(24), 5911–5913 (2004).
- [50] D. Nataraj, N. Ooike, J. Motohisa, and T. Fukui, Fabrication of one-dimensional GaAs channel-coupled InAs quantum dot memory device by selective-area metal-organic vapor phase epitaxy, *Appl. Phys. Lett.* **87**, 193103 (2005).
- [51] Y. Arakawa and H. Sakaki, Multidimensional quantum well laser and temperature dependence of its threshold current, *Appl. Phys. Lett.* **40**, 939 (1982).
- [52] N. Kirstaedter, N. N. Ledentsov, M. Grundmann, D. Bimberg, V. M. Ustinov, S. S. Ruvimov, M. V. Maximov, P. S. Kop'ev, Z. I. Alferov, U. Richter, P. Werner, U. Gosele, and J. Heydenreich, Low threshold, large T_0 injection laser emission from (InGa)As quantum dots, *Electron. Lett.* **30**(17), 1416 (1994).

- [53] F. Heinrichsdorff, C. Ribbat, M. Grundmann, and D. Bimberg, High-power quantum-dot lasers at 1100 nm, *Appl. Phys. Lett.* **76**(5), 556–558 (2000).
- [54] X. Huang, A. Stintz, H. Li, L. F. Lester, J. Cheng, and K. J. Malloy, Passive mode-locking in 1.3 μm two-section InAs quantum dot lasers, *Appl. Phys. Lett.* **78**, 2825 (2001).
- [55] M. Kuntz, G. Fiol, M. Lämmlin, D. Bimberg, M. G. Thompson, K. T. Tan, C. Marinelli, R. V. Penty, I. H. White, V. M. Ustinov, A. E. Zhukov, Y. M. Shernyakov, and A. R. Kovsh, 35 GHz mode-locking of 1.3 μm quantum dot lasers, *Appl. Phys. Lett.* **85**, 843 (2004).
- [56] F. Hopfer, A. Mutig, M. Kuntz, G. Fiol, D. Bimberg, N. N. Ledentsov, V. A. Shchukin, S. S. Mikhrin, D. L. Livshits, I. L. Krestnikov, A. R. Kovsh, N. D. Zakharov, and P. Werner, Single-mode submonolayer quantum-dot vertical-cavity surface-emitting lasers with high modulation bandwidth, *Appl. Phys. Lett.* **89**, 141106 (2006).
- [57] M. Lämmlin, G. Fiol, C. Meuer, M. Kuntz, F. Hopfer, A. R. Kovsh, N. N. Ledentsov, and D. Bimberg, Distortion-free optical amplification of 20-80 GHz modelocked laser pulses at 1.3 μm using quantum dots, *Electronics Lett.* **42**, 697 (2006).
- [58] A. Lochmann, E. Stock, O. Schulz, F. Hopfer, D. Bimberg, V. Haisler, A. Toropov, A. Bakarov, and A. Kalagin, Electrically driven single quantum dot polarised single photon emitter, *Electron. Lett.* **42**(13), 774–775 (2006).
- [59] E. Stock, T. Warming, I. Ostapenko, S. Rodt, A. Schliwa, J. A. Töfflinger, A. Lochmann, A. I. Toropov, S. A. Moshchenko, D. V. Dmitriev, V. A. Haisler, and D. Bimberg, Single-photon emission from InGaAs quantum dots grown on (111) GaAs, *Appl. Phys. Lett.* **96**, 093112 (2010).
- [60] W. Unrau, D. Quandt, J.-H. Schulze, T. Heindel, T. D. Germann, O. Hitzemann, A. Strittmatter, S. Reitzenstein, U. W. Pohl, and D. Bimberg, Electrically driven single photon source based on a site-controlled quantum dot with self-aligned current injection, *Appl. Phys. Lett.* **101**(21), 211119 (2012).
- [61] F. C. Frank and J. H. v. d. Merwe, *Proc. Roy. Soc. Lond. A* **198**, 205 (1949).
- [62] M. Volmer and A. Weber, *Zeitschr. f. phys. Chem.* **119**, 277 (1926).
- [63] V. A. Shchukin and D. Bimberg, Spontaneous ordering of nanostructures on crystal surfaces, *Rev. Modern Physics* **71**, 1125 (1999).

- [64] I. N. Stranski and L. Krastanow, Zur Theorie der orientierten Ausscheidung von Ionenkristallen aufeinander, *Sitzungsber. Akad. Wiss. Wien, Math.-Naturwiss. Kl., Abt. 2B* **146**, 797 (1938).
- [65] K. Jacobi, Atomic structure of InAs quantum dots on GaAs, *Progress in Surface Science* **71**, 185–215 (2003).
- [66] J. Marquez, L. Geelhaar, and K. Jacobi, Atomically resolved structure of InAs quantum dots, *Appl. Phys. Lett.* **78**(16), 2309–2311 (2001).
- [67] C. Cohen-Tannoudji, B. Diu, and F. Laloe, *Quantenmechanik - Band I und II*, Gruyter, 2nd edition, 1999.
- [68] M. Grundmann, O. Stier, and D. Bimberg, InAs/GaAs pyramidal quantum dots: Strain distribution, optical phonons, and electronic structure, *Phys. Rev. B* **52**, 11969–11981 (1995).
- [69] O. Stier, M. Grundmann, and D. Bimberg, Electronic and optical properties of strained quantum dots modeled by 8-band-k.p theory, *Phys. Rev. B* **59**, 5688 (1999).
- [70] A. Schliwa, M. Winkelkemper, and D. Bimberg, Impact of Size, Shape and Composition on Piezoelectric Effects and the Electronic Properties of InGaAs/GaAs Quantum Dots, *Phys. Rev. B* **76**, 205324 (2007).
- [71] International Technology Roadmap for Semiconductors (ITRS), Executive Summary, 2011 Edition, (2011).
- [72] P. Pavan, R. Bez, P. Olivo, and E. Zanoni, Flash memory cells - An overview, *Proceedings of the IEEE* **85**(8), 1248–1271 (1997).
- [73] F. Masuoka, M. Asano, H. Iwahashi, T. Komuro, and S. Tanaka, A new flash EEPROM cell using triple polysilicon technology, *IEEE IEDM Tech. Dig.* , 464–467 (1984).
- [74] Landolt-Bornstein - Group III Condensed Matter, in *SpringerMaterials - The Landolt-Bornstein Database*, volume 41A2b, accessed April 2012, doi: 10.1007/b83098.
- [75] T. Müller, F. F. Schrey, G. Strasser, and K. Unterrainer, Ultrafast intraband spectroscopy of electron capture and relaxation in InAs/GaAs quantum dots, *Appl. Phys. Lett.* **83**(17), 3572–3574 (2003).
- [76] M. Geller, A. Marent, E. Stock, D. Bimberg, V. I. Zubkov, I. S. Shulgunova, and A. V. Solomonov, Hole capture into self-organized InGaAs quantum dots, *Appl. Phys. Lett.* **89**(23), 232105 (2006).

- [77] M. Russ, C. Meier, B. Marquardt, A. Lorke, D. Reuter, and A. D. Wieck, Quantum dot electrons as controllable scattering centers in the vicinity of a two-dimensional electron gas, *Phase Transitions* **79**(9-10), 765–770 (2006).
- [78] B. Marquardt, M. Geller, A. Lorke, D. Reuter, and A. D. Wieck, Using a two-dimensional electron gas to study nonequilibrium tunneling dynamics and charge storage in self-assembled quantum dots, *Appl. Phys. Lett.* **95**, 022113 (2009).
- [79] M. Russ, C. Meier, A. Lorke, D. Reuter, and A. D. Wieck, Role of quantum capacitance in coupled low-dimensional electron systems, *Phys. Rev. B* **73**, 115334 (2006).
- [80] A. Rack, R. Wetzler, A. Wacker, and E. Schöll, Dynamical bistability in quantum-dot structures: Role of Auger processes, *Phys. Rev. B* **66**(16), 165429 (2002).
- [81] M. Geller, C. Kapteyn, L. Müller-Kirsch, R. Heitz, and D. Bimberg, 450 meV hole localization energy in GaSb/GaAs quantum dots, *Appl. Phys. Lett.* **82**(16), 2706–2708 (2003).
- [82] A. Marent, M. Geller, D. Bimberg, A. P. Vasi'ev, E. S. Semenova, A. E. Zhukov, and V. M. Ustinov, Carrier storage time of milliseconds at room temperature in self-organized quantum dots, *Appl. Phys. Lett.* **89**(7), 072103 (2006).
- [83] T. Nowozin, A. Marent, M. Geller, D. Bimberg, N. Akçay, and N. Öncan, Temperature and electric field dependence of the carrier emission processes in a quantum dot-based memory structure, *Appl. Phys. Lett.* **94**, 042108 (2009).
- [84] M. Lannoo and J. Bourgoin, *Point Defects in Semiconductors I - Theoretical Aspects*, volume 22 of *Springer Series in Solid-State Sciences*, Springer, Berlin, 1981.
- [85] P. Blood and J. W. Orton, *The Electrical Characterization of Semiconductors: Majority Carriers and Electron States*, Academic Press, London, 1992.
- [86] C. Kapteyn, *Carrier Emission and Electronic Properties of Self-Organized Semiconductor Quantum Dots*, Mensch & Buch Verlag, Berlin, 2001, Dissertation, Technische Universität Berlin.
- [87] M. Geller, *Investigation of Carrier Dynamics in Self-Organized Quantum Dots for Memory Devices*, Dissertation, Technische Universität Berlin, 2007.
- [88] U. Bockelmann and G. Bastard, Phonon scattering and energy relaxation in two-, one-, and zero-dimensional electron gases, *Phys. Rev. B* **42**, 8947 (1990).

- [89] R. Ferreira and G. Bastard, Phonon-assisted capture and intradot Auger relaxation in quantum dots, *Appl. Phys. Lett.* **74**(19), 2818 (1999).
- [90] J. Bourgoin and M. Lannoo, *Point Defects in Semiconductors II - Experimental Aspects*, volume 35 of *Springer Series in Solid-State Sciences*, Springer, Berlin, 1983.
- [91] D. V. Lang and C. H. Henry, Nonradiative recombination at deep levels in GaAs and GaP by lattice-relaxation multiphonon emission, *Phys. Rev. B* **35**(22), 1525–1528 (1975).
- [92] J. Frenkel, On pre-breakdown phenomena in insulators and electronic semiconductors, *Phys. Rev.* **54**, 647 (1938).
- [93] G. Vincent, A. Chantre, and D. Bois, Electric field effect on the thermal emission of traps in semiconductor junctions, *J. Appl. Phys.* **50**(8), 5484 (1979).
- [94] W. Nolting, *Grundkurs theoretische Physik - Band 5/2: Quantenmechanik*, Springer, Berlin Heidelberg, 2004.
- [95] P. W. Fry, J. J. Finley, L. R. Wilson, A. Lemaitre, D. J. Mowbray, and M. S. Skolnick, Electric-field-dependent carrier capture and escape in self-assembled InAs/GaAs quantum dots, *Appl. Phys. Lett.* **77**(26), 4344 (2000).
- [96] J. Gelze, *Ladungsträgerdynamik in Quantenpunkt-basierten Speicherbausteinen*, Diplomarbeit, TU-Berlin, 2009.
- [97] W. Nolting, *Grundkurs Theoretische Physik - Band 7: Viel-Teilchen-Theorie*, Springer, Berlin Heidelberg, 2009.
- [98] R. J. Warburton, B. T. Miller, C. S. Dürr, C. Bödefeld, K. Karrai, J. P. Kotthaus, G. Medeiros-Ribeiro, P. M. Petroff, and S. Huant, Coulomb interactions in small charge-tunable quantum dots: A simple model, *Phys. Rev. B* **58**(24), 16221–16231 (1998).
- [99] A. Schliwa, M. Winkelkemper, and D. Bimberg, Few-particle energies versus geometry and composition of $\text{In}_x\text{Ga}_{1-x}\text{As}/\text{GaAs}$ self-organized quantum dots, *Phys. Rev. B* **79**, 075443 (2009).
- [100] W. Walukiewicz, Hole mobility in modulation-doped heterostructures: GaAs-AlGaAs, *Phys. Rev. B* **31**(8), 5557 (1985).
- [101] D. Belitz and S. D. Sarma, Plasmon linewidth in metals and semiconductors: A memory-function approach, *Phys. Rev. B* **34**, 8264–8269 (1986).

-
- [102] W. Götze and P. Wölfle, Homogeneous Dynamical Conductivity of Simple Metals, *Phys. Rev. B* **6**, 1226 (1972).
- [103] G. Kiesslich and T. Brandes, Remote impurity scattering in a 2DHG, (2009), private communication.
- [104] L. Guo, E. Leobandung, L. Zhuang, and S. Y. Chou, Fabrication and characterization of room temperature silicon single electron memory, *J. Vac. Sci. Technol. B* **15**(6), 2840 (1997).
- [105] S. Luryi, Quantum capacitance devices, *Appl. Phys. Lett.* **52**, 501 (1988).
- [106] D. K. Schroder, *Semiconductor material and device characterization*, John Wiley Sons, Hoboken, New Jersey, 3rd edition, 2006.
- [107] D. V. Lang, Deep-level transient spectroscopy: A new method to characterize traps in semiconductors, *J. Appl. Phys.* **45**(7), 3023 (1974).
- [108] G. L. Miller, D. V. Lang, and L. C. Kimerling, Capacitance Transient Spectroscopy, *Ann. Rev. Mat. Sci.* **7**, 377 (1977).
- [109] H. G. Grimmeiss and C. Ovrén, Fundamentals of junction measurements in the study of deep energy levels in semiconductors, *J. Phys. E: Sci. Instrum.* **14**, 1032 (1981).
- [110] M. Geller, E. Stock, C. Kapteyn, R. L. Sellin, and D. Bimberg, Tunneling emission from self-organized In(Ga)As/GaAs quantum dots observed via time-resolved capacitance measurements, *Phys. Rev. B* **73**(20), 205331 (2006).
- [111] O. Engström, M. Kaniewska, M. Kaczmarczyk, and W. Jung, Electron tunneling from quantum dots characterized by deep level transient spectroscopy, *Appl. Phys. Lett.* **91**, 133117 (2007).
- [112] S. Anand, N. Carlsson, M.-E. Pistol, L. Samuelson, and W. Seifert, Deep level transient spectroscopy of InP quantum dots, *Appl. Phys. Lett.* **67**(20), 3016 (1995).
- [113] S. Anand, N. Carlsson, M.-E. Pistol, L. Samuelson, and W. Seifert, Electrical characterization of InP/GaInP quantum dots by space charge spectroscopy, *J. Appl. Phys.* **84**(7), 3747 (1998).
- [114] C. M. A. Kapteyn, F. Heinrichsdorff, O. Stier, R. Heitz, M. Grundmann, N. D. Zakharov, D. Bimberg, and P. Werner, Electron Escape from InAs Quantum Dots, *Phys. Rev. B* **60**(20), 14265 (1999).

- [115] C. M. A. Kapteyn, M. Lion, R. Heitz, D. Bimberg, P. N. Brunkov, B. V. Volovik, S. G. Konnikov, A. R. Kovsh, and V. M. Ustinov, Hole and electron emission from InAs quantum dots, *Appl. Phys. Lett.* **76**(12), 1573 (2000).
- [116] C. M. A. Kapteyn, M. Lion, R. Heitz, D. Bimberg, C. Miesner, T. Asperger, and G. Abstreiter, Many-particle effects in Ge quantum dots investigated by time-resolved capacitance spectroscopy, *Appl. Phys. Lett.* **77**(25), 4169 (2000).
- [117] O. Engström, M. Malmkvist, Y. Fu, H. Ö. Olafsson, and E. Ö. Sveinbjörnsson, Thermal emission of electrons from selected s-shell configurations in InAs/GaAs quantum dots, *Appl. Phys. Lett.* **83**(17), 3578–3580 (2003).
- [118] S. Schulz, S. Schnüll, C. Heyn, and W. Hansen, Charge-state dependence of InAs quantum-dot emission energies, *Phys. Rev. B* **69**(19), 195317 (2004).
- [119] P. Omling, L. Samuelson, and H. G. Grimmeis, Deep level transient spectroscopy evaluation of nonexponential transients in semiconductor alloys, *J. Appl. Phys.* **54**(9), 5117 (1983).
- [120] D. S. Day, M. Y. Tsai, B. G. Streetman, and D. V. Lang, Deep-level-transient spectroscopy: System effects and data analysis, *J. Appl. Phys.* **50**(8), 5093 (1979).
- [121] R. C. Ashoori, H. L. Störmer, J. S. Weiner, L. N. Pfeiffer, S. J. Pearton, K. W. Baldwin, and K. W. West, Single-Electron Capacitance Spectroscopy of Discrete Quantum Levels, *Phys. Rev. Lett.* **68**(20), 3088 (1992).
- [122] H. Drexler, D. Leonard, W. Hansen, J. P. Kotthaus, and P. M. Petroff, Spectroscopy of quantum levels in charge-tunable InGaAs quantum dots, *Phys. Rev. Lett.* **73**(16), 2252 (1994).
- [123] B. T. Miller, W. Hansen, S. Manus, R. J. Luyken, A. Lorke, J. P. Kotthaus, S. Huant, G. Medeiros-Ribeiro, and P. M. Petroff, Few-electron ground states of charge-tunable self-assembled quantum dots, *Phys. Rev. B* **56**(11), 6764 (1997).
- [124] R. J. Luyken, A. Lorke, A. O. Govorov, J. P. Kotthaus, G. Medeiros-Ribeiro, and P. M. Petroff, The dynamics of tunneling into self-assembled InAs dots, *Appl. Phys. Lett.* **74**(17), 2486 (1999).
- [125] G. Medeiros-Ribeiro, D. Leonard, and P. M. Petroff, Electron and hole energy levels in InAs self-assembled quantum dots, *Appl. Phys. Lett.* **66**(14), 1767 (1995).
- [126] C. Bock, K. H. Schmidt, U. Kunze, S. Malzer, and G. H. Dohler, Valence-band structure of self-assembled InAs quantum dots studied by capacitance spectroscopy, *Appl. Phys. Lett.* **82**(13), 2071–2073 (2003).

- [127] D. Reuter, P. Schafmeister, P. Kailuweit, and A. D. Wieck, Frequency-dependent $C(V)$ spectroscopy of the hole system in InAs quantum dots, *Physica E* **21**, 445–450 (2004).
- [128] D. Reuter, P. Kailuweit, A. D. Wieck, U. Zeitler, O. Wibbelhoff, C. Meier, A. Lorke, and J. C. Maan, Coulomb-Interaction-Induced Incomplete Shell Filling in the Hole System of InAs Quantum Dots, *Phys. Rev. Lett.* **94**, 026808 (2005).
- [129] M. Geller, B. Marquardt, A. Lorke, D. Reuter, and A. D. Wieck, A Two-Dimensional Electron Gas as a Sensitive Detector for Time-Resolved Tunneling Measurements on Self-Assembled Quantum Dots, *Nanoscale Research Letters* **5**, 829–833 (2010).
- [130] B. Marquardt, M. Geller, B. Baxevanis, D. Pfannkuche, A. D. Wieck, D. Reuter, and A. Lorke, Transport spectroscopy of non-equilibrium many-particle spin states in self-assembled quantum dots, *Nat. Commun.* **2**, 209 (2011).
- [131] B. Marquardt, A. Beckel, A. Lorke, A. D. Wieck, D. Reuter, and M. Geller, The influence of charged InAs quantum dots on the conductance of a two-dimensional electron gas: Mobility vs. carrier concentration, *Appl. Phys. Lett.* **99**(22), 223510 (2011).
- [132] J. M. Elzerman, R. Hanson, L. H. W. v. Beveren, B. Witkamp, L. M. K. Vandersypen, and L. P. Kouwenhoven, Single-shot read-out of an individual electron spin in a quantum dot, *Nature* **430**, 431–435 (2004).
- [133] S. Gustavsson, R. Leturcq, B. Simovič, R. Schleser, T. Ihn, P. Studerus, and K. Ensslin, Counting Statistics of Single Electron Transport in a Quantum Dot, *Phys. Rev. Lett.* **96**, 076605 (2006).
- [134] S. Gustavsson, R. Leturcq, M. Studer, I. Shorubalko, T. Ihn, K. Ensslin, D. C. Driscoll, and A. C. Gossard, Electron counting in quantum dots, *Surface Science Reports* **64**(6), 191–232 (2009).
- [135] T. Nowozin, A. Marent, L. Bonato, A. Schliwa, D. Bimberg, E. P. Smakman, J. K. Garleff, P. M. Koenraad, R. J. Young, and M. Hayne, Linking structural and electronic properties of high-purity self-assembled GaSb/GaAs quantum dots, *Phys. Rev. B* **86**, 035305 (2012).
- [136] G. Stracke, A. Glacki, T. Nowozin, L. Bonato, S. Rodt, C. Prohl, A. Lenz, H. Eisele, A. Strittmatter, A. Schliwa, U. W. Pohl, and D. Bimberg, Growth of $\text{In}_{0.25}\text{Ga}_{0.75}\text{As}$ quantum dots on GaP utilizing a GaAs interlayer, *Appl. Phys. Lett.* **101**, 223110 (2012).

- [137] T. Nowozin, L. Bonato, A. Högner, A. Wiengarten, D. Bimberg, W.-H. Lin, S.-Y. Lin, C. J. Reyner, B. L. Liang, and D. L. Huffaker, 800 meV localization energy in GaSb/GaAs/Al_{0.3}Ga_{0.7}As quantum dots, *Appl. Phys. Lett.* **102**, 052115 (2013).
- [138] S.-Y. Lin, C.-C. Tseng, W.-H. Lin, S.-C. Mai, S.-Y. Wu, S.-H. Chen, and J.-I. Chyi, Room-temperature operation type-II GaSb/GaAs quantum-dot infrared light-emitting diode, *Appl. Phys. Lett.* **96**, 123503 (2010).
- [139] C.-C. Tseng, S.-C. Mai, W.-H. Lin, S.-Y. Wu, B.-Y. Yu, S.-H. Chen, S.-Y. Lin, J.-J. Shyue, and M.-C. Wu, Influence of As on the Morphologies and Optical Characteristics of GaSb/GaAs Quantum Dots, *IEEE Journal of Quantum Electronics* **47**(3), 335 (2011).
- [140] P. N. Brounkov, A. Polimeni, S. T. Stoddart, M. Henini, L. Eaves, P. C. Main, A. R. Kovsh, Y. G. Musikhin, and S. G. Konnikov, Electronic structure of self-assembled InAs quantum dots in GaAs matrix, *Appl. Phys. Lett.* **73**(8), 1092 (1998).
- [141] A. Wiengarten, *Type-II nanostructures for a novel memory device*, Masterarbeit, Technische Universität Berlin, 2012.
- [142] E. P. Smakman, J. K. Garleff, R. J. Young, M. Hayne, P. Rambabu, and P. Koenraad, GaSb/GaAs quantum dot formation and demolition studied with cross-sectional scanning tunneling microscopy, *Appl. Phys. Lett.* **100**, 142116 (2012).
- [143] O. Flebbe, H. Eisele, T. Kalka, F. Heinrichsdorff, A. Krost, D. Bimberg, and M. Dähne-Prietsch, Atomic structure of stacked InAs quantum dots grown by metal-organic chemical vapor deposition, *J. Vac. Sci. Technol. B* **17**(4), 1639 (1999).
- [144] W.-H. Lin, M.-Y. Lin, S.-Y. Wu, and S.-Y. Lin, Room-Temperature Electroluminescence of Type-II GaSb/GaAs Quantum Rings, *IEEE Photonics Technology Letters* **24**(14), 1203 (2012).
- [145] L. Pedesseau, J. Even, A. Bondi, W. Guo, S. Richard, H. Folliot, C. Labbe, C. Cornet, O. Dehaese, A. L. Corre, O. Durand, and S. Loualiche, Theoretical study of highly strained InAs material from first-principles modelling: application to an ideal QD, *J. Phys. D: Appl. Phys.* **41**, 165505 (2008).
- [146] A. Beyer, J. Ohlmann, S. Liebich, H. Heim, G. Witte, W. Stolz, and K. Volz, GaP heteroepitaxy on Si(001): Correlation of Si-surface structure, GaP growth conditions, and Si-III/V interface structure, *J. Appl. Phys.* **111**, 083534 (2012).

- [147] Landolt-Bornstein - Group III Condensed Matter - Gallium phosphide (GaP), energies and capture cross sections of hole traps, in *SpringerMaterials - The Landolt-Bornstein Database*, volume 41A2b, accessed December 2012, doi: 10.1007/10860305_52.
- [148] J. R. Taylor, *An introduction to error analysis*, University Science Books, Sausalito, 1997.
- [149] A. M. Högner, *GaSb-quantum dots as storage units in memory cells*, Diplomarbeit, Technische Universität Berlin, 2010.
- [150] C. G. V. d. Walle, Band lineups and deformation potentials in the model-solid theory, *Phys. Rev. B* **39**(3), 1871 (1989).
- [151] S. M. North, P. R. Briddon, M. A. Cusack, and M. Jaros, Electronic structure of GaSb/GaAs quantum dots, *Phys. Rev. B* **58**(19), 12601 (1998).
- [152] S.-H. Wei and A. Zunger, Calculated natural band offsets of all II-VI and III-V semiconductors: Chemical trends and the role of cation d orbitals, *Appl. Phys. Lett.* **72**, 2011 (1998).
- [153] H.-S. Ling and C.-P. Lee, Evolution of self-assembled InAs quantum ring formation, *J. Appl. Phys.* **102**, 024314 (2007).
- [154] T. Nowozin, A. Marent, G. Hönig, A. Schliwa, D. Bimberg, A. Beckel, B. Marquardt, A. Lorke, and M. Geller, Time-resolved high-temperature detection with single charge resolution of holes tunneling into many-particle quantum dot states, *Phys. Rev. B* **84**, 075309 (2011).
- [155] T. Nowozin, A. Marent, D. Bimberg, A. Beckel, B. Marquardt, A. Lorke, and M. Geller, Time-resolved detection of many-particle hole states in InAs/GaAs quantum dots using a two-dimensional hole gas up to 77 K, *phys. stat. sol. c* **9**(2), 243–246 (2012).
- [156] nextnano³, nextnano GmbH, Germany, <http://www.nextnano.de>, accessed 2010.
- [157] A. Savitzky and M. J. E. Golay, Smoothing and Differentiation of Data by Simplified Least Squares Procedures, *Anal. Chem.* **36**(8), 1627–1639 (1964).
- [158] C. Kindel, S. Kako, T. Kawano, H. Oishi, Y. Arakawa, G. Hönig, M. Winkelkemper, A. Schliwa, A. Hoffmann, and D. Bimberg, Exciton fine-structure splitting in GaN/AlN quantum dots, *Phys. Rev. B* **81**, 241309(R) (2010).
- [159] 1D Poisson Program, by G. Snider, University of Notre Dame, USA, <http://www3.nd.edu/~gsnider/>, accessed 2008.

-
- [160] M. Field, C. G. Smith, M. Pepper, D. A. Ritchie, J. E. F. Frost, G. A. C. Jones, and D. G. Hasko, Measurements of Coulomb blockade with a noninvasive voltage probe, *Phys. Rev. Lett.* **70**, 1311–1314 (1993).
- [161] K. Yano, T. Ishii, T. Hashimoto, T. Kobayashi, F. Murai, and K. Seki, Room-temperature single-electron memory, *IEEE Transactions on Electron Devices* **41**(9) (1994).
- [162] K. K. Likharev, Single-electron devices and their applications, *Proceedings of the IEEE* **87**(4), 606–632 (1999).
- [163] E. F. Schubert, A. Fischer, and K. Ploog, The Delta-Doped Field-Effect Transistor (Delta-Fet), *IEEE Transactions on Electron Devices* **33**(5), 625–632 (1986).
- [164] E. F. Schubert, editor, *Delta-doping of Semiconductors*, Cambridge University Press, 2005.
- [165] A. D. Andreev and E. P. O'Reilly, Theory of the electronic structure of GaN/AlN hexagonal quantum dots, *Phys. Rev. B* **62**(23), 15851–15870 (2000).
- [166] A. D. Andreev and E. P. O'Reilly, Optical transitions and radiative lifetime in GaN/AlN self-organized quantum dots, *Appl. Phys. Lett.* **79**(4), 521 (2001).

Danksagung

An dieser Stelle möchte ich mich bei all denen bedanken, die zum Gelingen dieser Arbeit beigetragen haben.

Als erstes möchte ich Prof. Dieter Bimberg für die Möglichkeit danken, in seiner Arbeitsgruppe über das spannende Thema der quantenpunktbasierten Speicher promovieren zu können. Neben der exzellenten finanziellen Ausstattung, war es vor allem sein Vertrauen in meine Arbeit, das es mir ermöglichte, selbstorganisiert und eigenverantwortlich zu arbeiten, und so dem Ziel, einen QD-Flash zu bauen, ein Stück weit näher zu kommen und dabei noch eine Menge zu lernen. Vielen Dank!

Prof. Axel Lorke danke ich für die Übernahme des Zweitgutachtens, Prof. Michael Lehmann für den Prüfungsvorsitz.

Es gibt zwei Personen, denen ich besonders danken muss, denn sie haben mein wissenschaftliches Denken und meine methodischen Fähigkeiten entscheidend geprägt: Andreas Marent und Martin (Paul) Geller. Andreas hat über vier Jahre meinen Weg in der Wissenschaft erfolgreich und dazu kurzweilig begleitet. Paul danke ich vor allem für seine stete telefonische Fernmotivation („Doch, doch, das geht!“). Beiden danke ich für viele physikalische und nicht-physikalische Diskussionen.

Einen entscheidenden Anteil am Zustandekommen dieser Arbeit haben Annika Högner, Leo Bonato, Michael Narodovitch und Alissa Wiengarten, deren Diplom-, Master- und Bachelorarbeiten ich betreuen durfte. Darüberhinaus danke ich Leo Bonato für die entspannte und produktive Büroatmosphäre.

Andreas Beckel danke ich besonders für die fruchtbaren Diskussionen rund um MODFETs, Kontaktwiderstände und Tunnelmessungen. Vor allem bin ich ihm bei den Ersatzschaltbildern und Simulationen zu Dank verpflichtet. Auch Bastian Marquardt möchte ich an dieser Stelle danken.

Andrei Schliwa und Gerald Hönig danke ich für steten theoretischen Input und die 8-band- $\mathbf{k}\cdot\mathbf{p}$ -Rechnungen, sowie für die einhergehenden Erläuterungen und Diskussionen.

Für das umfangreiche Probenwachstum danke ich Alexander Glacki, Gernot Stracke und André Strittmatter aus Berlin, Robert J. Young und Manus Hayne aus Lancaster, Wei-Hsun Lin und Shih-Yen Lin aus Taiwan, Charles J. Reyner, Baolai L. Liang und Diana L. Huffaker aus Los Angeles.

Ganz besonders möchte ich auch Kathrin Schattke für ihr unermüdliches Engagement in der Epitaxie danken.

Ohne einen funktionierenden Reinraum können die besten Proben nicht vermessen werden, deshalb muss ich den Säulen des Reinraums danken: Mirko Stubenrauch, Kristijan Posilovic, Dejan Arsenijević, Philip Moser, Gunter Larisch, Ronny Schmidt, Stephan Bock und Werner Hofmann. Bei Mirko möchte ich mich besonders für die Rezeptentwicklung bedanken.

Für die X-STM-Messungen und die produktive und freundschaftliche Kooperation im Rahmen des QD2D-Projekts danke ich Erwin P. Smakman, Jens K. Garleff und Paul M. Koenraad von

der TU Eindhoven.

Keine Wissenschaft ohne ein wenig Administration! Deshalb gilt mein Dank Ulrike Grupe, Roswitha Koskinas, Hella Farrell, Ines Rudolph, Doreen Nitzsche, Susanne Ludwig und Thu Hoang. Auch bei Arleta Kraszewski, meinem Draht in die Verwaltung, möchte ich mich bedanken. Sie alle haben dazu beigetragen, dass ich neben der Organisation der Arbeitsgruppenfinanzen auch noch promovieren konnte.

Holger Schmeckebeer danke ich besonders für den steten Einsatz an der Druckerfront, Gernot Stracke für all die Lösungen bei Computerproblemen.

Ohne die tägliche Mittagsrunde wäre das Mittagessen nur halb so lecker, kurzweilig und informativ. Deshalb danke ich den aktuellen Mitgliedern Tobias Heindl, Caspar Hopfmann, Manuel Gschrey und Fabian Gericke, sowie den ehemaligen Andreas Marent, Erik Stock und Till Warming für stetes Infragestellen und Erklären der physikalischen und nicht-physikalischen Welt.

Bei der gesamten Arbeitsgruppe möchte ich mich für das produktive und kollegiale Gruppenklima bedanken.

Meinen Eltern, Reinhard und Annette, bin ich zu tiefstem Dank verpflichtet. Sie haben mich bei allem, was ich je unternommen habe, immer unterstützt und stets an mich geglaubt.

Meiner Lebensgefährtin Claudia Stoll danke ich, dass sie an meiner Seite für mich da ist.